The Dissertation Committee for Aaron Berkeley Albrecht Certifies that this is the approved version of the following dissertation:

Dynamic Response of Metal-Polymer Bilayers Subjected to Blast Loading

Committee:

Krishnaswamy Ravi-Chandar, Supervisor

Chad Landis

Kenneth Liechti

Mark Mear

Michael Marder

Dynamic Response of Metal-Polymer Bilayers Subjected to Blast Loading

by

Aaron Berkeley Albrecht, B.S.; M.S.E.

Dissertation

Presented to the Faculty of the Graduate School of

The University of Texas at Austin

in Partial Fulfillment

of the Requirements

for the Degree of

Doctor of Philosophy

The University of Texas at Austin

December 2012

Dedication

To those select teachers who have shaped the course of my life,

when the student was ready, you appeared. Thank you.

Acknowledgements

Without the constant support of my wife and family none of this would be possible.

This work was performed under a program entitled “Dynamic Response of Metal-Polymer Bilayers - Viscoelasticity, Adhesion and Failure” sponsored by the Office of Naval Research (ONR Grant Number N00014-09-1-0541, Program Manager: Dr. Roshdy Barsoum); this support is gratefully acknowledged.

Dynamic Response of Metal-Polymer Bilayers Subjected to Blast Loading

Aaron Berkeley Albrecht, Ph.D.

The University of Texas at Austin, 2012

Supervisor: Krishnaswamy Ravi-Chandar

The use of compliant coatings, in particular polyurea, for improved blast protection of structures has been reported recently in the literature. The goal of this research is to develop a comprehensive understanding of the reasons for improved performance of coated structures through experimentation and correlation with simulation. The different factors influencing the response of an elastomer coated ductile metal subjected to a blast load have been examined and quantified. First, dynamic strain localization in the metal is a precursor to ductile failure; this was characterized for the metal of interest with and without the polymer coating. Experiments with the expanding ring/tube and experiments have demonstrated that for Al 6061-O and Al 3003-H14, the localization strain is unaffected by both deformation rate and the polymer coating; however, two important effects of the coating have been explored. First the additional mass of the coating provides an inertial resistance. Second, the flow resistance of the polymer provides continued dissipation of energy even after the metal has yielded potentially preventing failure in the metal, or at least containing fragments. These effects were examined for two different types of polymers – polyurea, an elastomer and polycarbonate, a thermoplastic shear yielding polymer. It is shown that these two effects can be used to tailor the coating to optimize blast protection of the bilayer system.

In order to take advantage of this optimization, the constitutive behavior of the elastomer coating must be determined at strain rates and loading conditions that are experienced in the blast loading; these strain rates are in the range of 1000 to 10,000 per second. This has been accomplished through a hybrid method that combines measurements with numerical simulations to extract the constitutive response of the material. The strain rate dependent behavior of polyurea for rates in the range of 800-8000 per second has been determined by measuring the spatio-temporal evolution of the particle velocity and strain in a thin strip subjected to high speed impact loading that generates uniaxial stress conditions and comparing this with numerical simulations of the one-dimensional problem using the method of characteristics. A similar scheme to track the particle velocity and strain during the axisymmetric deformation of a membrane subjected to high speed loading has also been developed; this requires two projections of the deformation to be obtained in order to facilitate the measurement of axial and kink waves in the membrane. The finite volume method is adapted for simulations of these dynamic uniaxial and axisymmetric problems with a view towards simulating shock waves that are expected to form in some loading conditions. The hybrid method is used once again to characterize the constitutive response. The axisymmetric experiments have demonstrated the inability of the uniaxial models for both polyisoprene rubber and polyurea to completely capture their behavior during a more complex loading, and left a need for further work on characterizing the dynamic constitutive response of these polymers.

Table of Contents

List of Tables

List of Figures

Chapter 1: Introduction

Blast protection has become an important problem in many military and civilian structures. In this regard, a rather interesting phenomenon has been observed experimentally; coating structural components with a layer of a compliant polymer, typically an elastomer with a glass transition temperature significantly below the use temperature, decreases the propensity of the structure to fracture and fragment (Mathews, 2004; Barsoum and Dudt, 2009). This observation has spawned a large number of research efforts aimed at understanding and optimizing the performance of these composite structures, but full quantitative characterization has remained elusive. The goal of this research is to develop a comprehensive understanding through experimentation and correlation with simulation.

Polymer coatings to improve the blast performance of structures under blast loadings are commercially available. Specialty Products Inc. markets the coating under the brand name of Dragonshield: "Dragonshield BC™ spray-applied, blast mitigating polymer represents a breakthrough in plural component polyurea technology. This product offers superior energy absorbing and fragment containment capabilities through its unique combination of high tensile strength, elongation, and strain modulus" (SPI, Inc. 2009). The application to armor is also described: "DRAGONSHIELD-HT™ is a high build, fast set, polymer with a combination of physical properties which have proven to be very effective as an Energy Absorbing (EA) material. DRAGONSHIELD-HT™ polymer has been tested and verified as a protective material for mitigating damage caused during a blast event. When placed on the interior wall of a structure, Dragonshield effectively reduces pressure levels occupants must physically endure, while protecting them from fragmenting projectiles. This reduction in pressure also minimizes the

deflection of the wall during a blast event". The ability to spray the polyurea onto existing structures is an important aspect of this application; however, quantitative estimates of the efficiency are not available.

Coating structures is not the only way polymers have been used to improve blast resistance. They are also used in transparent armor applications where transparency to visible and other wavelengths is essential. There have been numerous studies of the dynamic failure behavior of ceramics used as transparent armor (see, for example Patel et al 2000, Shockey et al 2008, Strassberger 2009). Glass, laminated with alternating layers of polymers of varying thickness and fracture properties, is also a very commonly used as transparent armor (Bless and Chen, 2010). The fracture behavior of glass is rather well understood after nearly a century of investigations; however, the design of these multilayered structures, and characterization of their performance, requires experimental measurements of the properties of individual constituents of the multilayer system. In particular, while glass can be characterized as an elastic-brittle material, the rate-dependent material properties of the polymer interlayers must be characterized in order to analyze their response to high strain-rate loading. Adhesion of the interlayers is also expected to be an important factor in the behavior of the composite structure.

In this dissertation, we describe several techniques which have been developed to probe each area of interest. We begin with a focus on performing experiments to reveal the underlying deformation of the metallic specimen without and with a polymer coating. In particular, tubular specimens under uniform radial expansion are considered; this results in either a uniaxial stress state or a uniaxial strain state depending on the dimensions of the tube. Real-time diagnostics using high-speed photography and post-mortem examinations are used to determine the deformation and failure characteristics of the metal and metal-polymer bilayer systems. These experiments have led to the

understanding that the energy dissipation by the coating is due in part to its own resistance to deformation and in part to an inertial resistance provided by the addition of mass to the system. Design criteria have been developed to weigh these factors and optimize the efficiency of the coating.

In order to implement these design criteria properly, the high rate constitutive behavior of the elastomer must be known. The split-Hopkinson bar apparatus has evolved into the most common method for dynamic material characterization (see for example, Subhash and Ravichandran, 2000); it uses a small sample in order to establish a uniform stress and strain state in the specimen, avoids detailed analysis of wave propagation through the specimen material, and therefore eliminates the need for *a priori* knowledge of the material behavior. However, the assumption of uniformity of the stress and deformation within the specimen is rather severe, and limits the applicability of this technique to a certain class of materials and certain range of strain rates. For tension testing, the specimens are usually quite small and the strain rates obtained are typically in the range of about 10^2 –10^3 s^{-1}; the technique is better suited for compression characterization, with strain rates reaching nearly 10^4 s^{-1}. The measurement of strain-rate dependent tensile behavior of soft materials with a Hopkinson bar, particularly for large stretch levels, is fraught with difficulties; in addition to the problems arising from impedance mismatch with the loading bars that causes a very low signal to noise ratio, lateral inertia effects in the specimen, and the general nonhomogeneity of the stress and deformation in this test scheme provide very restrictive conditions under which the split Hopkinson bar may be used in tension. Furthermore, for applications in many soft materials, very large stretch levels are encountered; this necessitates long duration pulses – for example, to reach a stretch of two at a strain rate of 10^3 s^{-1} a pulse duration of 2 ms is required! Recently, Youssef and Gupta (2011) have developed a laser ablation based

method for characterizing the high strain rate response of polyurea; in this method, the propagation of a short-duration stress pulse through the specimen is used to back out the stress strain curve at strain rates on the order of 10^5 s^{-1}; however, due to the short duration of the loading, the peak strains attained are in the range of 2%. Youssef and Gupta (2011) were able to use this method to probe the linearly elastic and viscoelastic response of polyurea.

We suggest that any test method designed to investigate the dynamic constitutive behavior of soft materials at large strain-rates to very large strain levels must deal with transient states in a hybrid or inverse approach; such an approach places no restrictions on specimen length and it is not necessary to establish uniformity of stress state or strain-rate; in addition, there is no limit to the strain level that can be attained in the test specimen. In fact, the method is quite general and could be used for any material without restrictions. Expanding on the work of Niemczura and Ravi-Chandar (2011) by introducing rate dependence through viscoplasticity, the dynamic tensile response of a transparent elastomer, polyurea, is explored. A thin strip is fixed at one end and a velocity is applied to the other. By monitoring the nonlinear strain wave propagation with high speed imaging it is possible to establish that polyurea can be modeled with a modified Clifton-Zhou viscoplastic model for stretch rates in the range of 800-8000 s^{-1}. Blast loads however produce more complex loading conditions. In order to simulate the biaxial stress states expected in these circumstances, a dynamic membrane test was developed in which a thin membrane is impacted with a projectile. The ensuing axisymmetric deformation is recorded with two high speed cameras, again allowing for tracking of the nonlinear wave propagation which can be used to validate the material models developed during uniaxial testing. Polyisoprene rubber as well as polyurea were examined through the membrane

test and found to exhibit behavior which differed from that predicted by the dynamic uniaxial results.

We begin by discussing the expanding ring/tube experiment in Chapter 2. This test provides a means for examining the effect that polymer coatings have on the dynamic fracture and fragmentation of ductile metals, specifically Al 6061-O. In Chapter 3, we investigate and quantify the uniaxial dynamic tensile behavior of polyurea through an inverse method by monitoring the nonlinear wave propagation during dynamic stretching of long thin specimens and comparing that to simulated results based on the method of characteristics. The two-dimensional dynamic membrane deformation test which allows probing of the high rate biaxial behavior of both polyisoprene and polyurea is introduced in Chapter 4. Chapter 5 addresses the question of how the possible formation of tensile shocks can be accounted for during simulation by applying an alternative to the method of characteristics formulation – the finite volume method. Finally, the results and remaining challenges are summarized in Chapter 6.

Chapter 2: Dynamic Response of Aluminum and Polymer Coated Aluminum Tubes

2.1 BACKGROUND

The expanding ring experiment has been used by numerous investigators to study the deformation and failure of bare aluminum alloy and aluminum alloy with polymer coating (Niordson, 1965, Benson and Grady, 1983, Zhang and Ravi-Chandar, 2006, 2008, 2010, Zhang et al 2009). In these experiments, thin ring specimens are expanded by an electromagnetic loading device. The setup includes a 25μF capacitor, charged to several kV and then discharged through a small coil. The specimen is placed around that coil and the current induced in the specimen generates a magnetic field which is repelled by the magnetic field produced by the current flowing in the coil. This Lorentz force causes rapid radial expansion of the specimen with strain rates on the order of 10^4 s^{-1}.

The expansion of the ring specimen is monitored in real time by the use of a high speed camera placed along the axis of the ring. The high speed images allow the measurement of the ring radius as a function of time and therefore to record hoop strain. The general deformation processes of the ring that were observed and quantified in these studies can be broken down into several distinct phases. Initially, there is a period of uniform expansion which is continues until a critical strain is reached. At this critical strain, necks develop simultaneously at numerous locations around the ring. These necks grow as the expansion continues and eventually some of them result in fracture. After fracture, the fragments are unloaded but they continue their motion in the outward radial direction with significant kinetic energy. In this Chapter, we use the same apparatus as in the work of Zhang and Ravi-Chandar (2010) and examine the response of polymer coated aluminum tube specimens.

2.2 ALUMINUM 6061-O

In this section we describe the constitutive behavior of the Al 6061-O used in the expanding tube experiments. Quasi-static tensile tests (Zhang and Ravi-Chandar, 2006) demonstrated that the Al 6061-O can be modeled as a power law hardening material with the following representation: $\tau = \tau_y(1+\beta\varepsilon_p)^n$, where τ is Cauchy stress, and ε_p is true plastic strain. The material parameters obtained by fitting to the experimental response are $\beta = 14165$, $n = 0.22$, and $\tau_y = 25MPa$. During the quasi-static tensile tests, localization in the form of a neck was seen to occur at a strain of $\varepsilon_N^{qs} = 0.22$. As shown by Considère, a limit load is attained under uniaxial tension when:

$$dP = Ad\tau + \tau dA = 0 \tag{2.1}$$

For the power law hardening material described above, the limit load will be reached at a true strain that is nearly equal to the hardening exponent ($\varepsilon = n - \frac{1}{\beta}$). However, to have true uniaxial tension, the specimen should be thin and have a cross-sectional aspect ratio near 1. As the aspect ratio increases beyond about five, a second form of localization – sheet mode necking – emerges. The radial expansion of a tube or equivalently, the stretching of a plate provides different geometric constraints than those seen in the ring experiments. The question of localization in thin sheets of material under a variety of stress states is dealt with extensively in the literature on sheet metal forming; the strain state dependent localization strain is often referred to as the forming limit and can be established from the maximum load theory. Consider a biaxial load indicated by T_1 and $T_2 = \alpha T_1$; the limit load in this case will occur when $dT_1 = td\tau_1 + \tau_1 dt = 0$, where t is the thickness of the sheet and τ_1 is the true stress in the first principal direction. For a power hardening material the limit load, or forming limit, can be shown to correspond to the strain state given by:

$$\varepsilon_1 + \varepsilon_2 = n \tag{2.2}$$

The forming limit can be plotted in strain space; Figure 2.1 shows a forming-limit-diagram (FLD) where Eq. (2.2) is plotted as a dashed line. The dash-dotted line shows the strain state experienced in uniaxial tension, $\varepsilon_1 = -2\varepsilon_2$. The localization strain in uniaxial tension is then where that dash-dotted line crosses the forming limit (i.e. at $\varepsilon_1 = -2\varepsilon_2 = 2n$ for a power-law hardening material). Plane strain ($\varepsilon_2 = 0$) on the other hand would simply follow the vertical axis in the FLD and indicate that localization is expected at $\varepsilon_1 = n$.

2.3 POLYUREA

Polyurea is a common elastomer that has been used to coat surfaces in a wide range of applications. The usage of polyurea is driven by its chemical and abrasion resistance under many different environments. There are many different formulations available but the polyurea in the present work is formed by reaction of Isonate 143L (Dow Chemical) and Versalink P1000 (Air Products) with weight ratio of 1:4. The Versalink is degassed under vacuum at 30 °C with constant stirring until no bubbles are observed. The Versalink and Isonate are then mixed under vacuum in a weight ratio of 1:4 for 2 minutes. The next step depends on the final use. This study uses polyurea in several different experiments, each having its own requirements of the process. Regardless of the final use, however, the above preparation and mixing steps remain unchanged. In the case of coating the rings, the polyurea is poured into a purpose built Teflon mold with the ring. The mold establishes the coating thickness. The coated ring specimen is left to cure at room temperature in the mold for 24 hours and is ready for testing after a minimum of 7 days has passed. Coating of the tubes is accomplished with a two-step process. In the first step, the mixture of Isonate and Versalink is slowly poured

over the aluminum tube which is mounted on a slowly rotating Teflon mandrel. Because the mixture is extremely viscous, the mixture does not drip off the sample if the rotation speed is adjusted properly. The rotation of the mandrel is continued until the polyurea cures completely (in about 10 minutes). The specimen is left to cure on the mandrel for 7 days. The mandrel is then placed in a lathe and the polyurea is gradually machined down[1] to the desired thickness, typically in the range of 0.3 to 0.5 mm.

The quasi-static and dynamic constitutive behaviors have been examined by a number of investigators. A typical quasi-static tensile response of polyurea is shown in Figure 2.2, where the nominal stress, σ (force per original area) is plotted against the engineering strain, $\gamma = l/l_0 - 1 = \lambda - 1$ (λ, the ratio of the current length to the original length, is the stretch). This test was performed using one of the specimens from the same batch of specimens used for dynamic tensile characterization discussed in Chapter 3. Repeat tests on specimens from the same batches indicated very little variability, but the differences from different batches are influenced significantly by small changes in stoichiometry (see Roland et al. 2007, for a discussion of this variability). The initial modulus of elasticity is often taken to be around 100 to 200 MPa (see Chakkarapani et al, 2006, Amirkhizi et al. 2006, Zhao et al. 2007, Qiao et al. 2011) but the measured initial slope in this case was closer to 70 MPa[2]. Beyond a stress level of about ~2 MPa, (corresponding to a strain of ~0.05) the quasi-static stiffness decreases significantly and continuously, and a nonlinear stress-strain response is observed to large strain levels. After a nominal strain of ~0.6 the nominal stress remains nearly constant at about 4.4 MPa. Beyond a strain of about 3.2, a steep increase in the stress is observed with final

[1] When machining a soft material such as a polyurea, to achieve a smooth surface finish, a very sharp lathe tool is essential. Minimizing the feed speed and maximizing rotational speed also aids in decreasing surface roughness.

[2] In fact, there is never a truly linear region from which a proper elastic modulus can be extracted.

failure at a strain of about 5.8. It has been reported by Roland et al. (2007) that the stretch at which this stiffening occurs can be adjusted significantly by altering the stoichiometry. It is worth noting that the aluminum alloy on which this polyurea is coated will fracture long before the strain range where the polymer stiffening is reached. A number of dynamic compressive experiments have reported significant increases in stiffness as well as stress levels corresponding to the inelastic region due to rate effects (Amirkhizi et al. 2010; Yi et al. 2006). We have found that there is far less rate dependence in tension, a finding that is discussed in Chapter 4.

2.4 POLYCARBONATE

Polycarbonate was also considered as a coating material for the metal/polymer bilayer system. This choice was motivated by the fact that polycarbonate is a thermoplastic polymer with a shear yielding response; plastic flow occurs at a stress level of 50 to 80 MPa, but to logarithmic strain levels of about 0.6; in contrast, the Al 6061-O attains a stress level of about 140 MPa at a strain level of 0.22, but strain localization occurs at this level resulting in specimen failure. Since polycarbonate is in its glassy state at room temperature, it also exhibits a high stiffness (~2.5 GPa). Polycarbonate is modeled as an elastic-plastic material with an initial modulus of 2.5 GPa up to a strain level, $\varepsilon = 0.025$, after which the tangent modulus is reduced to 20 MPa. Beyond $\varepsilon = 0.6$, the polycarbonate is assumed to stiffen up again with a modulus equal to that of the original elastic modulus. This model does not incorporate intrinsic material softening that is typically used in constitutive models for such shear yielding polymers, but is capable of capturing the inelastic response of polycarbonate (Lu and Ravi-Chandar, 1999). The polycarbonate is applied as an external coating on Al 6061-O tubes by machining a

sleeve out of polycarbonate tube stock to dimensions of 16.25 mm mean radius and 0.5 mm wall thickness. A sliding fit is employed so that the sleeve can be fitted on the aluminum samples without the risk of damaging the very ductile metallic specimen. Although the polycarbonate is transparent in its stock form, once machined the surface finish becomes opaque, making it difficult to observe the electro-etched circular patterns on the metal surface. In order to overcome this problem, a staggered circular pattern is painted onto the surface of the polycarbonate sleeve by means of a stainless steel mask. The mask is aligned with the sleeve in such a way that the row and column directions of the pattern match the hoop and axial strain directions in the aluminum specimen; the separation of the painted circles in the hoop and axial directions is 1.778 mm and 1.015 mm respectively. These dimensions are used to measure the strain of the sample in real time; post mortem analysis is also performed on the chemically etched pattern on the aluminum in order to determine the local strains.

2.5 EXPANDING TUBE EXPERIMENT

2.5.1 Experimental Setup

In this work, an electromagnetic loading device was used for expanding Al 6061-O tubes coated with a layer of polyurea or polycarbonate; the details of construction and use of the loading device and the associated diagnostics are described in detail in Zhang and Ravi-Chandar (2006, 2010); here we provide a brief summary. The experimental arrangement is shown in Figure 2.3. This device includes a 25 μF capacitor and a choice of two copper coils, with 6-turn and 12-turn windings, which are encased in epoxy. For the experiments shown in this work, two lengths of Al 6061-O tube samples were used: 18 mm and 36 mm. All specimens were 30.5 mm in diameter and 0.5 mm wall thickness.

A Cordin Model 550 high-speed camera is used to monitor the expansion of the samples. This camera can record 30 frames with a resolution of 1000 x 1000 pixels; the magnification used results in a spatial resolution of 0.118 mm per pixel. The camera is synchronized with the experiment to record the event at a framing rate of ~150,000 frames per second; the expansion of the specimen can be followed for about 200 μs. Two xenon flash lamps are used to illuminate the sample; a conical diffusing reflector is also employed, as per the configuration seen in Figure 2.3a. In order to facilitate viewing the entire cylindrical surface of the specimen shown in Figure 2.3b, the conical mirror arrangement described in Figure 2 of Zhang and Ravi-Chandar (2010) is used; the unwrapping software discussed in that work allows for real time measurements of strain on the entire cylindrical surface of the sample.

In order to measure the local strain from the unwrapped reflection of the sample surface observed in the conical mirror, the tube surfaces were electrolytically etched[3] with a pattern of circles 2.719 mm in external diameter. The samples were then coated with their respective polymer cladding. The tube specimens are placed outside the coil – epoxy assembly. In these tests, the capacitor is charged to a maximum voltage of 16.5 kV, and then discharged through the coil, generating a rapidly alternating current; typical variation of the current with time can be found in Figure 2.4. As a result of this current flowing through the coil, a current is induced in the Al 6061-O tube; the interaction between the current in the coil and that in the sample generates repulsive Lorentz forces that apply a radial body force on the specimen, causing the characteristic high speed

[3] The etching is achieved by an electrolytic process. A fabric covered electrode (anode) is wetted with an electrolyte (Electrolyte solution LNC 9 by Lectroetch). A mask with the desired pattern is laid on the anode. The aluminum specimens are then fitted onto a Teflon mandrel and slowly rolled over the mask while in contact with the cathode of the circuit. As the circuit is closed, aluminum particles migrate from the sample through the openings in the mask, to the anode, etching a pattern on the specimens. Once the etching is complete the samples are washed with Formula 1 All Purpose Cleaner by Lectroetch.

radial expansion of the sample (note that the coil is firmly embedded in epoxy and is therefore immobile). The expansion speeds generated in these tests range from 55 m/s to 141 m/s; for the ~30 mm diameter specimens, this corresponds to strain rates in the range of ~3600 – 9200 s^{-1}.

2.5.2 Experimental Observations

Experiments were performed on 10 aluminum 6061-O samples, 4 using polycarbonate (PC) sleeves and 6 with polyurea (PU) coatings. The polyurea coated specimens exhibited expansion speeds of 55 - 141.3 m/s or strain rates of ~3600 – 9200 s^{-1}. In contrast, for the same range of imposed load levels, the polycarbonate coated specimens experienced expansion of speeds of 64.6 – 90.4 m/s or strain rates of ~4200 – 5900 s^{-1}. Table 1.1 shows the experimental conditions for each of these tests. Results from twelve uncoated Al 6061-O specimens are reported in Zhang and Ravi-Chandar (2010), where the expansion speeds were in the range of 69 to 196 m/s or strain rates of ~4,000 – 12,000 s^{-1}. Results from the PU and PC coated specimens are reported in detail in Morales et al. (2011).

Figures 2.5 and 2.6 present two selected sequences of images from expanding tube experiments of Al 6061-O tubes with polyurea and polycarbonate coatings, respectively. We will refer to these as Al/PU and Al/PC specimens. All images contain two views of the sample; at the center of each image the direct view of the expanding tube as seen in the direction of its longitudinal axis can be observed. Secondly, the reflection of the specimen surface in the conical mirror can be seen as an annular image around the direct view. This second image can be unwrapped using the conical mirror projection mapping technique discussed in Zhang and Ravi-Chandar (2010), allowing for

quantitative interpretation of the behavior of the specimen surface, such as the tracking of real time local strain evolution on the sample. Figures 2.7 and 2.8 show the unwrapped image sequences corresponding to the samples seen in Figures 2.5 and 2.6, where the entire surface of the cylindrical samples can clearly be observed, albeit with some distortion arising from the barreling of the cylindrical specimen. The evolution of the hoop and axial strains, as well as the onset of fracture, can be clearly observed from these images.

Using the images from Figures 2.5-2.8, it is possible to determine the strain evolution of the samples in two different ways. First, from the direct view, an average global strain evolution can be calculated by measuring the change in the mean radius of the sample. This measurement must be taken as an average because the expansion of the specimen is not perfectly uniform, resulting in a slight elliptical shape of the expanded tube. Second, the local hoop and axial strain evolution can be obtained by measuring the evolution of particular patterns on the specimen surfaces as a function of time. This is possible by using the unwrapped images of the events. It is worth noting that during the tests, the samples tend to barrel slightly as they expand; this means that the edges of the sample will be at a further distance from the conical mirror than the middle portions of the sample, causing a slight error in the size of the circles in the reflected image. This discrepancy induces a scaling error in the unwrapped image, affecting the measured strain. The center portion (lengthwise) of the sample is affected less by this phenomenon, therefore taking the local measurements of strain here will yield a more representative value for the local strain of the specimen. It must also me considered that the barreling of the specimen implies that the radial expansion of the center section of the tube will be greater than that of the edges. Since the average global strain is determined by measuring the variation of the sample radius at the edge closest to the camera, the obtained strain

level will be smaller than that measured locally according to the above provisions; the level of the discrepancy will depend on the degree of barreling observed. Figures 2.9 and 2.10 show the evolution of average global strain and local strain for the tests presented in Figures 2.5-2.8.

The evolution of deformation in the expanding tubes can be broken down into three phases similar to those in the expanding ring. First, there is a period of uniform radial expansion. Second, as the strain reaches a critical limit given by the FLD, uniform plastic straining ends and as expected, localization in the form of sheet-mode necking occurs. Similar to the observation on the rings, such localization occurs independently at numerous locations on the tube surface; with increasing time, the strain increases within these localization bands. Finally, cracks nucleate and grow from the locations where these localization bands intersect; these cracks then propagate along shear bands and break the specimen into numerous fragments.

Figures 2.11, 2.12, and 2.13, show the average (global) hoop strain time histories of all the polyurea and polycarbonate coated samples tested in this work, as well as the 18 mm bare aluminum samples reported in Zhang and Ravi-Chandar (2010). The point at which the specimen exhibited cracking is marked by an X; the portion of the curves beyond this point is shown by a dashed line since this really does not correspond to strain, but merely radial movement of the fragments.

- The bare Al6061-O samples (Figure 2.11) fractured into fragments at strain levels in the range of 0.35 to 0.6, and then the fragments simply moved away radially with significant residual kinetic energy. The maximum expansion speed observed at a charge of 14 kV was 196 m/s, corresponding to a strain rate of 12,800 s^{-1}. If the charge is low enough, such as 11.5 kV and 12 kV, the samples do not have

enough energy to reach the required localization strain, and the specimens do not fail, but decelerate and stop deforming, after straining to about 0.2 to 0.35.

- The polyurea coated samples (Figure 2.12) exhibit a very similar response; at small charge levels, the specimens stop deforming after about 100 μs. As the loading intensity is increased, the Al/PU bilayer eventually reaches the strain threshold where the Al strain localizes and fails, with the fragments contained within the intact polyurea. However, the Al/PU bilayer appears to withstand a larger discharge (13 kV and 14 kV) without reaching failure than the bare Al specimen. At higher charge voltages (15 and 16 kV), the Al specimen fractures as the strain level reaches about 0.5.
- Finally, for the polycarbonate coated samples (Figure 2.13), the maximum observed expansion speed achieved at the highest discharge voltage of 16 kV was 90.4 m/s corresponding to a strain rate of 5900 s^{-1}; the maximum strain reached for this case was 0.41. This level is below the strain threshold for strain localization and hence the Al/PC specimens did not exhibit any failure, either in the metal or in the polymer.

Before proceeding to analyze the response of the polymer coated aluminum tubes, we examine the details of the deformation in the tube to identify the strain evolution and the onset of strain localization. Optical images of the inner surface of the fragments from three experiments (Test 2 of Zhang and Ravi-Chandar 2010, PU-3 and PC-4) are shown in Figure 2.14; localization bands are clearly visible in all specimens, but such bands are not as well developed in the Al/PC specimen. Note that the Al and Al/PU specimens are fragments, with arrested cracks visible as well, but the Al/PC specimen was cut and mounted in an inclined position in order to be able to observe the inner surface of the Al tube. Optical images of the assembled fragments of the Al and Al/PU specimen and the

intact Al/PC specimen are shown in Figure 2.15. Clearly, the Al specimen has fragmented into a number of pieces (Figure 2.15a) and the Al/PU specimen has broken into five pieces (Figure 2.15c), but the Al/PC specimen (Figure 2.15b) is fully intact; neither the aluminum nor the polycarbonate exhibited any signs of failure. Identically to what was observed by Zhang and Ravi-Chandar (2010), the electrolytically etched circles on the aluminum samples tested deform into ellipses (this can be observed in Figure 2.15 as well); measuring the length of the major and minor axes of these ellipses allows for an estimate of the maximum strains experienced by the samples. *Post mortem* measurements of the ellipses were used to obtain the principal logarithmic strains, ε_1 and ε_2, (where ε_1 corresponds to the hoop direction $\varepsilon_1 > \varepsilon_2$) from the surfaces of a large number of recovered fragments (for the Al/PC specimens, the polycarbonate coating was cut and removed in order to observe and measure the etching on the surface of the aluminum). Figures 2.16 and 2.17 show these measurements for the polyurea and polycarbonate coated specimens respectively on a forming limit diagram. Figure 2.16 presents data from four tests with polyurea coating on the aluminum, including both 18 and 36 mm long tubes (strain rates are in the range of 3600 – 8900 s^{-1}). Figure 2.17 shows data from four tests as well, but corresponding to polycarbonate coating, although only for 18 mm long samples (strain rates in the range of 4200 – 5900 s^{-1}).

In these figures, data from tubes expanded at different speeds are distinguished by different colors, blue corresponding to the slowest speeds and red to the highest. Additionally, strains measured from regions where no localization was evident under optical micrography are plotted as open symbols, while the strains measured from regions where a shear band was observed crossing an ellipse are plotted as filled symbols. In addition to the circles, two lines are included. The dash-dot line corresponds to a state of uniaxial stress, with $\varepsilon_1 = -2\varepsilon_2$, while the dashed line represents the theoretical quasi-

static forming limit for sheet materials (see Eq. (4) of Zhang and Ravi-Chandar, 2010). Analogous to the Al 6061-O tests in Zhang and Ravi-Chandar, (2010), there is considerable scatter in the data for the polyurea and polycarbonate coated samples as well. This is again caused by two factors; first, the local measurements of strain are influenced by the curvature of the specimen to appear systematically larger, particularly the minor principal strains. Secondly, for strains measured on ellipses containing a shear band, the distortion provided by the shear band is neglected. The main observations from these forming limit diagrams (FLDs) are described below.

- In both Al/PU and Al/PC specimens, most of the measured data fall in the region $\varepsilon_1 \geq -2\varepsilon_2$, following the pattern observed in Zhang and Ravi-Chandar, (2010) for the uncoated specimens. However, for the coated specimens, the data is not spread evenly around the uniaxial stress path; the data traces a steeper line than the $\varepsilon_1 = -2\varepsilon_2$ condition, implying that the stress state is migrating just slightly from a uniaxial stress towards a plane-strain condition $(\varepsilon_2 = 0)$. Furthermore, for the Al/PU coated tubes, the 36 mm samples seem to migrate[4] more towards the plane-strain condition than the 18 mm samples, as is expected from the observations made in Zhang and Ravi-Chandar, (2010). It can also be observed that the Al/PC samples (all 18 mm in length) exhibit a larger shift towards the plane strain condition than the polyurea coated specimen of the same length. This indicates that the polycarbonate coating seems to have a greater influence on the stress state of the aluminum than the polyurea.

[4] It is noted that plastic anisotropy could contribute to this migration; the extent of this anisotropy in extruded tubes has not been characterized, but the inertial effects are in addition to the effect of anisotropy.

- For the polyurea coated samples, the expanding velocities are in the range of 55 – 136.1 m/s. All specimens, including the ones that stopped deforming as a result of low loading levels, show shear bands throughout their surface.
- For the polycarbonate covered samples, the expanding velocities are in the range of 64.6 – 90.4 m/s. No localizations were observed in specimens PC-1, PC-2 and PC-3. However, the sample PC-4 showed very faint shear bands throughout its internal surface; the average local strains attained in this specimen corresponds to an average hoop strain of 0.50 and an average longitudinal strain of -0.24. The other specimens exhibit lower average local strains and do not show localization bands. It is worth noting that specimen PC-3, with a higher expansion speed of 90.4 m/s, exhibits no shear localization but has very similar average strains (average hoop strain = 0.47, average longitudinal strain = -0.21) to the specimen PC-4, suggesting that the formation of distinguishable shear bands occurs in the range of 0.47 to 0.50 average hoop strain and -0.21 to -0.24 average longitudinal strain; these appear to be slightly above the quasi-static forming limit for the Al 6061-T6.
- Additionally it can be noted that for the polyurea covered samples, most measured circles demonstrate strain levels above or close to the forming limit for the material. Since all the samples show clear shear localization, and are located immediately above the predicted forming limit, *this is indicative that the polyurea coating does not affect the quasi-static forming limit for the aluminum* under this forming operation, and therefore the material behaves almost identically to the bare aluminum samples in Zhang and Ravi-Chandar, (2010).
- Finally, from the data of the polycarbonate coated samples, the forming limit does not seem to agree with the quasi-static forming limit predicted for the uncoated

aluminum specimens. It is observed that there are a significant number of open symbols above the quasi-static forming limit dash-dot line in Figure 2.17. This implies that the forming limit seems to have shifted upward, allowing for a larger strain level without the onset of localization. From the experimental data shown here it is difficult to determine this new forming limit exactly; however, an upward shift of the quasi-static limit by 6% strain would seem to fit better to the observed results. This may be caused by a modification of the stress state of the aluminum caused by a pressure loading applied by the polymer on the top surface of the tube and needs to be explored further.

From Table 1.1, and Figures 2.16 and 2.17, it is evident that the strain levels achieved by the Al/PU samples were considerably larger than those experienced by the Al/PC, despite the fact that the charging voltages used in the tests were in the same range (13-16 kV). It can be inferred that adding a coating reduces the strain the aluminum can experience, since the acceleration of the additional mass will consume some of the energy that would otherwise be used in straining the metal. However, it can also be noted that the actual added mass from the coatings is relatively similar for both polyurea and polycarbonate, and the vast difference in the strain levels observed (~25% difference in maximum hoop strain) is due to the fact that plastically deforming the polycarbonate requires a much larger amount of energy than that needed to elastically deform the polyurea, as is expected from the material properties. This higher resistance accounts for the larger effect on the stress state of the aluminum as described before. Further discussion of these results is considered in the following section through numerical modeling and simulations.

2.5.3 Modeling and Numerical Simulations

Our experimental observations demonstrate that final deformation of the tubes is dependent on the applied driving force as well as the geometric and the material properties of the coatings. In this section, we explore the underlying phenomena in order to determine the role of the polymer coating in retarding/inhibiting the deformation/failure of the metal substrate. This is accomplished first through a simple one-dimensional analysis and is then followed by a three dimensional numerical simulation.

In order to explore the influence of the polymer coating on the uniform expansion of the metal substrate, we consider a one dimensional formulation as in Zhang and Ravi-Chandar (2006). The electromagnetic loading system can be modeled as two simple RLC circuits. The capacitor and coil form one circuit and the expanding ring the other. This allows us to describe the radial acceleration of the ring as a series of coupled differential equations depending on the current, inductance and constitutive behavior of the ring. By grouping the electromagnetic forcing terms in Eq. (8) from Zhang and Ravi-Chandar (2006) as $F(t)$, and rearranging terms, the radial acceleration of the ring/tube can be expressed as

$$A\rho r\ddot{r} = F\left(r,t\right) - \sigma A \tag{2.3}$$

where r is the ring radius, A is the specimen cross-sectional area, ρ is the mass density, and σ is the plastic flow resistance of the specimen. In the case of an aluminum specimen that is coated with a polymer, Eq. (2.3) can be modified as suggested in Zhang and Ravi-Chandar (2010) and written as

$$(\rho_{Al}A_{Al} + \rho_{Pu}A_{Pu})r\ddot{r} = F\left(r,t\right) - (\sigma_{Al}A_{Al} + \sigma_{Pu}A_{Pu}) \tag{2.4}$$

where ρ_{AL} and ρ_p, A_{AL} and A_p, σ_{AL} and σ_p are the density, cross-sectional area and flow strength of the Al6061-O and the polymer, respectively. It is clear from Eq. (2.4)

that in contrast to the Al specimen, the Al/PU or Al/PC composite has two additional terms that resist the applied force; first, the added mass on the left hand side of Eq. (2.4) contributes to a decrease in the acceleration of the tube to a given load simply by increasing the inertial resistance. Both polyurea and polycarbonate are of similar density; therefore, their inertial contribution should be very similar. The second factor is the contribution from the stress in the polymer; this provides additional resistance to expansion and corresponds to the second term inside the parenthesis on the right hand side of Eq. (2.4). For the same cross-section of the coating, it is clear that the polycarbonate can provide a significantly larger resistance to flow than polyurea because $\sigma_{PC} >> \sigma_{PU}$. Even as the modulus and flow stress of the polyurea increase with strain rate, the stress in the polyurea may not reach levels comparable to that of polycarbonate. Clearly, we see in the experiments that the Al/PC specimens experience significantly smaller strain levels in comparison to the Al/PU specimens when subjected to the same loading conditions. It is clear that optimization of the coating can be considered by taking a polymer with a high flow stress and low density; this supports the use of polycarbonate or the hunt for another formulation of polyurea that can provide a significantly higher flow stress.

The complete response of the Al/polymer composite can only be addressed through direct numerical simulations. Such simulations have been performed to assist in understanding how inertia and strength influence the deformation and failure of the Al/polymer composite system. Furthermore, these simulations also provide some insight into how the coatings can be tailored for optimal design. In order to capture adequately the deformations experienced during the expansion of the tube, a three dimensional finite element model was used. While the full three dimensional geometry is needed to capture the deformations associated with the tube expansion, it is sufficient to look at only a

quarter symmetry model of the tube as indicated in Figure 2.18a. The features of the simulation are similar to that reported in Zhang and Ravi-Chandar (2010) for the bare Al specimens; in the present work, two modifications are made, the first to include the polymer coating, and the second to incorporate the loading as a body force, but applied only on the aluminum part, thereby mimicking the applied loading more closely. The tube geometry resembles that of the 18 mm wide tube experiment ($r_i = 15.25$ mm, $r_o = 15.75$ mm, and $w = 18$ mm). The coating thickness is varied depending on the simulation. The tube is discretized with a $243 \times 5 \times 180$ ($\text{arc} \times t \times w$) mesh using eight node linear brick elements with reduced integration and hourglass control (C3D8R). 0.1% of the total number of elements is randomly selected as material defects to trigger localization. Similarly, the coating is discretized with $251 \times t \times 180$ ($\text{arc} \times t \times w$) mesh using eight node linear brick elements with reduced integration and hourglass control (C3D8R) where t depends on the thickness of the coating with an element size similar that in the tube. The tube material is taken to follow the same power law hardening model for Al 6061-O described earlier. The material is assumed to not exhibit any softening or damage until the logarithmic plastic strain reaches $\varepsilon_p = 1$; beyond this point, the strength of the material is dropped to a small value in order to mimic failure. We note that this simple model is not as a proper model of failure, but is expedient in the present work where our objective is to capture the early stages of the onset of localization and the unloading in the vicinity of the localization. The defects are assumed to possess yield strength of 25 MPa and exhibit no strain hardening. The polyurea layer is modeled using the Marlow formulation of a hyperelastic material, calibrated based on uniaxial test data shown in Figure 2.2. The polycarbonate is modeled as an elastic-plastic material with an initial modulus of 2.5 GPa up to a strain level $\varepsilon = 0.25$, after which it has a tangent modulus of 20 MPa. Beyond $\varepsilon = 0.6$, the polycarbonate is assumed to stiffen up again to

a tangent modulus equal to that of the original elastic modulus. The actual densities of polycarbonate and polyurea are quite similar and have been taken to be equal (1200 kg/m^3) in these simulations.

In the experiment, the aluminum tube is accelerated radially by a body force due to electromagnetic loading. The amplitude of the body force is proportional to the product of the current in the solenoid and the induced current in the tube. These currents have been measured using inductive noncontact probes and therefore a body force amplitude curve with respect to time can be created. This curve is used to specify the body force amplitude applied to the aluminum tube during the simulation. A scaling factor is used to adjust the amplitude and achieve the desired outward radial velocity. The baseline curve of the loading is shown in Figure 2.18b. The baseline amplitude is the lowest amplitude that will still cause failure in the bare aluminum specimen.

We now consider the results of three simulations corresponding to Al, Al/PU and Al/PC specimens, all subjected to the same loading. The Al specimen and the polyurea and polycarbonate coatings were of the same thickness ($t = 0.5$ mm). The time evolution of the hoop strain of elements along the inner diameter at the midline of the tube is shown in Figure 2.19. The localization strain level and the range of reported failure strains are also marked in this figure. As discussed earlier for sheet materials under biaxial tension, the critical necking strain is $\varepsilon_{SN} = 2n$. The Al-6061-O has a hardening exponent of $n = 0.22$ so we expect localization to occur at $\varepsilon_{SN} = 0.44$. Failure strain is more ambiguous and, instead of offering some specific value, we have shown the typical range of maximum strain measured post mortem in failed aluminum tube samples; typical macroscopic average strain at failure has been measured to be in the range $\varepsilon_f = 0.55 - 0.65$. The initial velocity of expansion is 150 m/s for the bare Al specimen and ~100 m/s in both polymer coated specimens. The initial expansion rate of the

polymer coated specimens is slightly smaller than that of the bare aluminum; this is attributed to the added mass of the polymer as discussed above. Both the Al/PU and Al/PC specimens strained to a smaller level than the bare Al, with the Al/PC not exceeding the localization strain, while the Al/PU went just above this threshold. Contour plots of the effective plastic strain obtained from these three simulations at selected time steps are shown in Figure 2.20 to examine the effect of the polymer coating. As described in Zhang and Ravi-Chandar (2010), the bare Al specimen exhibits strain localization and failure (Figure 2.20a); eventually the fragments fly away with significant kinetic energy with the fragments have a residual velocity of 40 m/s. The maximum strain level attained by the Al with the polyurea coating exceeded the strain localization threshold and this simulation exhibits strain localization (Figure 2.20b). The Al-tube with the polycarbonate coating, on the other hand, was unable to expand to a global strain level larger than about 0.4, due to the higher strength of the polycarbonate (Figure 2.20c). The residual velocity in both cases is about ~ 2.5 m/s; essentially, both the polyurea and the polycarbonate coatings stopped the expansion of the Al specimen. At the end of the simulation time, the Al specimen had fragmented into pieces each with significant kinetic energy, the Al/PU had strain localized but not fragmented, and the Al/PC specimen had contained the loading with just uniform plastic deformation over both the Al and the PC. The variation of the hoop stress in the coating with time is shown in Figure 2.21. It is now easy to distinguish between the added mass effect and the increased strength effect. While both the polymers increase the mass by the same amount, it should be noted that the maximum principal stress attained by the polyurea is only about 6-8 MPa, while the polycarbonate reached a maximum stress that is about an order of magnitude greater, ~80 MPa. Thus, polycarbonate, with nearly the same mass as the polyurea, but with a much larger strength in the range of 60 to 90 MPa, is more effective in inhibiting the failure of the Al,

not by altering the localization response but simply by providing a dissipative mechanism for absorbing the energy in the Al part of the composite specimen. Around 100 μs, when the applied loading is terminated, dynamic oscillations of the polycarbonate can be observed in Figure 2.21. Note that these oscillations with amplitude of about 6 – 7 MPa can apply a compressive stress on the Al tube that is on the order of 200 MPa, well above compressive yield. Localized wrinkling was observed in some of the experiments; this needs to be examined more completely to explore all failure mechanisms in the Al tube.

With this understanding of the role of the polymer, we can now consider some issues related to the optimal design of polymer coatings. First, we explore the effect of varying the thickness of the polyurea coating while keeping the imposed driving force and the material strength constant. This simulation allows examination of the "added mass" effect in contrast to the previous simulations where the mass of the coating was maintained constant while varying the strength. Figure 2.22 shows the average true hoop strain of elements along the inner diameter at the midline of the tube for several coating thicknesses. The range of strains for onset of localization and failure in the Al are also marked in this figure. Figure 2.22 shows that an increase in the polyurea coating thickness results in a decrease of the expansion velocity in the early stages; all three coating thicknesses result in a rapid deceleration of the tube beyond about 80 μs. For the two thinner coatings – 0.25 mm and 0.5 mm – the peak strain levels exceed the localization threshold and the strain in the Al localizes along bands; however, at this point the specimen has very little kinetic energy. For the thickest coating, the resistance provided by the added mass polyurea is sufficient to stop the Al from straining even to the localization threshold. From these simulations, it is apparent that the main effect of the polyurea in providing additional resistance to the expansion of the Al/PU composite

specimen is based on its mass; as the coating thickness is increased the strain is reduced to below failure strain and even below localization strain.

In the above simulations, we have maintained a constant applied force, and varied the coating materials and thicknesses; however, this approach results in an increase in the total weight of the structure. In many design scenarios, maintaining the overall weight of the structure is of critical importance. So, the following question arises: what is the consequence of designing a coated structure with the constraint of keeping the mass constant? In the last set of simulations, this was accomplished by modifying the thicknesses of the polyurea and polycarbonate coatings to result in the same total mass as the bare Al specimen. Since the densities of the two polymers is nearly the same and much smaller than the Al, $\rho_{PU} \sim \rho_{PC} \sim 0.43\rho_{AL}$ the mass is maintained constant by reducing the thickness of the Al to αt_{AL} and adding a coating of thickness $t_p = (1-\alpha) t_{AL}\rho_{AL} / \rho_p$. Figure 2.23 shows the results of simulations in which the tube thickness was reduced to 0.35 mm $(\alpha = 0.7)$ and that mass was replaced with an $t_p = 0.336$ mm coating of polyurea and polycarbonate. Since the body force is applied only to the Al part of the specimen, its magnitude was scaled to account for the reduction in driven mass and still maintain the same total force as in the 0.5 mm thick uncoated tube. In interpreting the results, it should be noted that the higher strength Al is replaced by a significantly weaker polyurea and a somewhat weaker polycarbonate. The results are clear; in comparison to the full thickness Al specimen, the Al/PU specimen experiences a greater expansion. The Al part of the specimen fragments after attaining strains of around 0.6; these fragments are, of course now contained within the polyurea, and as the polyurea expands to strain levels of around one, it is expected that the metal fragments will be slowed down; the simulations have not been performed to reach this stage. In contrast, the polycarbonate coating is sufficiently strong to resist the expansion of the

metal; the strain levels still reach localization and failure threshold, but the kinetic energy of the expanding metal is nearly fully dissipated in the deformation of the polycarbonate. The ability of polycarbonate to carry significant hoop stress long beyond the failure of the aluminum means that this composite structure, on a per unit mass basis, is much more resistant to blast loading than either the Al or the Al/PU. The improved resistance however may be understated by the results of the simulation due to the assumption that the polyurea is rate independent. In the next section, we introduce a method to quantify the dynamic tensile response of polyurea to pursue this aspect further.

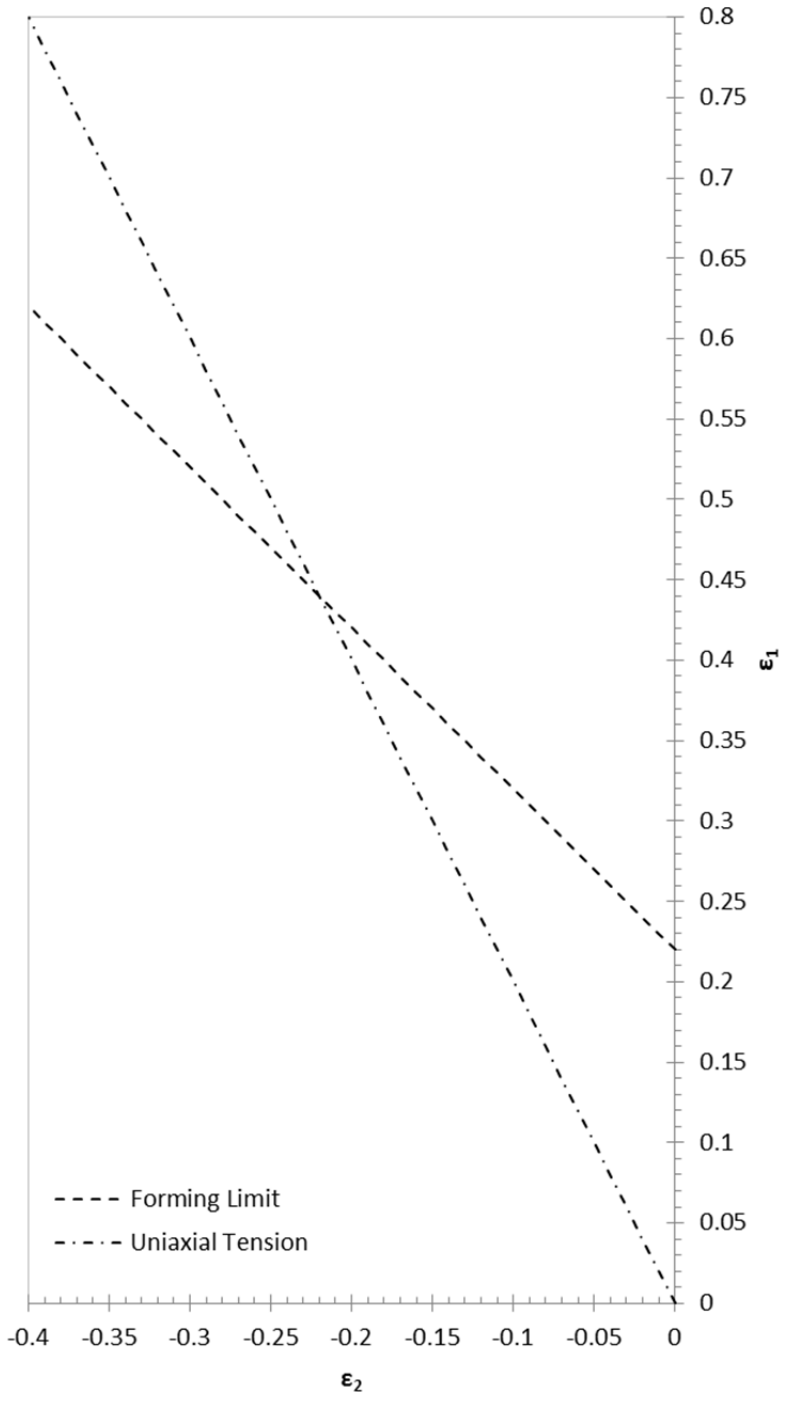

Figure 2.1: General Forming Limit Diagram (FLD) with forming limit and uniaxial tension lines

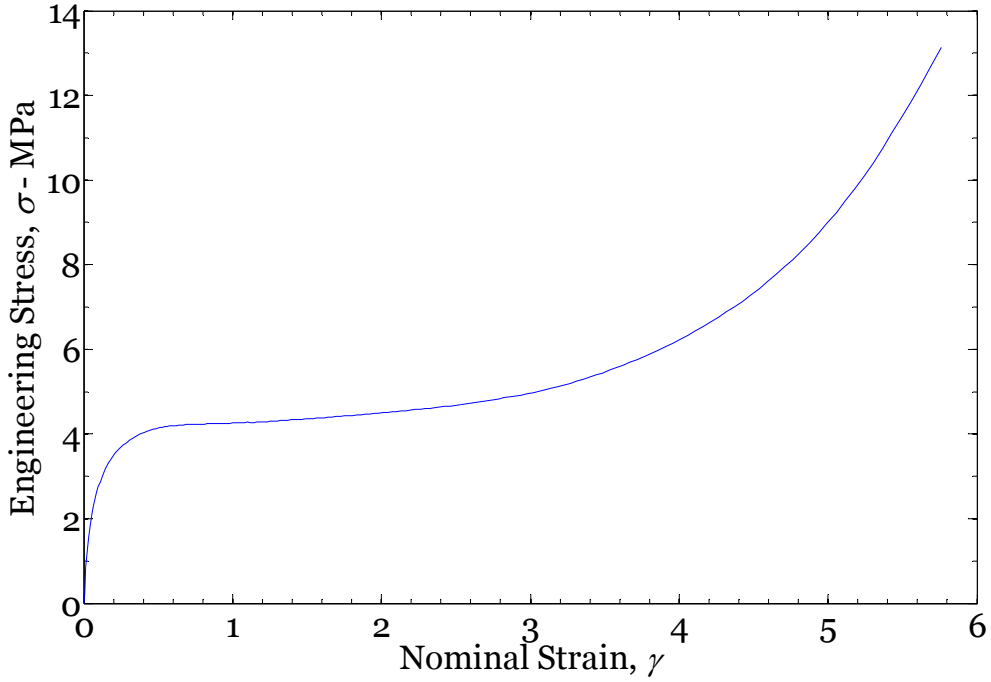

Figure 2.2: Quasi-static stress-strain response of polyurea ($\dot{\gamma}$= 0.1 s^{-1}).

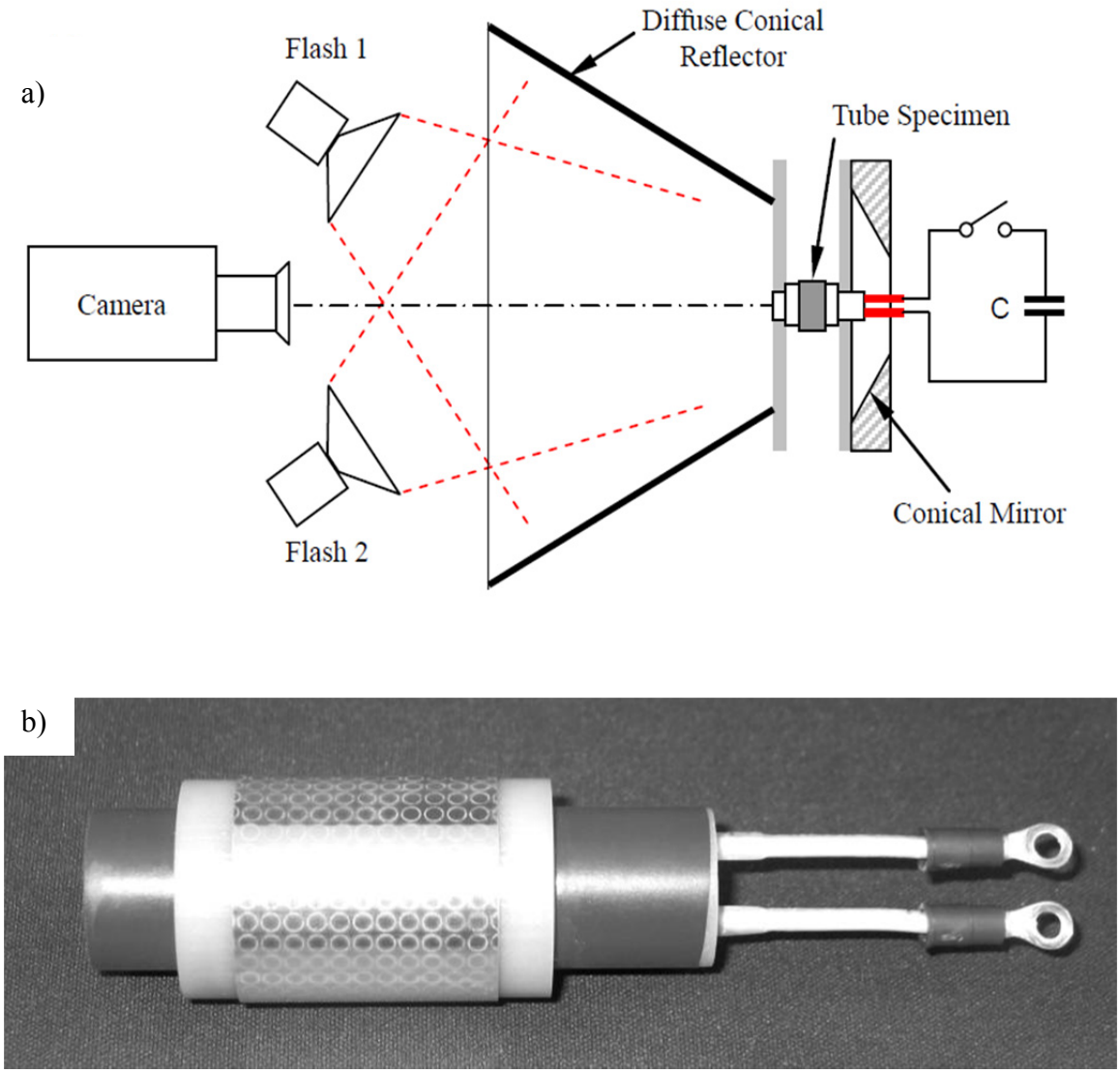

Figure 2.3: a) Schematic diagram of the experimental setup for the expanding tube experiment. The conical mirror placed coaxially with the solenoid and the tube specimen, provides a complete projection of the surface of the expanding cylindrical specimen; b) Photograph of the solenoid and the tube specimen; a pattern of 2.5 mm diameter circles is electrolytically etched on the outer surface of the specimen in order to facilitate strain measurements. (Zhang and Ravi-Chandar 2007)

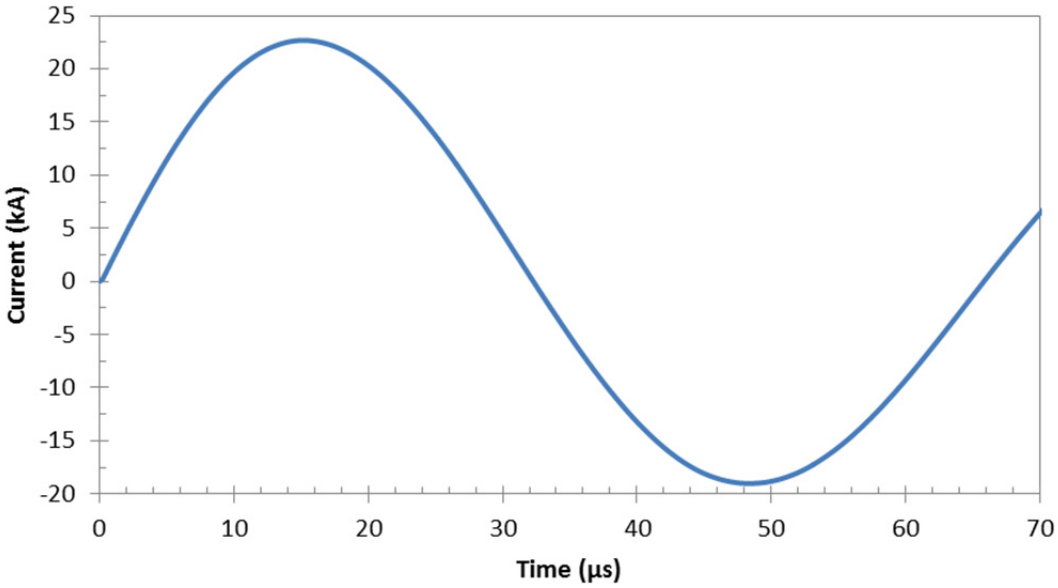

Figure 2.4: Typical variation in current in solenoid measured by Rogowski probe

Table 1.1: List of high speed expanding tube tests on polymer coated Al 6061-O samples

Test number	Coating material	Tube length (mm)	Charge voltage (kV)	Tube thickness (mm)	Coating thickness (mm)	Expansion velocity[a] (m/s)	Strain rate (s^{-1})
PC-1	Polycarb	18	13	0.51	0.49	64.6	4236
PC-2	Polycarb	18	14	0.50	0.50	83.3	5462
PC-3	Polycarb	18	15	0.51	0.50	90.4	5928
PC-4	Polycarb	18	16	0.53	0.49	82.4	5403
PU-1	Polyurea	18	14	0.50	0.32	102.8	6741
PU-2	Polyurea	18	15	0.50	0.32	141.3	9266
PU-3	Polyurea	18	16	0.50	0.34	136.1	8925
PU-4	Polyurea	36	13	0.50	0.45	81.4	5338
PU-5	Polyurea	36	15	0.50	0.70	55	3607
PU-6	Polyurea	36	15	0.50	0.50	101.5	6656

[a] The steady ring expansion speed reached in the 15-50μs interval is quoted, following the procedure used in Parts I-IV.

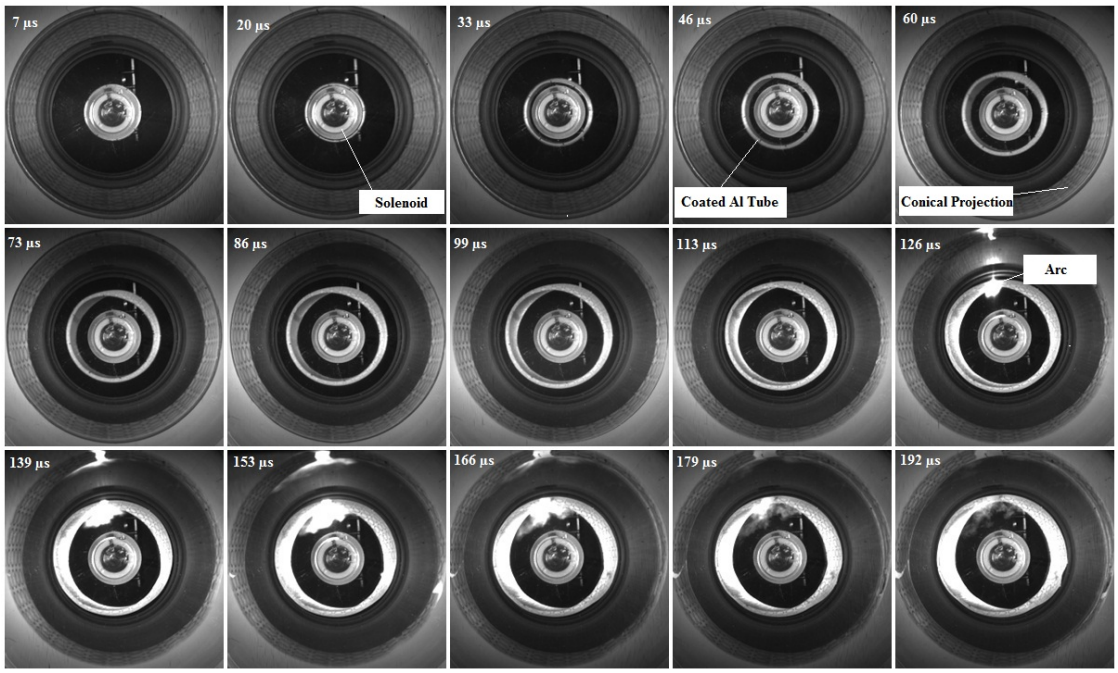

Figure 2.5: High speed images showing expansion of an Al 6061-O tube (w = 18mm) with a polyurea coating, expanding at 136.1 m/s (Test PU-3).

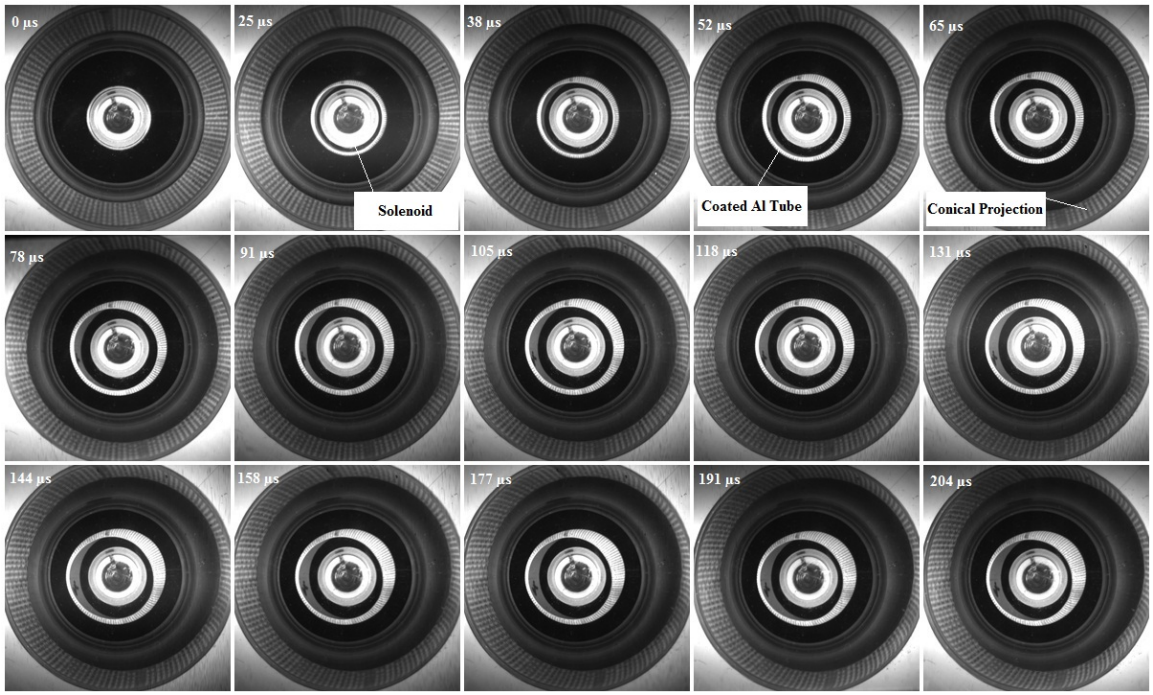

Figure 2.6: High speed images showing expansion of an Al 6061-O tube (w = 18mm) with a polycarbonate coating, expanding at 90.4 m/s (Test PC-3).

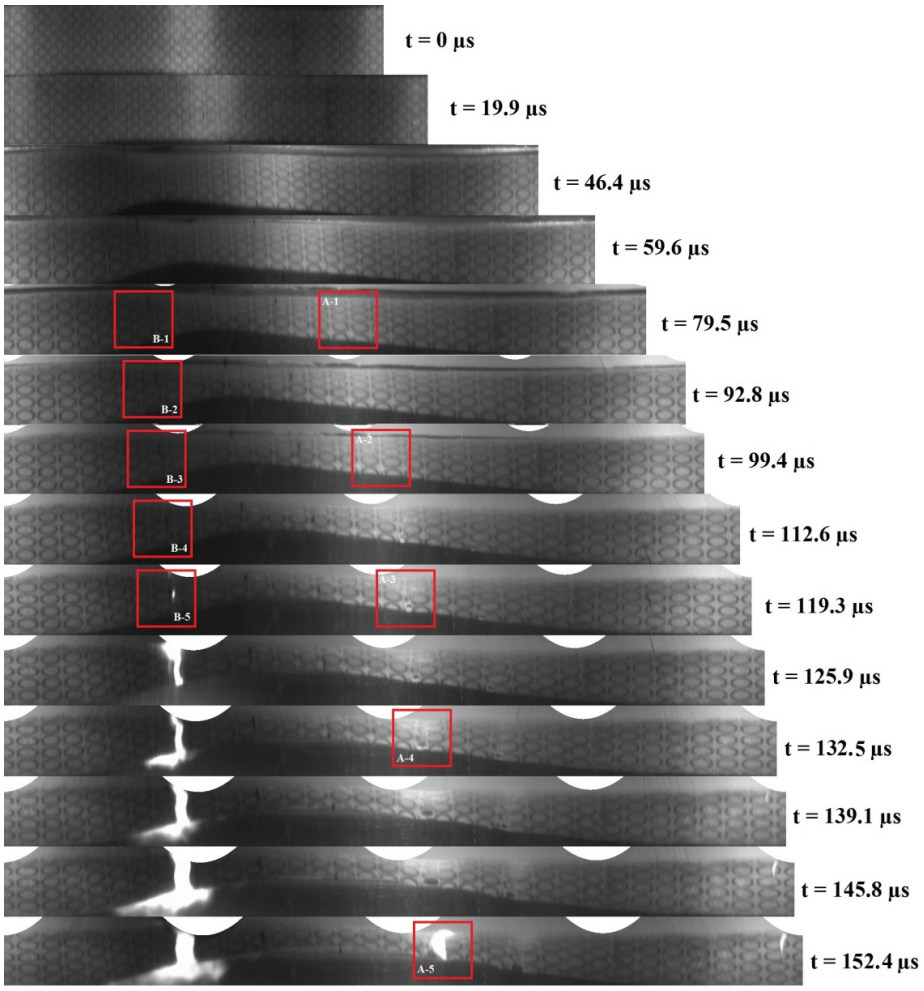

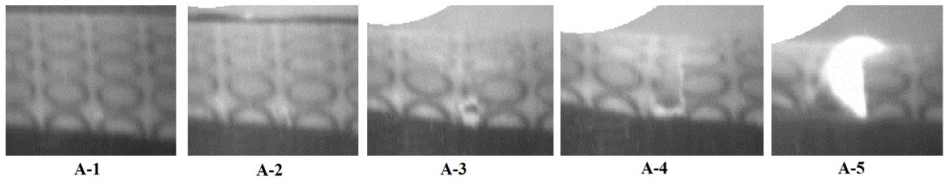

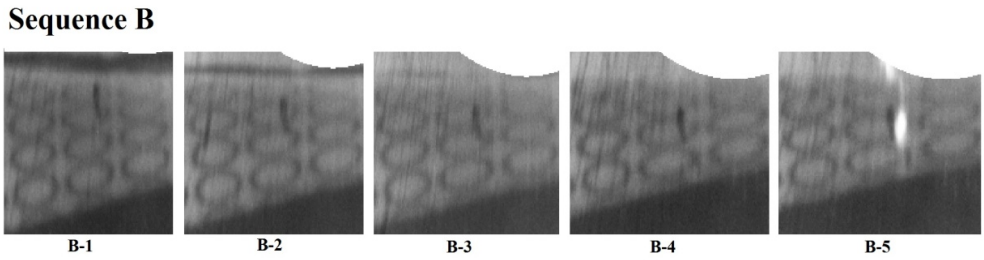

Figure 2.7: Sequence of unwrapped images for Al 6061-O tube (w = 18mm) with a polyurea coating expanding at 136.1 m/s (Test PU-3) indicating the deformation on the surface of the cylinder.

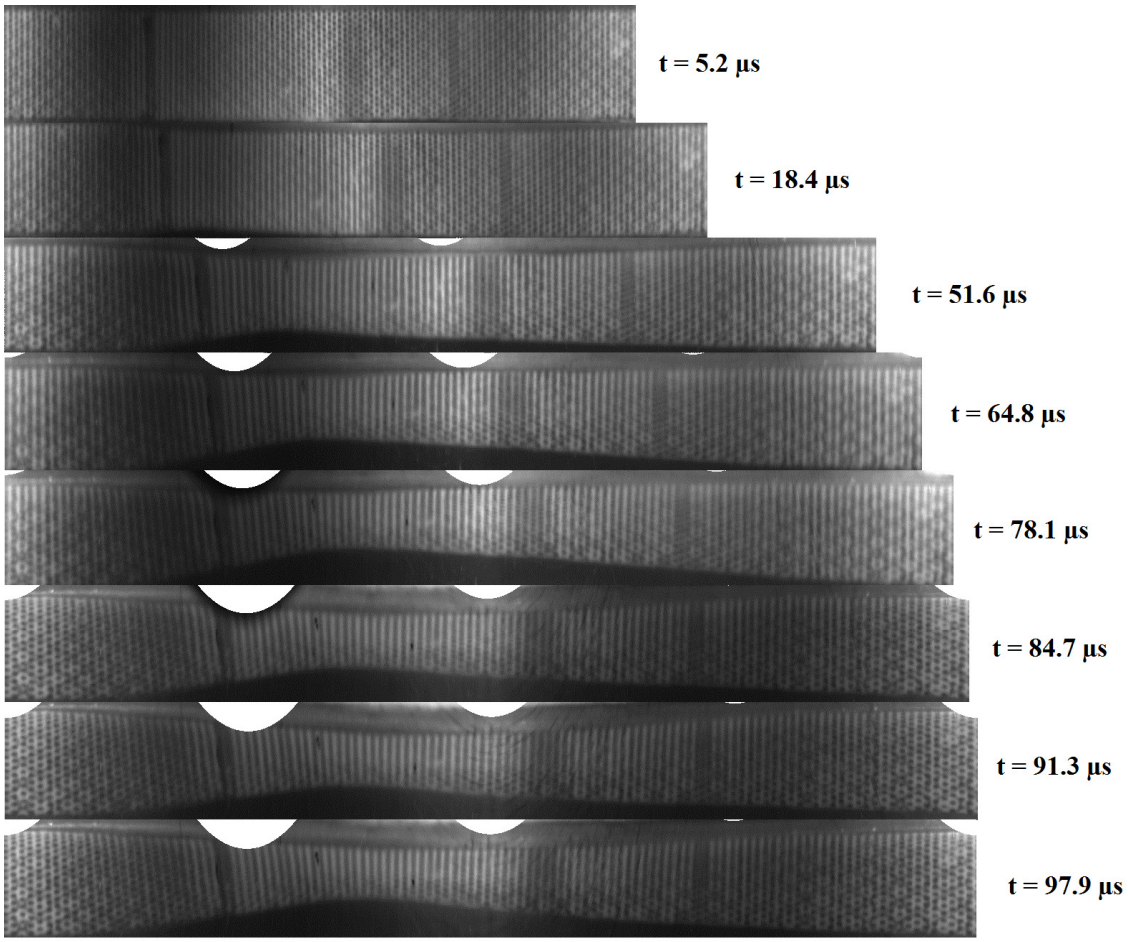

Figure 2.8: Sequence of unwrapped images for an Al 6061-O tube (w = 18mm) with a polycarbonate coating expanding at 90.4 m/s (Test PC-3) indicating the deformation on the surface of the cylinder.

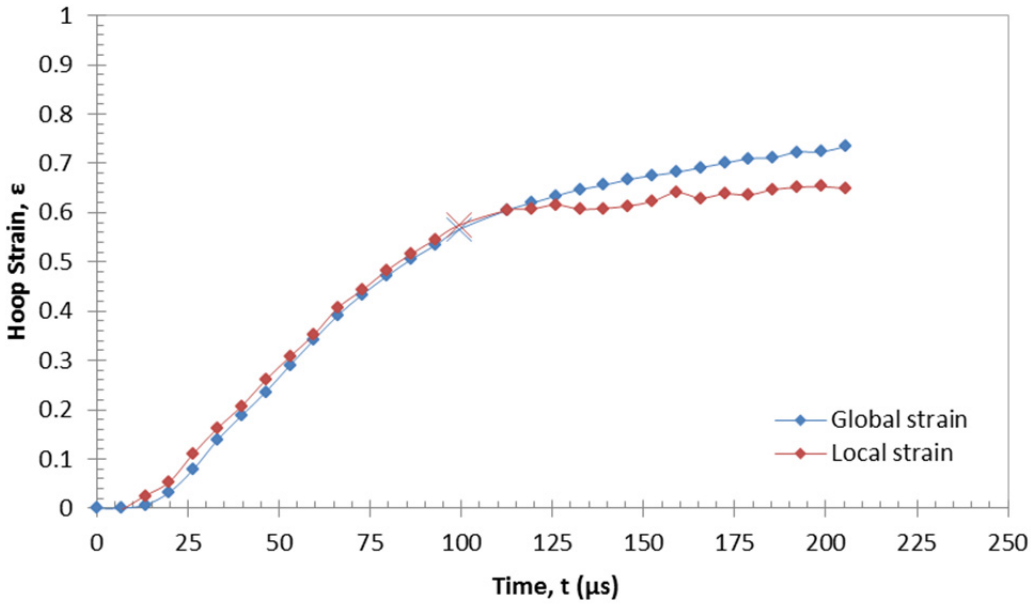

Figure 2.9: Variation of hoop strain with time for Test PU-3: the global quantity was determined by measuring the variation of average tube radius, while the local strain was obtained from measurements of the deformation of an etched circle on the sample surface. The X marks the fracture point.

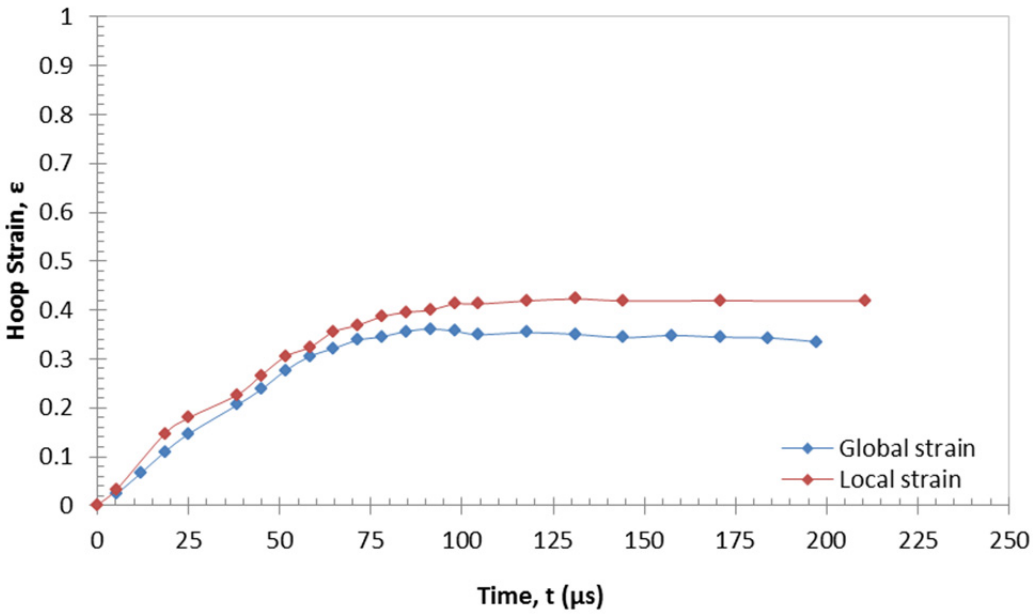

Figure 2.10: Variation of hoop strain with time for Test PC-3: the global quantity was determined by measuring the variation of average tube radius, while the local strain was obtained from measurements of the deformation of a staggered circle pattern painted on the coating surface.

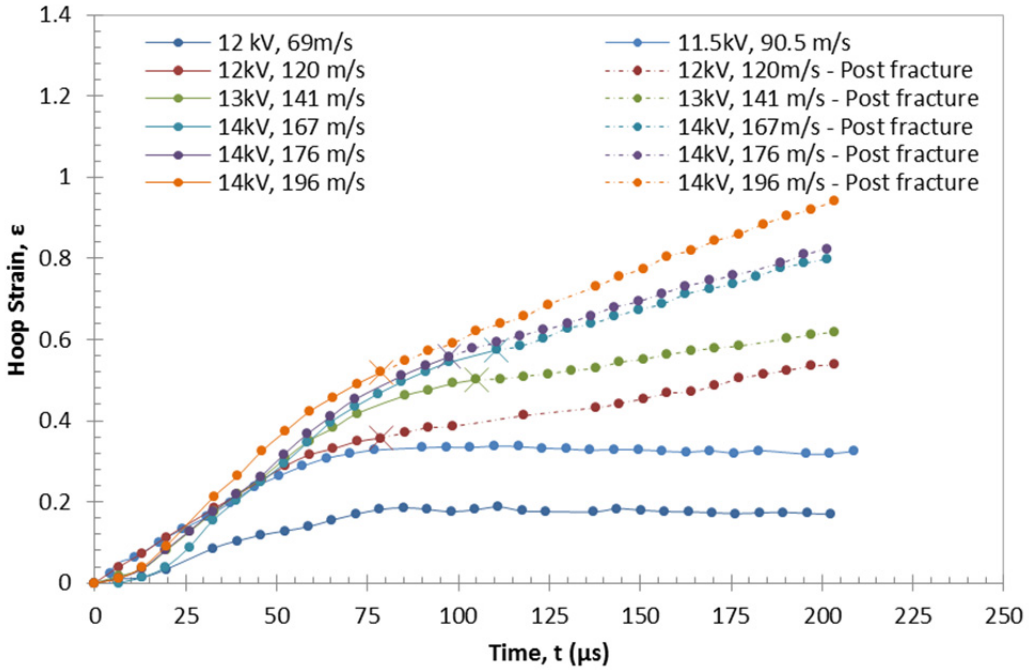

Figure 2.11: Variation of hoop strain with time for uncoated Al 6061-O 18 mm tubes used in Zhang and Ravi-Chandar (2010): Note the rigid body expansion observed in all the fractured specimens. The samples that did not fracture hit a plateau after the driving force was extinguished. The X marks the fracture point.

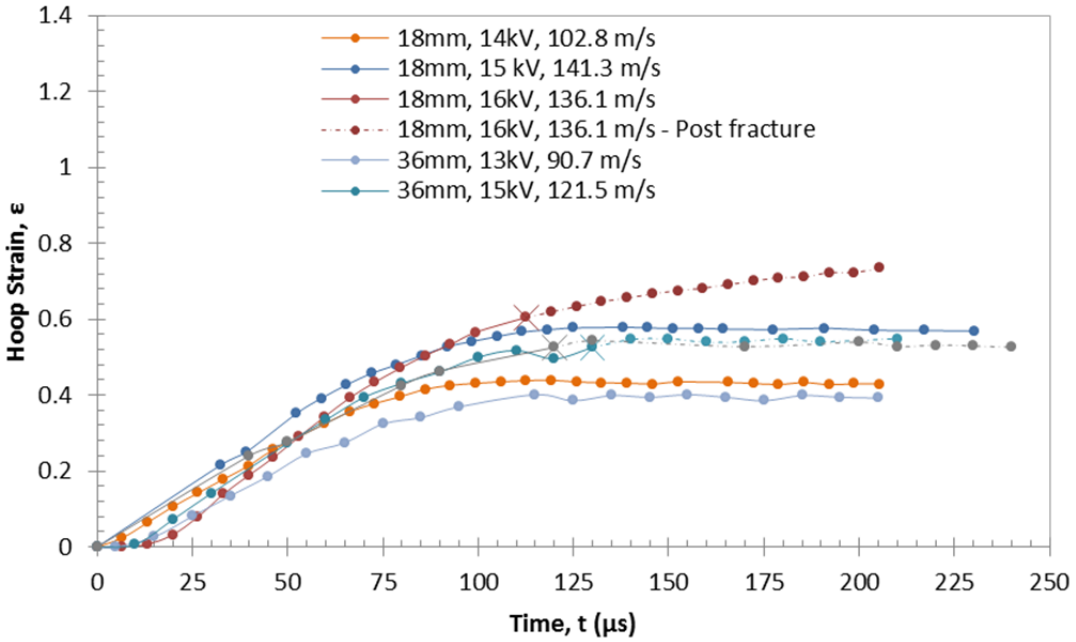

Figure 2.12: Variation of hoop strain with time for polyurea coated Al 6061-O tubes of 18 mm and 36 mm lengths: Note the rigid body expansion observed in all the fractured specimens. The samples that did not fracture hit a plateau after the driving force was extinguished. The X marks the fracture point.

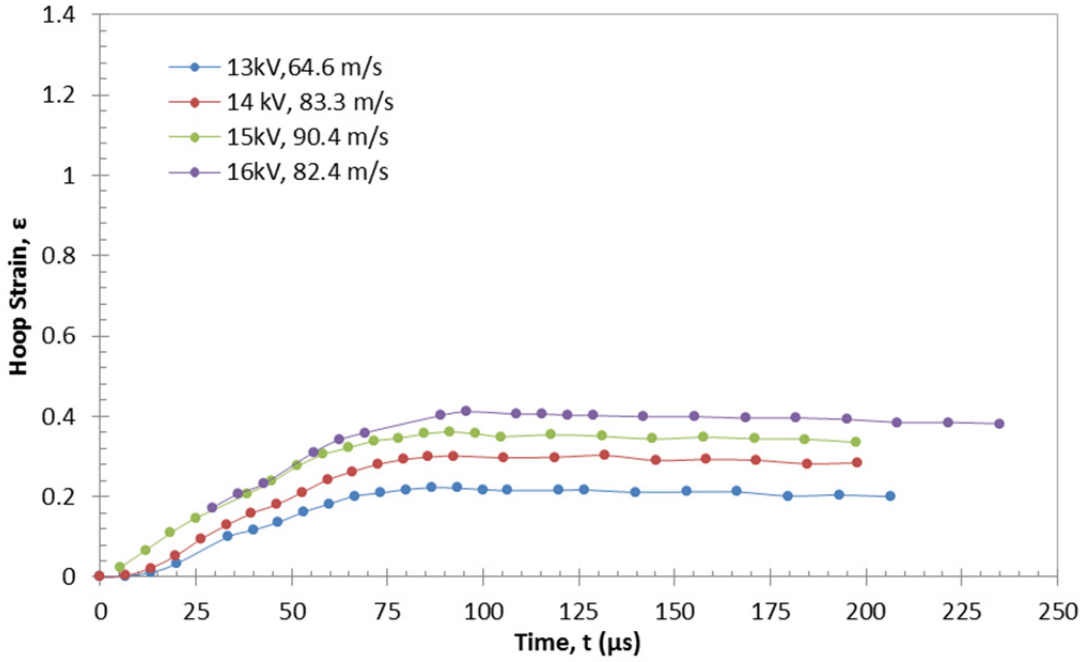

Figure 2.13: Variation of hoop strain with time for 18 mm long polycarbonate coated Al 6061-O tubes: Note that the samples did not fracture, hitting a plateau after the driving force was extinguished.

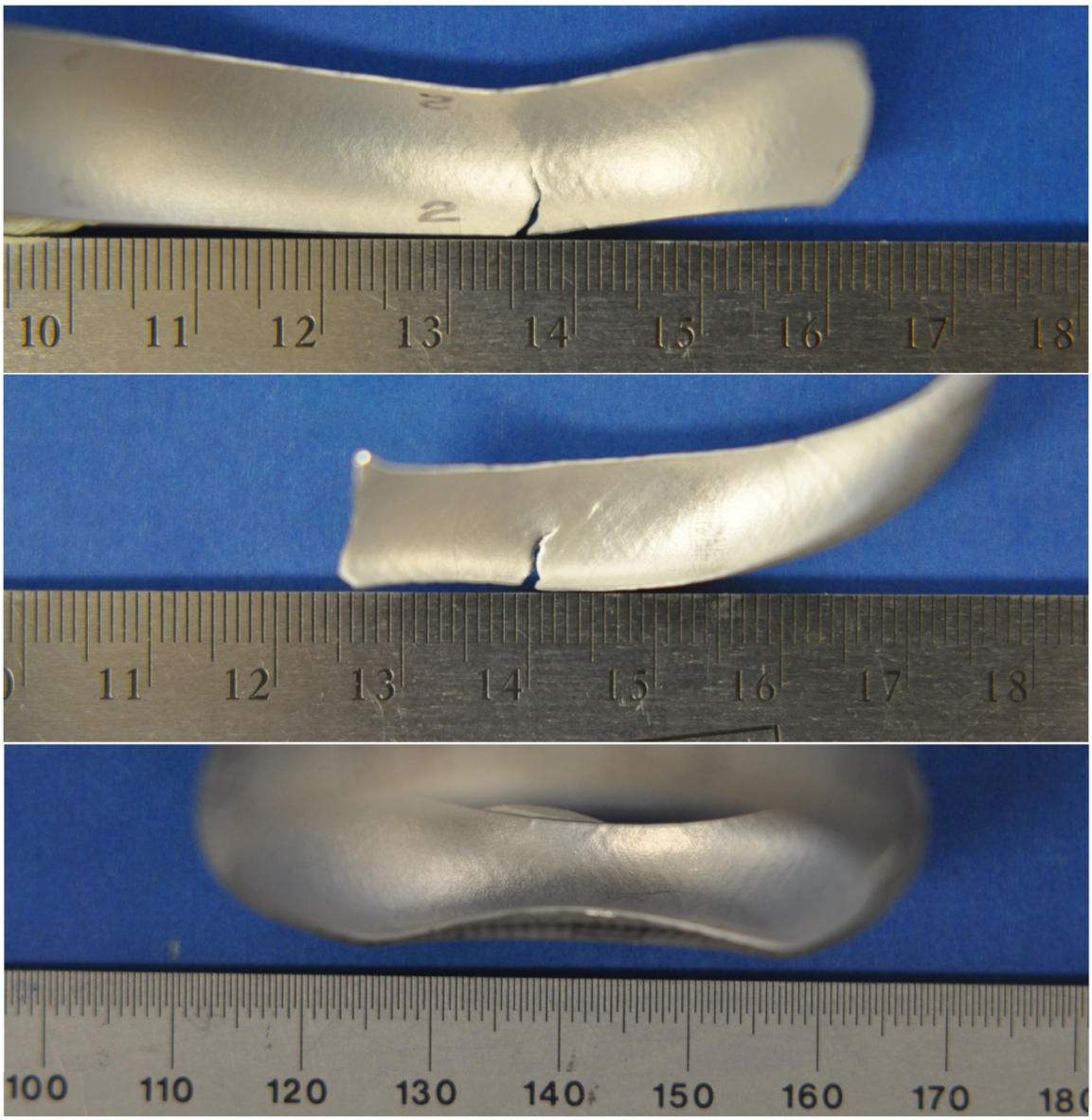

Figure 2.14: Variation of localization band intensity and distribution for different tests. The top image corresponds to an 18 mm long bare Al 6061-O cylinder under a 12 kV discharge, generating an expansion velocity of 120 m/s (Test 2 in Zhang and Ravi-Chandar, 2010). The middle image corresponds to Test PU-3. The lower image corresponds to Test PC-4. Note how in the top image, the most defined localization bands occur around the crack and become less defined as you move away from it. In the other two images, the distribution of the localization bands is uniform throughout, being a lot more defined for the Test PU-3.

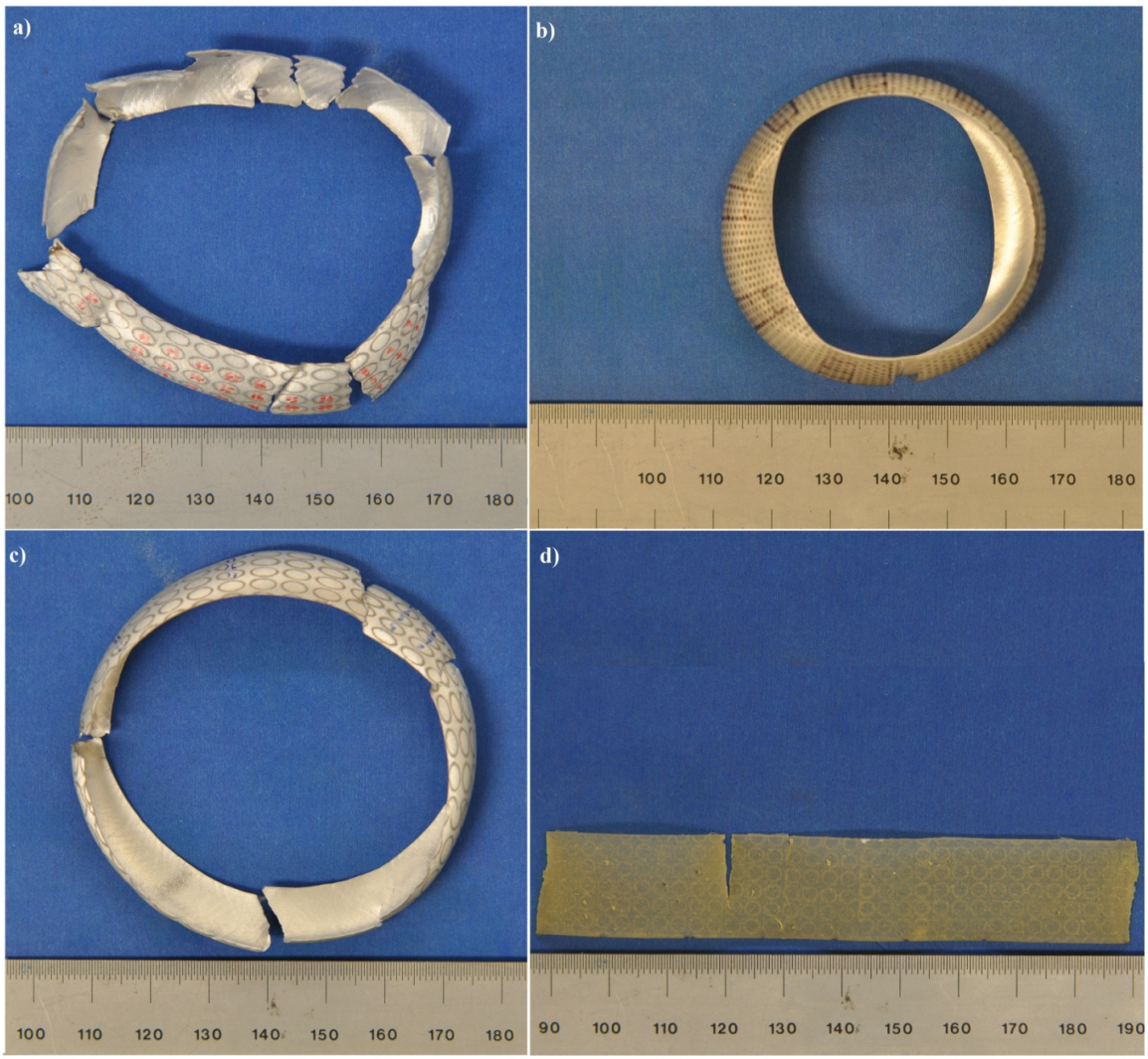

Figure 2.15: Expansion comparisons for bare Al 6061-O, polyurea coated Al 6061-O and polycarbonate coated Al 6061-O. Image a) corresponds to a bare Al 6061-O tube, 18 mm long, expanded with a discharge voltage of 14 kV and attaining a radial expansion speed of 196 m/s. Image b) corresponds to a polycarbonate coated Al 6061-O tube, 18 mm long, expanded with a discharge voltage of 16 kV and attaining a radial expansion speed of 82.4 m/s (Test PC-4). Finally, images c) and d) correspond to a polyurea coated Al 6061-O tube, 18 mm long, expanded with a discharge voltage of 16 kV and attaining a radial expansion speed of 136.1 m/s. Note that image c) shows the expanded aluminum tube and d) the polyurea coating. The coating has contracted back approximately to its original dimensions, implying that the polyurea coating absorbs energy via elastic deformation. The polycarbonate coating does so in the form of plastic deformation.

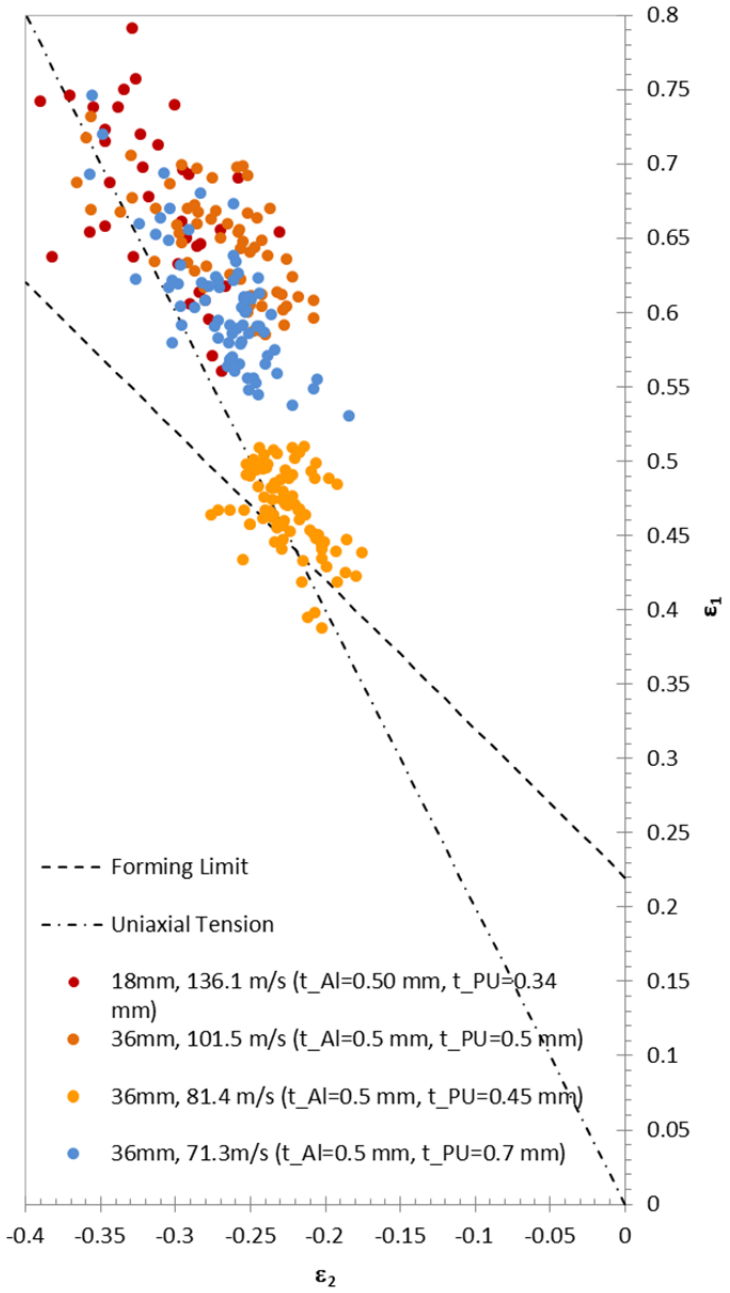

Figure 2.16: Dynamic Forming Limit diagram for Polyurea coated samples. Open circular symbols correspond to principal strains measured from regions where no localization is observed (none in this figure), and the filled circular symbols correspond to regions where localization is observed. The dash-dot line indicates the uniaxial path $\varepsilon_1 = -2\varepsilon_2$, and the dashed line indicates the quasi-static forming limit $\varepsilon_1 + \varepsilon_2 = n$ based on the maximum tension criterion.

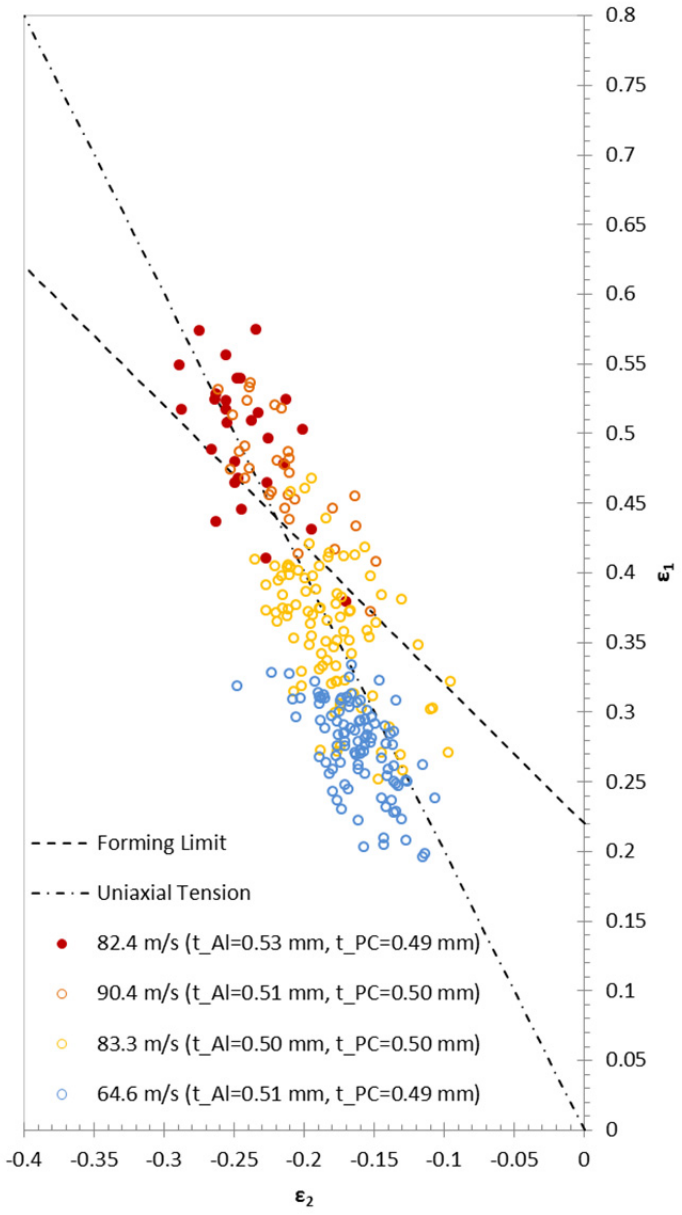

Figure 2.17: Dynamic Forming Limit diagram for Polycarbonate coated samples. Open circular symbols correspond to principal strains measured from regions where no localization is observed, and the filled circular symbols correspond to regions where localization is observed. The dash-dot line indicates the uniaxial path $\varepsilon_1 = -2\varepsilon_2$, and the dashed line indicates the quasi-static forming limit $\varepsilon_1 + \varepsilon_2 = n$ based on the maximum tension criterion.

a)

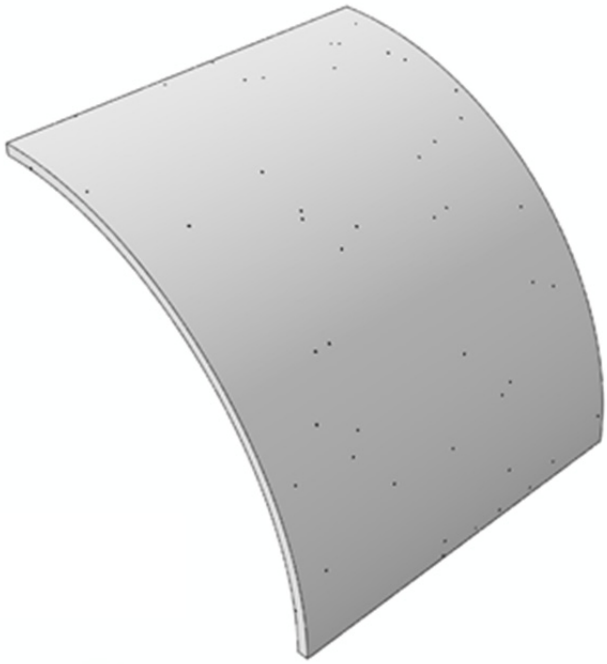

b)

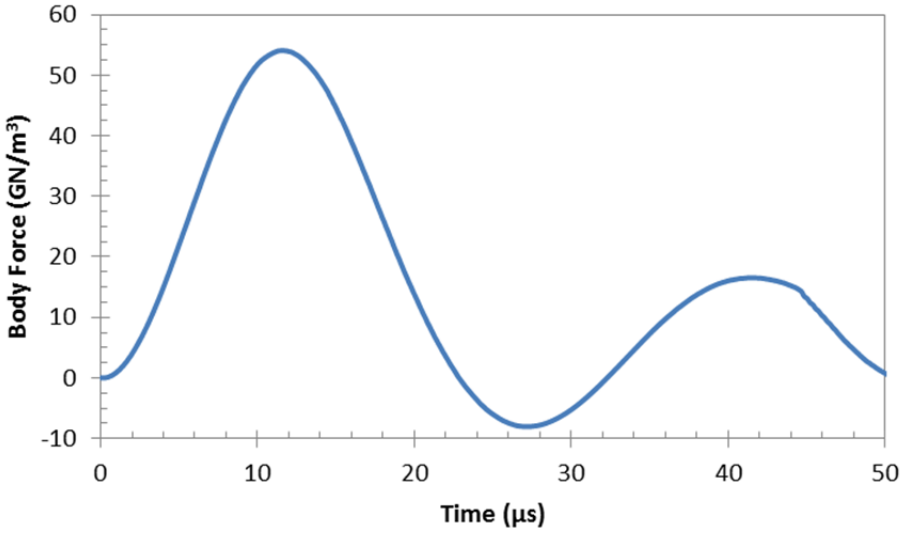

Figure 2.18: a) Quarter symmetry finite element model of the tube with 0.1% elements with material defects. b) Body force loading experienced by all points on the Al tube.

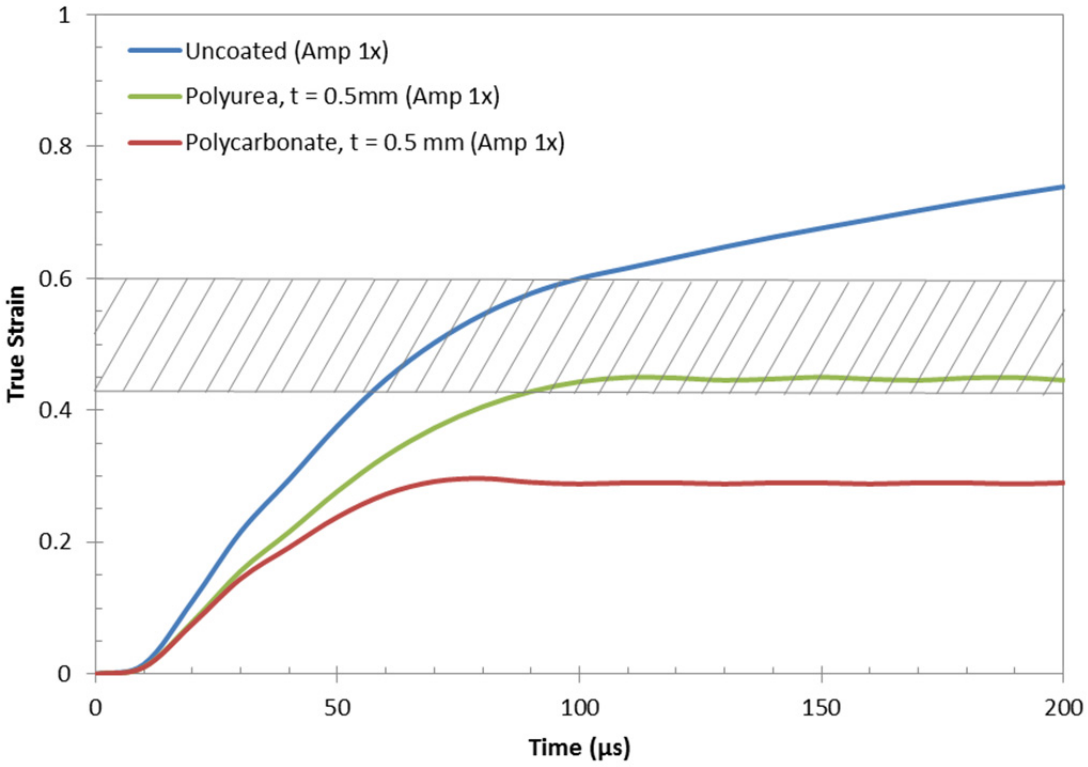

Figure 2.19: Variation of the hoop strain with time. The hashed region corresponds to the range of average strains at which failure occurs.

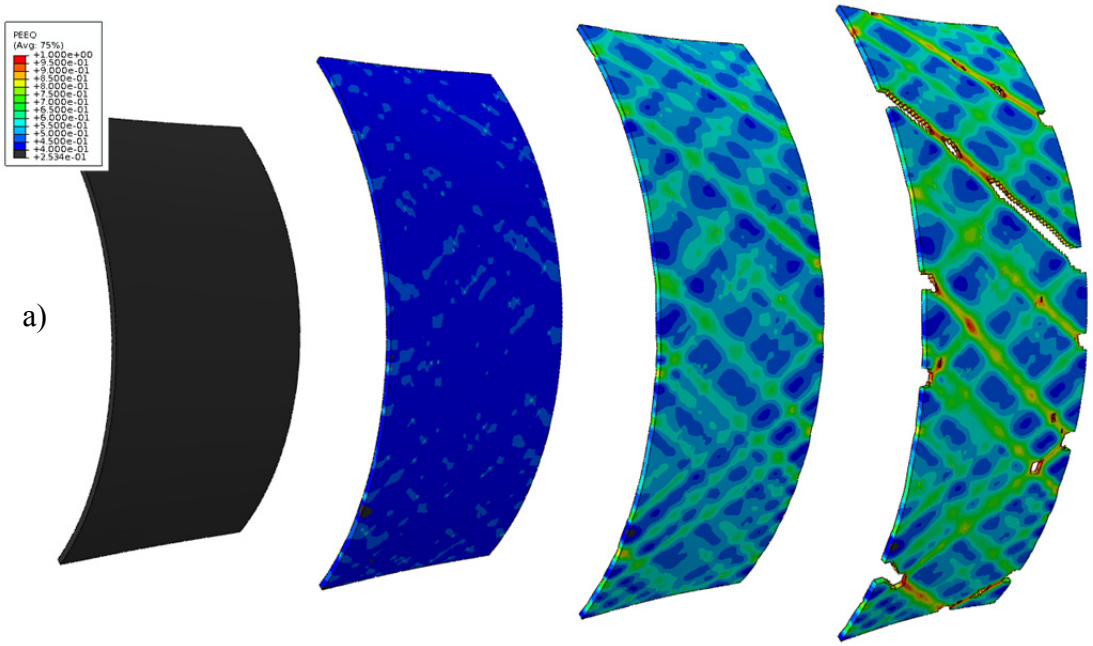
PEEQ
(Avg: 75%)
+1.000e+00
+9.500e-01
+9.000e-01
+8.500e-01
+8.000e-01
+7.500e-01
+7.000e-01
+6.500e-01
+6.000e-01
+5.500e-01
+5.000e-01
+4.500e-01
+4.000e-01
+2.534e-01
a)
$t = 40\mu s$
$t = 60\mu s$
$t = 80\mu s$
$t = 100\mu s$

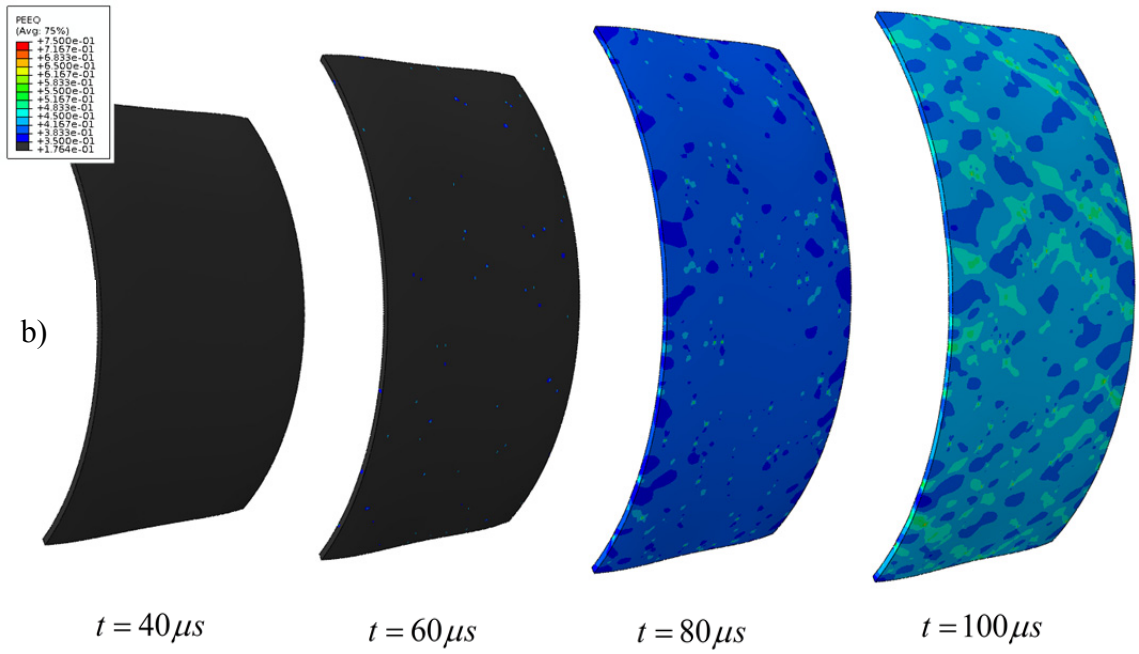
PEEQ
(Avg: 75%)
+7.500e-01
+7.167e-01
+6.833e-01
+6.500e-01
+6.167e-01
+5.833e-01
+5.500e-01
+5.167e-01
+4.833e-01
+4.500e-01
+4.167e-01
+3.833e-01
+3.500e-01
+1.764e-01
b)
$t = 40\mu s$
$t = 60\mu s$
$t = 80\mu s$
$t = 100\mu s$

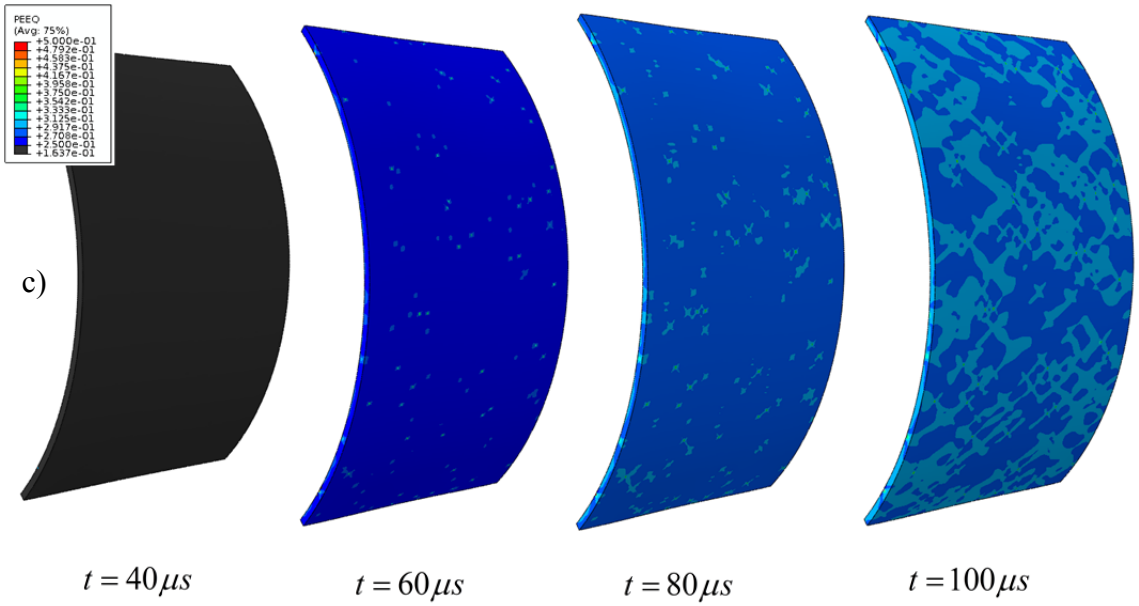

Figure 2.20: Contour plots of equivalent plastic strain from three simulations with identical applied force. (a) Bare Al 6061-O specimen, with $t_{AL} = 0.5$ mm; (b) Al/PU specimen with $t_{AL} = 0.5$ mm and $t_{PU} = 0.5$ mm; (c) Al/PC specimen with $t_{AL} = 0.5$ mm and $t_{PC} = 0.5$ mm. For (b) and (c), the coating has been masked, and only the strain in the Al tube is shown. The hoop stress in the coating layer was uniform at the levels indicated in Figure 2.21.

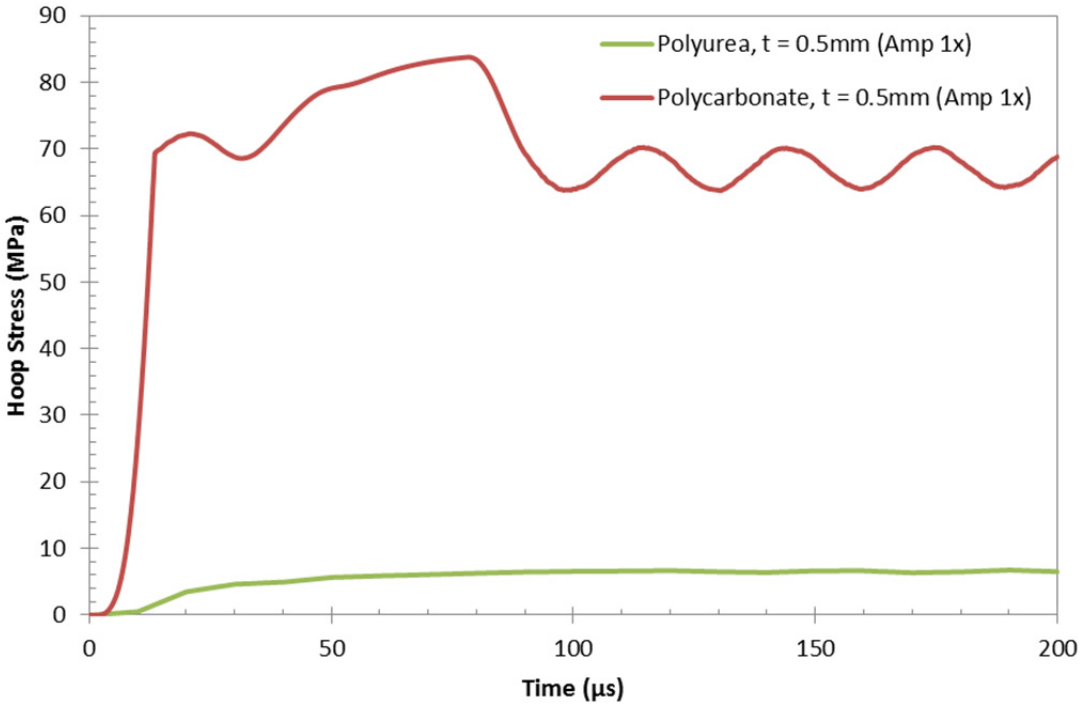

Figure 2.21: Variation of the hoop stress in the polyurea and polycarbonate coating.

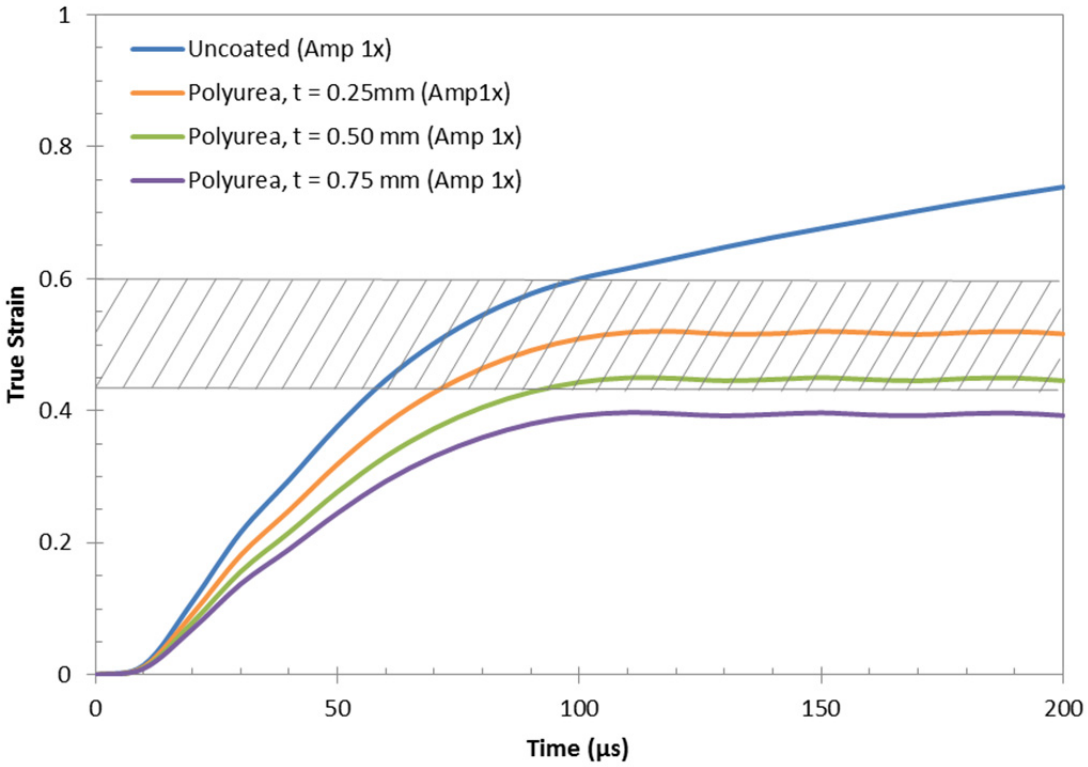

Figure 2.22: Variation of the hoop strain with time from four simulations with different thickness polyurea coatings.

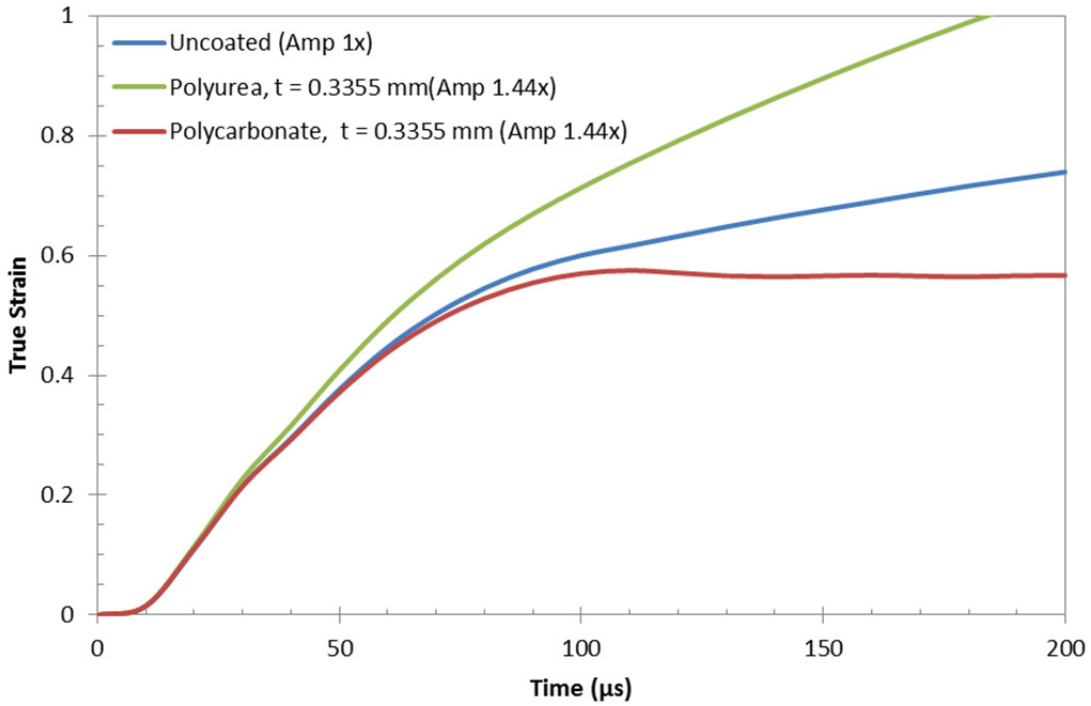

Figure 2.23: Variation of the hoop strain with time for three simulations with the same total mass and same applied loading.

Chapter 3: Dynamic Tension

3.1 INTRODUCTION

In this chapter, we illustrate the hybrid method of material characterization. Since it is very difficult to establish conditions of uniform deformation and stress under arbitrary dynamic loading, any test method designed to investigate the dynamic constitutive behavior of soft materials at large strain-rates to very large strain levels must deal with transient states in a hybrid or inverse approach; such an approach places no restrictions on specimen length and it is not necessary to establish uniformity of stress state or strain-rate; in addition, there is no limit to the strain level that can be attained in the test specimen.

We begin by describing the simple one-dimensional boundary-initial value problem of a long thin strip of the specimen with one end that is fixed at a clamp and with a known velocity history imposed at the other end to provide some insight as to how such a test could be performed. This is the classic problem originally considered in the context of plastic wave propagation in metals by von Karman and Duwez (1950), with the only difference being in the addition of real-time diagnostics to measure the strain and particle velocity as a function of time. The propagation of the nonlinear waves into the specimen imposes a transient state in the specimen with a nonuniform stress, strain, and strain-rate at each material point along the length of the strip, thereby enabling the material behavior to be interrogated under a larger range of loading conditions in one test. Nonlinear one-dimensional wave propagation theory provides the tools necessary to analyze this behavior and extract the material behavior through an inverse analysis. The theory and implementation for nonlinear elastic materials was covered by Niemczura and Ravi-Chandar (2011) and is reviewed below followed by a modification to capture the more rate dependent behavior of polyurea.

3.2. ONE-DIMENSIONAL NON LINEAR WAVE PROPAGATION THEORY

3.2.1 Non Linear Elastic Materials

The governing equations for the one dimensional problem are well-developed and are given here for completeness. Consider a one-dimensional semi-infinite strip of the material occupying $0 \le x < \infty$, where x represents the position of a material point in the reference configuration. Assuming that the transverse dimensions of the strip specimen are small, inertia effects associated with the transverse motion are neglected. Under such conditions, the motion of material points in the strip can be represented by the one kinematic quantity, $u(x,t)$, the displacement in the *x*-direction; therefore, the current position of the material point x at any time t is given by $y(x,t) = x + u(x,t)$. The corresponding strain and particle velocity are given by $\gamma(x,t) = \partial u / \partial x$ and $v(x,t) = \partial u / \partial t$ respectively. The stretch corresponding to this strain is $\lambda(x,t) = 1 + \gamma(x,t)$. The governing equations of motion for this one-dimensional wave problem are obtained from the balance of linear momentum and kinematic compatibility:

$$\frac{\partial \sigma}{\partial x} = \rho \frac{\partial v}{\partial t} \tag{3.1}$$

$$\frac{\partial v}{\partial x} = \frac{\partial \gamma}{\partial t} \tag{3.2}$$

where ρ is the mass density per unit volume (assumed to be constant as a result of the material incompressibility) and σ is the nominal stress (force per reference area). Introducing the notation given below in Eq. (3.3) and noting that the constitutive behavior is represented by $\sigma = \sigma(\gamma)$, Eqs.(3.1) and (3.2) can be written in the standard quasilinear form in Eq. (3.4).

$$\mathbf{u} = \begin{Bmatrix} v \\ \gamma \end{Bmatrix}, \quad \mathbf{u}_t = \frac{\partial \mathbf{u}}{\partial t}, \quad \mathbf{u}_x = \frac{\partial \mathbf{u}}{\partial x} \tag{3.3}$$

$$\mathbf{u}_t + \mathbf{A}\mathbf{u}_x = \mathbf{0} \tag{3.4}$$

where $\mathbf{A} = \begin{bmatrix} 0 & -\sigma'/\rho \\ -1 & 0 \end{bmatrix}$ and $\sigma' = d\sigma/d\gamma$ is the slope of the stress-strain curve. At the end $x = 0$, the specimen is subjected to a velocity boundary condition $v(0,t) = v_0(t)$ in the x-direction; this generates a wave propagating into the material in the x-direction. Note that when the imposed particle velocity is in the negative x-direction, the wave is tensile. In specimens of finite length, if attention is restricted to short times such that the reflections from the other end of the specimen are not observed, one establishes a semi-infinite specimen; on the other hand, if longer times are considered such reflections are important and in this case, the velocity boundary condition at the end $x = L$ is $v(L,t) = 0$. In addition, suitable initial conditions need to be specified; for example, the initial strain and particle velocity along the specimen are prescribed: $\gamma(x,0) = g(x)$, $v(x,0) = h(x)$. Such preloading can be used to examine wave propagation in prestretched specimens. The nominal stress is related to the strain and strain-rate through a nonlinear stress-strain relationship appropriate to this one-dimensional problem for the particular material and needs to be determined using an inverse or hybrid procedure.

The system given in Eq. (3.4) can be solved using the method of characteristics. Solving for the eigenvalues of the coefficient matrix $\mathbf{A}$, it can be shown that there are two distinct characteristics which propagate in opposite directions at the Lagrangian wave speed $C = \sqrt{\sigma'/\rho}$. The governing equations can now be written in characteristic form by multiplying through by the left eigenvectors which results in the following two equations.

$$\frac{dv}{dt} \pm C\frac{d\gamma}{dt} = 0 \quad \text{when} \quad \frac{dx}{dt} = \mp C \tag{3.5}$$

If particle velocity and strain are known at one time step we can march that solution forward in time along the characteristics to obtain the solution at the next time step. To do this we must first discretize the equations in space and time. Figure 3.1 shows the spatial discretization at time k and $k+1$. Quantities evaluated at time step k are

indicated without a superscript. The particle velocity and total strain are known at each location x_i at time k. To solve for the two quantities at x_i at time $k+1$ we march the solution at time k forward along the two characteristics; the locations of x_+ and x_- from which characteristics arrive at x_i at time $k+1$ are determined by the size of the time step and the respective wave speeds C_+ and C_-. Linear interpolation is used to find the necessary field quantities at each x_+ and x_-. The explicit expressions for marching the solution are given below:

$$\begin{aligned} \varepsilon_i^{k+1} &= \frac{C_+\varepsilon_+ + C_-\varepsilon_- - v_+ + v_-}{C_+ + C_-} \\ v_i^{k+1} &= \frac{C_+C_-}{C_+ + C_-}\left[\varepsilon_- - \varepsilon_+ + \frac{v_+}{C_+} + \frac{v_-}{C_-}\right] \end{aligned} \tag{3.6}$$

This is a modified form of the upwind-differencing scheme commonly used in computational fluid mechanics. Note that proper accounting of boundary conditions must be provided. Typically, the particle velocity or strain is prescribed and the other quantity is obtained from the characteristic that leaves the domain of interest as illustrated in Figure 3.1.

3.2.2 Viscoplastic Materials

Since we wish to consider nonlinear, rate-dependent materials, a viscoplastic model is considered in terms of the true-stress and logarithmic strain. In the uniaxial state considered here, the generic form of the constitutive equation can be written as follows:

$$\tau = E\left(\varepsilon - \varepsilon_p\right) \tag{3.7}$$

$$\dot{\varepsilon}_p = f\left(\tau, \varepsilon_p\right) \tag{3.8}$$

where $\tau = \lambda\sigma$ is the true stress, $\varepsilon = \ln\left(\lambda\right)$ is the true (logarithmic) strain, $\varepsilon_p = \varepsilon - \varepsilon_e$ is the plastic strain, ε_e is the elastic strain, and E is the modulus of elasticity. The time rate

of evolution of the plastic strain is taken to be a function of the plastic strain and the true stress. The particular functional form for the evolution of plastic strain in Eq. (3.8) will vary depending on the material examined; in the present work, we evaluated the Malvern, Johnson-Cook, Zhou-Clifton, and Bergstrom-Boyce models. The above equations can be written in the form of a quasi-linear system:

$$\frac{\partial}{\partial t}\begin{Bmatrix}\varepsilon\\ v\\ \varepsilon_p\end{Bmatrix}+\begin{bmatrix}0 & -e^{-\varepsilon} & 0\\ -e^{-\varepsilon}C^2 & 0 & e^{-\varepsilon}C_0^2\\ 0 & 0 & 0\end{bmatrix}\frac{\partial}{\partial X}\begin{Bmatrix}\varepsilon\\ v\\ \varepsilon_p\end{Bmatrix}=\begin{Bmatrix}0\\ 0\\ f\left(\tau,\varepsilon_p\right)\end{Bmatrix} \tag{3.9}$$

where $C_0=\sqrt{E/\rho}$ and $C=\sqrt{\left(E-\tau\right)/\rho}$. It should be noted that $C_0\sim C$ since τ is typically very small in comparison to E. Solving for the eigenvalues of this system, it can be shown that there are three distinct characteristics, two which propagate at nearly the elastic wave speed and a third stationary characteristic along which the plastic strain evolves. The governing equations can now be written in characteristic form:

$$\begin{aligned}&\dot{\varepsilon}_p=f\left(\tau,\varepsilon_p\right) && \text{on} \quad \frac{dx}{dt}=0\\ &\mp C\dot{\varepsilon}+\dot{v}\pm\frac{C_0^2}{C}\dot{\varepsilon}_p\mp\frac{C_0^2}{C}f\left(\tau,\varepsilon_p\right)=0 && \text{on} \quad \frac{dx}{dt}=\pm e^{-\varepsilon}C\end{aligned} \tag{3.10}$$

We follow a similar procedure as with the nonlinear elastic problem to solve the above system except now there is the addition of a third stationary characteristic. Again, we must discretize the equations in space and time. If the particle velocity, total strain, and plastic strain are known at one time step we can march that solution forward in time along the characteristics to obtain the solution at the next time step. Figure 3.2 shows the spatial discretization at time k and $k+1$. The particle velocity, total strain, and plastic strain are known at each location x_i at time k. To solve for the three quantities at x_i at time $k+1$ we march the solution at time k forward along the three characteristics; the locations of x_+ and x_- from which characteristics arrive at x_i at time $k+1$ are determined

by the size of the time step and the respective wave speeds $e^{-\varepsilon_+}C_+$ and $e^{-\varepsilon_-}C_-$. Linear interpolation is used to find the necessary field quantities at each x_+ and x_-. The explicit expressions for marching the solution are given below:

$$\begin{aligned}
\varepsilon_{pi}^{k+1} &= \varepsilon_{pi} + f(\varepsilon_{pi})\Delta t \\
\varepsilon_i^{k+1} &= \frac{C_+\varepsilon_+ + C_-\varepsilon_- - v_+ + v_-}{C_+ + C_-} \\
&\quad + \frac{1}{C_+ + C_-}\left[\frac{C_0^2}{C_+}\left(\varepsilon_{pi}^{k+1} - \varepsilon_{p+} - f(\tau_{p+},\varepsilon_{p+})\Delta t\right) + \frac{C_0^2}{C_-}\left(\varepsilon_{pi}^{k+1} - \varepsilon_{p-} - f(\tau_{p-},\varepsilon_{p-})\Delta t\right)\right] \\
v_i^{k+1} &= \frac{C_+C_-}{C_+ + C_-}\left[\varepsilon_- - \varepsilon_+ + \frac{v_+}{C_+} + \frac{v_-}{C_-}\right] \\
&\quad - \frac{C_+C_-}{C_+ + C_-}\left[\frac{C_0^2}{C_+^2}\left(\varepsilon_{pi}^{k+1} - \varepsilon_{p+} - f(\tau_{p+},\varepsilon_{p+})\Delta t\right) + \frac{C_0^2}{C_-^2}\left(\varepsilon_{pi}^{k+1} - \varepsilon_{p-} - f(\tau_{p-},\varepsilon_{p-})\Delta t\right)\right]
\end{aligned} \tag{3.11}$$

Given a constitutive model of the form in Eqs. (3.7) and (3.8), Eq. (3.11) can be used to identify the particle velocity and strain at any point as a function of time. However, we are interested in the inverse problem: the particle velocity and strain histories are determined through direct experimental measurements and the problem of identification of the constitutive model is examined.

3.3 EXPERIMENTAL SETUP

We now turn to a description of how the above boundary-initial value problem is implemented in the laboratory; a close up view of the experimental setup focusing on the test section is shown in Figure 3.3. The test apparatus is an air gun with a 2 meter long barrel. A guiding slot, along which a polycarbonate slider will travel, has been cut into half the length of the barrel. The slider is initially placed at the end of the slot and the polyurea specimen is wrapped around it as shown in the figure[5]. The ends of the polyurea

[5] In some later tests, the specimen was glued to the slider to prevent slippage.

specimen are then clamped at a distance L from the slider, typically ~180 mm. When the air gun is triggered, a hardened steel projectile is shot down the barrel toward the slider. Upon impact, the slider launches forward stretching the specimen. In order to monitor the wave propagation and make quantitative measurements of the strain and particle velocity, marker lines are drawn on the specimen. A plastic stencil was made with slots that are spaced at a uniform distance (2 mm in most cases); since the specimens were transparent[6], they were dusted with a light coat of white spray paint and then a black indelible ink maker was used to scribe lines on the specimen through the stencil. Various line thicknesses and spacing have been used; the optimum combination depends on the length of specimen that is within the field of view of the camera frame. The goal of this optimization is to achieve maximum spatial and temporal resolution while accounting for the limited number of pixels available in the image. The motion is recorded with a Photron SA1 high-speed video camera with a framing rate of 270,000 fps and a resolution of 1024x16. The typical physical region viewed in the camera is 2.18 mm high by 140 mm long, providing a resolution of 7.3 pixels/mm; in some tests, a smaller field of view (about 40 mm long) was used to improve the spatial resolution. Niemczura and Ravi-Chandar (2011) have used a variant of this method to examine nonlinear elastic waves in polyisoprene and nitrile rubbers.

There are a number of experimental factors that need special attention in order to minimize the measurement errors. The axial alignment of the specimen with the direction of movement of the projectile is particularly important. Small misalignments and friction between the guiding rail and the slider introduce a rotary wobble to the slider holding the

[6] The transparency was influenced significantly by the mixing procedure; when the Versalink and Isonate were not mixed adequately, it resulted in an opaque, stiff polymer with a very small stretch to failure. By ensuring proper mixing with a stirrer, it was possible to obtain specimens that were transparent and yellow in color.

specimen, and therefore produce twisting or kinking type out-of-plane motion that is superposed on the expected axial wave motion. Geometric imperfections of the specimens may also play a role. Variations in cross-sectional dimensions might introduce geometric dispersion of the wave and should be avoided. A last point to note is that the material itself may not be perfectly homogenous. While all the bubbles were removed by degassing the Isonate and Versalink prior to mixing, upon mixing bubbles are reintroduced and because the working time is so short it is not possible to remove them all by vacuum. There are a small number of bubbles present in the specimens. Long portions of the strips are free of the voids and specimens must be extracted from these sections.

When the high speed images are played back as a video at reduced speeds, the propagation of a tensile wave through the specimen is easily identifiable[7]. In order to aid in the visual examination and quantitative interpretation of the data, a $y-t$ diagram of the particle trajectories is constructed through digital image processing: from each video image corresponding to time *t*, the intensity of one line of pixels corresponding to the center line of the specimen marked in Figure 3.3 is extracted; denote this as $I(y,t)$. A new image $I(i,j) = I(y(i),t(j))$ was created in which each *i* corresponds to the physical *y*-direction in the fixed laboratory frame, while each *j* corresponds to the time of each video frame. Thus, the resulting picture is a streak image of the markers that indicates the particle trajectories in $y-t$ space; such a particle trajectory diagram from one experiment on the polyurea specimen is shown in Figure 3.4.

The $y-t$ diagram in Figure 3.4 does not show the entire length of specimen but instead focuses on the first 90 mm. The marker lines on the specimens are ~0.6 mm wide

[7] A video file showing the propagation of nonlinear elastic waves in polyurea is attached to the Supplementary Material DVD of this dissertation.

and spaced ~0.8 mm apart. The entire specimen is stationary and unstretched until the projectile impacts the slider at 74 μs and imparts a particle velocity to the specimen; at this time, the left edge of the specimen begins moving to the left. The message of the impact propagates into the specimen at the appropriate wave speeds; the highest strain-rates should occur in the region nearest the point of impact. Particle velocity and strain measurements can be obtained from these images and analyzed to extract the constitutive behavior. But before we begin this task, a couple features that are apparent in the image warrant further discussion. Along the front edge of the specimen several lines seem to just appear a short time after impact. These lines were initially sitting on the front face of the slider. Since the specimen is free to move on the slider the lines that were on the front portion of the slider simply came around the corner to the side of the slider. This can be taken into account in the analysis by considering only those marker lines that were visible in the initial image and using the measured velocity on the first of these lines as the boundary condition; the red line identified in Figure 3.4 was digitized and used as the point where the velocity boundary condition is prescribed. Also apparent in Figure 3.4 are several bright regions along the front edge of the specimen; these are artifacts caused by light being reflected in different directions due to the slight wobble of the slider about its axis. This wobble can create some noise in collected data and therefore, the data analyzed in the following section was collected only from material points originally 4mm away from the front end of the specimen.

The $y-t$ diagram of the type shown in Figure 3.4 *constitutes the primary diagnostic measurement in this experiment*. The particle trajectories are extracted from the $y-t$ diagram by using an edge tracing algorithm to follow the left and right edges of each line. This measurement provides the current position $y(x,t) = x + u(x,t)$ of the material points at the edge of each line. From these measurements, we may calculate the

strain and particle velocity throughout the specimen as a function of time. Note that this differentiation introduces errors. This error may be minimized by using a high spatial magnification with a small field of view and a high temporal sampling; it can be reduced further by a smoothing procedure that uses spline fits followed by a moving average filtering operation. It is also possible to use digital image correlation methods; however, when the strains reach the large levels encountered in the present experiments, the speckle patterns experience significant degradation and the correlation methods fail. It is possible to use the digital image correlation when the interest is in very high strain rates, but at small strain levels. The experimental method described above was initially implemented by Niemczura and Ravi-Chandar, (2011) to investigate the constitutive response of rubbers at high strain rates.

The ability to deform to large stretches, on the order of 10, for polyisoprene rubber is well known. The potential for the creation of tensile shocks occurs due to the inflection in the uniaxial stress strain response which occurs in the range of stretches between 3 to 4. As noted earlier, the Lagrangian wave speed is directly dependent on the tangent modulus therefore an inflection will result in an increase in the wave speed causing a shock to develop. This stretch range is achievable with the dynamic tension testing apparatus described above therefore the formation of tensile shocks should be possible; however, the results show that in the actual material the shock does not occur in the predicted stretch regime, suggesting the constitutive law must be modified to capture the true behavior at high rates.

Despite the mentioned discrepancy between predictions based on the quasistatic behavior and the experimental results at high rates, Niemczura and Ravi-Chandar, (2011) still found it possible to describe the response of latex rubber with a rate independent material model. When the strip was impacted no shocks formed. Instead, they observed

that the $y-t$ diagram showed a monotonically decreasing wave speed, meaning that the expected stiffening did not occur. The few other studies where dynamic tension of rubber was directly examined suggest that while the initial stiffness is greatly increased at high rates, above 350 s^{-1} little additional rate dependence is seen. These observations suggest a simple power law type behavior with the form given in Eq. (3.12) could effectively capture the dynamic tensile behavior of polyisoprene rubber.

$$\sigma = \sigma_0 + \mu(\gamma - \gamma_0)^n \tag{3.12}$$

Indeed, with the following parameters, $\mu = 0.93$ MPa, $n = 0.6$, $\gamma_0 = 0.03$, Niemczura and Ravi-Chandar, (2011) were able to predict the particle displacement as a function of time along the length of the specimen for strains up to 2.75 as long as the strain rate was above 500 s^{-1}. In Chapter 4, we will examine the applicability of these uniaxial results to biaxial loading by monitoring the wave propagation during the dynamic deformation of a rubber membrane.

3.4 CHARACTERIZATION OF RATE DEPENDENT MATERIALS

3.4.1 Polyurea

The polyurea used for the dynamic tension tests was prepared in the same manner and with the same formulation as that described in Section 2.1.4. After the mixture is degassed for two minutes, it is poured onto a large steel plate to which mold release has been applied. The plate is then passed under a blade fixed approximately 1.5 mm above the surface. This process spreads the polyurea into a film of uniform thickness. The film is then allowed to cure for 7 days; the polyurea is then peeled off the plate as a single sheet and sliced with a razor blade and a straight edge into long thin strips to be used in

the dynamic tension experiments. These strips are typically about 350 mm long with cross sectional dimensions of 1.40 ± 0.05 mm thickness and 5.00 ± 0.10 mm width.

Numerous experiments were performed over a range of impact speeds from about 60 to 100 m/s, resulting in stretch rates over a range from 800 to 8000 s^{-1}. One of these, Test PU-A, is described in detail in this section. Figure 3.5 shows the experimentally recorded particle velocity and strain histories at material points spaced 10 mm apart for Test PU-A. Figure 3.6 shows the corresponding particle velocity and strain profiles at 50 μs time intervals[8]. Initially, both velocity and strain are zero along the entire length. As time increases the left end of the specimen is accelerated in the negative x direction causing the particle velocity and the strain to increase near the impact end. The propagation of the strain and particle velocity profiles into the specimen can be seen readily in these figures and are used in the following to determine the constitutive properties of the material.

By tracing the movement of each material point to within one pixel resolution (i.e., a displacement of at least one pixel corresponding to 0.137 mm), it is observed that the fastest measurable disturbance propagates at a speed of 316 m/s. Until this characteristic (wave) arrives, a material point does not feel the effects of the velocity imposed at the left end. We take this to correspond to the elastic wave speed, and estimate the "dynamic elastic modulus" of the polyurea as $E_d = \rho C^2$; this estimate of 100 MPa is to be compared to the quasi-static measurement of 70 MPa and clearly indicates the influence of the viscoelastic material behavior. Note however that the strain associated with this wave is extremely small. Since the pixel resolution is quite low the

[8] It should be noted that these plots result from taking derivatives of the position data; therefore there is an inherent error from numerical differentiation that has been smoothed by a moving average filter. Furthermore, the slider interacts frictionally with the guiding slots in the barrel and provides a nonuniform boundary condition at the attachment point.

early elastic wave is not fully resolved and what we obtain is a lower bound on the elastic modulus. With increasing time, material points continue to accelerate and move to the left with increasing particle velocity and strain; this is the region of primary interest.

As is evident from Figure 3.5, the impact event does not generate a step increase in particle velocity, but only a rapid increase to about 40 m/s in the first 50 μs and then a more gradual increase to ~80 m/s over the next 100 μs. Corresponding to this, the strain profiles shown in Figure 3.5 indicate that the strain attains values in the range of about 0.6 at the impact point, and that the large strains move into the specimen slowly. The dissipative nature of the wave propagation is also evident from these figures by noting that the stretch rate and particle acceleration decrease continuously as the wave moves further into the specimen. The peak stretch rates occur at the location of the impact and are in the range of 8000 s^{-1}, but a few centimeters away the strain-rate has already decayed by an order of magnitude. This dissipation is a manifestation of highly nonlinear and rate-dependent behavior of the material.

As clearly demonstrated in the experiments above, the material experiences a wide range of strains (0 – 0.6), and strain-rates (800 – 8000 s^{-1}) at each location in this dynamic transient tension test. This fact makes for a very powerful test method because a single test provides experimental data for many loading conditions. Fitting a constitutive model to a single test will calibrate that model over a very large range of strains and strain-rates. Finding such a model, that can accurately capture the behavior over the entire spectrum of strains and strain-rates experienced in each test, does however prove to be quite a challenge. Many constitutive models have been proposed in the literature, covering a range of material response in metals and polymers, and are either purely empirical or motivated through micromechanical models that aim to capture the underlying deformation mechanisms; however, most of these viscoplastic models rely on

the nonequilibrium or "overstress" conditions that are generated at high strain rates, where the stress rises quickly and then approaches the "equilibrium stress" as the strain evolves in time. This is motivated by the fact that the nonequilibrium response is thermally assisted. In lieu of determining the exact model that describes all of polyurea's behavior in tension, we found one set of parameters which produced a satisfactory representation of the actual behavior in the stretch-rate range of 800 – 8000 per second.

Malvern (1951) suggested the following phenomenological model as a means to describe the high rate behavior of strain-rate dependent materials:

$$\dot{\varepsilon}_p = \dot{\varepsilon}_0 \left[\exp\left(\frac{\tau - g\left(\varepsilon_p\right)}{B} \right) - 1 \right] \tag{3.13}$$

where $g\left(\varepsilon_p\right)$ is the quasi-static or equilibrium stress-strain curve for the material and B and $\dot{\varepsilon}_0$ are materials constants. This is referred to as the overstress model because the strain-rate depends on the difference between the current stress and the equilibrium stress and is supposed to model thermally activated processes.

Johnson and Cook (1985) suggested a strain-rate dependent material response that can be written as follows:

$$\tau = \left[D_1 + D_2 \exp\left(D_3 \varepsilon_p \right) \right] \left(1 + D_4 \ln \dot{\varepsilon}_p \right) f\left[T\right] \tag{3.14}$$

where D_i are material parameters. This model has been calibrated for many metallic materials.

Bergstrom and Boyce (1998) used a two-part viscoplastic model that combines in parallel an equilibrium response and a time-dependent response to fit the strain-rate dependent response of carbon black filled Chloroprene rubber. The time-dependent part is written in the form:

$$\dot{\varepsilon}_p = \dot{\varepsilon}_0 \left(\lambda_{chain}^p - 1 \right)^c \left(\frac{\tau_B}{\hat{\tau}_B} \right)^m \tag{3.15}$$

where τ_B is the effective shear stress, λ_{chain}^{p} is a measure of the inelastic stretch in the chains and $\hat{\tau}_B \dot{\varepsilon}_p = \dot{\varepsilon}_0 \left(\lambda_{chain}^{p} - 1\right)^c \left(\frac{\tau_B}{\hat{\tau}_B}\right)^m$, $\dot{\varepsilon}_0$, c, and m are material constants.

Zhou and Clifton (1996) suggested the following phenomenological model as a means to describe the high rate behavior of 1045 steel:

$$\dot{\varepsilon}_p = \frac{\dot{\varepsilon}_1 \dot{\varepsilon}_2}{\dot{\varepsilon}_1 + \dot{\varepsilon}_2} \tag{3.16}$$

$$\dot{\varepsilon}_1 = \dot{\varepsilon}_0 \left[\frac{\tau}{g(k\varepsilon_p, T)}\right]^m \tag{3.17}$$

$$\dot{\varepsilon}_2 = \dot{\varepsilon}_m \exp\left[-\frac{a g(k\varepsilon_p, T)}{\tau}\right] \tag{3.18}$$

$$g(k\varepsilon_p, T) = g_0\left(k\varepsilon_p\right)\left[1 - \beta\left\{\left(\frac{T}{T_0}\right)^{\kappa} - 1\right\}\right] \tag{3.19}$$

where the function $g_0\left(k\varepsilon_p\right)$ is the quasi-static stress strain relation at a small strain-rate[9]. $\dot{\varepsilon}_0$, β and κ determine the thermal influence, T is the temperature and T_0 is a reference temperature. m and a are rate-sensitivity parameters. Note that Eq. (3.16) is valid only when $\tau > g$; otherwise $\dot{\varepsilon}_p = 0$. This model has been used for representing the response of other metallic materials such as copper and aluminum alloys. The model is attractive because it combines both a power-law and exponential response and is therefore able to represent a wide range of viscoplastic material behavior. However, we may need to modify the model to provide for stiffening when the polymer network is stretched highly, as in the Bergstrom and Boyce model.

---

[9] We have introduced a constant k in an effort to allow more flexibility in calibrating the measured response. The physical meaning of this is that the equilibrium response is somewhat stiffer than the quasi-static response. In this matter, we can only present a heuristic argument, since a detailed micromechanical model is not available. We suppose that the quasistatic response is attained only at extremely slow rates, when all possible configurations of the polymer chains can be sampled; in contrast, under the high strain-rate loading employed here, we conjecture that only some fraction of the possible configurations are sampled, naturally leading to a stiffer response.

Any one of the above phenomenological models can be introduced in the Riemann solution method described earlier to determine the particle trajectory and strain in the one-dimensional problem. The inverse method of identifying the model parameters relies on comparing the calculated particle trajectory and strain variation in the specimen with the measurements. It is essential to recognize that none of the above models pays any particular attention to the specific deformation mechanisms of the material. Simply identifying that the microscopic deformation mechanisms are thermally activated processes and hence must have an exponential or power-law form allows us to use models of this type for a wide range of materials. The specific material-based differences then arise in the calibration of the particular model. Through numerous trials, it was determined that except for the modified Zhou-Clifton model, none of the other models came close to replicating the measured response of the polyurea over the range of stretch-rates (800 to 8000 s^{-1}) and strains (0 – 0.6). The Zhou-Clifton model, with the parameters given in Table 3.1, provided the best fit between the observed material behavior and the calculated response. The particle trajectories calculated using the model are compared to the experimentally observed particle trajectories in Figure 3.7; for the sake of clarity, only selected lines are shown. The accuracy of the fit can be best demonstrated by considering the error in position; over the entire image, the mean position error between the measured trajectory and the calculated trajectory was within 2 pixels; we note that higher spatio-temporal resolution in the experiments could reduce this error significantly. The particle velocity and strain histories computed from the model are compared to the experimentally determined histories for the specimen PU-A in Figure 3.8. A similar comparison is shown for the particle velocity and strain profiles in Figures 3.9. The overall trends in the simulation appear to match reasonably well with the experimental measurements. Deviations between the simulation and experiment become pronounced

only for locations far from the impact point, corresponding to later times and smaller strain rates. This suggests the possible need for multiple models for capturing the overall dynamic response. In order to highlight this, results from a second test PU-B, focusing here only on the first 10 mm from the impact point, were examined; the impact speed in this case was about 70 m/s. Comparison of the experimental velocity and true strain profiles in the first 10 mm region with the predicted response is shown in Figure 3.10. It is noted that the material parameters calibrated from Test PU-A were used in generating the predictions in Figure 3.10. Very good correlation is obtained between the prediction and measurements in terms of the particle velocity; somewhat larger errors arise in the strain comparisons, perhaps due to the larger gage lengths involved in the strain measurements. The spatio-temporal evolution of stretch-rate in Test PU-B is shown in the contour plot in Figure 3.11; it is clear that the stretch-rate is highly nonuniform both spatially and temporally. Stretch-rates reach about 8000 s^{-1}, but only over a small spatio-temporal domain. However, as pointed out earlier, this is precisely the advantage of this test method. Rather than insisting on achieving a constant stretch-rate, one single test provides a way to calibrate the model over a wide range of strains and strain rates. Similarly, good fits were obtained in all the other tests performed at different impact velocities, with the same calibrated material properties.

Finally, the stress-strain paths taken by several material points are shown in Figure 3.12 by the solid red lines, with the full understanding that each material point experiences a time varying stretch rate. The stress-strain responses predicted by the Zhou-Clifton model for different constant stretch-rates are shown in this figure by the blue lines; the quasi-static stress strain curve is shown by the blue dashed line. It is clear that since the stretch-rate in the experiment varies with time, the stress-strain paths taken by the material points in the experiments do not follow any one particular constant

stretch-rate curve, but migrate between these curves. Also, from this comparison, for a stretch-rate of 8000 s^{-1} we expect the "flow stress" to be at most three times that expected in quasi-static loading. We note that in their simulation of a polyurea-coated aluminum ring, Zhang et al (2009) indicated that multiplying the quasi-static stress strain curve by a factor of five was sufficient to reproduce the experimentally observed expansion of the polyurea-coated aluminum ring at a strain-rate of about 15,000 s^{-1} and is in the same range as the inferred stress-strain curve suggested in the present work. Based on the quality of the comparison between the experiment and the calibrated model, we can indicate that the tensile behavior of polyurea for strains below 80% at stretch-rates in the range of ~800-8000 s^{-1} can be represented by the model in Eqs. (3.16)-(3.19), with the parameters provided in Table 3.1.

Circumventing the numerous difficulties associated with the classical split-Hopkinson apparatus, the classical experiment of von Karman and Duwez has been reconstructed with modern diagnostic instrumentation. This experiment permits the evaluation of the tensile response of materials with very few limitations. In particular, the particle velocity and strain are measured at a number of material points as a function of time and used to extract the material constitutive response through an inverse process. As an illustrative example, this method is used to show that the Zhou-Clifton viscoplastic material model can be used to characterize the high strain-rate tensile response of a transparent elastomer, polyurea to large strains. The response of this material has been captured using a modified viscoplastic constitutive relation over stretch rates ranging from 800 – 8000 s^{-1}.

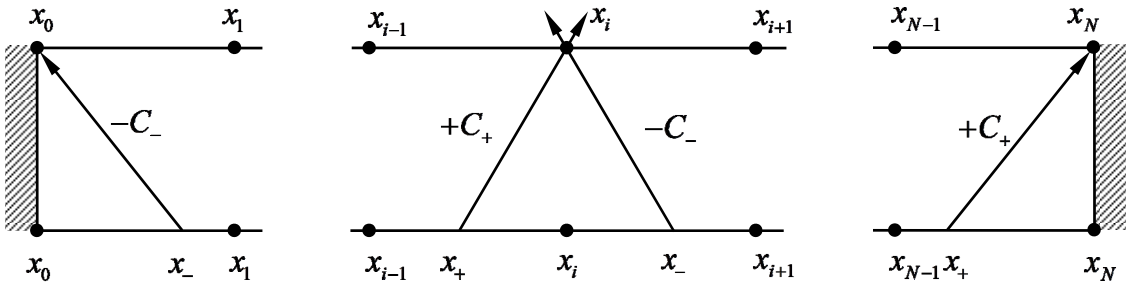

Figure 3.1: Stepwise calculation by the method of characteristics for nonlinear elasticity

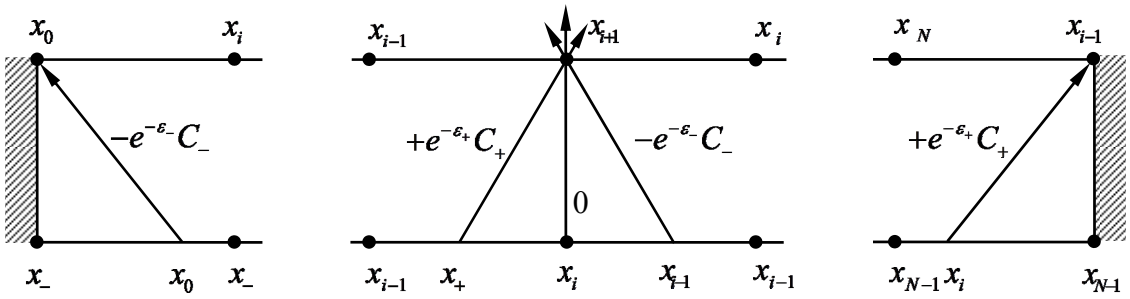

Figure 3.2: Stepwise calculation by the method of characteristics for viscoplasticity

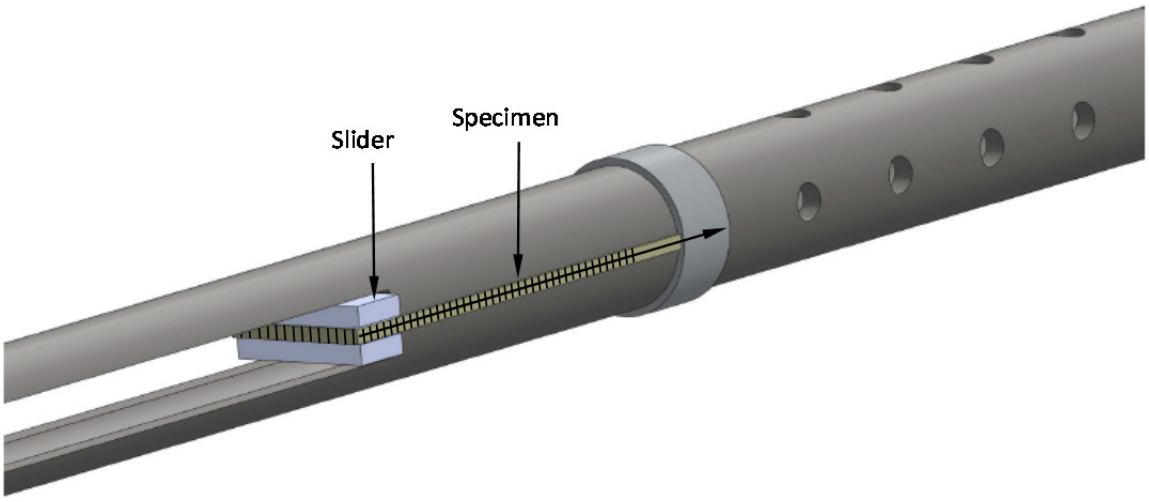

Figure 3.3: Experimental arrangement for generating impact-induced tensile waves. Black lines are drawn on the specimen; the x-direction is indicated by the arrow.

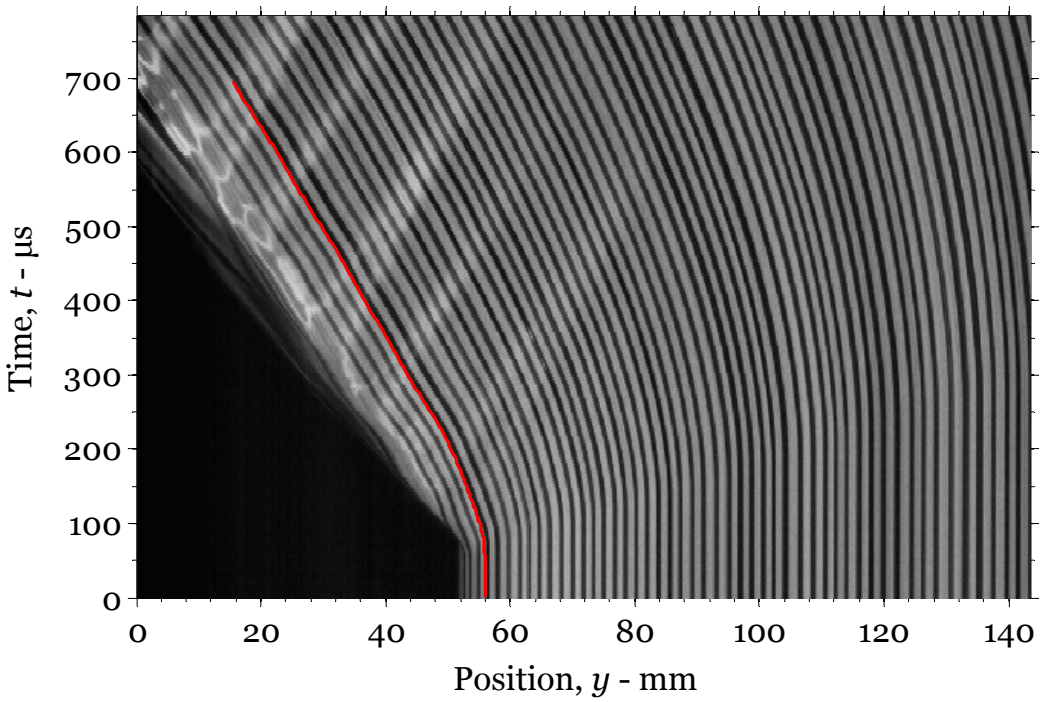

Figure 3.4: Particle trajectory diagram for Test PU-A in laboratory frame. Solid red line shows the edge trace from which the velocity boundary condition applied in simulations is extracted.

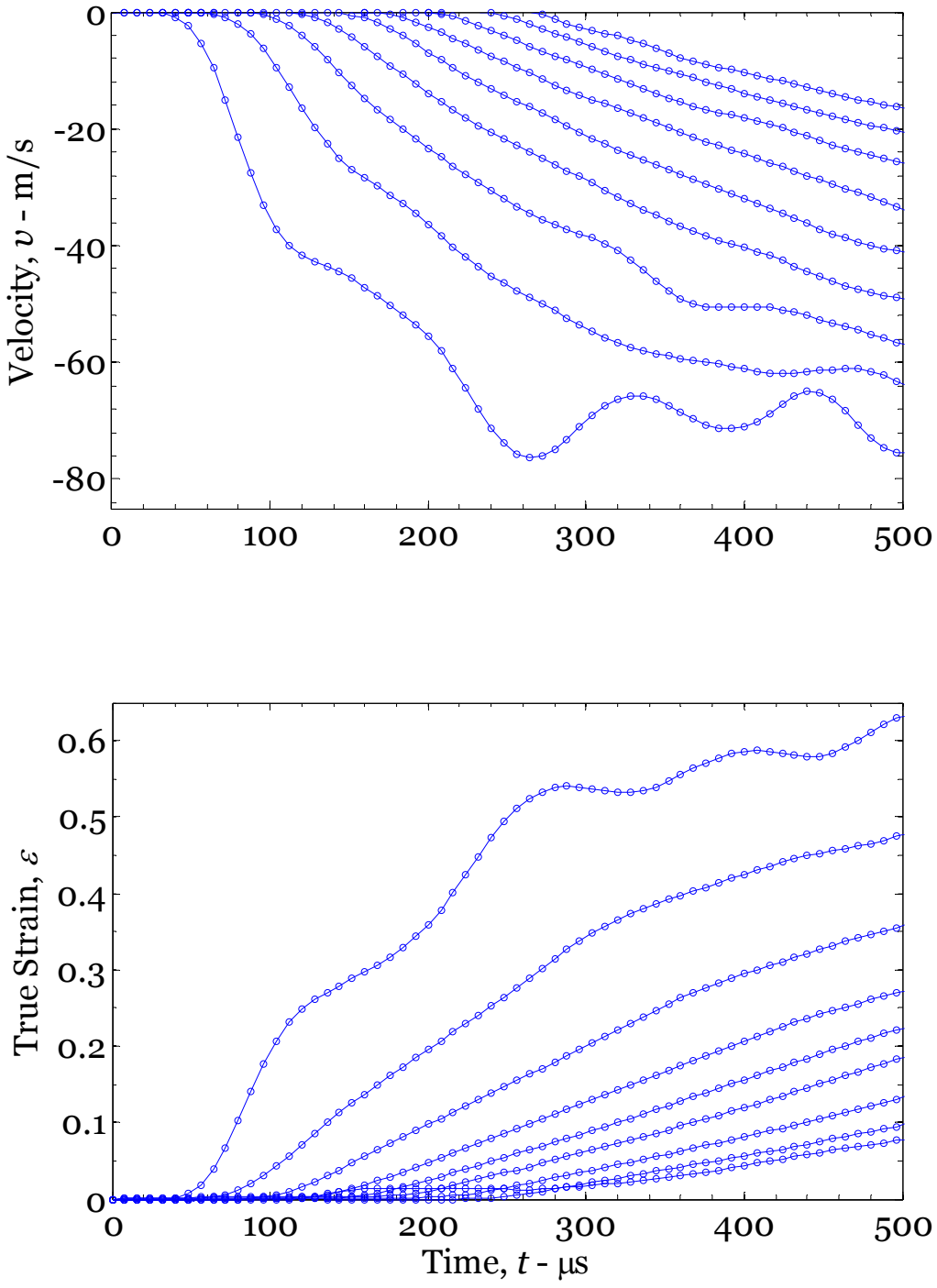

Figure 3.5: Velocity and true strain histories at material points spaced 10 mm apart for Test PU-A.

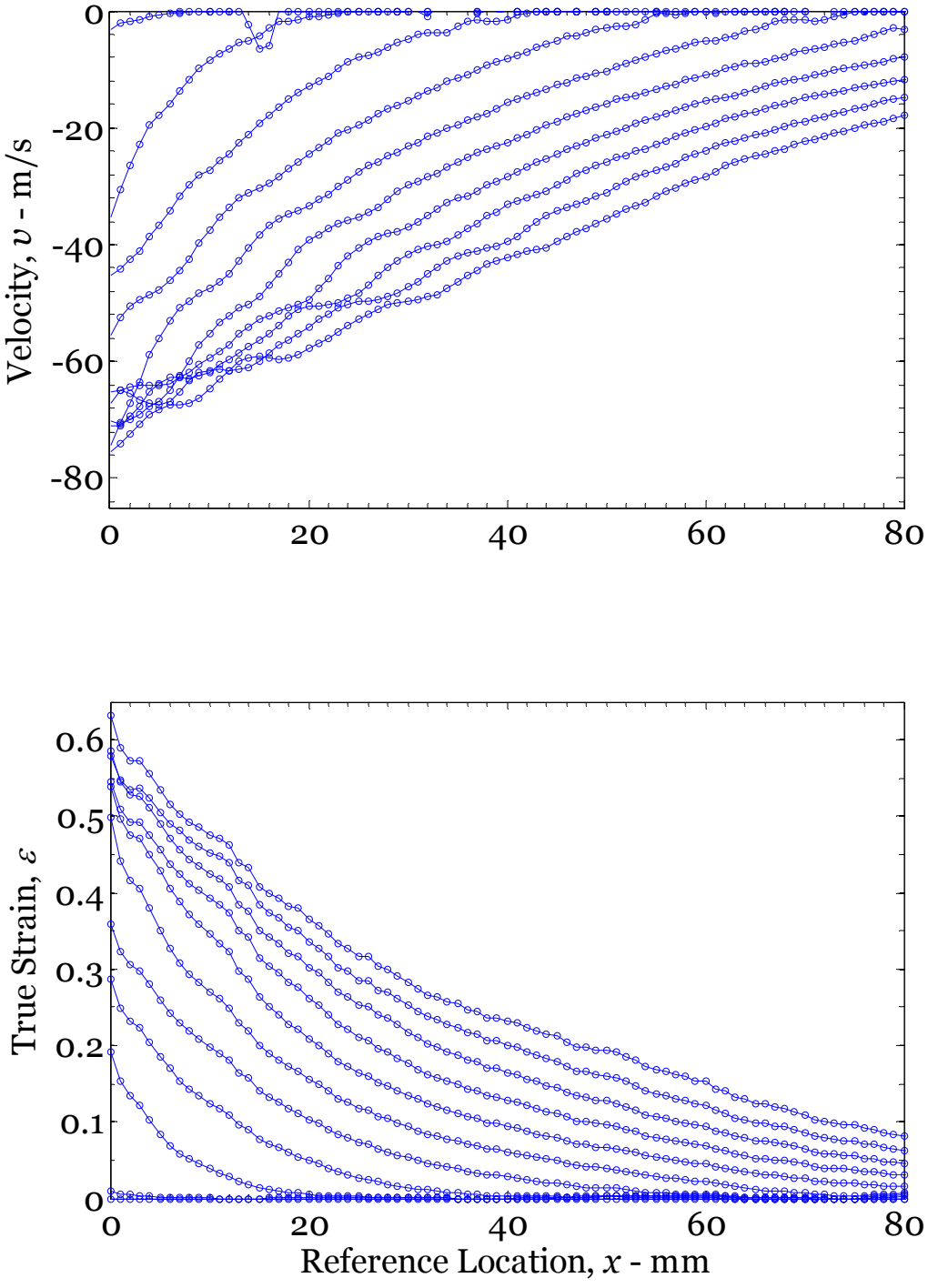

Figure 3.6: Velocity and true strain profiles along the length of the specimen every 50 μs for Test PU-A

Table 3.1: Zhou-Clifton model parameters for polyurea

E (MPa)	ρ (kg/m^3)	$\dot{\varepsilon}_0$	$\dot{\varepsilon}_m$	m	a	k
100	1200	0.1	1.0 E7	10	20	1.5

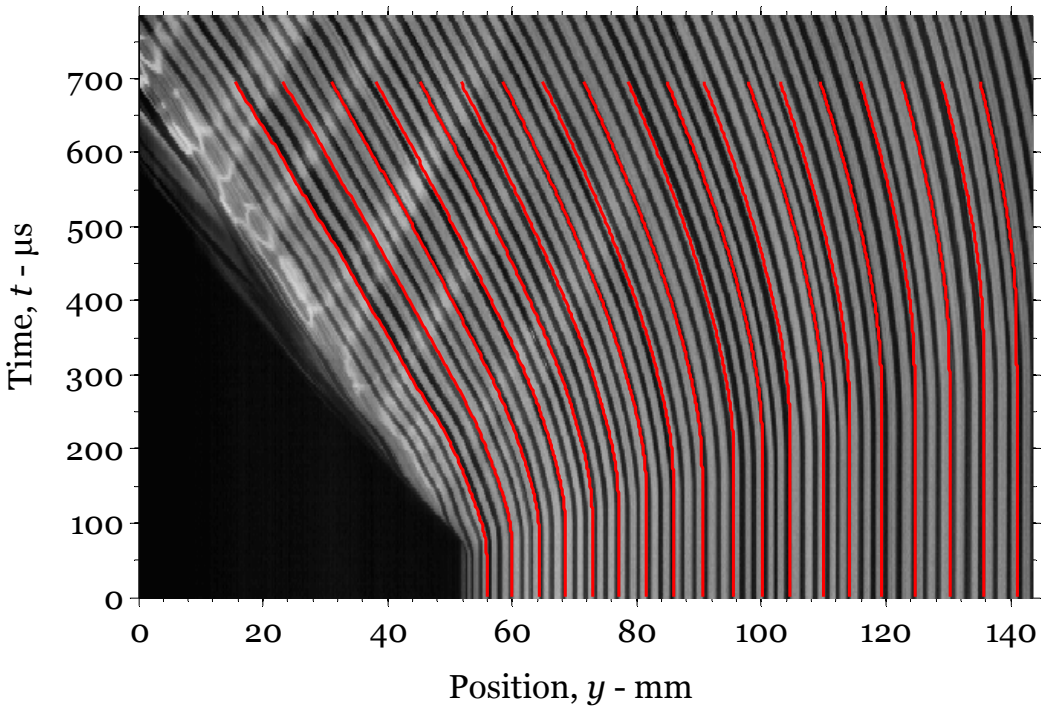

Figure 3.7: Particle trajectory diagram for Test PU-A in laboratory frame. Solid red lines show the simulated particle paths at selected locations.

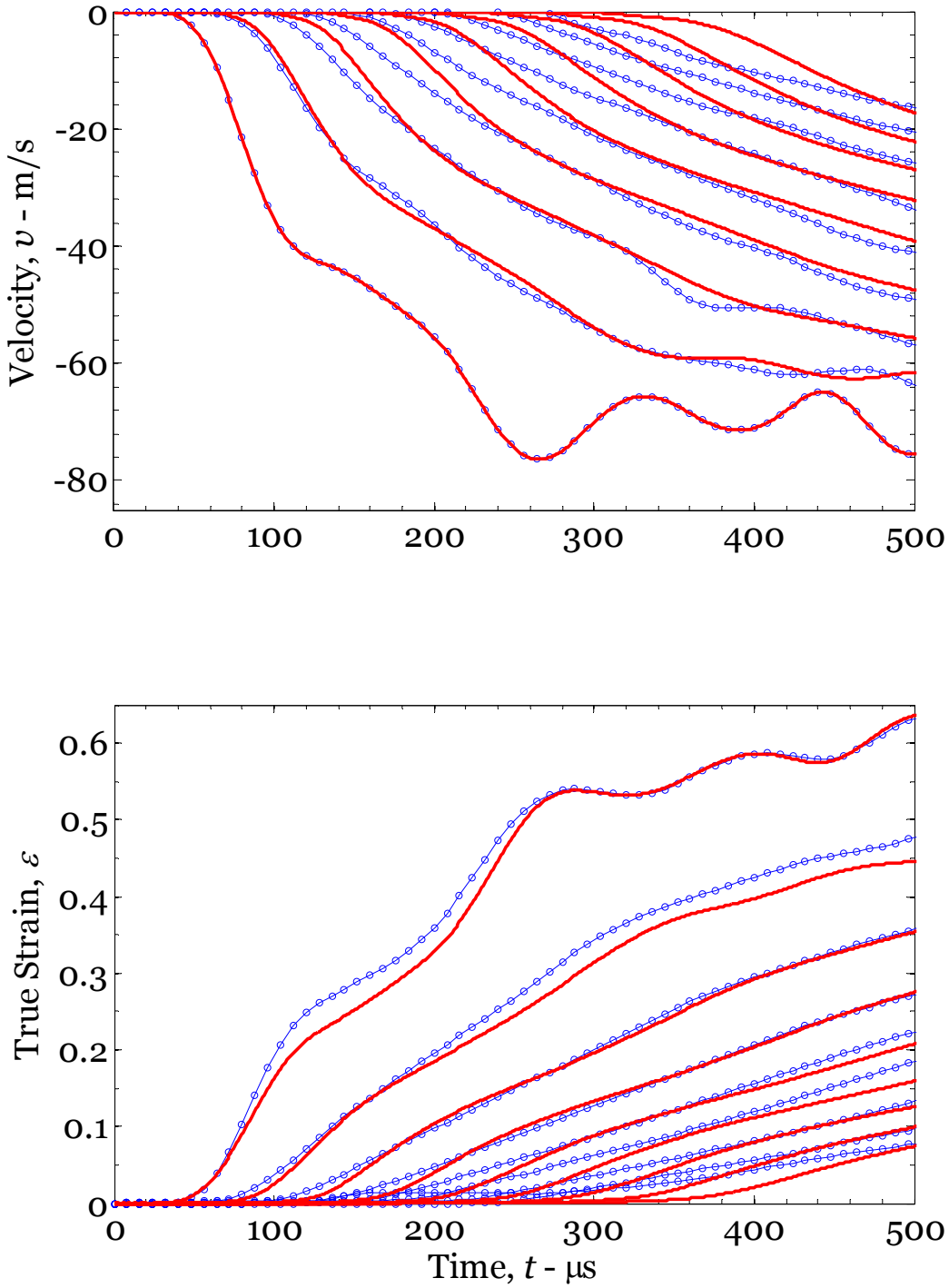

Figure 3.8: Comparison of measured (blue) and simulated (red) velocity and true strain histories at material points spaced 10 mm apart for Test PU-A.

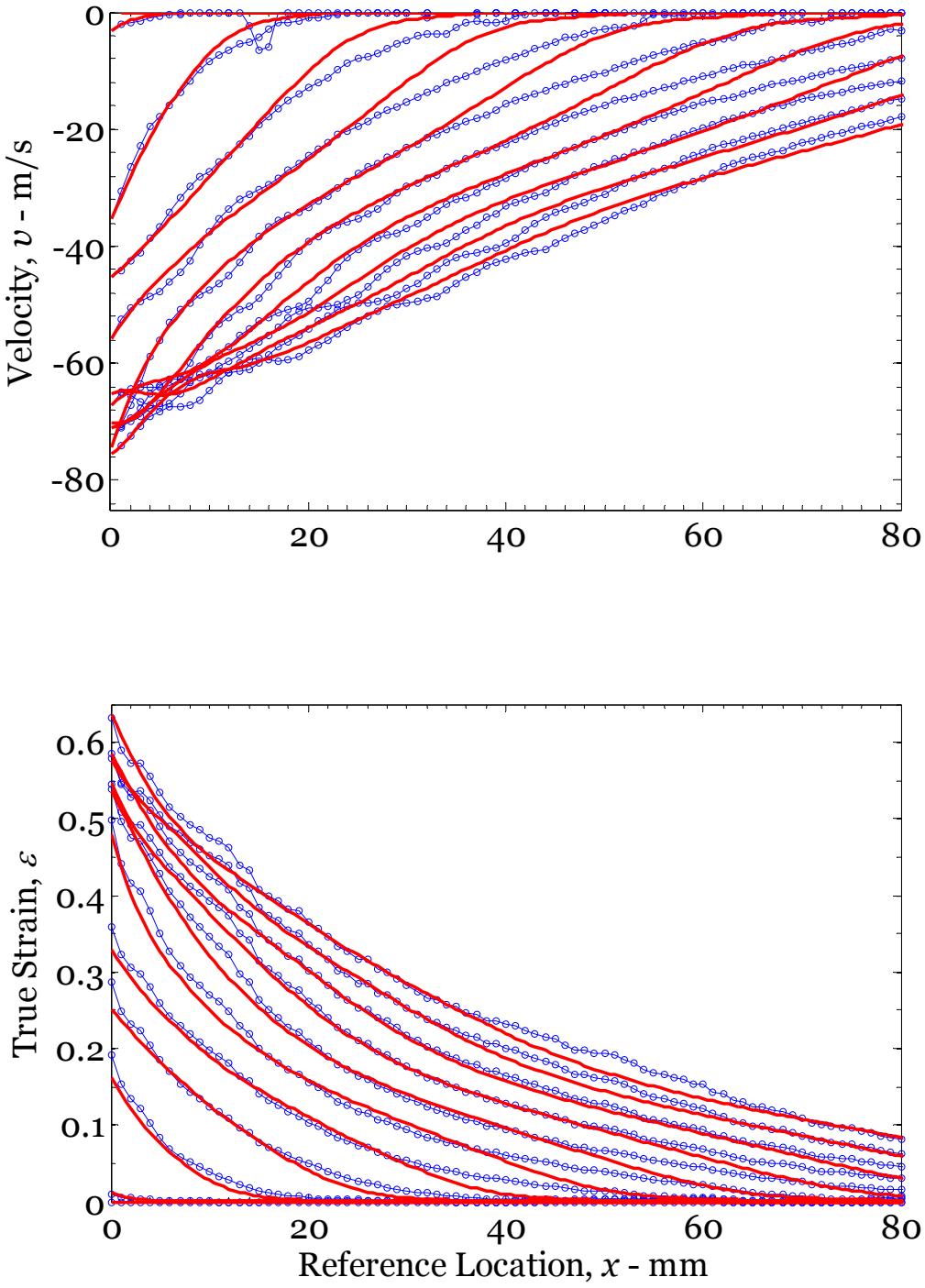

Figure 3.9: Comparison of measured (blue) and simulated (red) velocity and true strain profiles along the length of the specimen every 50 μs for Test PU-A.

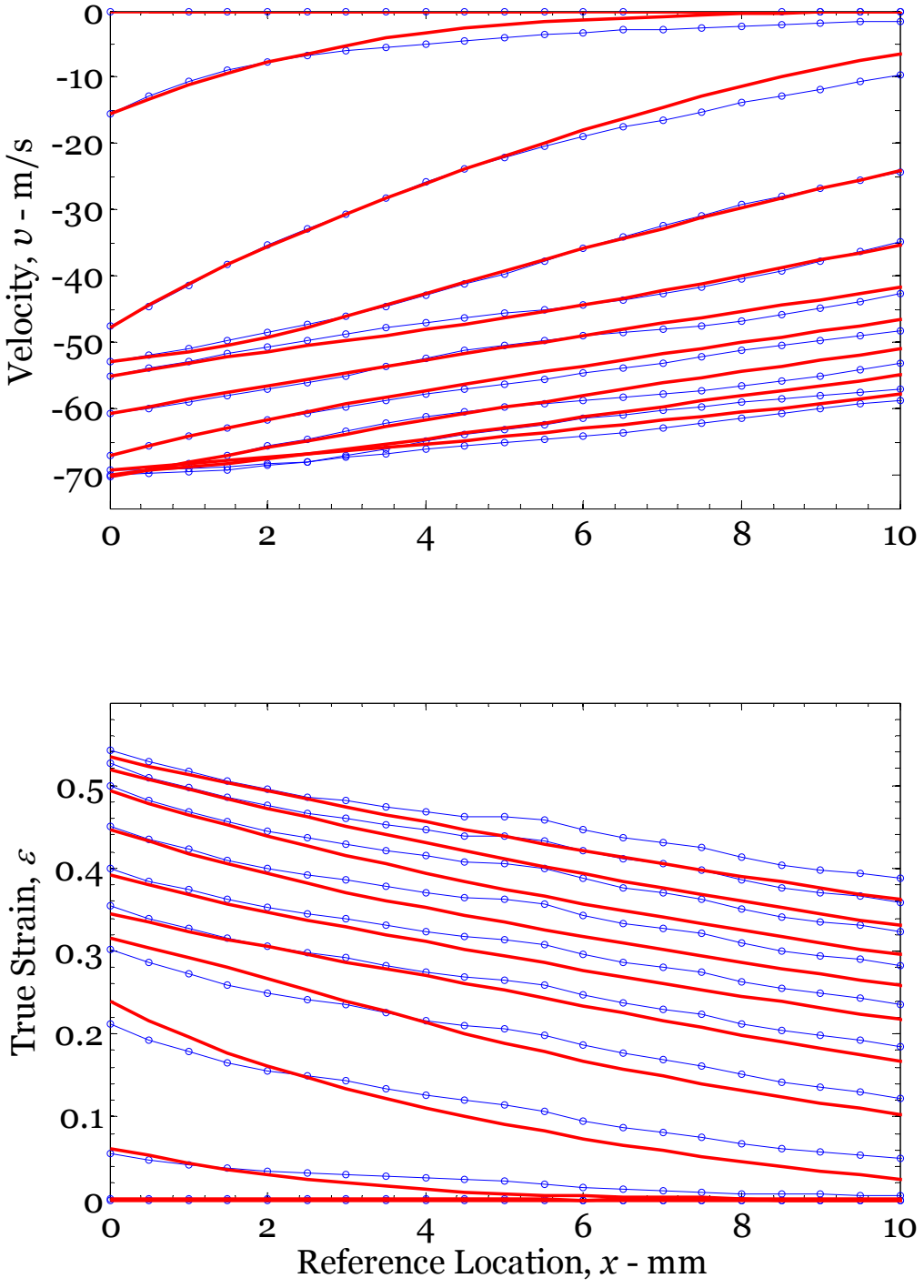

Figure 3.10: Comparison of measured (blue) and predicted (red) velocity and true strain profiles over the first 10mm for Test PU-B every 50 μs .

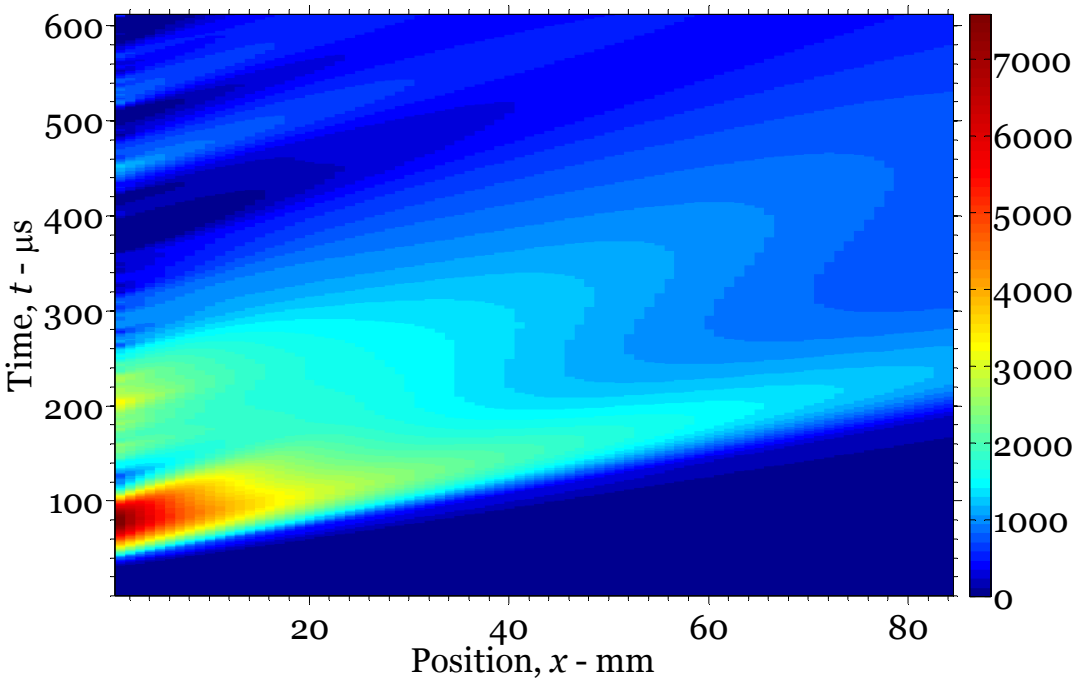

Figure 3.11: Contour plot showing the spatio-temporal variation in the stretch rate $\dot{\lambda}$ Test PU-B.

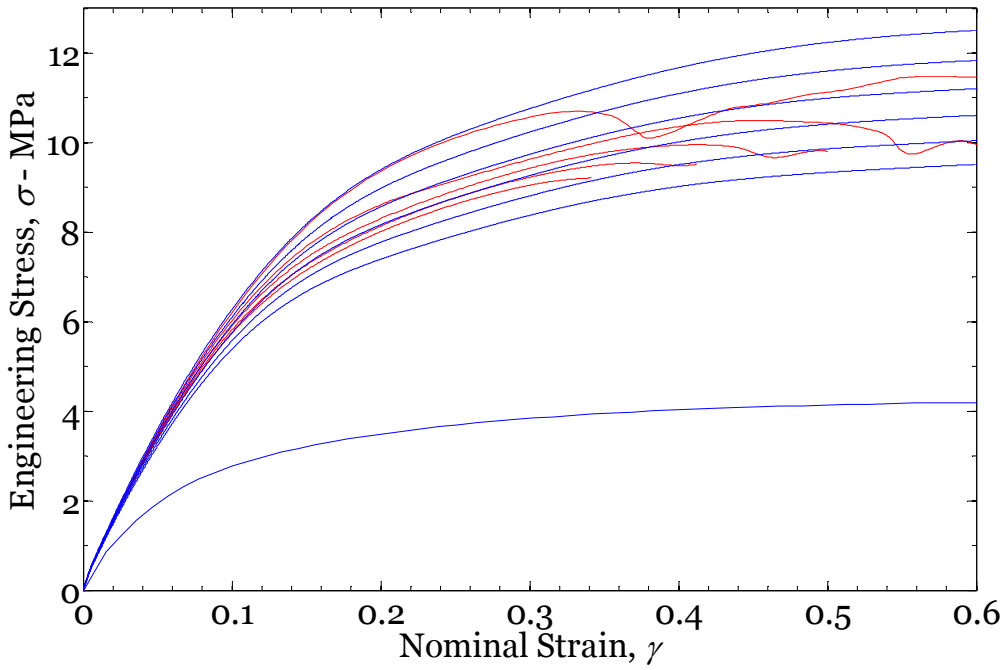

Figure 3.12: Stress-strain path predicted by the Zhou-Clifton model for constant stretch rates (0.1, 250, 500, 1000, 2000, 4000, 8000 s-1) are shown in blue. The stress-strain paths followed by material points spaced 10mm apart in the one-dimensional impact experiment Test PU-B are shown in red.

Chapter 4: Dynamic Membrane Deformation

4.1 INTRODUCTION

The dynamic tension experiment described in Chapter 3 provides a method for the determination of the dynamic properties of materials, particularly polymers that exhibit large deformations, in uniaxial tension; however, when used as a blast protective coating a polymer is more likely to experience a biaxial stress state. It is therefore necessary to prove that the constitutive behavior characterized during uniaxial stretching can be generalized to biaxial stress. The dynamic membrane experiment seeks to accomplish this goal through a framework very similar to that of the dynamic uniaxial tension test.

We begin by introducing the theory of large deformation axisymmetric wave propagation in nonlinear elastic solids. From that derivation we obtain the quasilinear system of governing equations. Just as in the one-dimensional problem, we apply the method of characteristics to obtain solutions. This method is then generalized to address viscoplastic material behavior in order to include the rate-dependent response of polyurea. Next we describe the experimental setup, the data collection techniques, and some experimental results on polyisoprene rubber and polyurea membrane samples.

4.2 TWO-DIMENSIONAL WAVE PROPAGATION IN MEMBRANES

4.2.1 Non Linear Elastic Materials

The first step in the introduction to wave propagation in axisymmetric membranes is to develop the large deformation equilibrium equations for a membrane subjected to a static pressure load. By adding the appropriate inertial term we will then obtain the equations of motion which can be nondimensionalized and rearranged into a standard quasilinear form following the procedures outlined by Cristescu (1967).

Consider an axisymmetric membrane deformed by a pressure load as shown in the free body diagram of a slice of the membrane in Figure 4.1. The initial geometry is defined by radial and axial coordinates, $r_0(s_0)$ and $z_0(s_0)$, where s_0 is the position of a material point in the initial (reference) configuration. The membrane is assumed to have an initial thickness h_0. The meridional position in the deformed (current) configuration is denoted by s; the deformed geometry is denoted by the current values of the radial and axial coordinates: $r(s)$ and $z(s)$. The current thickness is denoted by $h(s)$; it is assumed that a pressure $P(s)$ which, depends on current material coordinate s, is imposed on the membrane as well. The pressure load creates internal stresses in the membrane. The true stress in the meridional direction $\tau_1(s)$ is indicated in the free-body-diagram, Figure 4.1. The meridional view free-body-diagram with a cut along the axis illustrated in Figure 4.2, shows $\tau_2(s)$, the true hoop stress. Summing the forces in the vertical and horizontal directions yields the two equilibrium equations:

$$\frac{\pi}{2}P(s)\left[r(s+ds)^2 - r(s)^2\right] + \left(\tau_1 \pi r h\right)\Big|_s \sin\varphi - \left(\tau_1 \pi r h\right)\Big|_{s+ds} \sin\varphi = 0 \tag{4.1}$$

$$2P(s)r(s)\sin\varphi - 2\tau_2(s)hds + \int_{-\frac{\pi}{2}}^{\frac{\pi}{2}} \left[\tau_1 rh\cos\varphi\right]\Big|_s^{s+ds} \cos\theta d\theta = 0 \tag{4.2}$$

We can simplify both of the above equations by introducing the kinematic relations: $\sin\varphi = -\frac{dz}{ds}$ and $\cos\varphi = \frac{dr}{ds}$ (see Figure 4.2 for definition of the angle φ):

$$P(s)r\frac{dr}{ds} + \frac{d}{ds}\left(\tau_1 rh\frac{dz}{ds}\right) = 0 \tag{4.3}$$

$$P(s)r\frac{dz}{ds} - \tau_2 h + \frac{d}{ds}\left(\tau_1 rh\frac{dr}{ds}\right) = 0 \tag{4.4}$$

For the dynamic problem, we should include inertia and consider the shape as well as stress to be functions of position and time: (s,t). The resulting equations of motion are given as:

$$\rho hr\frac{\partial^2 w}{\partial t^2} = -Pr\frac{\partial r}{\partial s} + \frac{\partial}{\partial s}\left(\tau_1 hr\frac{\partial w}{\partial s}\right) \tag{4.5}$$

$$\rho hr\frac{\partial^2 r}{\partial t^2} = Pr\frac{\partial w}{\partial s} + \frac{\partial}{\partial s}\left(\tau_1 hr\frac{\partial r}{\partial s}\right) - \tau_2 h \tag{4.6}$$

Note that the substitution $w(s,t) = -z(s,t)$ has also been made. These equations can be mapped back to the reference coordinate system and then rewritten in the standard quasi-linear form; the details are given by Cristescu (1967) and only the final result is provided here. The radius of the initially flat membrane $\left(w(s_0) = 0\right)$ is taken to be R; note that for the flat membrane we can set $s_0 = r_0$. The three principal stretches in the meridional, circumferential (hoop) and thickness directions can be defined from the following three relations:

$$\lambda_1 = \frac{ds}{dr_0} = \sqrt{\left(\frac{dr}{dr_0}\right)^2 + \left(\frac{dw}{dr_0}\right)^2} \tag{4.7}$$

$$\lambda_2 = \frac{r}{r_0} \tag{4.8}$$

$$\lambda_3 = \frac{h}{h_0} = \frac{1}{\lambda_1\lambda_2} \tag{4.9}$$

The last of the above equations has introduced the assumption that the material is incompressible i.e., $\lambda_1\lambda_2\lambda_3 = 1$. The density is ρ_0 and the initial pressure (atmospheric pressure) is P_0. The pertinent nondimensional parameters are listed below; a subscript of 0 refers to reference configuration while quantities without a subscript refer to current configuration.

$$\begin{gathered}\eta = \frac{r}{R} \quad \eta_0 = \frac{r_0}{R} \quad \omega = \frac{w}{R} \quad \xi^2 = \frac{P_0 t^2}{\rho_0 R h_0} \quad p = \frac{PR}{h_0} \quad p_o = \frac{P_0 R}{h_0} \\ F = \frac{\tau_1(\lambda_1,\lambda_2)}{p_0\lambda_1^2} \quad F_1 = \frac{\partial F}{\partial \lambda_1} \quad F_2 = \frac{\partial F}{\partial \lambda_2}\end{gathered} \tag{4.10}$$

The four primary unknown kinematic variables – the radial and axial stretches and particle velocities – are also expressed in a non-dimensionalized form as:

$$u = \frac{\partial \eta}{\partial \eta_0} \quad v = \frac{\partial \omega}{\partial \eta_0} \quad x = \frac{\partial \eta}{\partial \xi} \quad y = \frac{\partial \omega}{\partial \xi} \tag{4.11}$$

Compatibility relations among these kinematic quantities can be obtained as in the one-dimensional problem:

$$\frac{\partial u}{\partial \xi} = \frac{\partial x}{\partial \eta_0} \tag{4.12}$$

$$\frac{\partial v}{\partial \xi} = \frac{\partial y}{\partial \eta_0} \tag{4.13}$$

The four governing equations can then be combined to form a quasilinear system and written in the form

$$\mathbf{u}_{\xi} + \mathbf{A}\mathbf{u}_{\eta_0} + \mathbf{b} = \mathbf{0} \tag{4.14}$$

where

$$\mathbf{u}(\eta_0, \xi) = \begin{Bmatrix} u(\eta_0, \xi) \\ v(\eta_0, \xi) \\ x(\eta_0, \xi) \\ y(\eta_0, \xi) \end{Bmatrix} \tag{4.15}$$

$$\mathbf{A}(\mathbf{u}(\eta_0, \tau), \tau) = \begin{bmatrix} 0 & 0 & -1 & 0 \\ 0 & 0 & 0 & -1 \\ -\left(F + \frac{u^2}{\lambda_1} F_1\right) & -\frac{uv}{\lambda_1} F_1 & 0 & 0 \\ -\frac{uv}{\lambda_1} F_1 & -\left(F + \frac{v^2}{\lambda_1} F_1\right) & 0 & 0 \end{bmatrix} \tag{4.16}$$

and

$$\mathbf{b} = \begin{Bmatrix} 0 \\ 0 \\ b_x \\ b_y \end{Bmatrix} = \begin{Bmatrix} 0 \\ 0 \\ \frac{\lambda_1 \lambda_3 \tau_2}{\eta_0 p_0} - \frac{\lambda_2 pv}{\eta_0 p_0} - \frac{uF}{\eta_0} + \frac{u(\lambda_2 - u)}{\eta_0} F_2 \\ \frac{\lambda_2 pu}{\eta_0 p_0} - \frac{vF}{\eta_0} + \frac{v(\lambda_2 - u)}{\eta_0} F_2 \end{Bmatrix} \tag{4.17}$$

This quasilinear system can be solved using the method of characteristics. There are four distinct eigenvalues for this system: $\lambda^{1,2} = \pm\sqrt{F}$, $\lambda^{3,4} = \pm\sqrt{F + \lambda_1 F_1}$. Each of these eigenvalues defines the speed of a characteristic but we see there are two different types of characteristics in this case. Let us define two wave speeds $C_1 = \sqrt{F}$ and $C_2 = \sqrt{F + \lambda_1 F_1}$. For ease of interpretation, these wave speeds, given in their nondimensionalized forms above, are given explicitly in terms of Cauchy stress, stretch, and density below.

$$C_1 = \sqrt{\frac{\tau_1}{\rho_0 \lambda_1^2}} \tag{4.18}$$

$$C_2 = \sqrt{\frac{1}{\rho_0 \lambda_1}\left(\frac{\partial \tau_1}{\partial \lambda_1} - \frac{\tau_1}{\lambda_1}\right)} \tag{4.19}$$

C_2 is largely dependent on the tangent modulus, and therefore can be understood as the axial wave speed in a membrane. C_1 depends on the Cauchy stress, and is therefore initially significantly slower than the axial wave speed; it is analogous to the transverse wave speed in a string, except that it applies to the transverse wave in a membrane; we will call this the *kink wave speed*. Each of the eigenvalues of $\mathbf{A}$ has an associated left eigenvector which will be used to put the quasilinear system into characteristic form. Those eigenvectors are given below.

$$\lambda^{1,2} = \pm C_1 \quad \Rightarrow \quad l^{1,2} = \left\{\mp C_1 v, \pm C_1 u, v, -u\right\} \tag{4.20}$$

$$\lambda^{3,4} = \pm C_2 \quad \Rightarrow \quad l^{3,4} = \left\{\mp C_2 u, \mp C_2 v, u, v\right\} \tag{4.21}$$

"Multiplying" Eq. (4.14) by each of these eigenvectors produces an ordinary differential equation (ODE) which is satisfied along the respective characteristic. The result is the following set of four equations:

$$\mp C_1 v \frac{du}{d\xi} \pm C_1 u \frac{dv}{d\xi} + v\frac{dx}{d\xi} - u\frac{dy}{d\xi} + v b_x - u b_y = 0 \quad \text{when} \quad \frac{d\eta_0}{d\xi} = \pm C_1 \tag{4.22}$$

$$\mp C_2 u\frac{du}{d\xi}\mp C_2 v\frac{dv}{d\xi}+u\frac{dx}{d\xi}+v\frac{dy}{d\xi}+ub_x+vb_y=0 \quad \text{when} \quad \frac{d\eta_0}{d\xi}=\pm C_2 \tag{4.23}$$

Note, it is not possible to define Riemann invariants or variables in this case, but nevertheless, the equations can be written in characteristic form. If u, v, x, and y are known at one time step we can march that solution forward in time along the characteristics to obtain the solution at the next time step. Figure 4.3 shows the spatial discretization at time k and $k+1$. The four dependent variables are known at each location η_{0i} at time k. To solve for the four quantities at location η_{0i} and time $k+1$ we march the solution at time k forward along the four characteristics that initiate at the locations η_{01+}, η_{02+}, η_{01-}, and η_{02-} to arrive at the location η_{0i} at time $k+1$. Linear interpolation is used to find the necessary field quantities at time k. We are then left with the following matrix inverse problem to find the unknown quantities.

$$\begin{Bmatrix} u_i^{k+1} \\ v_i^{k+1} \\ x_i^{k+1} \\ y_i^{k+1} \end{Bmatrix} = \begin{bmatrix} -C_{1+}v_{1+} & C_{1+}u_{1+} & v_{1+} & -u_{1+} \\ C_{1-}v_{1-} & -C_{1-}u_{1-} & v_{1-} & -u_{1-} \\ -C_{2+}u_{2+} & -C_{2+}v_{2+} & u_{2+} & v_{2+} \\ C_{2-}u_{2-} & C_{2-}v_{2-} & u_{2-} & v_{2-} \end{bmatrix}^{-1} \begin{Bmatrix} x_{1+}v_{1+}-y_{1+}u_{1+}-v_{1+}b_{x1+}\Delta\xi+u_{1+}b_{y1+}\Delta\xi \\ x_{1-}v_{1-}-u_{1-}y_{1-}-v_{1-}b_{x1-}\Delta\xi+u_{1-}b_{y1-}\Delta\xi \\ -C_{2+}\lambda_{12+}^2+x_{2+}u_{2+}+y_{2+}v_{2+}-u_{2+}b_{x2+}\Delta\xi-v_{2+}b_{y2+}\Delta\xi \\ C_{2-}\lambda_{12-}^2+x_{2-}u_{2-}+y_{2-}v_{2-}-u_{2-}b_{x2-}\Delta\xi-v_{2-}b_{y2-}\Delta\xi \end{Bmatrix}$$

(4.24)

Note that proper accounting of boundary conditions must be provided. In the experiments performed in this work the outer radius is clamped to a rigid plate and an impact with a fast moving ball is imposed at the center. These boundary and loading conditions will be implemented by fixing the outer edge and applying a known radial and out of plane velocity at some inner radius close to the center (as determined from the measurement). The other quantities along the boundary are obtained from the characteristics that leave the domain of interest as illustrated in Figure 4.3. Note that the applied pressure is set to zero for all of our simulations. A code written in MATLAB is used to solve this

boundary-initial value problem; once again, a semi-inverse method is used to match the measured deformation with the calculated deformation and determine the suitability of constitutive models.

4.2.2 Viscoplastic Materials

One of our objectives is to test the validity of the dynamic viscoplastic constitutive behavior of polyurea that was established through the one dimensional dynamic tension test in Section 3.4.1 for a biaxial loading condition. The use of a viscoplastic model implies the decomposition of total stretch into elastic and plastic components and the use of an evolution law to find the plastic portion of the stretch. This section details how the procedure discussed above for nonlinear elastic materials is modified to account for viscoplastic behavior. The evolution of the plastic components of the stretch introduces two additional variables and equations into the quasilinear system, with corresponding changes to the solution by the method of characteristics. Discussion of the particular material model to be used will be deferred until a later section describing the actual tests.

The difference from the nonlinear elastic formulation arises due to the assumption inherent in viscoplasticity that the stress is dependent only on the elastic stretch. That notion requires a decomposition of the stretch into an elastic and plastic part: i.e., $\lambda_1 = \lambda_{1e}\lambda_{1p}$; therefore, the stress can be written in terms of the total and plastic stretch: $\tau_\alpha = \tau_\alpha\left(\lambda_1, \lambda_2, \lambda_{1p}, \lambda_{2p}\right)$. While this does not change the form of any of the nondimensional variables or quantities introduced in Eq. (4.10), the dependence of stress on plastic stretch will require two additional parameters.

$$F_{1p} = \frac{\partial F}{\partial \lambda_{1p}}, \quad F_{2p} = \frac{\partial F}{\partial \lambda_{2p}} \tag{4.25}$$

We need evolution laws for the two independent components of plastic stretch which are written in a general form as follows:

$$\dot{\lambda}_{1p} = f_1\left(\tau_1, \tau_2, \lambda_1, \lambda_2\right) \tag{4.26}$$

$$\dot{\lambda}_{2p} = f_2\left(\tau_1, \tau_2, \lambda_1, \lambda_2\right) \tag{4.27}$$

Noting the additional dependencies in stress, and adding the two evolution laws we can again derive the quasilinear system of the form $\mathbf{u}_\xi + \mathbf{A}\mathbf{u}_{\eta_0} + \mathbf{b} = \mathbf{0}$, this time with some new terms, and two new equations:

$$\mathbf{u}\left(\eta_0, \xi\right) = \begin{Bmatrix} u\left(\eta_0, \xi\right) \\ v\left(\eta_0, \xi\right) \\ x\left(\eta_0, \xi\right) \\ y\left(\eta_0, \xi\right) \\ \lambda_{1p}\left(\eta_0, \xi\right) \\ \lambda_{2p}\left(\eta_0, \xi\right) \end{Bmatrix} \tag{4.28}$$

$$\mathbf{A}\left(\mathbf{u}\left(\eta_0, \xi\right), \xi\right) = \begin{bmatrix} 0 & 0 & -1 & 0 & 0 & 0 \\ 0 & 0 & 0 & -1 & 0 & 0 \\ -\left(F + \dfrac{u^2}{\lambda_1} F_1\right) & -\dfrac{uv}{\lambda_1} F_1 & 0 & 0 & -F_{1p} u & -F_{2p} u \\ -\dfrac{uv}{\lambda_1} F_1 & -\left(F + \dfrac{v^2}{\lambda_1} F_1\right) & 0 & 0 & -F_{1p} v & -F_{2p} v \\ 0 & 0 & 0 & 0 & 0 & 0 \\ 0 & 0 & 0 & 0 & 0 & 0 \end{bmatrix} \tag{4.29}$$

and

$$\mathbf{b}=\begin{Bmatrix}0\\0\\b_x\\b_y\\-\dot{\lambda}_{1p}\\-\dot{\lambda}_{2p}\end{Bmatrix}=\begin{Bmatrix}0\\0\\\dfrac{\lambda_1\lambda_3\tau_2}{\eta_0 p_0}-\dfrac{\lambda_2 pv}{\eta_0 p_0}-\dfrac{uF}{\eta_0}+\dfrac{u\left(\lambda_2-u\right)}{\eta_0}F_2\\\dfrac{\lambda_2 pu}{\eta_0 p_0}-\dfrac{vF}{\eta_0}+\dfrac{v\left(\lambda_2-u\right)}{\eta_0}F_2\\-f_1\left(\tau_1,\tau_2,\lambda_1,\lambda_2\right)\\-f_2\left(\tau_1,\tau_2,\lambda_1,\lambda_2\right)\end{Bmatrix} \tag{4.30}$$

This quasilinear system can be solved using the method of characteristics. This time we will have six eigenvalues, two of which are repeated: $\lambda^n=\pm\sqrt{F},\pm\sqrt{F+\lambda_1 F_1},0,0$ where we recognize the nonzero values as C_1 and C_2, the kink and axial wave speeds, respectively. The two zero eigenvalues indicate the two stationary characteristics along which the plastic stretches evolve. We can solve for the six left eigenvectors, and write the quasilinear system in characteristic form.

$$\lambda^{1,2}=\pm C_1 \quad\Rightarrow\quad l^{1,2}=\left\{\mp C_1 v,\pm C_1 u,v,-u,0,0\right\} \tag{4.31}$$

$$\lambda^{3,4}=\pm C_2 \quad\Rightarrow\quad l^{3,4}=\left\{\mp C_2 u,\pm C_2 v,u,v,\mp\frac{F_{1p}\lambda_1^2}{C_2},\mp\frac{F_{2p}\lambda_1^2}{C_2}\right\} \tag{4.32}$$

$$\lambda^{5,6}=0 \quad\Rightarrow\quad l^{5,6}=\left\{\underset{\sim}{0}\right\} \tag{4.33}$$

"Multiplying" the quasilinear form by each of these eigenvectors produces six ODEs, each of which is satisfied along the respective characteristic. The result is the following set of six equations:

$$\mp C_1 v\frac{du}{d\xi}\pm C_1 u\frac{dv}{d\xi}+v\frac{dx}{d\xi}-u\frac{dy}{d\xi}+vb_x-ub_y=0 \quad\text{when}\quad \frac{d\eta_0}{d\xi}=\pm C_1 \tag{4.34}$$

$$\mp C_2 u\frac{du}{d\xi}\mp C_2 v\frac{dv}{d\xi}+u\frac{dx}{d\xi}+v\frac{dy}{d\xi}+ub_x+vb_y\pm\frac{F_{1p}\lambda_1^2}{C_2}f_1\pm\frac{F_{2p}\lambda_1^2}{C_2}f_2=0 \quad\text{when}\quad \frac{d\eta_0}{d\xi}=\pm C_2 \tag{4.35}$$

$$\begin{aligned} \frac{d\lambda_{1p}}{d\xi} &= f_1\left(\tau_1,\tau_2,\lambda_1,\lambda_2\right) \\ \frac{d\lambda_{2p}}{d\xi} &= f_2\left(\tau_1,\tau_2,\lambda_1,\lambda_2\right) \end{aligned} \quad \text{when} \quad \frac{d\eta_0}{d\xi} = 0 \tag{4.36}$$

If u, v, x, y, λ_{1p}, and λ_{2p} are known at one time step we can march that solution forward in time along the characteristics to obtain the solution at the next time step. Figure 4.3 shows the spatial discretization at time k and $k+1$. The six dependent variables are known at each location η_{0i} time k. To solve for the six quantities at location η_{0i} and time $k+1$ we march the solution at time k forward along the six characteristics that initiate at the locations η_{0i}, η_{01+}, η_{02+}, η_{01-}, and η_{02-} to arrive at the location η_{0i} at time $k+1$. Note that λ_{1p} and λ_{2p} at η_{0i} and time $k+1$ can each be found directly as a function of the known quantities at location η_{0i} time k by integrating Eq. (4.36). That leaves four quantities to be determined at $k+1$. Linear interpolation is used to find the necessary field quantities at time k and we are left with the following matrix inverse problem to find the unknown quantities.

$$\begin{Bmatrix} u_i^{k+1} \\ v_i^{k+1} \\ x_i^{k+1} \\ y_i^{k+1} \end{Bmatrix} = \begin{bmatrix} -C_{1+}v_{1+} & C_{1+}u_{1+} & v_{1+} & -u_{1+} \\ C_{1-}v_{1-} & -C_{1-}u_{1-} & v_{1-} & -u_{1-} \\ -C_{2+}u_{2+} & -C_{2+}v_{2+} & u_{2+} & v_{2+} \\ C_{2-}u_{2-} & C_{2-}v_{2-} & u_{2-} & v_{2-} \end{bmatrix}^{-1} \cdots$$

$$\begin{Bmatrix} v_{1+}x_{1+} - u_{1+}y_{1+} - v_{1+}b_{x1+}\Delta\xi + u_{1+}b_{y1+}\Delta\xi \\ v_{1-}x_{1-} - u_{1-}y_{1-} - v_{1-}b_{x1-}\Delta\xi + u_{1-}b_{y1-}\Delta\xi \\ -C_{2+}\lambda_{12+}^2 + u_{2+}x_{2+} + v_{2+}y_{2+} + \frac{F_{1p2+}\lambda_{1p2+}^2}{C_{2+}}\left(\lambda_{1pi}^{k+1} - \lambda_{1p2+} - f_{12+}\Delta\xi\right) + \frac{F_{2p2+}\lambda_{1p2+}^2}{C_{2+}}\left(\lambda_{2pi}^{k+1} - \lambda_{2p2+} - f_{22+}\Delta\xi\right) - u_{2+}b_{x2+}\Delta\xi - v_{2+}b_{y2+}\Delta\xi \\ C_{2-}\lambda_{12-}^2 + u_{2-}x_{2-} + v_{2-}y_{2-} - \frac{F_{1p2-}\lambda_{1p2-}^2}{C_{2-}}\left(\lambda_{1pi}^{k+1} - \lambda_{1p2-} - f_{12-}\Delta\xi\right) - \frac{F_{2p2-}\lambda_{1p2-}^2}{C_{2-}}\left(\lambda_{2pi}^{k+1} - \lambda_{2p2-} - f_{22-}\Delta\xi\right) - u_{2-}b_{x2-}\Delta\xi - v_{2-}b_{y2-}\Delta\xi \end{Bmatrix}$$

(4.37)

In the experiments on polyurea, the outer radius is clamped and the center is impacted with a fast moving ball. These boundary and loading conditions will be implemented by fixing the outer edge and applying a known radial and out of plane velocity at some inner radius close to the center (as determined from the experimental measurement). The other quantities along the boundary are obtained from the characteristics that leave the domain of interest as illustrated in Figure 4.3. Note that the pressure is set to zero for all simulations. All that remains is the choice of an appropriate viscoplastic material model. The process of generalizing our modified version of the Zhou-Clifton model to the plane stress state experienced in the membrane is described in Sec 4.5.3.

4.3 EXPERIMENTAL SETUP

We now turn to a description of how the above boundary-initial value problem is implemented in the laboratory. The test setup consists of the circular clamp holding the specimen and an air gun. Two different size clamps were used with radius $R = 3$ in and $R = 5.5$ in. An oblique view of the non-impact surface of a rubber membrane in the test apparatus ($R = 5.5$ in) is shown in Figure 4.4. The circular frame is cut from an aluminum block; a 12 in diameter O-ring is placed between the rubber and one of the aluminum plates to clamp the rubber securely and prevent slipping. The smaller diameter specimen holder of similar construction was only used for polyurea. The barrel of the air gun is placed at least one meter behind the surface of the specimen in order to prevent the air burst following the projectile from affecting the deformation of the membrane; such a large separation between the muzzle and the specimen provides significant challenges to aiming the projectile on the center of the membrane.

When the air gun is fired a projectile is launched from the 0.56 in diameter barrel at a velocity in the range of 50-160 m/s depending on the projectile and pressure used. A

one-half inch diameter spherical steel ball, and two cylindrical nylon bullets that were custom-machined to an ogive nose were used. The benefit of the steel ball is that because of its symmetry, it creates an axisymmetric deformation, regardless of its orientation at impact. However, due to the fact that the ball is slightly smaller than the barrel diameter, much of the air pressure rushes around the ball, causing two main problems. First, this excess space results in the maximum speed being limited to rather small values of around 50 m/s. Second, the extra airflow around the ball diminishes the ability to aim the projectile correctly. The ball also develops unpredictable spin travelling down the length of the non-rifled barrel which, even over the short flight distance, creates difficultly in hitting the exact center of the membrane. In contrast, the cylindrical nylon bullets were machined to provide a sliding fit in the barrel, resulting in improved ability to aim as well as increase the speed due to the tight fit and the decreased mass. The projectile however has the problem of rotating (tumbling) a bit during flight along axes other than the flight path which results in slightly skewed impact loading; in order to take this into account, the axial and radial motion of one set of markers on the specimen was digitized and used to characterize the imposed loading.

The motion of the membrane is monitored by two Photron SA1 high-speed video cameras, one oriented perpendicular to the propagation direction of the projectile, providing a meridional view and the other recording at an oblique angle in order to obtain a projection of the membrane (as indicated in Figure 4.4). The oblique view allows for observation of the axisymmetry of the deformation as well as the exact location of impact. In some tests, the rim of the circular clamp obscures the initial impact and deformation of the membrane in the meridional view so the oblique view is crucial for measurement of the exact time and location of impact as well as the kink wave speed. The meridional view allows for the precise measurement of the deformed profile; in cases

when the deformation remains truly axisymmetric, all the kinematic quantities of the deformation of the membrane can be determined completely from the meridional profile. The frame rate was adjusted depending on the membrane material used. The rubber specimens are typically recorded at 10,800 frames per second, whereas the polyurea specimens are recorded at 20,000 frames per second. The deformation of the polyurea is much less than that of the polyisoprene rubber, but the wave speeds are much higher; hence the need for an increased frame rate.

In order to quantify the deformation, Lagrangian markers are drawn on the specimen. A stencil was used to draw the circumferential lines shown in Figure 4.4, which provide the most complete and accurate data collection. Measurement of the location of Lagrangian markings along the deformed profile allows for determination of the axial and radial displacement of the marked points; this is the principal measurement in each frame. From these measurements, the principal stretches, and the particle velocities in the radial and axial directions can be obtained through numerical differentiation. Furthermore, tracing the motion of the Lagrangian marker closest to the ball provides an efficient way to deal with the boundary condition to be used in the simulations, and avoid the complications that arise in the area of contact with the projectile. The process of adding Lagrangian markers to the specimen warrants further detail because of some unique challenges in marking thin samples of polyisoprene rubber. First, the majority of pens and markers have difficulty transferring ink to the surface of the smooth polyisoprene rubber. The extra fine point oil-based opaque paint markers from Sharpie®[10] work best. The other challenge is even the slight pressure of dragging a pen tip causes stretching and wrinkling of the thin and soft rubber sheet. This

[10] Sharpie® is a registered U.S. trademark of Sanford

hurdle is overcome by using an Avery®[11] adhesive label paper to the back of the rubber sheet to decrease the tendency to stretch and wrinkle. Even with the adhesive sheet, a very gentle touch is required to avoid the pen tip getting stuck and stretching and wrinkling the sheet.

4.4 EXPERIMENTAL RESULTS

4.4.1 Polyisoprene Rubber

We describe the details of two tests to illustrate the data collection and analysis process. In a later section we will compare these experimental results with simulations. The two tests were performed with impact speeds of 150 m/s and 160 m/s and will be referred to as Test A and Test B respectively.

Both tests used a nylon bullet with an air-gun pressure of 120 psi. The data collection begins with images taken from the side view; a selected sequence of images from Test A is shown in Figure 4.5 and similarly for Test B in Figure 4.6, where the meridional view and oblique view are shown as pairs[12]. As a result of minor misalignments in the air-gun, discussed above, the impact typically occurs slightly off center; therefore, the impact point and the time variation of the radial and out of plane locations of each Lagrangian marker are recorded. In the first image for each test, Figure 4.5a and Figure 4.6a, the point of impact is marked with a red 'x' symbol and the initial location of each Lagrangian marker that is tracked in subsequent frames is marked with green '+' symbol on the meridional view of the undeformed membrane. Each of these points is tracked throughout the experiment as illustrated in the subsequent frames. The

[11] Avery is a registered U.S. trademark of Avery Denison Corporation

[12] A video file of the oblique and meridional views of Test A is attached to the Supplementary Material DVD of this dissertation.

tracking of the position of Lagrangian points along the evolving profile of the membrane is the primary diagnostic measurement from the membrane tests. These measurements allow calculation of the evolution of the principal stretches as well as particle velocities at the selected points in the membrane and interpolate for points in-between. Due to the rather coarse spacing of the measurement points and the difficulty in recording exact position, the raw data is fairly noisy. Applying a simple moving average filter using 5 data points, however, cleans it up significantly.

The general features of the wave propagation in the membrane can be discerned from the images in Figures 4.5 and 4.6. As indicated in Section 4.2.1, the axial wave propagates the fastest, and with its arrival brings a radial inward movement of the circular Lagrangian markers as can be observed easily in each test. Concomitant with the axial wave is a contraction in the hoop direction that may manifest itself much later as a fine set of wrinkles (buckles) in the thin membrane; we will explore this in Section 4.5.3 through numerical simulations. The axial wave is followed by the slower kink wave; while the axial wave stretches the membrane and keeps the membrane in its initial plane, the kink wave brings with it a dramatic change in the out-of-plane displacement and velocity as well as the meridional stretch. It should be noted that both the axial and kink waves are nonlinear waves, and that their speeds depend on the stress/stretch state. In particular, the axial wave is expected to slow down with increasing stretch while the kink wave will increase in speed with increasing stretch. The measured principal stretches, (λ_1, λ_2) for Test A and B are plotted as a function of the normalized radial position η_0 in Figures 4.7 and 4.8 at time increments of 275 μs. We note that there is a uniform small initial stretch in each test which is visible in Figure 4.8[13]. The corresponding variations of

[13] This arises from the procedure of clamping the specimen in the circular holding frame.

the out-of-plane particle velocity, $\dot{z}(\eta_0, t)$, are plotted as a function of the normalized radial position η_0 in Figure 4.9, at the same time increments. The arrival of the axial wave cannot be seen easily in these plots, but the approximate arrival of the kink wave is marked in each curve by an asterisk. Ahead of the kink wave, stretch state reaches $(\lambda_1 = 1.4, \lambda_2 = 0.9)$, but just behind the kink wave, the meridional stretch λ_1 jumps to a maximum of about 9 in Test A and 10 in Test B with an accompanying hoop stretch λ_2 of 0.5 and 0.6 respectively. With progression of time, the kink wave goes towards the fixed boundary with the large stretch following the kink wave. From these measurements, it is also possible to get an estimate of the stretch rate. This data suggests a maximum stretch rate of 10^4 s^{-1} was achieved, well above the rate saturation boundary of 500 s^{-1} identified by Niemczura and Ravi-Chandar, (2011) for the polyisoprene rubber in dynamic uniaxial tension.

The out-of-plane particle velocity is nearly zero prior to the arrival of the kink wave; immediately behind the kink wave, the particle velocity increases rapidly to that imposed by the projectile. Even though this data is noisy due to limits in experimental resolution, it appears that the out-of-plane velocity reaches a steady value behind the kink wave. The kink wave speed can be obtained from the out-of-plane velocity plots or directly from measurement of the kink position: the oblique view camera images provide a better indication of the location of the kink wave. In order to measure the Lagrangian kink wave speed properly, the time at which the kink wave reaches each concentric circle is recorded. The kink position has been plotted as a function of time for three tests in Figure 4.10. Test A and B are at similar speeds but the third example is at a much slower speed, a third of that of the other two. Despite the dramatic difference in impact velocity, the kink waves propagate with the same speed of ~25m/s for the first 2 ms. Beyond 2 ms the axial wave, reflected from the outer boundary, arrives at the kink front and causes

deviation in the propagation of the kink wave. The initial 2 ms however demonstrates that, as predicted, the kink speed is a function of the material, not the impact speed.

4.4.2 Polyurea

The polyurea membrane samples (thickness 1.4 mm) are produced in essentially the same manner as the dynamic tension samples. These sheet samples are limited to approximately 10 in width which limits the size of the membrane that can be produced. The specimen has 12 holes cut in it so that it can be clamped between the fillet plate and the steel securing ring; this leaves a 6 in diameter specimen for the impact experiment. Several experiments were performed on polyurea samples with the setup described above. All of the tests used the steel ball as the projectile, an air-gun pressure of 200 psi, and had an impact speed of approximately 80 m/s; therefore, we address only one test in detail.

The data collection begins with images taken with the high speed camera; a selected sequence of images from the test is shown in Figure 4.11, where the meridional and oblique views are shown as pairs. The thickness of the specimen provides enough resistance that the air ahead of the projectile does not affect the deformation, hence the placement of the barrel directly behind the specimen. However, the projectile still hit the specimen slightly off center; therefore, the impact point and the time variation of the radial and out of plane locations of each Lagrangian marker are recorded from the high speed images. In the first image, Figure 4.11a, the point of impact is marked with a red ‘x’ symbol and the initial location of each visible Lagrangian marker that is tracked in subsequent frames is marked with green ‘+’ symbol on the meridional view of the undeformed membrane. Note that only two points are visible initially; the remainder are

obscured by the clamping nuts. As the deformation progresses more points are tracked as they become visible. The initial spacing of the lines is known, 2.5 mm. The tracking of the position of Lagrangian points along the evolving profile of the membrane is the primary diagnostic measurement from the membrane tests. These measurements allow calculation of the evolution of the principal stretches as well as particle velocities throughout the portion of the membrane not obscured by the clamp. Due to the rather coarse spacing of the measurement points and the difficulty in recording exact position, the raw data is fairly noisy. Applying a simple moving average filter cleans it up significantly.

The general features of the wave propagation in the membrane can be discerned from the images in Figures 4.11. The axial wave in polyurea propagates so quickly that it is essentially undetectable from these images; we note that this is because polyurea is far stiffer than the polyisoprene rubber discussed in the previous section. This stiffness also restricts the inward radial movement behind the axial wave to very small magnitudes. As in the case of polyisoprene rubber, the axial wave is followed by the slower kink wave that brings with it a change in the out-of-plane velocity as well as the meridional stretch but we cannot actually see that change from the meridional view because the initial plane is not visible; at the time the Lagrangian marker becomes visible, the kink wave has already passed; therefore, the oblique view is the only source of data at and before arrival of the kink wave. The measured meridional stretch profiles for the visible markers are plotted in Figure 4.12 as a function of the normalized radial position η_0 at color coded 100 μs time increments. The corresponding out-of-plane particle velocity profiles, $\dot{z}(\eta_0, t)$, are plotted as a function of the normalized radial position η_0 in Figure 4.13, at the same color coded time increments. When interpreting these plots, it must be remembered that markers initially obscured by the clamps become visible only after the

kink wave has just passed them, thereby bringing out-of-plane motion to these points. It is clear from these figures that as the kink wave passes, the meridional stretch increases rapidly and reaches a value of 1.8; the propagation of the strain pulse can also be identified from this figure. The stretch rates in the central portions of the membrane are estimated to be as high as 4000 s^{-1}. The out-of-plane particle velocity profile shows the slow decrease in speed of the projectile; in fact, the membrane actually stops the ball. When reviewing Figure 4.13, note the earliest profile is the red line at the top of the plot. This indicates that the velocity of the inner most marker increased from 0 to 70 m/s in the first 250 μs and subsequently decreased gradually over the next 600 μs. During this time interval, the kink propagates radially outward imparting out-of-plane velocity to material points further from the center. As the material points peek out from behind the clamp and become visible to the camera, they can be tracked and are added to the profile; hence, as time progresses the recorded profile becomes longer. Figure 4.14 further clarifies the motion of the inner most point by plotting the velocity of the projectile as well as the Lagrangian marker at x = 7.5 mm as functions of time. At impact, the projectile is traveling at just above 80 m/s while the 7.5 mm mark is at rest. After ~50 μs the kink wave arrives at the 7.5 mm mark and accelerates it. The velocity peaks at 70 m/s and subsequently slows at the same rate as the projectile as it is decelerated by the resistance of the membrane.

The kink wave position can be obtained from the top view camera images. In order to measure the Lagrangian kink wave speed properly, the time that the kink wave reaches each hash mark is recorded and plotted as a function of position in Figure 4.15. From this figure, it can be seen that the kink wave propagates at a nearly constant velocity of 95 m/s; the velocity remaining constant is similar to the observation in the softer polyisoprene rubber.

4.4.3 Summary of Results on Membranes under Normal Impact

The results of the impact experiments on polyisoprene and polyurea yield the following observations:

- The axial wave causes significant in-plane stretching of the membrane, setting the conditions in which the kink wave develops;
- The kink wave follows in the pre-stretched membrane with increasing speed and eventually settles to a steady-state value that appears to be independent of the impact velocity;
- The kink wave causes a very large jump in the out-of-plane particle velocity, and therefore the stretch rate;
- Behind the kink wave, the stretch increases rapidly to very high levels and may approach failure of the membrane.

One last experimental observation to consider before moving to the simulations is the possibility of wrinkling. Compressive stress in a very thin sheet can cause wrinkling and indeed, this has been observed in some of the experiments (see Figure 4.16 which shows that wrinkling can develop in the vicinity of the kink wave). This image shows the wrinkles at about 1 ms after their initiation so they have had some time to develop. In this test the rubber was impacted at 53 m/s with the ½" diameter steel ball. The primary difference between the two tests is impact speed. Vermorel et al. (2006) studied this wrinkling phenomenon at the kink wave by using a linear elastic buckling analysis. In their tests unconstrained specimens were impacted at about 5 m/s. We will examine the possibility of wrinkling through an analysis of the nonlinear membrane impact problem.

Quantitative measurements of the above mentioned aspects of the membrane response provides an opportunity for calibration of material constitutive models through an inverse method of comparing the experimental measurements to simulations of the response; this is explored in the next section.

4.5 SIMULATIONS OF MEMBRANE IMPACT RESPONSE

4.5.1 Generalization of Rate Independent Constitutive Behavior to 2D

The procedure for determining the wave propagation behavior during the dynamic axisymmetric deformation of a membrane of a general nonlinear elastic material has already been outlined in Section 4.2. The only remaining ingredient necessary to connect the theory with experiments on the polyisoprene rubber and polyurea is the specification of a particular material model. The work described in Chapter 3 suggests two possibilities to consider for the polyisoprene rubber: the quasistatic behavior or, if the strain rate is high enough, the rate-saturated behavior captured by the power law model Eq. (3.12). These two uniaxial behaviors must then be generalized to address the biaxial stress encountered in the deformation of the membrane.

Niemczura and Ravi-Chandar (2011) found that the high rate behavior of polyisoprene rubber in dynamic tension was captured reasonably well with a simple power-law type model with the form of Eq. (3.12). In an attempt to generalize this to multiaxial loading, it was found that the dynamic uniaxial tensile behavior can also be closely matched by a material with the Mooney-Rivlin strain energy:

$$W = \mu_1 \left(I_1 - 3 \right) + \mu_2 (I_2 - 3) \tag{4.38}$$

$$I_1 = \lambda_1^2 + \lambda_2^2 + \lambda_3^2 \tag{4.39}$$

$$I_2 = \lambda_1^2 \lambda_2^2 + \lambda_2^2 \lambda_3^2 + \lambda_3^2 \lambda_1^2 \tag{4.40}$$

The constants which most closely fit the uniaxial behavior indicated by Niemczura and Ravi-Chandar (2011) are $\mu_1 = 0.17$ MPa and $\mu_2 = 0.22$ MPa. Then the biaxial Cauchy stress vs. stretch relationship for an incompressible material can be represented as:

$$\tau_{1,2} = 2\mu_1\left(\lambda_{1,2}^2 - \frac{1}{\lambda_1^2\lambda_2^2}\right) + 2\mu_2\left(\lambda_1^2\lambda_2^2 - \frac{1}{\lambda_{1,2}^2}\right) \tag{4.41}$$

While the model generalized from the dynamic uniaxial properties seems like the candidate most likely to match the dynamic behavior in biaxial tension, the membrane test imparts stretches far beyond those achieved in the dynamic uniaxial tests. The maximum stretch reaches values greater than nine in a membrane test whereas it seldom exceeded four in the uniaxial tension test. Achieving these higher stretches brings us back to a question posed earlier: is the secondary stiffening seen in the quasistatic tension of rubber eliminated completely during dynamic stretching or is it just delayed to larger stretches? If it is only delayed then the Mooney-Rivlin model will never be able to properly capture the behavior. Instead we need something more similar to the quasistatic curve at larger stretches. Lopez-Pamies (2009) has developed a strain energy function that accomplishes this objective with a generalization of the Neo-Hookean material model:

$$W(I_1) = \frac{3^{1-\alpha_1}}{2\alpha_1}\mu_1\left(I_1^{\alpha_1} - 3^{\alpha_1}\right) + \frac{3^{1-\alpha_2}}{2\alpha_2}\mu_2\left(I_1^{\alpha_2} - 3^{\alpha_2}\right) \tag{4.42}$$

The uniaxial tension response of this model fits the quasistatic response of polyisoprene rubber quite well with the following parameters: $\alpha_1 = 0.78$, $\alpha_2 = 4.12$, $\mu_1 = 0.5$ MPa, $\mu_2 = 680$ Pa. The biaxial Cauchy stress vs. stretch relationship for an incompressible material can easily be represented as:

$$\tau_{1,2} = \left(3^{1-\alpha_1}\mu_1 I_1^{\alpha_1 - 1} + 3^{1-\alpha_2}\mu_2 I_1^{\alpha_2 - 1}\right)\left(\lambda_{1,2}^2 - \frac{1}{\lambda_1^2\lambda_2^2}\right) \tag{4.43}$$

There are approximations with each of these models. Imposing the dynamically calibrated Mooney-Rivlin (we will refer to this as the DCMR model) model assumes that the stiffness decreases monotonically, while the Lopez-Pamies fit to the quasistatic uniaxial behavior (we will refer to this as the Q-LP model), if nothing else, will have a much lower initial stiffness than the dynamic tension tests require. Also, with the Q-LP model, we have the possibility to create shocks.

From these basic measurements we begin the process of trying to understand the dynamic constitutive behavior of the rubber. The difference in kink and axial wave speeds creates the possibility of a jump. The dimensional forms of kink and axial wave speeds are given in Eqs. (4.18) and (4.19). If we first consider the DCMR model, we can plot these two wave speeds as a function of stretch in the meridional direction. We assume a uniaxial stress state with the full understanding that the true state is somewhat different from that. These two wave speeds are plotted for the DCMR model in Figure 4.17a. This material model has a stiffness which decreases monotonically with stretch and hence two wave speeds never cross each other; furthermore, the axial wave speed does not have a minimum. It is useful to note that the kink wave speed predicted by this model is very close to the 25 m/s measured in the experiment. If we plot the same two wave speeds for the Q-LP model however (Figure 4.17b) a very different result arises: there is a minimum in the axial wave speed but there is the additional complication that the axial wave speed decreases below the kink wave speed for stretches between 2.4 and 4.3. The upshot of this analysis is that the axial wave increases the stretch thereby facilitating the propagation of the kink wave, but because higher amplitude axial waves propagate slower than higher amplitude kink waves, the kink waves catch up with the axial wave; a natural expectation is that the speed of the kink wave in an initially

unstretched membrane will correspond to that stretch where the axial and kink waves have nearly the same speed. This can be written as:

$$\lambda_1 \frac{\partial \tau_1}{\partial \lambda_1} = 2\tau_1\left(\lambda_1, \lambda_2\right) \tag{4.43}$$

Note that, in fact, this equality is never attained in the DCMR material model, but is possible in the Q-LP model at two different stretch levels.

4.5.2 Polyisoprene Simulation Results

We move now to the description of the simulations of the above described experiment. The procedure for simulating dynamic axisymmetric deformation of a membrane has been introduced in Section 4.2. The only steps necessary to apply that procedure to the test are to introduce dimensions, boundary conditions, and material properties. Dimensions and material density are easily measured; the boundary condition at the outer radius is fixed so there is no radial or out of plane motion. The inner radius boundary condition should, in principle, be the velocity of the impact point; however, the details of the contact zone between the projectile and the membrane cannot be easily determined. In the simulation however, it is sufficient to apply the known motion of any fixed point within the membrane. The time variation of radial and out-of-plane velocities of the impact point and a Lagrangian marker near the impact point ($r = 16.7mm$) measured in the 160 m/s test are given in Figure 4.18 and 4.19; this motion is imposed in the simulations, avoiding uncertainties associated with the state of contact between the projectile and the membrane. The material is modeled with the form of DCMR and Q-LP models discussed in Section 4.5.1

Figure 4.20 shows a selected sequence of images, showing an oblique view of the simulated membrane response. For visualization, the colors in Figure 4.20 indicate the

meridional stretch[14]; it is easily observed that an axial wave moves in the planar membrane, and is followed by the kink wave that brings along with it a large stretch as well as out-of-plane particle motion.

For quantitative comparison of the predictions with the experiments, the meridional profiles from the simulations with both the DCMR and Q-LP material models are plotted on the experimentally recorded images at selected time steps in Figure 4.21. In addition to the overall profile, the positions of the Lagrangian markers that identify the mid-width locations of the concentric circles are identified in the simulated profiles by an asterisk in order to enable visualization of the motion of reference points in comparison to that observed in the actual experiment.

These results show that while neither model captures the behavior exactly, the Q-LP based model, representing the generalization of the quasistatic stress strain behavior, deviates significantly from the experiments. There is clearly a curvature in the profile which is completely missing from the behavior predicted by the Q-LP model. With the DCMR model on the other hand, the membrane exhibits a much greater curvature than observed in the experiment. This is primarily apparent in the region with the highest stretches suggesting that the actual material does show some increase in stiffness by a greater amount than that provided in the DCMR model. One might conclude that both material models provide qualitatively reasonable results; they capture the propagation of the axial and kink waves, indicate the development of large stretches behind the kink wave, etc. However, quantitative matching requires additional features in the constitutive response.

[14] A video animation of the results of this simulation is attached to the Supplementary Material DVD of this dissertation.

To further examine this comparison we have plotted the profiles for the stretches, stresses, and out of plane velocity for the DCMR and Q-LP models in Figures 4.22 through 4.26. The figures containing predictions of kinematic quantities should be compared to the measured results shown earlier. Starting with meridional stretch, when comparing the experimental results shown in Fig. 4.7a to the predictions in Fig. 4.22, the DCMR model clearly predicts a result closer to the physical measurement. The Q-LP model predicts a rather sharp jump in stretch from ~2.5 to 5 which does not decay during the time period examined; this features is absent from the experiment. The DCMR prediction does show a decrease in stretch around the inner boundary condition which is not seen in the experiment but it is possible that it is simply not resolved due to complications of measurements around the projectile. A similar decrease in magnitude, though of opposite sign, is seen in the DCMR predictions of circumferential stretch. This inflection is seen in the experimental data and is absent from the Q-LP simulations. While the predicted stress profiles in Figures 4.24 and 4.25 cannot be compared to experimental measurements, they do contain an poignant illustration of the reason for the differences between the DCMR and Q-LP results. The meridional stresses are similar but the hoop stresses are dramatically different. The Q-LP model shows essentially no hoop stress whereas the DCMR model has a spike at the inner boundary which decays rapidly but to a value still nearly an order of magnitude greater than that predicted by the Q-LP model. Comparison of the predicted and measured velocity profiles does not provide any clear distinctions. The hoop stress then is the key difference in the models and would lead us to believe that finding a model which predicts some middle ground between these two stresses is likely to be produce a displacement profile very similar to that measured in the experiment. On a final note, even with these large disparities, it is interesting to observe

that the kink wave speeds for both models seem to match that of the experiment reasonably well.

4.5.3 WRINKLING IN POLYISOPRENE MEMBRANES

In neither the 150 nor the 160 m/s impact test was significant wrinkling observed; however that was not the case for slower impact speeds. In the image taken from a test at 55 m/s impact, shown in Figure 4.16, wrinkles are observed in the vicinity of the kink wave. Vermorel et al. (2006) observed similar wrinkling at the kink wave during 5 m/s impact of an unconstrained rubber membrane. For wrinkling to occur, a compressive stress must develop. Two variables affect the possibility of those stresses developing: impact velocity and initial stretch. If we look first to the simulations of the high speed impacts, specifically the hoop stress profiles shown in Figure 4.25, we note that not only was the hoop stress never negative, it never dropped below the initial stress level due to the initial stretch of the specimen for either material model.

When we simulate slower impact speeds we find a different result. We have two examples of slow speed impacts during which wrinkles form: the 55 m/s test performed in the same manner as the high speed tests described in the previous sections and the 5 m/s test performed by Vermorel et al. (2006). The 55 m/s test had a small initial stretch where as the 5 m/s test was on an unconstrained sheet of rubber meaning there were no initial stresses in the membrane. The meridional stretch profile for the simulation of the 55 m/s and 5 m/s are plotted in Figure 4.27 at time intervals of 275 μs and 1 ms respectively. The profiles for the 55 m/s impact are similar to those observed in the high speed simulations. The 5 m/s test however has a notably smaller maximum stretch which is to be expected. The hoop stress profiles for each of the simulations are plotted in

Figure 4.28. Immediately we see a different result. Looking first at the 55 m/s test, it can be noticed that the hoop stress does in fact dip below the stress imposed initially, suggesting the possibility of wrinkling. Not only does the stress dip below the initial value but the DCMR model predicts a compressive stress should develop. The Q-LP model skirts the line but because of that initial stretch, does not clearly drop into the compressive range. The 5 m/s simulation shows the same behavior of dipping below the initial stress value but since the initial stretch is negligible both material models predict compressive stresses develop in the hoop direction. We should note that as soon as these compressive stresses develop, wrinkling should occur, violating the assumption of axisymmetry and therefore invalidating the simulation results after that point. The important conclusion is that the possibility for wrinkle formation is based first and foremost on the impact speed. Clearly, an initial stretch can always be applied that will negate the chance of compressive stresses forming but similarly above a critical velocity, it is also not possible for compressive stresses to develop.

4.5.3 Viscoplastic Model Generalized to 2D

The procedure for determining the wave propagation behavior during the dynamic axisymmetric deformation of a viscoplastic membrane has already been outlined. The only remaining piece necessary to connect the theory with our experiments on polyurea is the specification of a particular material model. The work described in Chapter 4 suggests the modified Zhou-Clifton model is the best candidate for uniaxial tension. To verify that this model is also suitable in biaxial tension, it is necessary to find a method to appropriately generalize that model to multidimensional loading. The procedure

described below was inspired by the method used by Bergstrom and Boyce (2001) to decompose the elastic and inelastic stretches in their model.

The Zhou-Clifton model described in Chapter 3 provides a function for the evolution of true plastic strain $\dot{\varepsilon}_p$ in the case of uniaxial stress which is dependent on the overstress ratio. We first develop an expression for the evolution of the effective plastic strain as a function of the effective plastic stress. We use the Frobenius norm to determine these effective states: the effective Cauchy stress τ_{eff} is given below for a state of plane stress:

$$\tau_{eff} = \sqrt{tr\left[\boldsymbol{\tau}'\boldsymbol{\tau}'\right]} = \frac{1}{3}\sqrt{\left(2\tau_1 - \tau_2\right)^2 + \left(2\tau_2 - \tau_1\right)^2 + \left(\tau_1 + \tau_2\right)^2} \tag{4.43}$$

where $\boldsymbol{\tau}'$ is the deviatoric part of the Cauchy stress tensor. As has been mentioned before, use of a viscoplastic model suggests that the deformation can be decomposed into elastic and plastic components, which in terms of the deformation gradient tensor can be written as $\mathbf{F} = \mathbf{F}_e\mathbf{F}_p$. We then need a way to update the current plastic deformation tensor $\mathbf{F}_p$ with the evolution of effective plastic strain to relate the effective plastic strain evolution $\dot{\varepsilon}_{peff}$ from the Zhou Clifton model. Applying the deformation decomposition to the velocity gradient $\mathbf{L}$ we find it is possible separate the elastic and plastic velocities as shown:

$$\mathbf{L} = \dot{\mathbf{F}}\mathbf{F}^{-1} = \dot{\mathbf{F}}_e\mathbf{F}_e^{-1} + \mathbf{F}_e\dot{\mathbf{F}}_p\mathbf{F}_p^{-1}\mathbf{F}_e^{-1} = \mathbf{L}_e + \mathbf{F}_e\mathbf{L}_p\mathbf{F}_e^{-1} = \mathbf{L}_e + \tilde{\mathbf{L}}_p \tag{4.43}$$

If the spin tensor $\mathbf{W}_p$ is set equal to 0 for uniqueness then $\mathbf{L}_p$ is simply the rate of extension $\mathbf{D}_p$ and $\mathbf{D}_p = \dot{\gamma}\mathbf{N}$ where $\dot{\gamma}$ is the creep rate and $\mathbf{N}$ is the direction of driving stress. $\dot{\gamma}$ defines the magnitude of the plastic stretch increment based on the Zhou-Clifton model and $\mathbf{N}$ projects that value appropriately based on the direction of loading:

$$\dot{\gamma} = \lambda_{eff}\dot{\varepsilon}_{peff} \tag{4.43}$$

$$\mathbf{N} = \frac{\boldsymbol{\tau}'}{\tau_{eff}} = \frac{\boldsymbol{\tau} - \frac{1}{3}tr\left[\boldsymbol{\tau}\right]\mathbf{I}}{\sqrt{tr\left[\boldsymbol{\tau}'\boldsymbol{\tau}'\right]}} \tag{4.43}$$

Assuming plane stress and equating $\mathbf{L}_p$ and $\mathbf{D}_p$ we can then find explicit expressions for the two necessary components of plastic stretch rate:

$$\dot{\lambda}_{1p,2p} = \lambda_{1p,2p}\dot{\gamma}\left(\frac{2\tau_{1,2} - \tau_{2,1}}{3\tau_{eff}}\right) \tag{4.43}$$

These equations provide the detail needed in Eq. (4.43) for the determination of the plastic strain evolution.

4.5.4 Polyurea Simulation Results

Moving now to the results of simulations, we study the applicability of the Zhou-Clifton model that was found to work well in the uniaxial testing, to the case of biaxial loading. The membrane is assumed to be clamped at the outer diameter and the out of plane velocity shown in Figure 4.14 is imposed at a point 7.5 mm from the center of the membrane. The radial velocity of the inner radius is assumed to be 0. Figure 4.29 shows a comparison of the prediction of the model with the experiments; the meridional profiles from the simulations are plotted on the experimentally recorded images at selected time steps. There is clearly a large discrepancy between the actual behavior and that predicted by the simulation with the Zhou-Clifton material model generalized as indicated above.

There are two discrepancies which stand. First, the kink wave in the simulation moves faster than that seen in the actual experiment. The second, and presumably related, problem is that the actual deformed profile shows much more curvature than the simulation. Both these observations suggest that the polyurea specimens may not have been thin enough to be considered membranes and that bending might play an important role. This augmentation of the model is not considered here.

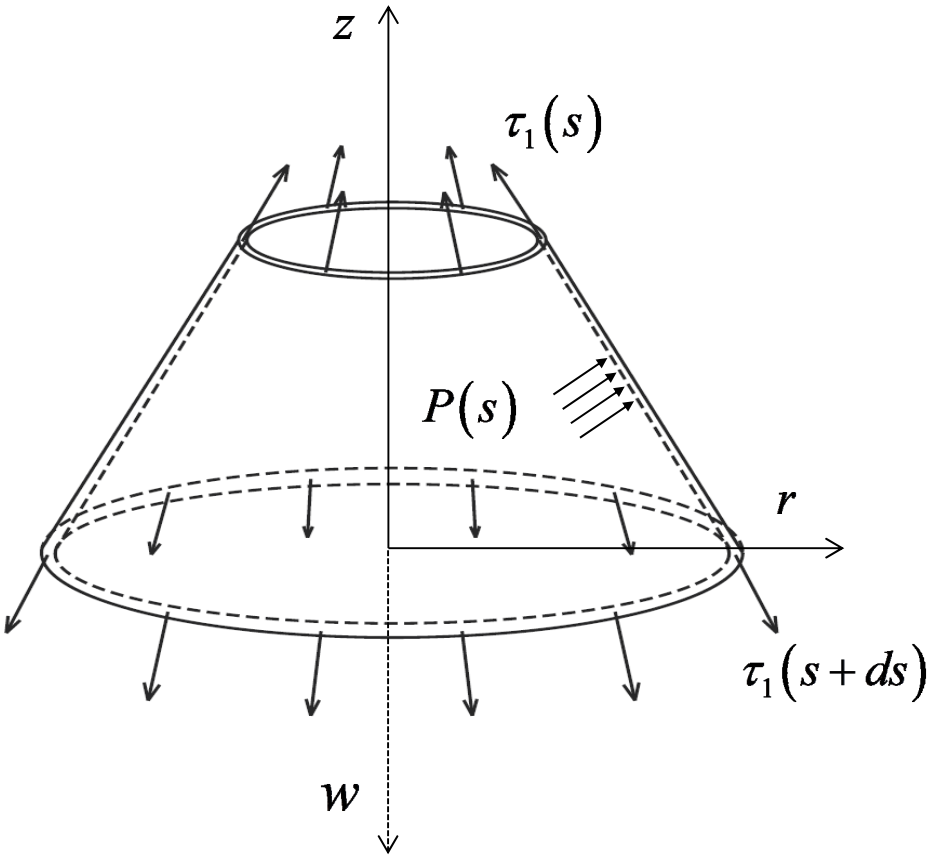

Figure 4.1: Free body diagram showing axisymmetric deformation of a membrane due to pressure load

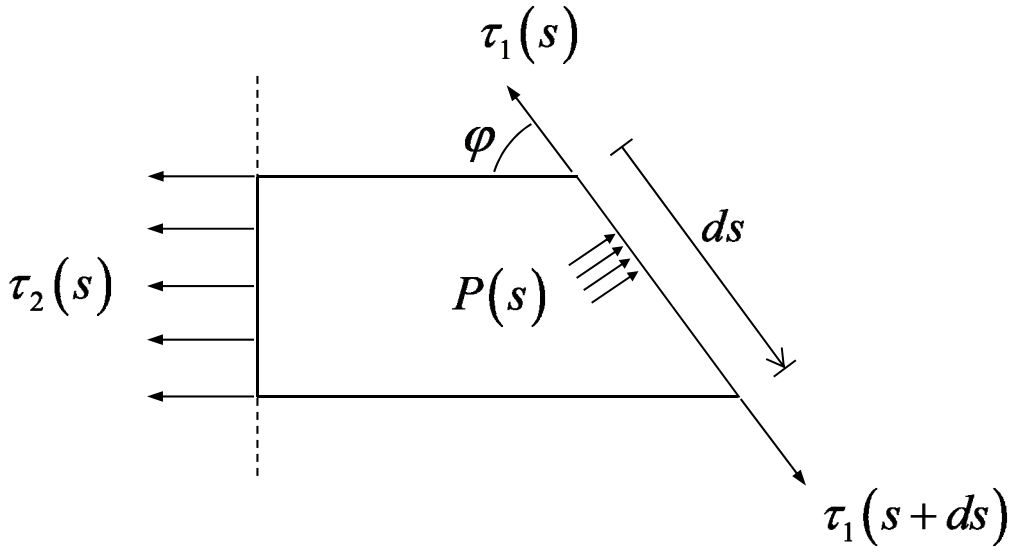

Figure 4.2: Meridional view of free body diagram of deformed membrane cut along vertical axis

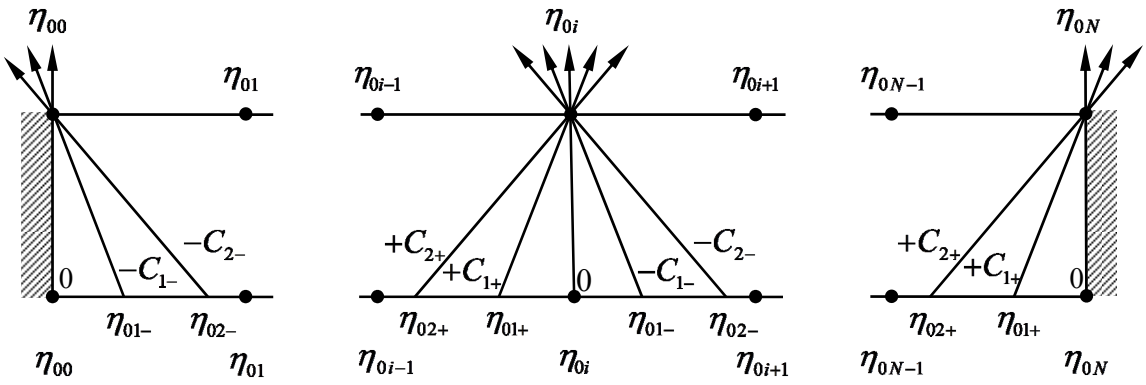

Figure 4.3: Stepwise calculation by the method of characteristics. Note the stationary characteristics only apply for the viscoplastic formulation.

Figure 4.4: Oblique view of nonimpact side of rubber membrane marked with concentric circles. Inner circle spacing = 5mm

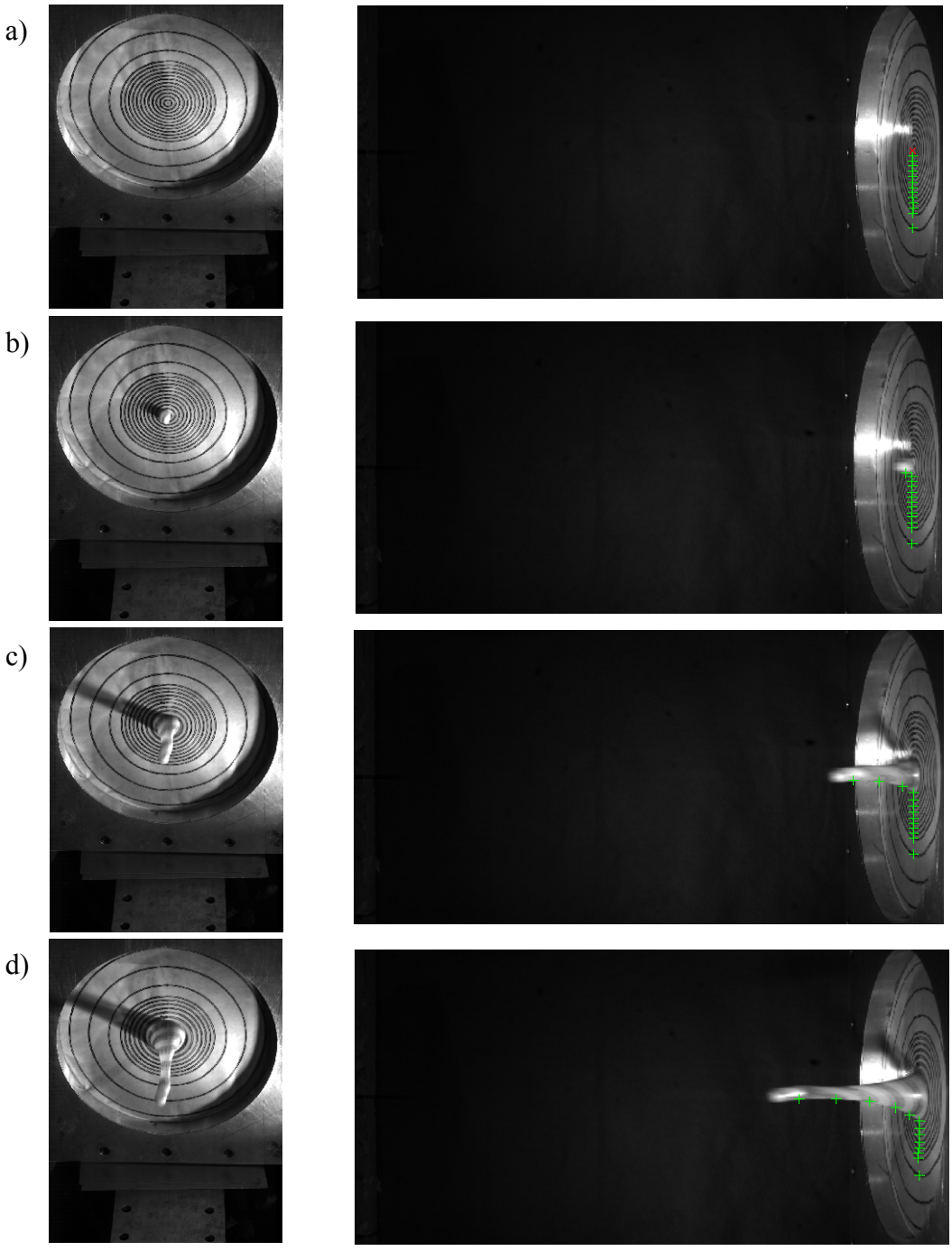

Figure 4.5: Evolution of membrane deformation in 150 m/s impact speed test. Impact point marked with red x in a). Location of material points tracked for measurement shown as green +'s. Time interval 463 μs

e)

f)

g)

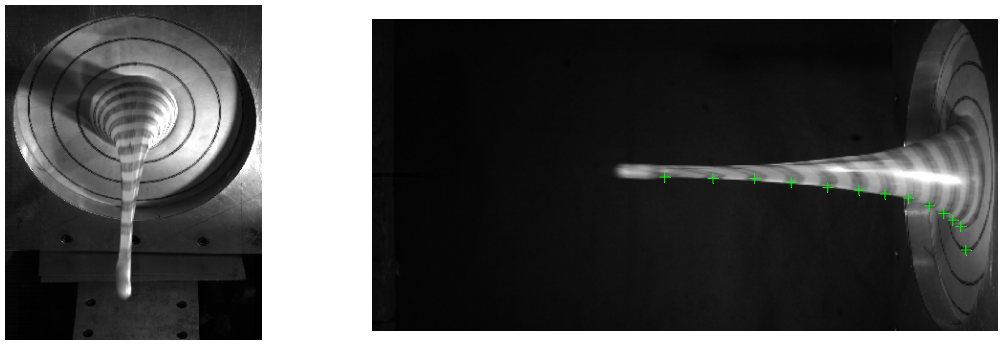

h)

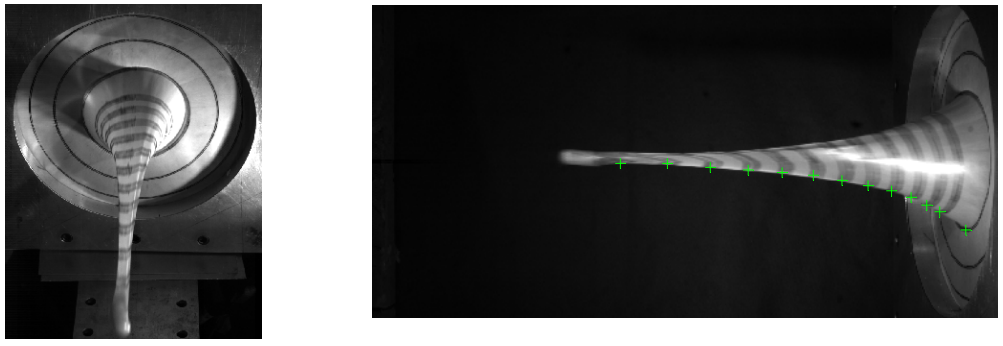

Figure 4.5: cont.

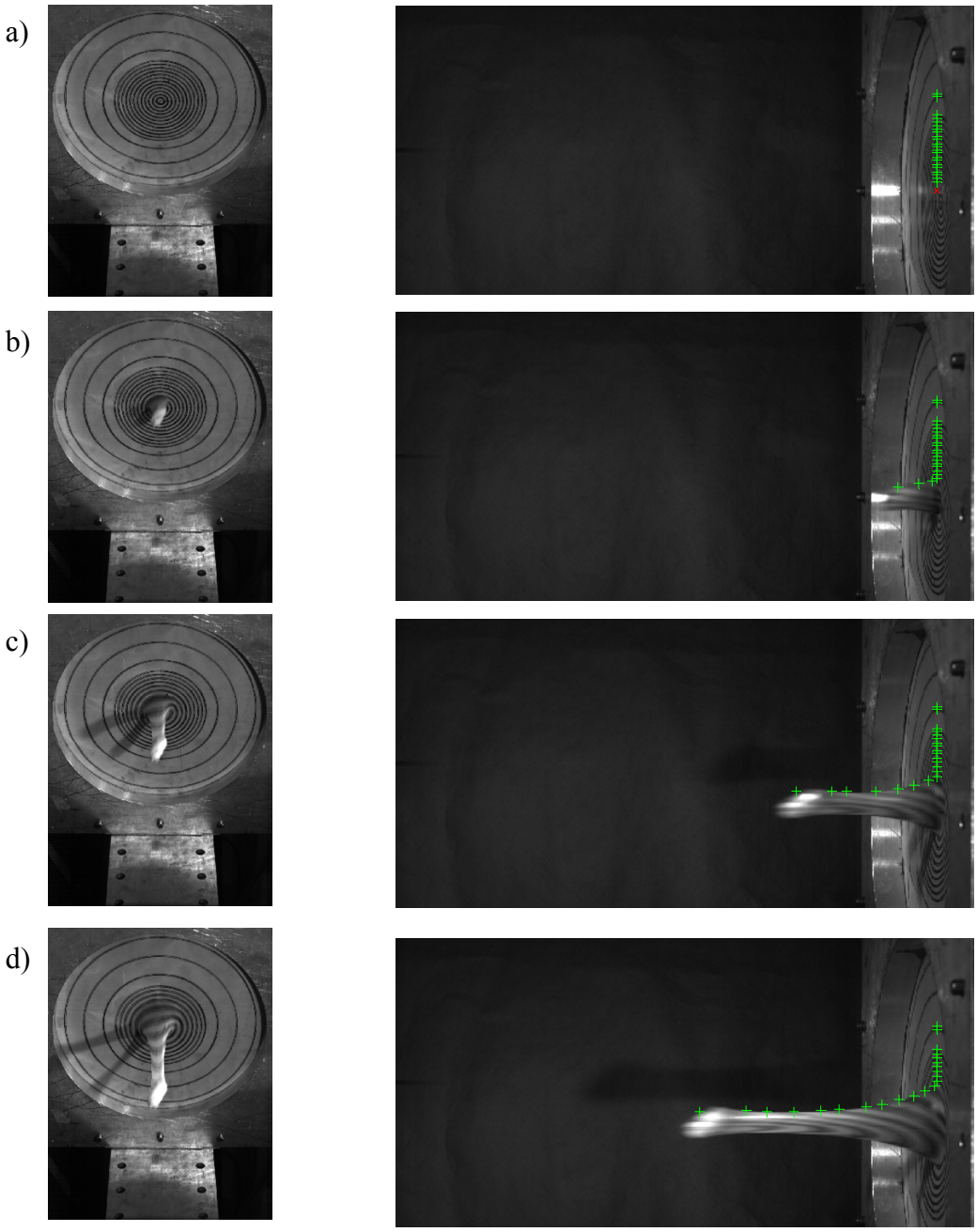

Figure 4.6: Evolution of membrane deformation in 160 m/s impact speed test. Impact point marked with red x in a). Location of material points tracked for measurement shown as green +'s. Time interval 463 μs

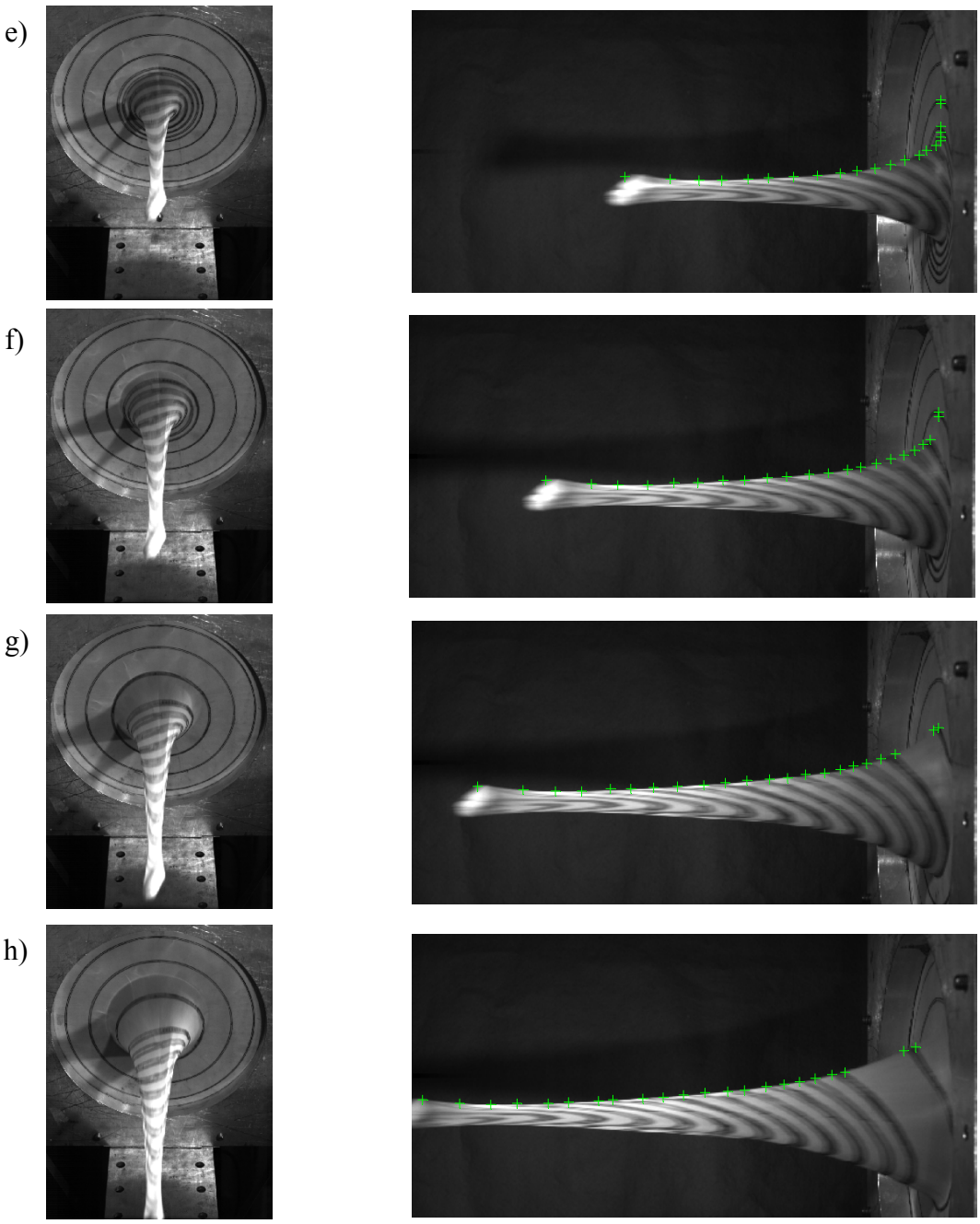

Figure 4.6: cont

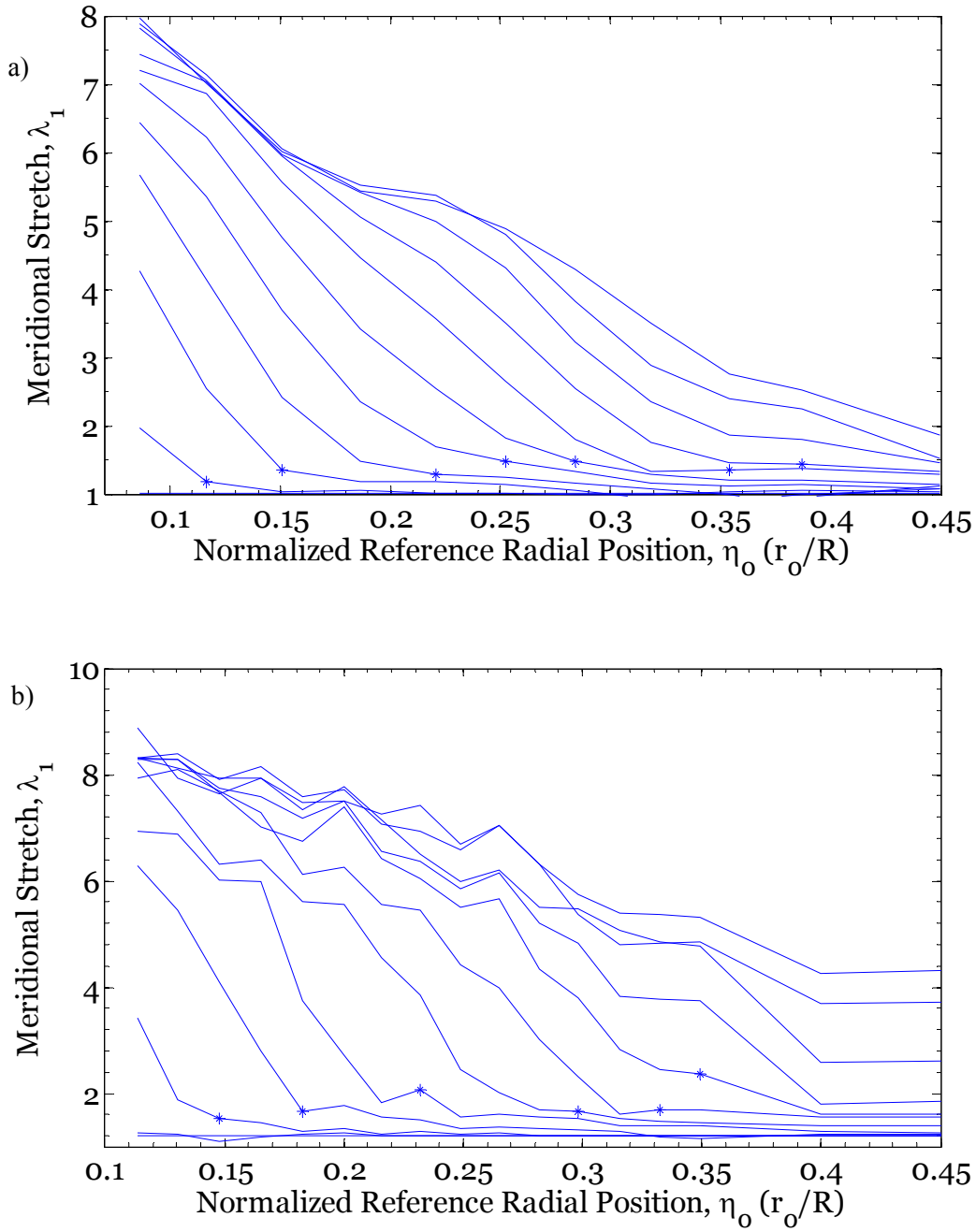

Figure 4.7: Measured meridional stretch profiles every 275 μs for two different impact speeds. a) 150 m/s b) 160 ms

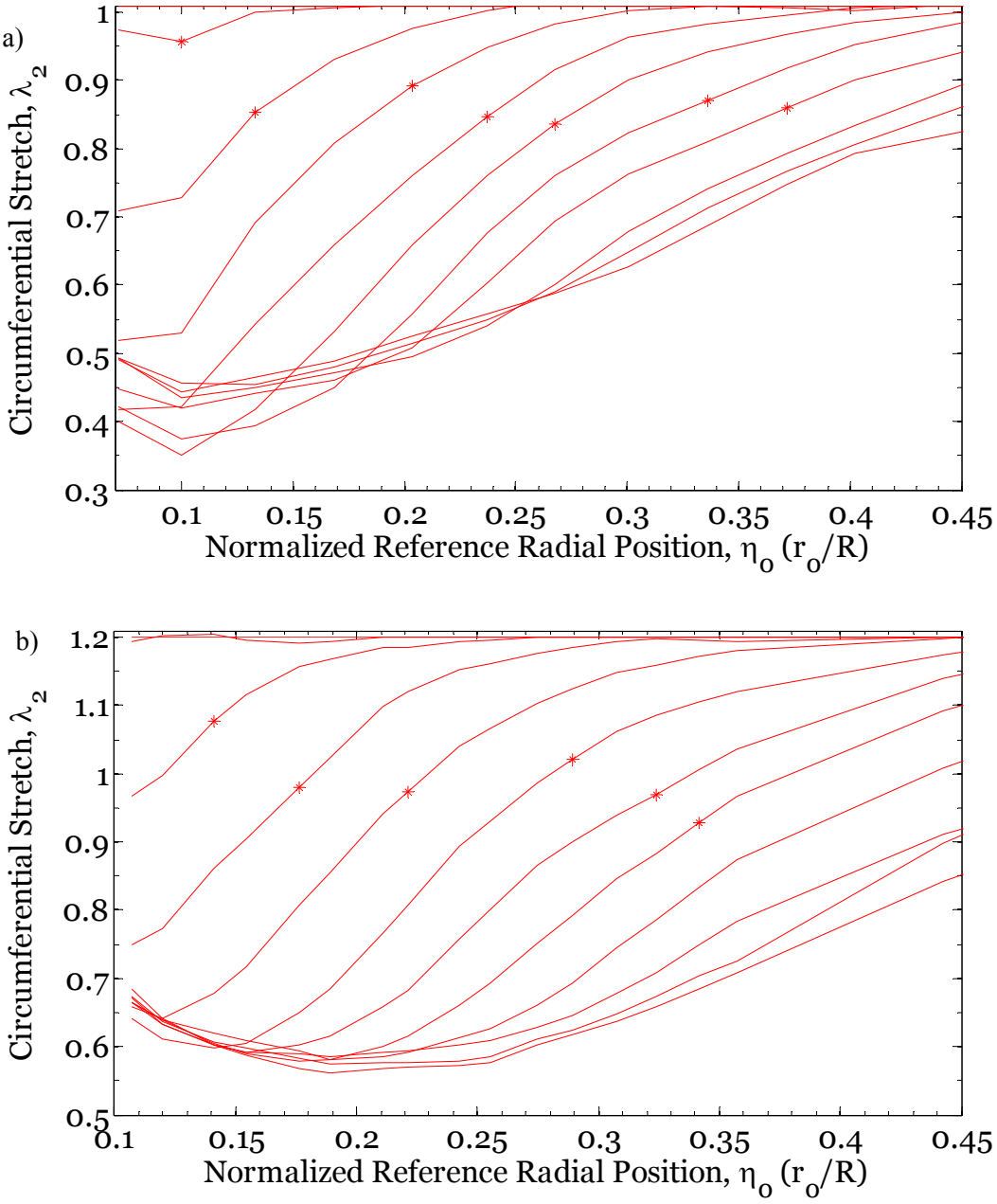

Figure 4.8: Measured circumferential stretch profiles every 275μs for two different impact speeds. a) 150 m/s b) 160 ms

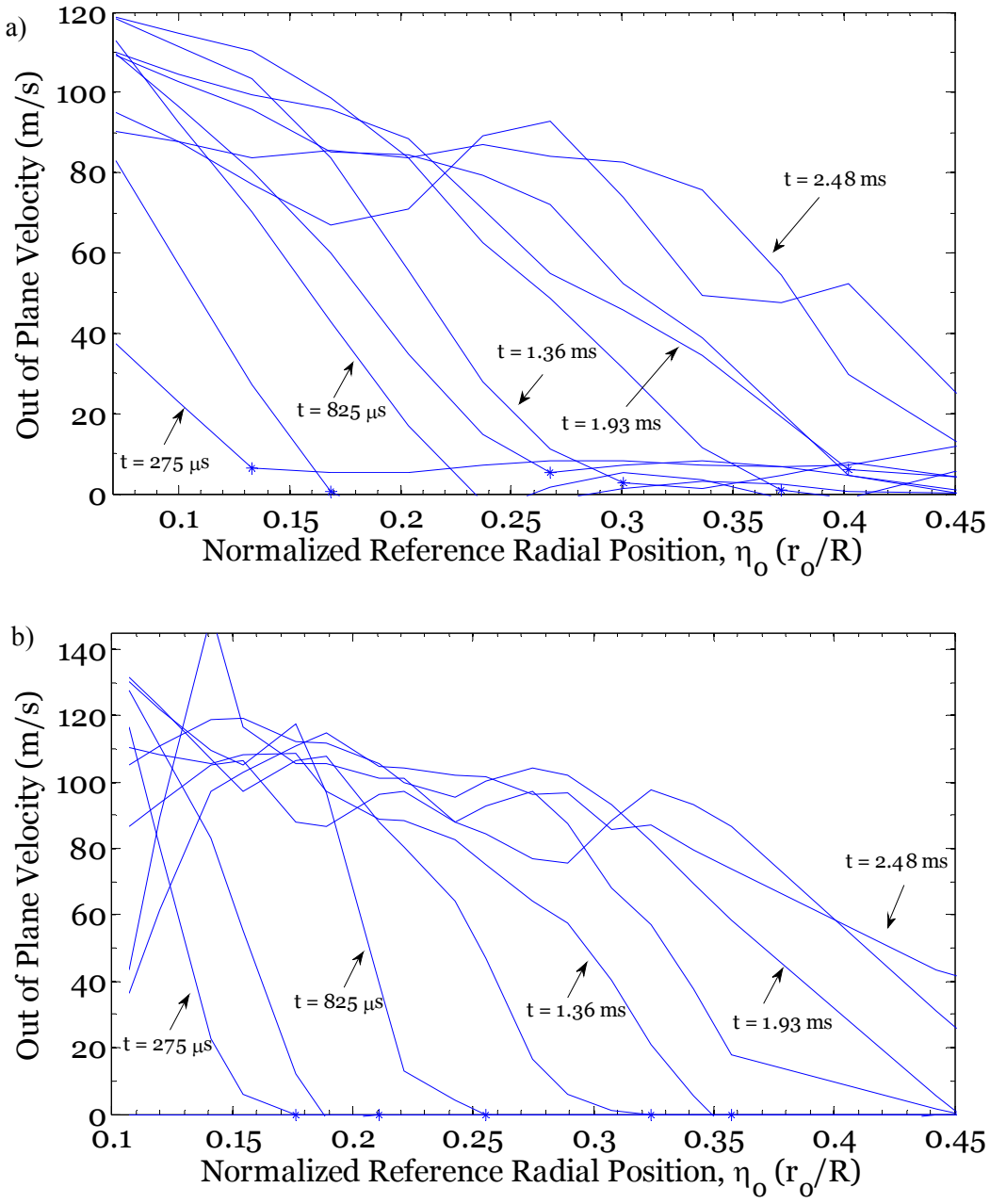

Figure 4.9: Measured out of plane velocity profiles every 275μs for two different impact speeds. a) 150 m/s b) 160 ms

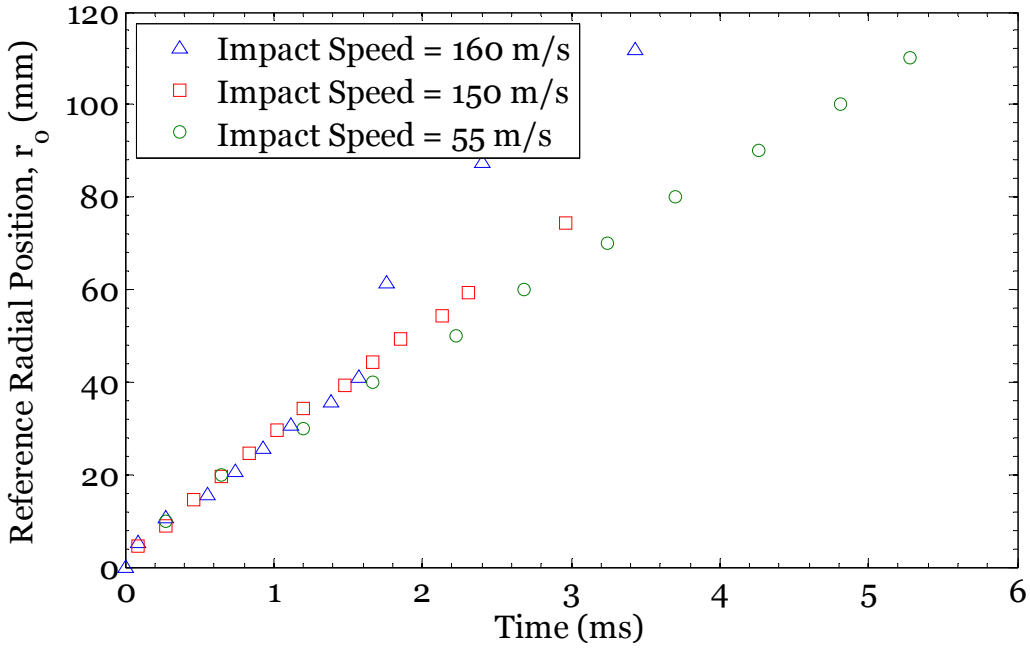

Figure 4.10: Comparison of measured kink wave position vs. time for three tests. Initial speed ~25m/s observed in all three tests

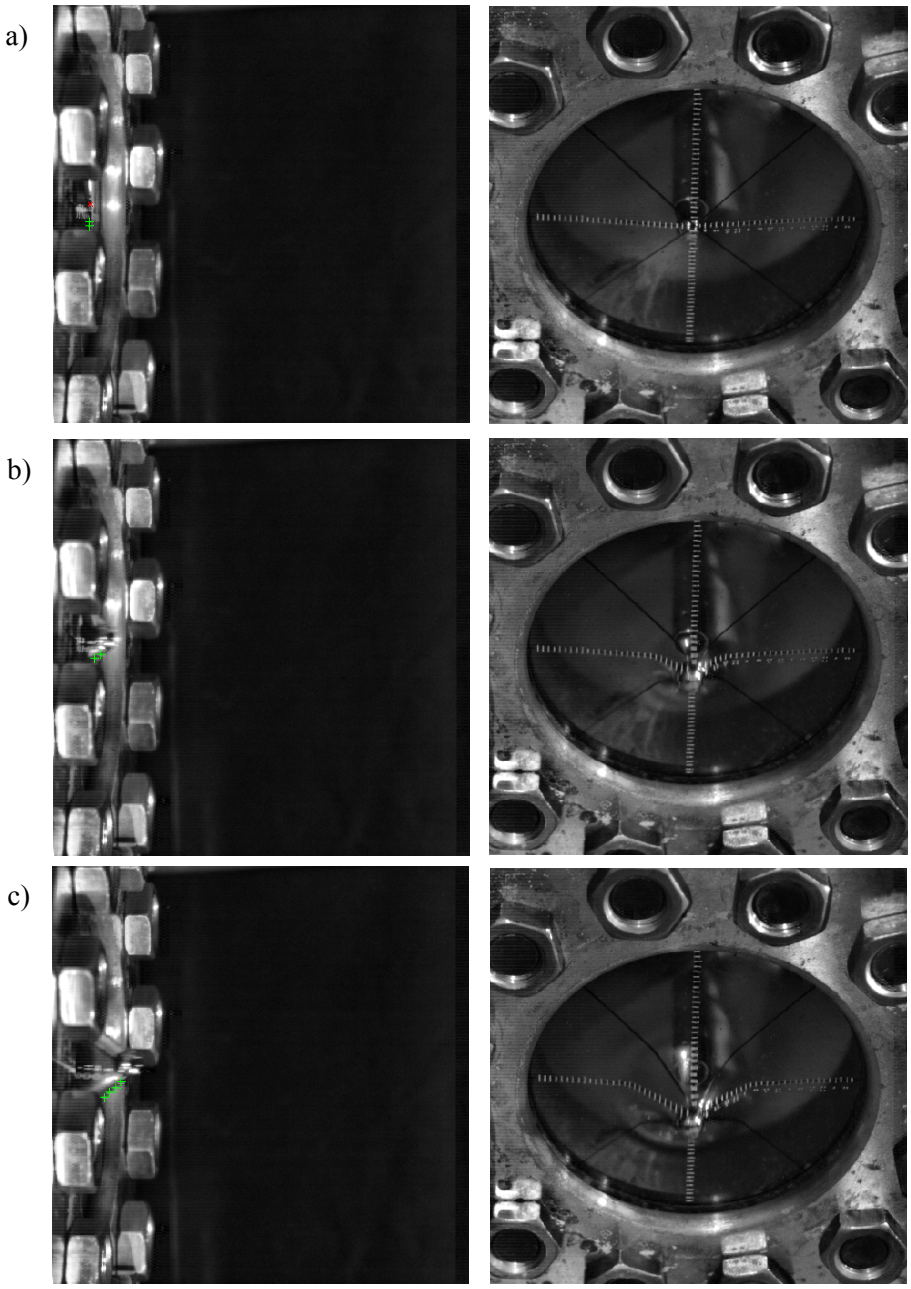

Figure 4.11: Evolution of polyurea membrane deformation in 80 m/s impact speed test. Impact point marked with red x in a). Location of material points tracked for measurement shown as green +'s. Time interval 150 μs

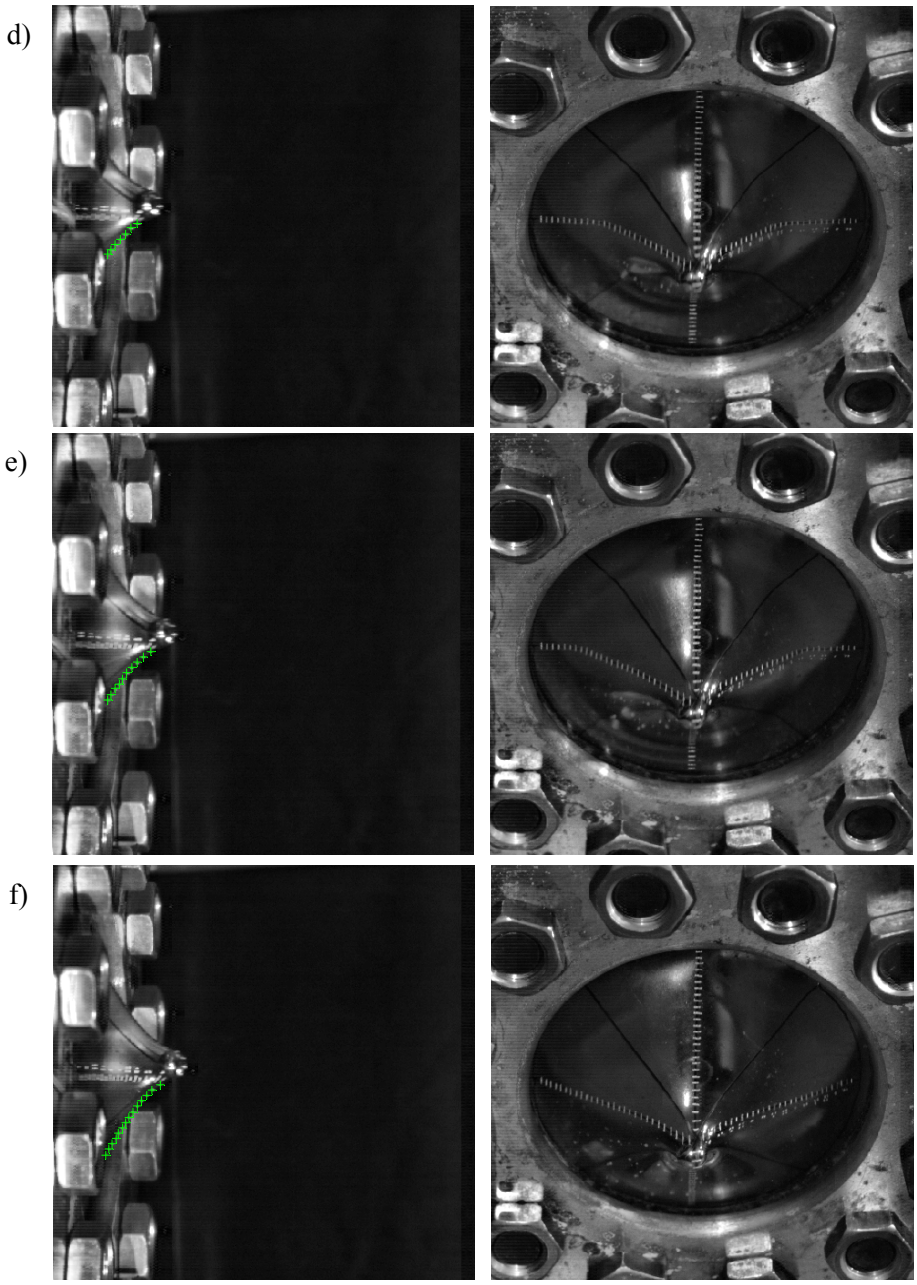

Figure 4.11: cont.

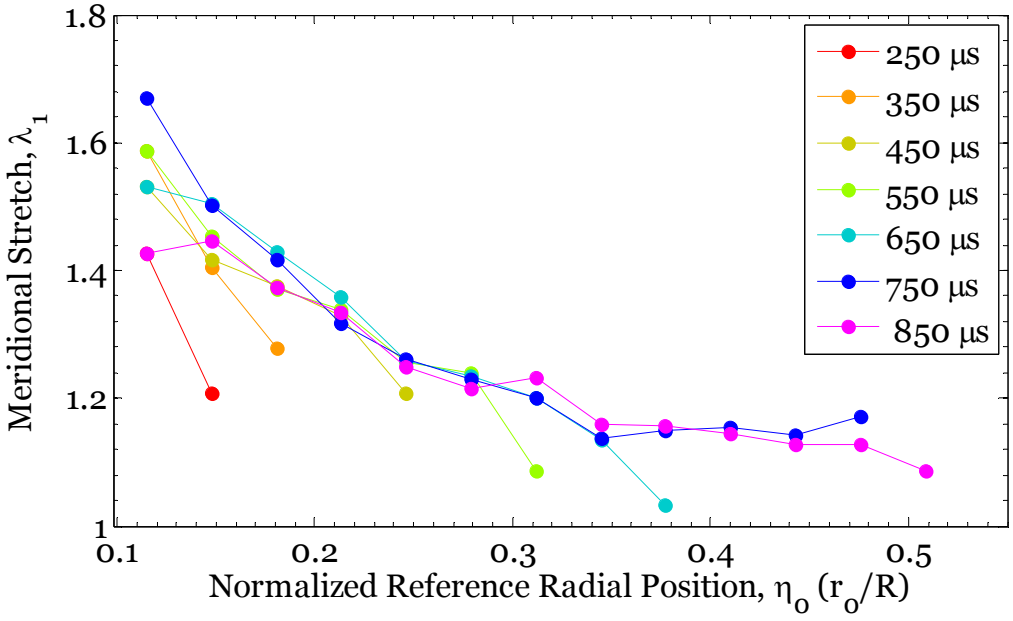

Figure 4.12: Measured meridional stretch profiles every 100 µs

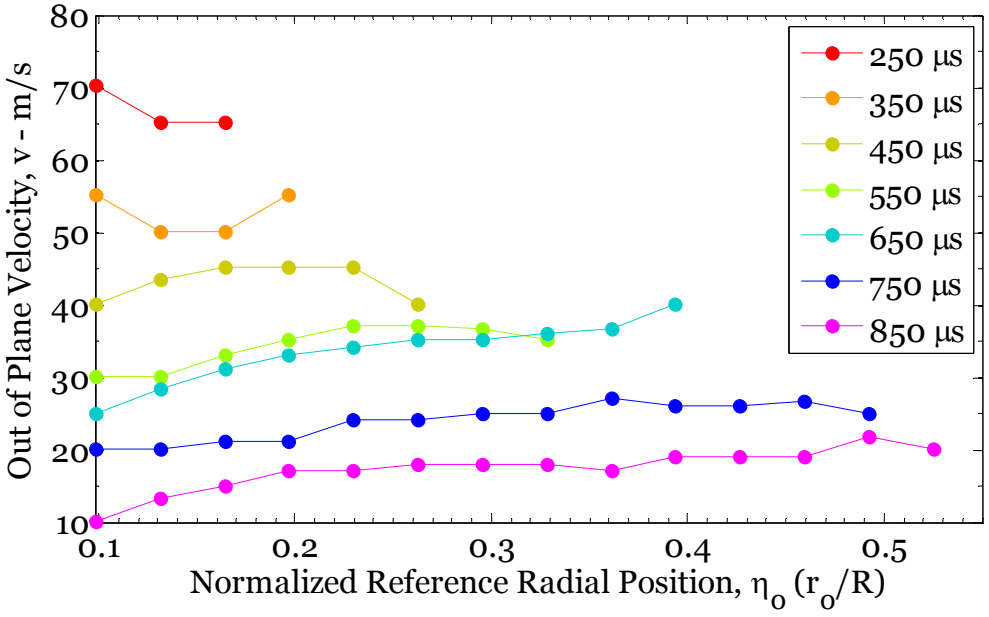

Figure 4.13: Measured out of plane velocity profiles every 100 µs

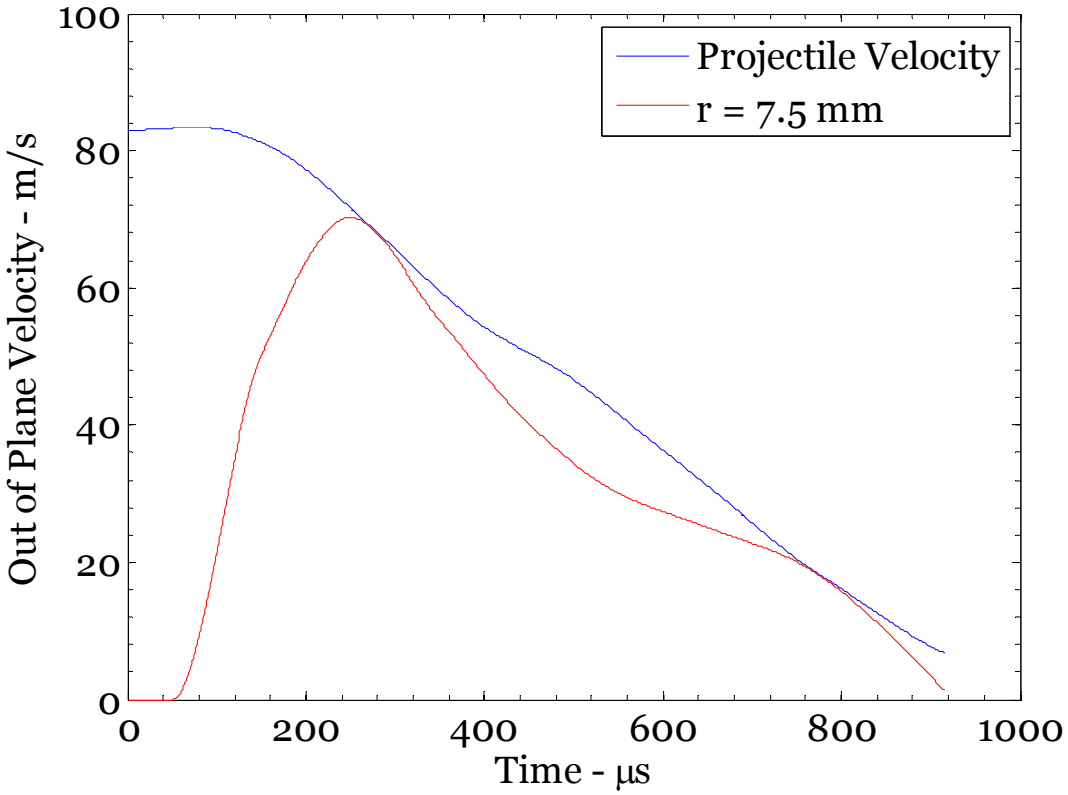

Figure 4.14: Comparison of projectile velocity and smoothed out of plane velocity of material point to be used as inner radial boundary condition in simulations

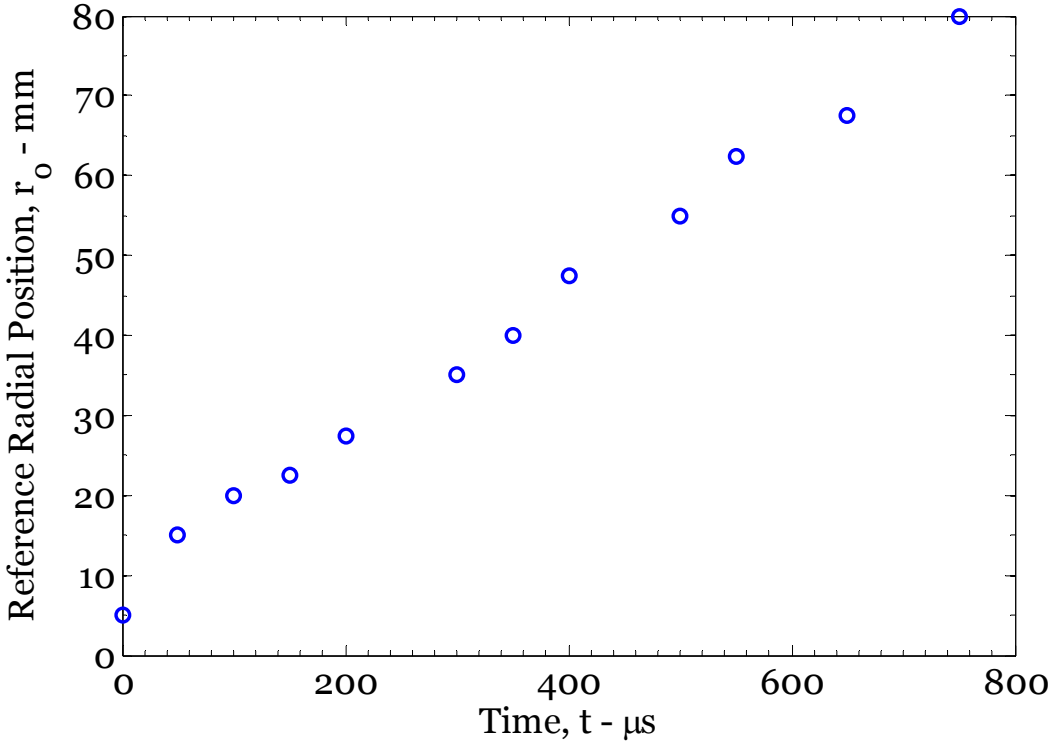

Figure 4.15: Measured kink wave positions vs. time for 80 m/s impact on polyurea.

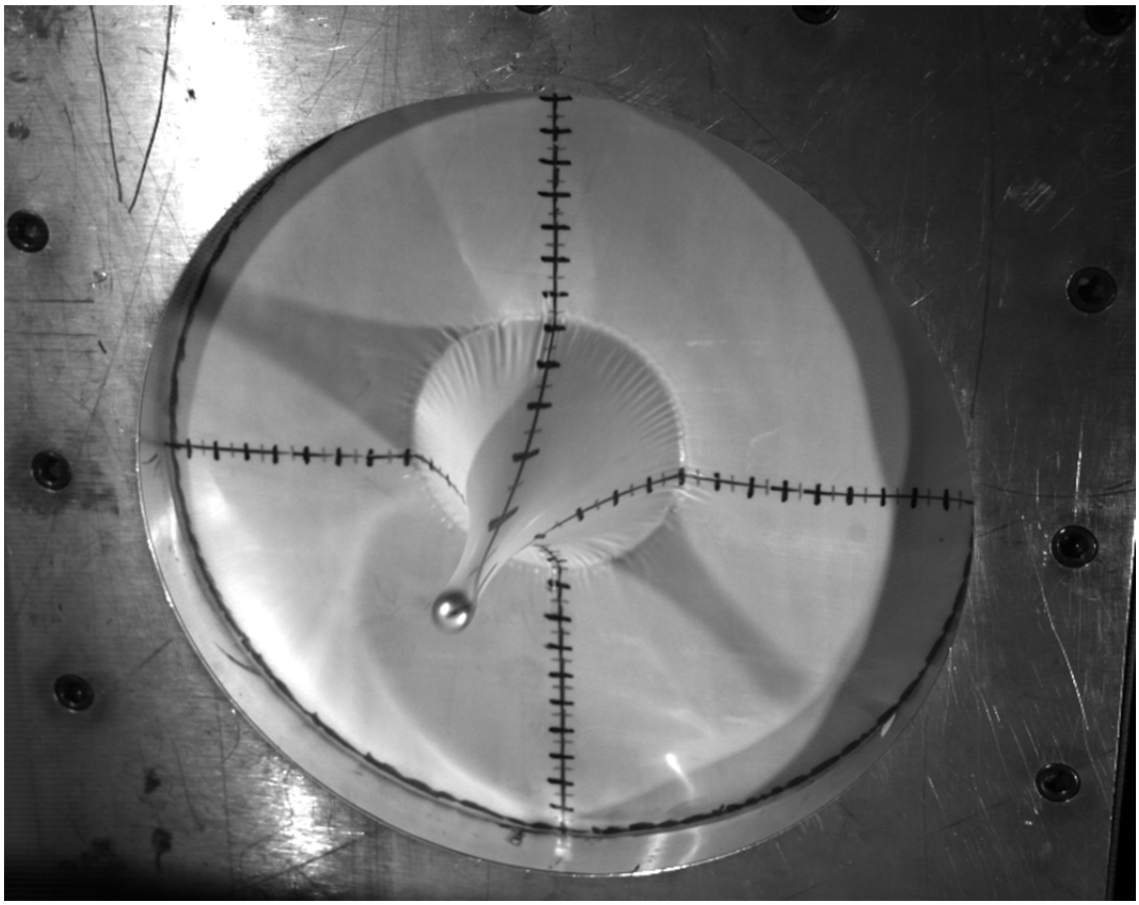

Figure 4.16: Oblique view of membrane, 2.3 ms after 55 m/s impact, showing wrinkles have formed around the kink wave

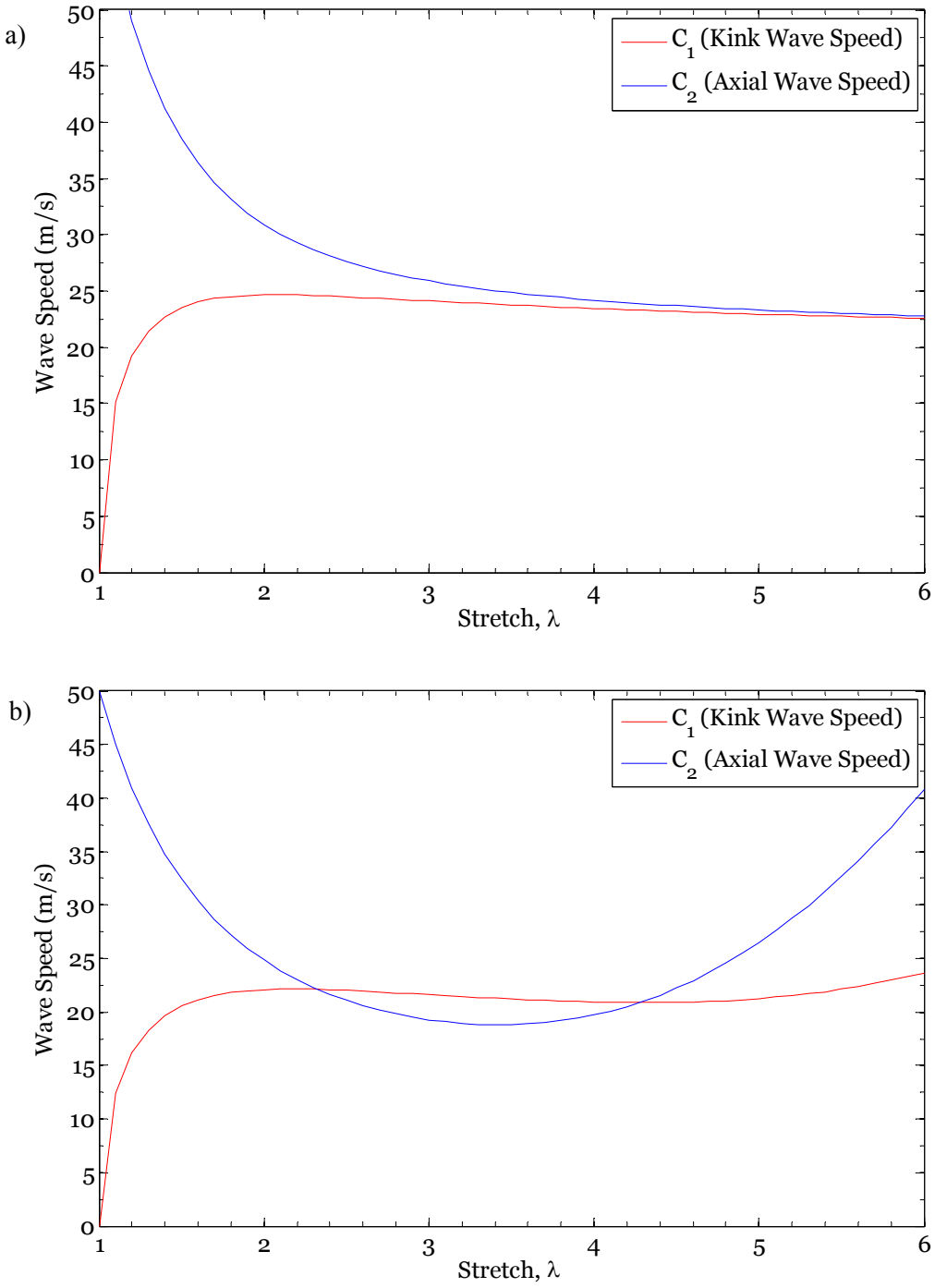

Figure 4.17: Kink and axial wave speed plotted as a function of stretch in uniaxial tension for a) DCMR material model and b) Q-LP material model

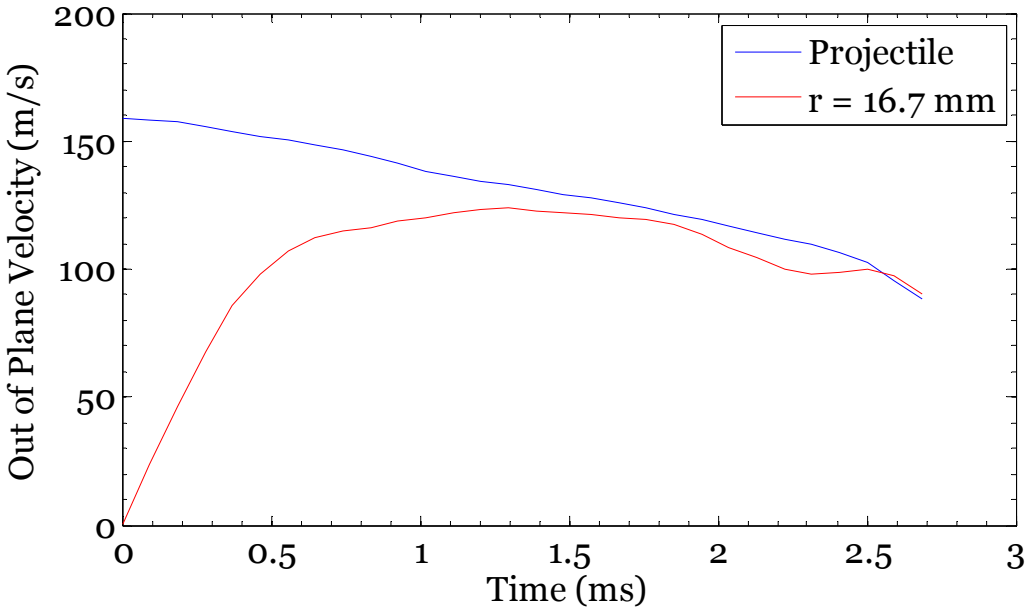

Figure 4.18: Comparison of projectile velocity and out of plane velocity of a material point to be used as inner radial boundary condition in simulations of 160 m/s impact

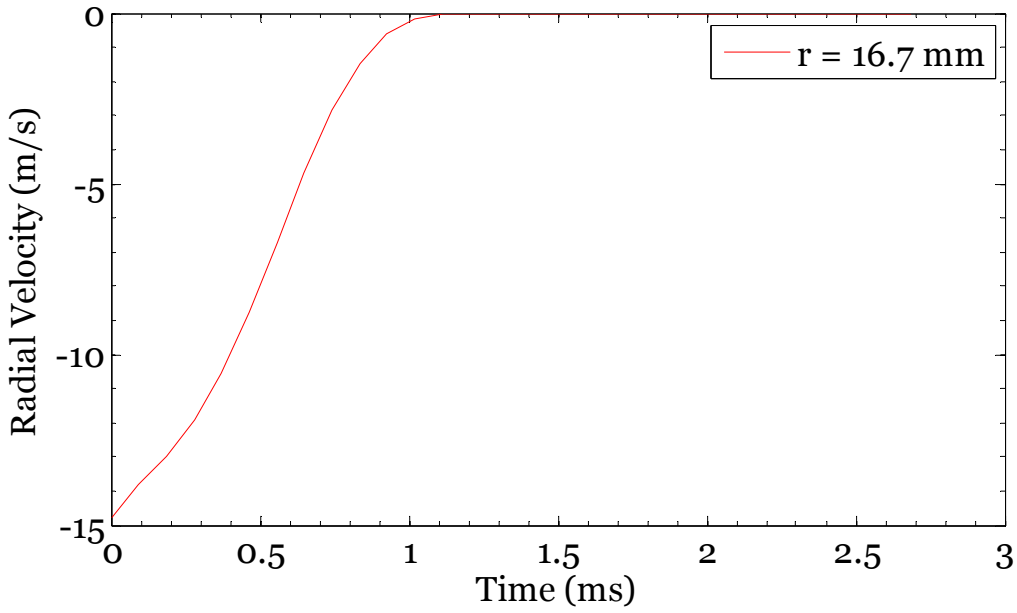

Figure 4.19: Radial velocity of a material point to be used as inner radial boundary condition in simulations of 160 m/s impact

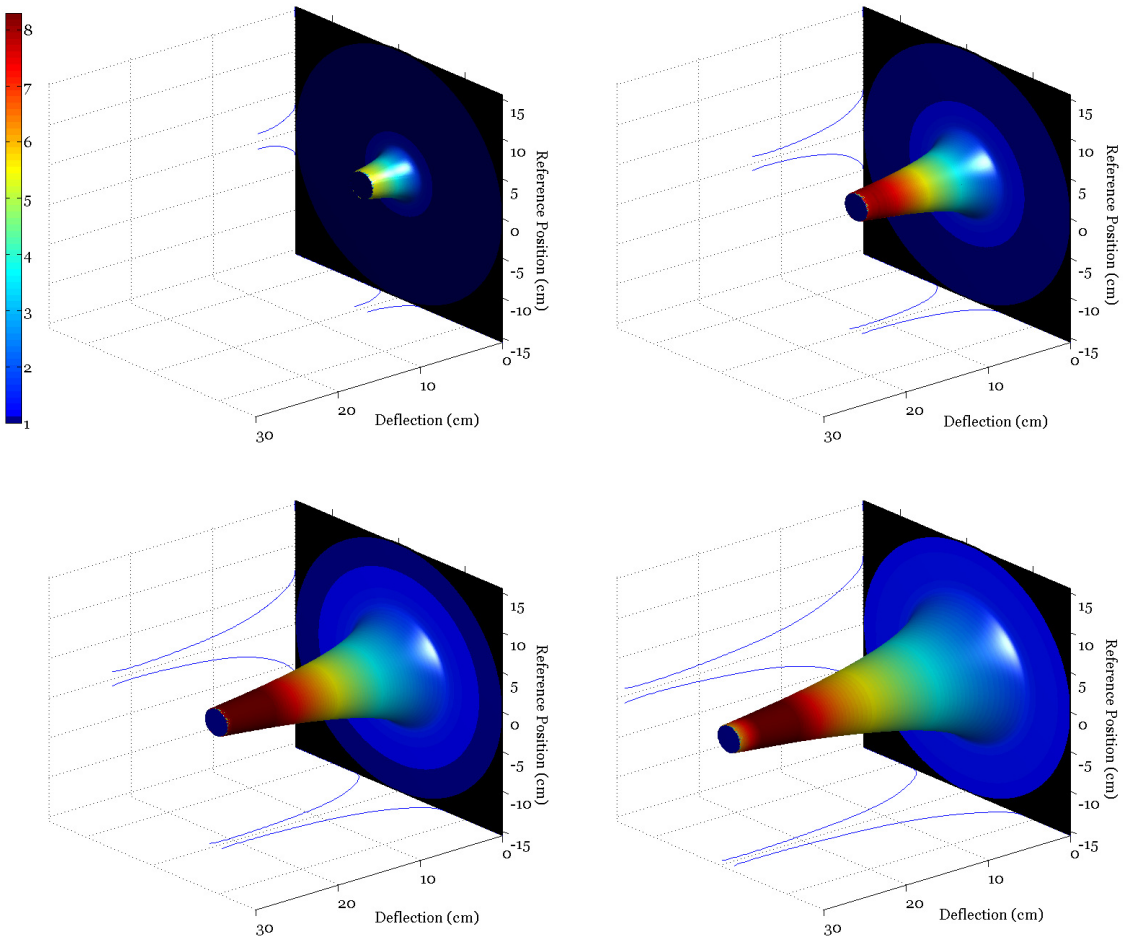

Figure 4.20: Oblique view of the simulation of 160 m/s impact on circular polyisoprene membrane using the DCMR material model. Color contours signify meridional stretch, λ_1.

a)

b)

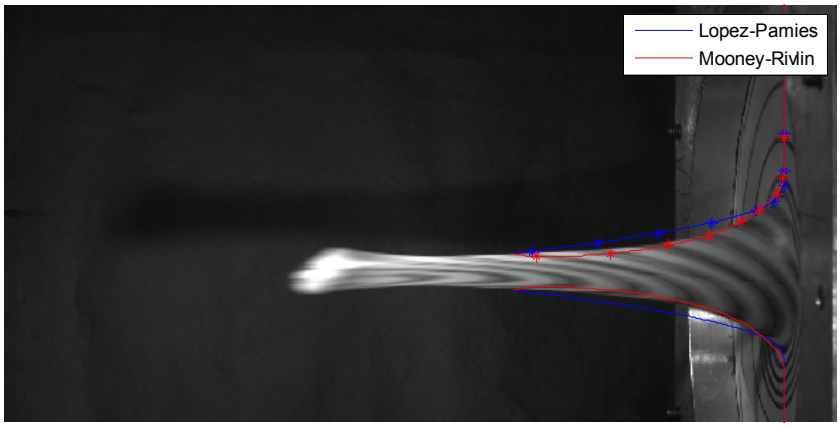

c)

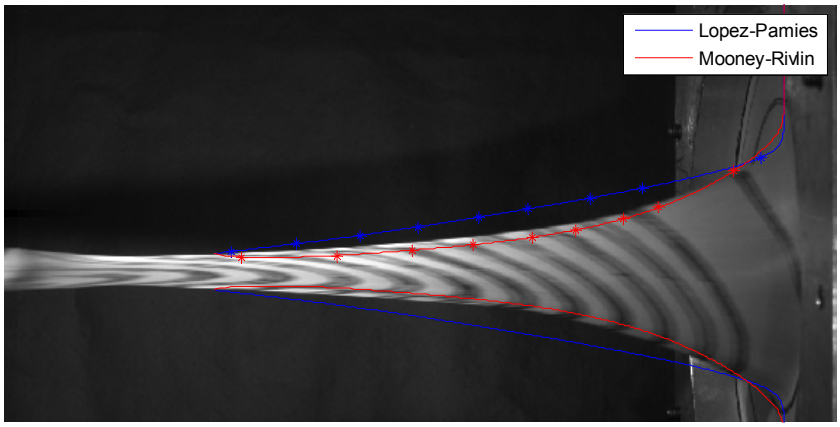

Figure 4.21: Predicted membrane profile overlaid on high speed images of actual deformation for 160 m/s impact test. Asterisks mark the material points at the midpoint of width for each concentric to show particle motion. a) t = 0 ms b) t = 1.4 ms c) t = 2.8 ms

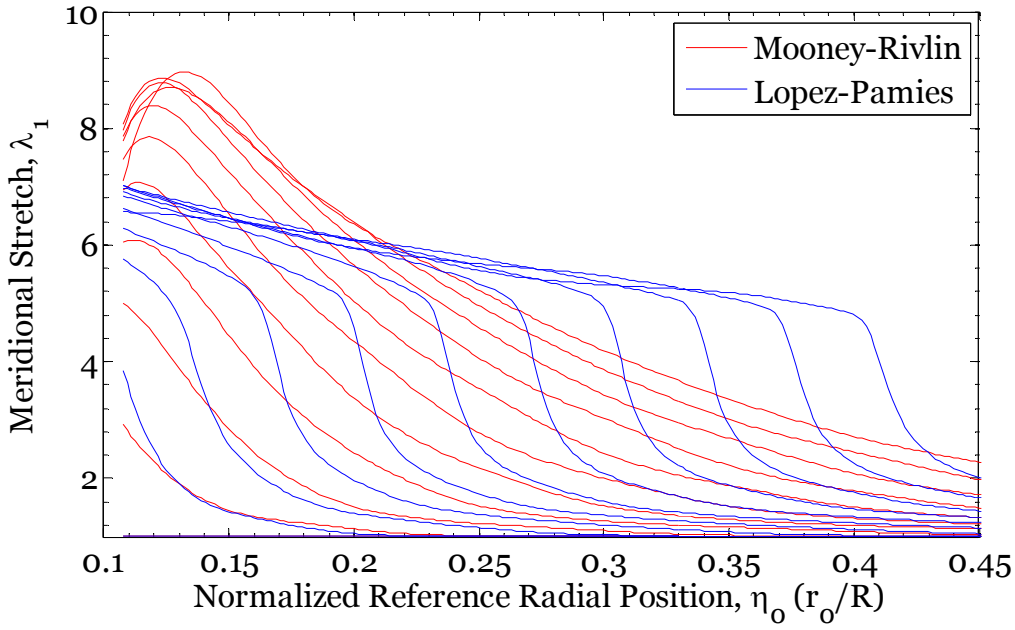

Figure 4.22: Comparison of meridional stretch profiles every 275 μs predicted by DCMR and Q-LP models for 160 m/s impact

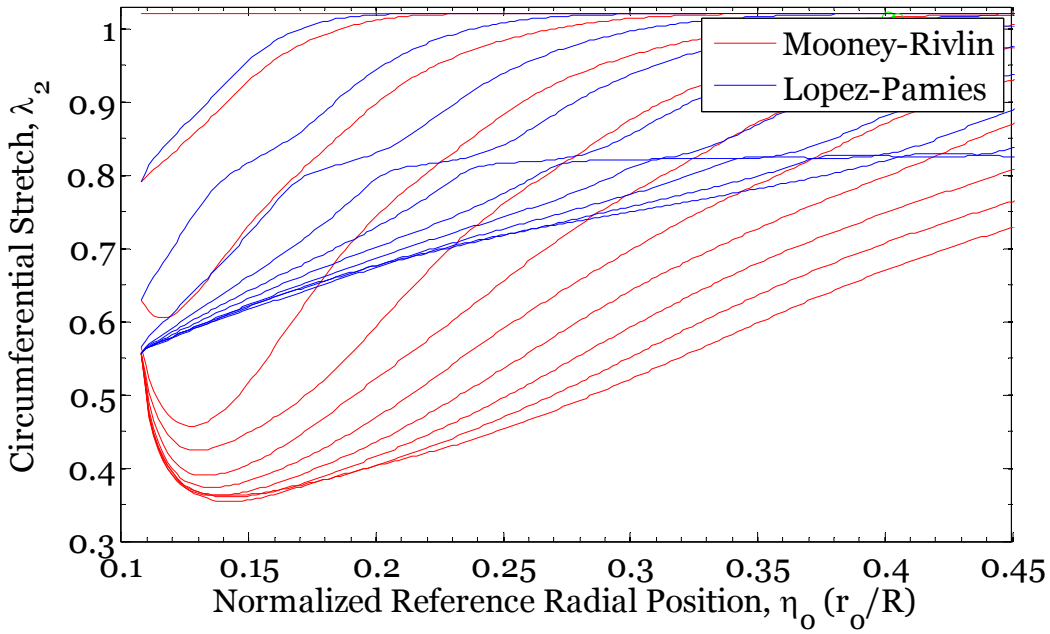

Figure 4.23: Comparison of circumferential stretch profiles every 275 μs predicted by DCMR and Q-LP models for 160 m/s impact

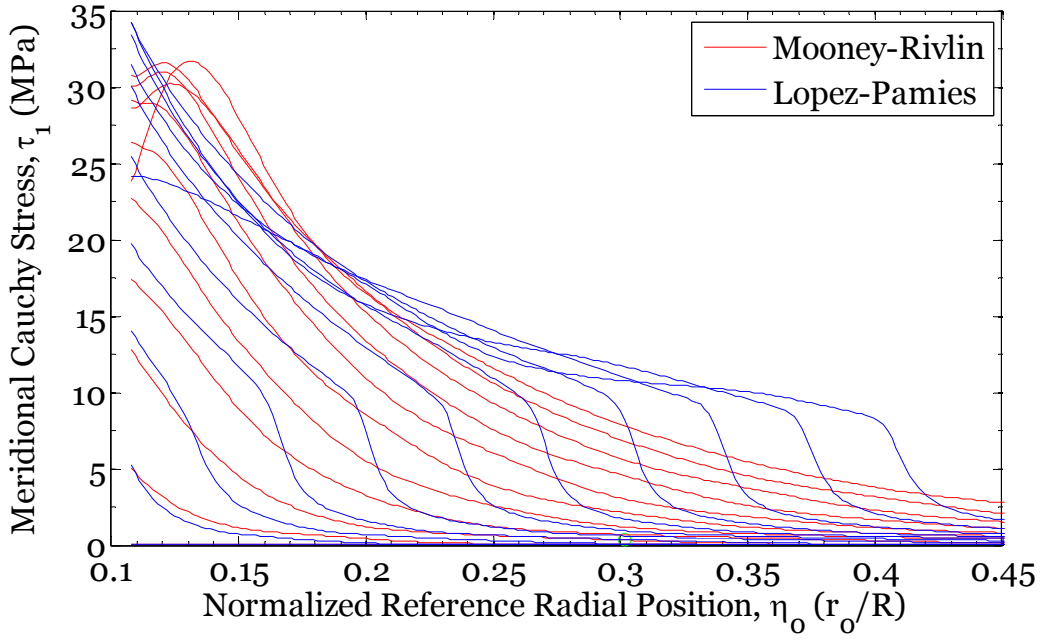

Figure 4.24: Comparison of meridional Cauchy stress profiles every 275 μs predicted by DCMR and Q-LP models for 160 m/s impact

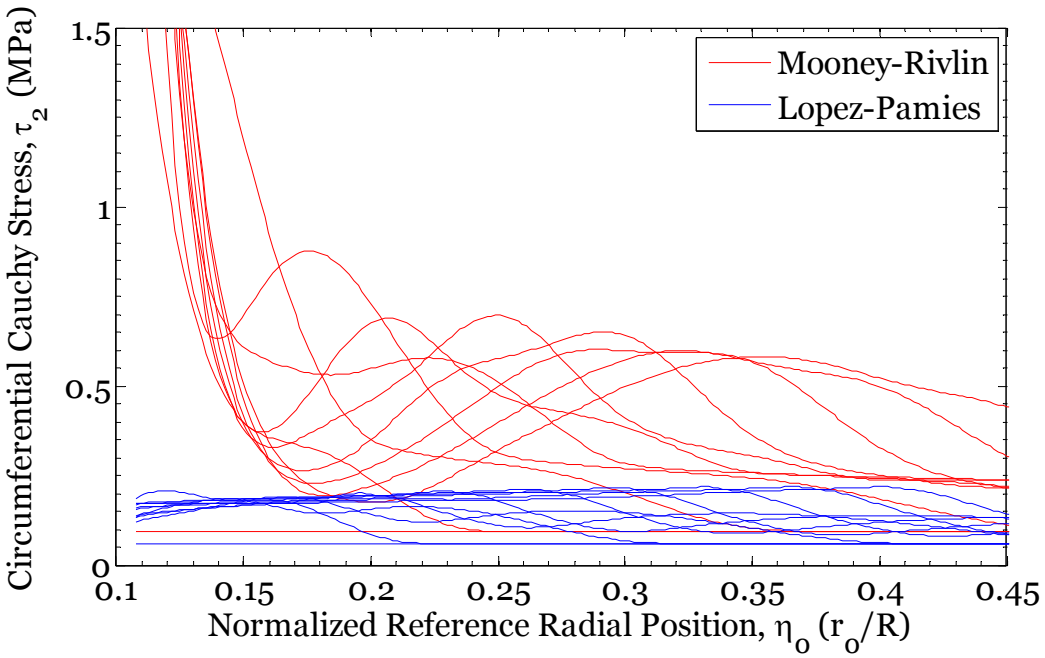

Figure 4.25: Comparison of circumferential Cauchy stress profiles every 275 μs predicted by DCMR and Q-LP models for 160 m/s impact

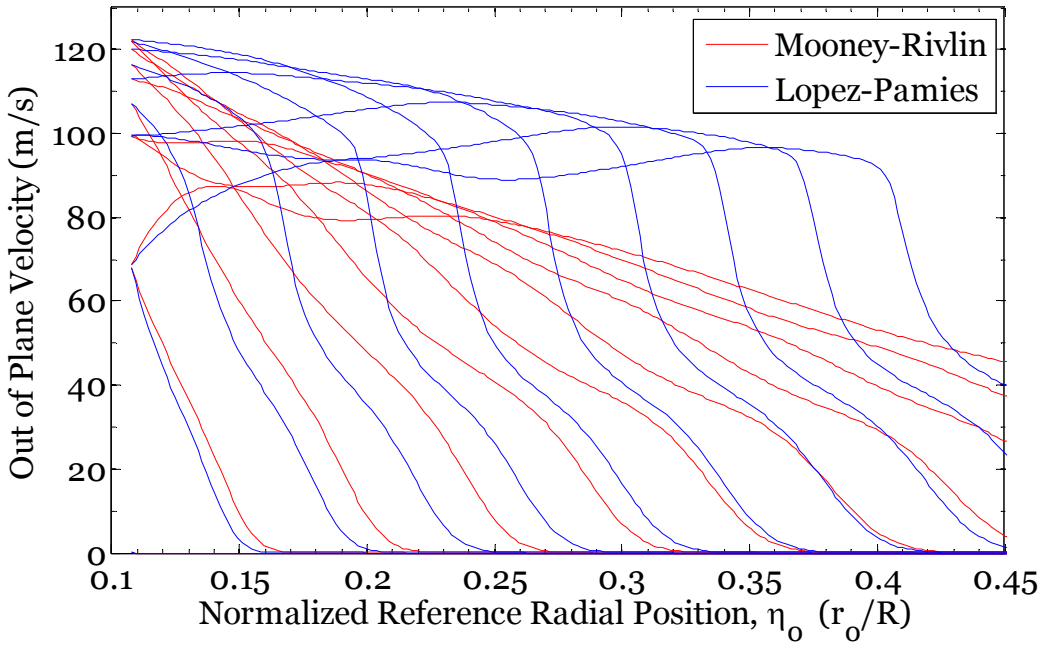

Figure 4.26: Comparison of out of plane velocity profiles every 275 μs predicted by DCMR and Q-LP models for 160 m/s impact

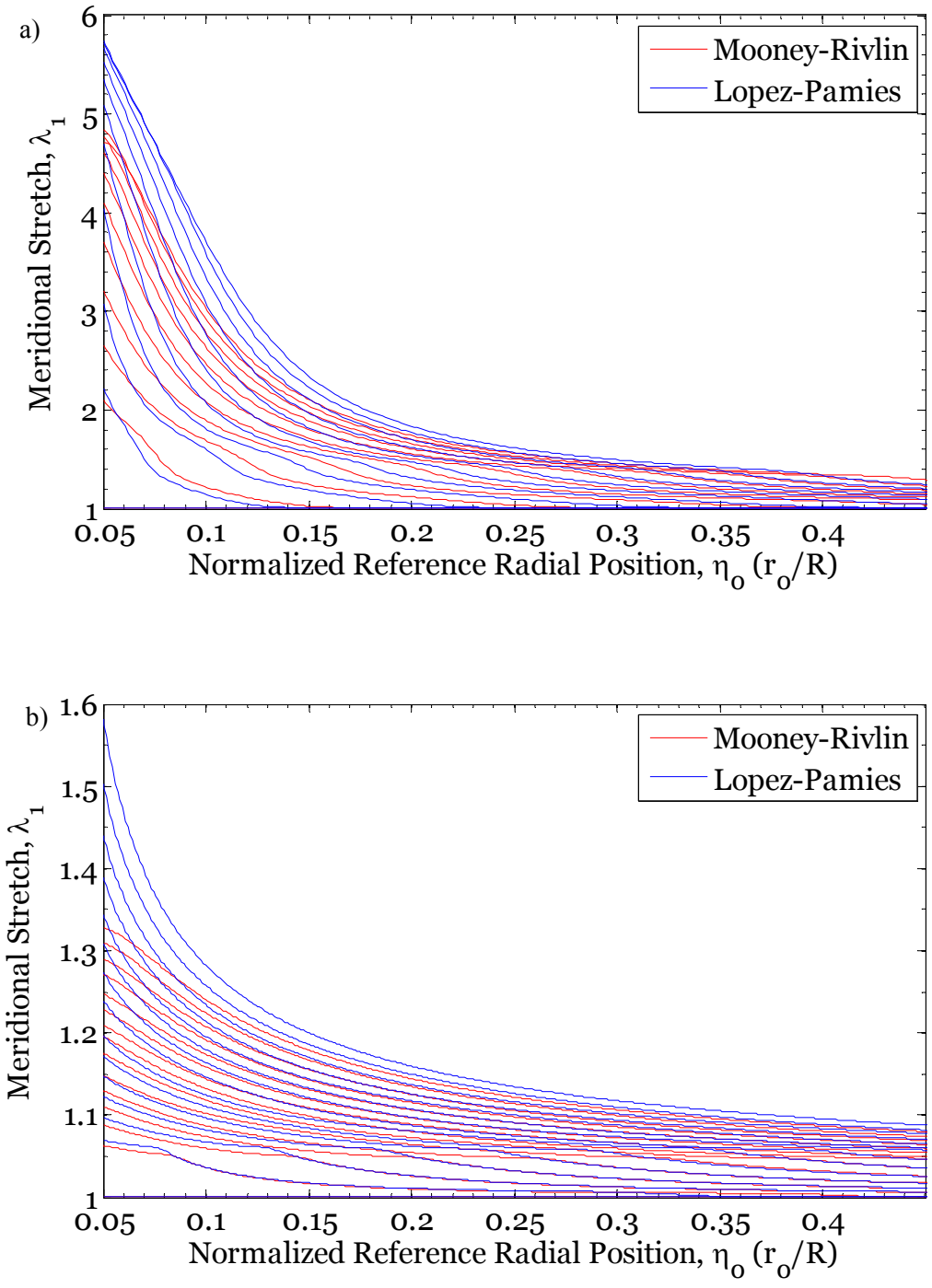

Figure 4.27: Comparison of meridional stress profiles predicted by DCMR and Q-LP models. a) 55 m/s impact every 275 μs b) 5 m/s impact every 1 ms.

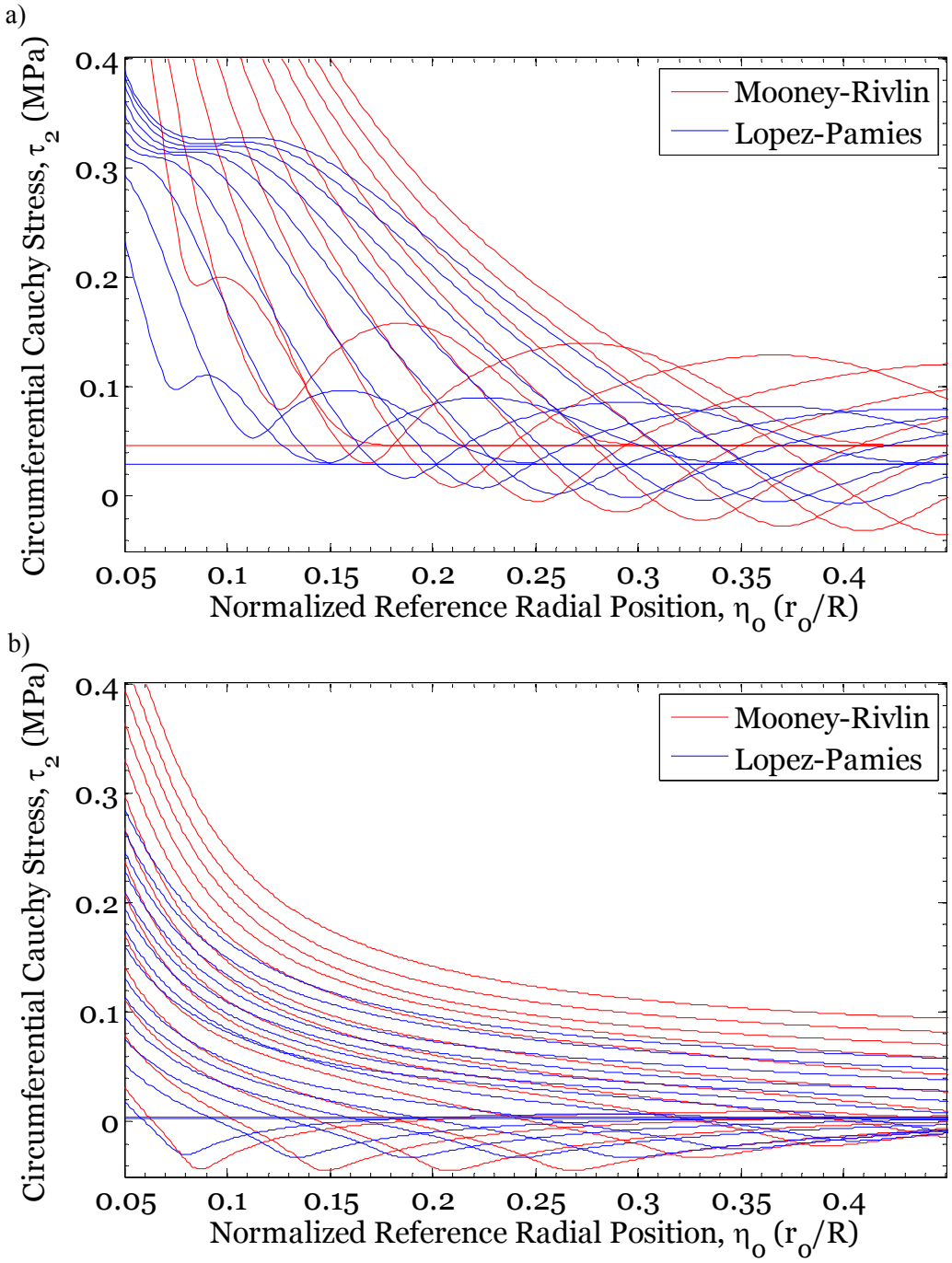

Figure 4.28: Comparison of circumferential Cauchy stress profiles predicted by DCMR and Q-LP models. a) 55 m/s impact every 275 μs b) 5 m/s impact every 1 ms.

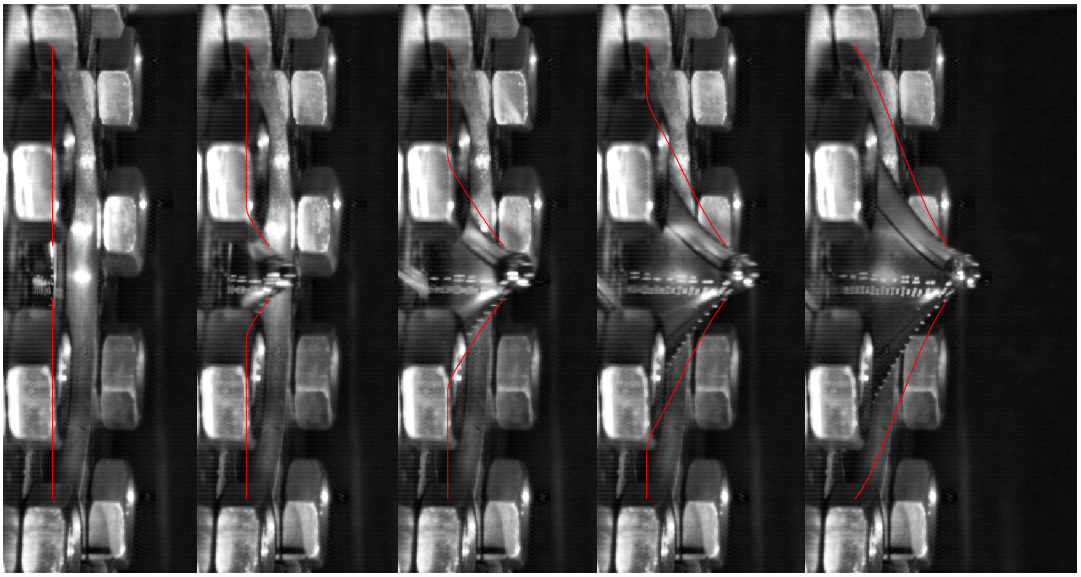

Figure 4.29: Series of image overlays comparing the predicted deformation profile of the polyurea membrane to the actual recorded profile ever 200 μs

Chapter 5: Wave Propagation using Finite Volume Method

5.1 INTRODUCTION

There are limitations to the method of characteristics solutions presented in the preceding chapters. If there is an inflection in the uniaxial stress strain curve, the wave speed will not decrease monotonically with increasing strain and this causes problems with crossing of characteristics (i.e. formation of shocks). All strains above the inflection point will propagate into the specimen faster than those lower strains already in the specimen creating a jump in strain. A similar problem can occur even without the inflection in the stress strain curve if unloading is considered. The lower strain levels will propagate into the stretched specimen at higher speeds again causing a jump in strain. In order to produce a robust algorithm that can deal with shocks as well as their reflection and intersection, another method is needed. A finite difference based method, while requiring more computational power, can handle these additional complications. Instead of propagating information along characteristics, the problem is broken into finite volume cells by the Godunov method over which an average value of the dependent variables can be found. A linearized version of the Riemann problem is then solved at each interface between cells and the cell averages are updated. The method described below is in large part that developed by LeVeque (1997, 2002) and Bale 2003.

These techniques were primarily (but not exclusively) developed and applied in computational gas dynamics; for the sake of completeness we first describe the method in detail. We begin by describing the solution to the *linear* Riemann problem. We then explain how this method can be generalized to solve nonlinear problems by a local gradient approach. Next we introduce the Godunov method in a general way which allows us to split the problem into the finite volume cells required for the necessary local linearization. The final step is then to solve the Riemann problem at each interface and

march the solution forward in time. Details relating to dealing with boundary conditions and extending the method to higher resolution are also discussed. With the method fully explained, we apply it first to several dynamic uniaxial example problems; then we look at a specific dynamic tension experiment possibly containing a shock. Finally, the method is generalized to two-dimensional problems and the same analysis is done for the dynamic membrane problem.

5.2 FINITE VOLUME METHOD FOR 1D NON LINEAR WAVE PROPAGATION WITH SHOCKS

5.2.1 Riemann Solution of Linear and Nonlinear Wave Equations

We begin by solving the Riemann problem for wave propagation in a linear elastic material; the governing equation is given in Eq. (3.4), with $\mathbf{A} = \begin{bmatrix} 0 & -E/\rho \\ -1 & 0 \end{bmatrix}$.

Initial conditions are imposed such that a discontinuity exists at $x = 0$.

$$\mathbf{u}(x,0) = \begin{cases} \mathbf{u}_L & x < 0 \\ \mathbf{u}_R & x > 0 \end{cases} \tag{5.1}$$

The evolution of $\mathbf{u}$ is obtained as in the method of characteristics described in Section 3.2, with some key differences. In Section 3.2, the nodal solution is interpolated, and propagated along the two characteristics which intersect at the next time step at the nodal point. In the finite volume method, we follow the two characteristics which emanate from the nodal point to the next time step and then obtain an average estimate of $\mathbf{u}$ in the entire cell at the next step.

Following the procedure outlined in Section 3.2, we arrive at the characteristic form given by Eq.(3.5) with the key difference that the wave speed C is now constant. That allows us to form the Riemann invariants R^1 and R^2.

$$R^{1,2} = v \pm C\gamma \tag{5.2}$$

When we write Eq.(3.5) in terms of these new characteristic variables we get the two very simple relations expressed as:

$$\frac{dR^{1,2}}{dt} = 0 \quad \text{when} \quad \frac{dx}{dt} = \mp C \tag{5.3}$$

Eq. (5.3) indicates that R^1 is constant along all lines with slope of $-C$ and R^2 is constant along all lines with slope of C. These are shown in Figure 5.1a and 5.1b respectively. The initial conditions imply that there is a jump in R^1 and R^2 at $x = 0$ that then propagates along the left and right going characteristics as indicated in the figure. In other words, the states on either side of the wave are constant but across the left-going characteristic, there is a jump ΔR^1 and the location of the jump moves to the left with speed $-C$. Correspondingly there is a jump ΔR^2 across the right going characteristic which moves to the right with a speed C. From the Figures 5.1a and 5.1b we see that each wave only affects one of the two characteristic variables. Putting these two together we get the result shown in Figure 5.2. Now, the Riemann invariants at any time step can be written in three sectors delineated by the two characteristic waves

$$R^{\alpha}(x,t) = R^{\alpha}\left(\frac{x}{t}\right) = \begin{cases} R^{\alpha L} & x < -Ct \\ R^{\alpha L} + \Delta R^{\alpha 1} = R^{\alpha R} - \Delta R^{\alpha 2} & -Ct < x < Ct \\ R^{\alpha R} & x > Ct \end{cases} \tag{5.4}$$

where $R^{\alpha L}$ and $R^{\alpha R}$ are known from the initial conditions. That system can now be transformed to a simpler form by writing it in terms of the original variable $\mathbf{u}$ instead of the Riemann invariants:

$$\mathbf{u}\left(\frac{x}{t}\right) = \begin{cases} \mathbf{u}^L & x < -Ct \\ \mathbf{u}^L + \mathbf{r}^1 \Delta R^1 = \mathbf{u}^R - \mathbf{r}^2 \Delta R^2 & -Ct < x < Ct \\ \mathbf{u}^R & x > Ct \end{cases} \tag{5.5}$$

where $\mathbf{r}^{\alpha}$ are the right eigenvectors of $\mathbf{A}$. The second line of Eq. (5.5) enforces continuity in the middle sector between the left and right going characteristics and shows that the initial jump in $\mathbf{u}$ is a linear combination of the right eigenvectors of $\mathbf{A}$ and the jumps in the Riemann invariants across the characteristics:

$$\mathbf{u}^{R} - \mathbf{u}^{L} = \sum_{\alpha=1}^{2} \mathbf{r}^{\alpha} \Delta R^{\alpha} \tag{5.6}$$

For a given initial condition Eq. (5.6) can be solved to find ΔR^{α}, and then Eq. (5.5) provides the solution to the basic linear Riemann problem.

If the problem is nonlinear however, things are a bit more complicated. In the nonlinear problem considered in Eq. (3.4) for example, the wave speed is a function of the strain. In general, it may not be possible to obtain the Riemann invariants or variables. When there are more than two equations involved in the quasi-linear partial differential equation, it may not be possible to find Riemann variables at all (Whitham, 1974). In such cases, the strategy commonly used is to break the problem up and examine locally linearized approximations. If we do this we can continue to use the results from the linear case which indicates that the jump in $\mathbf{u}$ is a linear combination of the right eigenvectors of $\mathbf{A}$. Making the assumption of a linear approximation to the actual solution at each time step we can use the result given in Eq. (5.6). Replacing ΔR^{α} with q^{α} to emphasize that we are no longer dealing with the characteristic variable we can write

$$\mathbf{u}^{R} - \mathbf{u}^{L} = \sum_{\alpha=1}^{2} \mathbf{r}^{\alpha} q^{\alpha} \tag{5.7}$$

The continuity relation above allows us to solve for q^{α}. We then have the solution to the local linearized problem.

$$\mathbf{u}\left(\frac{x}{t}\right) = \begin{cases} \mathbf{u}^{L} & x < -Ct \\ \mathbf{u}^{L} + \mathbf{r}^{1} q^{1} = \mathbf{u}^{R} - \mathbf{r}^{2} q^{2} & -Ct < x < Ct \\ \mathbf{u}^{R} & x > Ct \end{cases} \tag{5.8}$$

The above solution procedure allows a jump in $\mathbf{u}$ to be propagated along the characteristics to future time steps. The next question is to determine how the local linearized solution can be applied to spatially varying conditions; this is accomplished by the Godunov method.

5.2.2 Godunov Method for General Quasilinear Systems of Equations

The Godunov method is a finite difference scheme for solving partial differential equations. The first step is to discretize the spatial and temporal domain to define a control volume.

$$I_i = \left[x_{i-\frac{1}{2}}, x_{i+\frac{1}{2}} \right] \tag{5.9}$$

$$V \equiv I_i \times \left[t^n, t^{n+1} \right] \tag{5.10}$$

The key idea in this method is to consider the vector $\mathbf{u}$ to be constant in each spatial interval and integrate or average the governing Eq. (3.4) over each cell, first with respect to space and then with respect to time:

$$\frac{d}{dt} \int_{x_{i-\frac{1}{2}}}^{x_{i+\frac{1}{2}}} \mathbf{u}(x,t)\, dx + \int_{x_{i-\frac{1}{2}}}^{x_{i+\frac{1}{2}}} \mathbf{A}\mathbf{u}_x(x,t)\, dx = \mathbf{0} \tag{5.11}$$

$$\int_{x_{i-\frac{1}{2}}}^{x_{i+\frac{1}{2}}} \mathbf{u}\left(x,t^{n+1}\right) dx - \int_{x_{i-\frac{1}{2}}}^{x_{i+\frac{1}{2}}} \mathbf{u}\left(x,t^{n}\right) dx + \int_{t^n}^{t^{n+1}} \int_{x_{i-\frac{1}{2}}}^{x_{i+\frac{1}{2}}} \mathbf{A}\mathbf{u}_x(x,t)\, dx dt = \mathbf{0} \tag{5.12}$$

Next, the cell averages are defined as follows (note, all superscripts referring to the current time step have been suppressed):

$$\mathbf{U}_i^{n+1} = \frac{1}{\Delta x} \int_{x_{i-\frac{1}{2}}}^{x_{i+\frac{1}{2}}} \mathbf{u}\left(x,t^{n+1}\right) dx \tag{5.13}$$

$$\int_{t^n}^{t^{n+1}} \int_{x_{i-\frac{1}{2}}}^{x_{i+\frac{1}{2}}} \mathbf{A}\mathbf{u}_x\left(x,t\right) dx dt = \Delta t \int_{x_{i-\frac{1}{2}}}^{x_{i+\frac{1}{2}}} \mathbf{A}\mathbf{u}_x\left(x,t^{n+1}\right) dx \tag{5.14}$$

Calculation of these integrals over a single cell requires accounting for the fact that there will be two jumps in $\mathbf{u}$, one at the left going wave emanating from the right edge of the cell and the other at the right going wave emanating from the left edge of the cell; see Figure 5.3 for a graphical illustration. With the average value $\mathbf{U}$ being constant everywhere except at the jumps we can write:

$$\int_{x_{i-\frac{1}{2}}}^{x_{i+\frac{1}{2}}} \mathbf{A}\mathbf{u}_x\left(x,t^{n+1}\right) dx = \lambda^2_{i-\frac{1}{2}}\left(\mathbf{r}^2 q^2\right)_{i-\frac{1}{2}} + \lambda^1_{i+\frac{1}{2}}\left(\mathbf{r}^1 q^1\right)_{i+\frac{1}{2}} \tag{5.15}$$

where λ^α are the eigenvalues, $\mathbf{r}^\alpha$ are the right eigenvectors of $\mathbf{A}$, and q^α are given in Eq. (5.7). Substituting Eqs. (5.13) and (5.15) into Eq. (5.12) provides the equations necessary for determining the solution at the next time step:

$$\mathbf{U}_i^{n+1} = \mathbf{U}_i - \frac{\Delta t}{\Delta x}\left[\lambda^2_{i-\frac{1}{2}}\left(\mathbf{r}^2 q^2\right)_{i-\frac{1}{2}} + \lambda^1_{i+\frac{1}{2}}\left(\mathbf{r}^1 q^1\right)_{i+\frac{1}{2}}\right] \tag{5.16}$$

We solve this equation at each cell and then repeat at the next time step.

We consider velocity boundary conditions in all of our simulations. The simulation domain is extended to include one ghost node at either end x_0 and x_{N+1}. These ghost nodes allow us to treat the actual edge nodes the same way that we treat interior nodes. With a known velocity at x_1 we can solve for σ_0 using momentum balance and v_0 from continuity. Knowing the stress strain relation, we can use an implicit solver such as the Newton-Raphson method to find γ_0^n. A similar procedure can be followed for the opposite end.

$$\frac{\partial \sigma}{\partial x} = \rho\left(\frac{v_1^{n+1} - v_1^n}{\Delta t}\right) \approx \frac{\sigma_2 - \sigma_0}{2\Delta x} \tag{5.17}$$

$$\frac{\partial \gamma}{\partial t} = \frac{\partial v}{\partial x} \Rightarrow \frac{\gamma_1^{n+1} - \gamma_1^n}{\Delta t} \approx \frac{v_2^n - v_0^n}{2\Delta x} \tag{5.18}$$

At best, this method exhibits first order accuracy. We can expect even less accuracy depending on how nonlinear our relations are and if there are shocks. There are a variety of methods to extend this method to higher order accuracy. The corrections however can introduce nonphysical oscillations at jumps in the solution. These can be minimized by applying limiters. These techniques get quite sophisticated and have not been pursued to their full extent. However, the ideas presented here provided a satisfactory approximation of the solution to give a reasonable description of the dynamic behavior in our materials.

In order to extend Godunov's method to high resolution we must add the second order correction terms as shown below:

$$\mathbf{U}_i^{n+1} = \mathbf{U}_i - \frac{\Delta t}{\Delta x}\left[\lambda^2_{i-\frac{1}{2}}\left(\mathbf{r}^2 q^2\right)_{i-\frac{1}{2}} + \lambda^1_{i+\frac{1}{2}}\left(\mathbf{r}^1 q^1\right)_{i+\frac{1}{2}}\right] - \frac{\Delta t}{\Delta x}\left[\mathbf{F}_{i+\frac{1}{2}} - \mathbf{F}_{i-\frac{1}{2}}\right] \tag{5.19}$$

$$\mathbf{F}_{i\pm\frac{1}{2}} = \frac{1}{2}\sum_{p=1}^{2}\left|\lambda^p_{i\pm\frac{1}{2}}\right|\left(1-\frac{\Delta t}{\Delta x}\left|\lambda^p_{i\pm\frac{1}{2}}\right|\right)\lambda^p_{i\pm\frac{1}{2}}\left(\mathbf{r}^p q^p\right)_{i\pm\frac{1}{2}} \tag{5.20}$$

Without the correction terms, the solution exhibits smearing and apparent dissipation. These correction terms however, also introduce nonphysical oscillations around discontinuities in the solution. These oscillations can be reduced by modifying $\mathbf{F}$ in Eq. (5.20) through the use of a limiter function $\phi(\theta)$

$$\mathbf{F}_{i\pm\frac{1}{2}} = \frac{1}{2}\sum_{p=1}^{2}\left|\lambda^p_{i\pm\frac{1}{2}}\right|\left(1-\frac{\Delta t}{\Delta x}\left|\lambda^p_{i\pm\frac{1}{2}}\right|\right)\lambda^p_{i\pm\frac{1}{2}}\left(\mathbf{r}^p q^p\right)_{i\pm\frac{1}{2}}\phi\left(\theta^p_{i\pm\frac{1}{2}}\right) \tag{5.21}$$

where θ is a ratio found by comparing the jump in $\mathbf{U}$ across one wave in the current cell with the jump in $\mathbf{U}$ across the same direction wave in the neighboring cell looking in the upwind direction. For example, at node $i+\frac{1}{2}$:

$$\theta^p_{i+\frac{1}{2}} = \frac{\left(\mathbf{r}^p q^p\right)_I \cdot \left(\mathbf{r}^p q^p\right)_{i+\frac{1}{2}}}{\left(\mathbf{r}^p q^p\right)_{i+\frac{1}{2}} \cdot \left(\mathbf{r}^p q^p\right)_{i+\frac{1}{2}}} \quad with \quad I = \begin{cases} i-\frac{1}{2} & \lambda^p_{i+\frac{1}{2}} > 0 \\ i+\frac{3}{2} & \lambda^p_{i+\frac{1}{2}} < 0 \end{cases} \tag{5.22}$$

There are a number of choices for the limiter function (LeVeque 1997). Two common choices are minmod and monotonized-centered:

$$\phi(\theta) = \max\left[0, \min\left(1, \theta\right)\right] \tag{5.23}$$

$$\phi(\theta) = \max\left[0, \min\left(\frac{1+\theta}{2}, 2, 2\theta\right)\right] \tag{5.24}$$

In the next section we will simulate several benchmark initial and boundary value problems which highlight the gains achieved by moving from the method of characteristics to the finite volume method.

5.2.3 Comparison of Method of Characteristics and Finite Volume Method

The purpose of developing the finite volume solution method for this problem is to account properly for shocks in a relatively straight forward manner. With the procedure outlined above, the next step is to compare solutions using the method of characteristics (MC) and the finite volume method (FVM) for several example problems. We begin with several initial value problems, and then we move to the boundary value problem representing the dynamic tension test.

For the initial value problems, the goal is to simulate a one dimensional strip of infinite length. The constitutive model imposed is based on the quasistatic behavior of polyisoprene. Knowles (2002) suggested that the quasistatic stress strain response could be approximated by a cubic polynomial for ease of calculations. Niemczura and Ravi-Chandar (2011a) found indeed that the experimentally measured quasi-static stress-strain response for the polyisoprene could be approximated by a cubic relation of the form:

$$\sigma(\gamma) = E\left(a_3\gamma^3 + a_2\gamma^2 + \gamma\right) \tag{5.25}$$

with $a_3 = 0.0491$, $a_2 = -0.350$, and $E = 1.15$ MPa. The main feature of this cubic equation is that it captures the critical features of an inflection point in the stress strain curve that occurs at a strain $\gamma_c = 2.38$, and yet allows for easy calculations. We note that this model does not account for the hysteresis observed during unloading of the actual

material; therefore, any unloading shown in the following simulations is not truly representing the physical behavior of polyisoprene. Unless otherwise noted, all FVM solutions use the monotonized-centered limiter function.

We start the comparisons with an initial value problem with a step jump in strain at the center of the specimen. The left half is unloaded and the right half has a constant strain of 2, which is below the strain γ_c of 2.38. The evolution of the strains computed by the MC and the FVM are shown in Figure 5.4. Strain profiles are plotted every 300μs. The initial state of a step jump in strain is clearly visible but immediately there is a deviation in the two solutions. As the left side is loaded and the right side unloads, there must be an intermediate value across which continuity is enforced; this is accomplished as indicated in Eq. (5.7). The two methods find slightly different values of strain in the middle segment of the specimen; the discrepancy between the two results is due to the fact that linear interpolation is used between nodes in the MC while the FVM takes proper account of the discrete jumps that occur between nodes.

Looking to the left half of the specimen, we can see that both methods predict very nearly the same strain profiles. As noted earlier, the Lagrangian wave speed is directly dependent on the tangent modulus; therefore, smaller strains propagate the fastest with larger strains following at a later time. This is clearly visible from the spreading of the strain pulse with time. Looking to the right side we note a very different strain profile. The right side of the specimen is unloading and again, the smaller strains propagate faster than the larger strains; however it is not physically possible for the material to reach the lower strain before first experiencing the higher strain and therefore an unloading shock forms. The shock is a jump in strain, stress, and velocity, and propagates with specific shock speed that depends on the magnitude of the jump. The magnitude of the jump and

the shock speed $\dot{s}$ can be found from the Rankine-Hugonoit conditions that represent the conservation of momentum and mass:

$$[\![\sigma(\gamma)]\!] = \rho \dot{s} [\![v]\!] \tag{5.26}$$

$$[\![v]\!] = \dot{s} [\![\gamma]\!] \tag{5.27}$$

Combining these two equations we can find $\dot{s}$ in terms of the jump in stress and strain:

$$\dot{s} = \sqrt{\frac{[\![\sigma(\gamma)]\!]}{\rho [\![\gamma]\!]}} \tag{5.28}$$

The jump in strain is constant and therefore a constant shock speed is expected. The slight difference in jumps in strain between the two methods translates to a less than 2% difference in shock speed, with the smaller jump from the MC predicting the slower speed. The FVM predicts a jump from a strain of 2 to a strain of 0.7446 which implies a shock speed of 21.98 m/s based on Eq.(5.28) which matches perfectly with the speed of the shock in the figure; this confirms that the FVM accomplishes the balance of mass and momentum correctly. The MC on the other hand shows a shock that propagates at a slightly faster speed and it is not quite as sharp of a jump as seen in the FV solution; the difference from the FVM is entirely due to the interpolation in the numerical implementation of the MC.

In the next simulation we consider the same step jump in the initial strain distribution, but this time with a jump to a strain level of 6, well above the inflection point. This will allow us to probe the behavior in the concave region of the stress strain curve. The evolution of the strain profiles for the two solution methods are plotted in Figure 5.5. We see again that there is a strain level which is 'agreed' upon by the two sides – corresponding to equal traction and particle velocity – and this level propagates in both directions. There is a slight discrepancy in this level between the two solution methods; however, both methods indicate a value that is well above the inflection point.

This is important because the right hand side unloads along the concave region of the stress strain curve where the slope increases with strain; therefore the larger strains will travel faster than the slower strains. The result is the unloading fan observed on the right side of the figure instead of the unloading shocks seen in the previous simulation. The FVM exhibits small spikes in strain around the value which propagate in both directions. These are nonphysical and attributed to numerical errors.

On the other hand, the left portion of the specimen experiences both the concave and the convex portion of the stress strain curve. We see two distinct regions of the loading strain profiles; there is a lower strain region which propagates as expected from the previous simulation with the smallest strain traveling the fastest and larger strains following. Somewhere between a strain of 1.5 and 1.7 there is a jump in strain up to the middle value ~3.9. There are two points to note in these results: first note the large difference between the MC and the FV in the predicted shape of the strain profile in the transition between the fan and shock regions. The smooth transition from fan to shock is to be expected with MC due to the linear interpolation and becomes quite significant with large travel distances.

The second discrepancy between the two simulations is related again to the question of shock speed and which model accurately captures the correct speed of shock propagation. The FV shows a jump in strain from 1.53 to 3.90 which implies a constant shock speed of 19.12 m/s, exactly the shock speed observed by the FV solution. The MC solution predicts a higher shocks speed but beginning at a larger strain and ending at the same strain. That jump should have a slower shock speed, demonstrating again that the MC as implemented, does not properly capture the motion of the shock.

In the final two benchmark simulations we consider an initial distribution of strain following a hyperbolic tangent of the form $\gamma(x,0)=\gamma_0\left[1+\tanh(kx)\right]$. We will first

discuss the results with $\gamma_0 = 1$. The evolution of the strain profile is shown in Figure 5.6. The profiles show a similar behavior to that as the first simulation. A mid value of strain is agreed upon, and the left side loads to that mid value while the right side unloads to that value. That mid value is well below the inflection strain therefore we expect shocks only for the unloading portion (the right side). The loading portion follows the fan structure and the MC and FVM produce identical results. As expected, unloading side develops a shock; however, it takes some time because the initial strain distribution was not a shock. The lower strains must propagate further before they begin overtaking larger strains. Once the shock forms, the MC and FV solutions begin to differ slightly as expected.

Next, we look at the evolution of strain profiles with $\gamma_0 = 6$. The evolution of the strain profile is shown in Figure 5.7. In this case the mid value of strain is above the inflection point meaning the unloading all takes place in the concave portion of the stress strain curve and hence no unloading shocks will form on the right side. The loading on the left side must, however, follow a more complex path with both a fan region and a shock just as seen in the simulation with an initial condition of a step jump to a strain of 6 (see Figure 5.5). The hyperbolic tangent distribution however delays the formation of that shock because it takes some time for the faster traveling strain levels to overtake the lower levels. The simulations described above serve to highlight the benefit in the shock capturing ability of the FVM. We move now apply this method to the boundary value problem which simulates the dynamic tension test.

For the purpose of these comparisons we consider a 100 cm long one-dimensional strip specimen, with its right end $(x = L)$ fixed (corresponding to a clamped boundary) and a time-dependent velocity boundary condition $v(0,t) = V(t)$ applied at the left end $(x = 0)$. The applied velocity is then varied to explore the differences between the two

solution procedures. The material model will remain the cubic function approximating the quasistatic behavior of polyisoprene rubber given in Eq. (5.25) For the parameters given above, a shock is expected for a dynamic tension test with an impact speed over $v_c = 53$ m/s. As mentioned in Section 3.3, under high strain-rate loading conditions, the material did not follow the quasistatic response; nevertheless, this cubic model will be used here for the purpose of demonstrating the ability of the FVM to capture the onset of shocks accurately.

We begin by looking at the simulations corresponding to an imposed velocity of $v(0,t) = V(t) = 50H(t)$ m/s. The variation of the nominal strain as a function of position along the specimen, determined through both solution methods, is shown in Figure 5.8 at 100 μs time increments; the corresponding variation of the particle velocity is shown in Figure 5.9. As expected the results from the two solution methods are nearly identical. When step velocity is applied, there is a sharp jump in the particle velocity and strain in the specimen. As the wave propagates into the specimen, the wave spreads due to the varying wave speed of the material at different strains. Since the strains in the specimen are below the inflection point in the stress-strain curve, the wave speed decreases monotonically with strain. As a result the larger strains propagate more slowly, with the largest strain amplitudes propagating at approximately half the speed of the smallest strain amplitudes; this effect is seen clearly in Figures 5.8 and 5.9. The spreading of the strain profiles implies that the strain rate decreases as the strain pulse propagates into the specimen. While the strain and velocity profiles are very similar in the two simulations, note that the FVM solution maintains the sharp gradient at the wave front whereas the MC progressively smooths this transition; this is a result of the interpolation at the points each x_+ and x_- indicated in Section 3.2.1.

The contrast between the two methods is even more apparent at higher impact speeds, when shocks form. Next, we consider the simulations corresponding to an imposed velocity of $v(0,t) = V(t) = 100H(t)$ m/s; for this case, the maximum strain is far above the inflection point, and therefore the wave speed of the highest strains is greater than that of the lower strains. Though the higher strains have a faster wave speed, it is not physically possible for the material to reach the higher strain before first experiencing the lower strain and therefore a shock forms. Figures 5.10 and 5.11 show the strain and velocity profiles obtained with the two solution methods for the 100 m/s step input. As expected, the MC does not capture the sharp jump of the shock and as time progresses more and more smoothing occurs. The FVM however captures the sharp nature of the shock as well as the constant propagation speed. There is also a difference in the peak strain achieved in each simulation with the MC predicting a lower value, likely because of the smoothing resulting from the interpolation.

5.2.4 Shocks in Experiments

Niemczura and Ravi-Chandar, (2011) impacted rubber specimens at speeds as high as 65 m/s which, as the previous section demonstrated should have produced tensile shocks if the polyisoprene rubber was truly rate independent. Instead they found that at high rates, polyisoprene rubber does not follow the quasistatic stress strain behavior but that a power law Eq. (5.29) was able to capture the response with $\mu = 0.93$ MPa and $n = 0.6$:

$$\sigma = \mu\gamma^n \tag{5.29}$$

and that no shocks were formed in initially unstretched rubber specimens. These results pose an interesting question with regard to tensile shocks in rubber. Since there is no

inflection point in a power law, is it ever possible to produce shocks in rubber? It seems unlikely that the secondary stiffening seen in quasistatic stretching of rubber would be completely eliminated at high rates. We now explore the regions of higher stretch by means of faster impact speeds. The experimental setup described in Section 4.3 is based on the work of Niemczura et al. (2011) but allows for higher impact speeds. Maximum speeds upward of 100 m/s have been recorded with this new setup. This has allowed exploration of the higher strain and strain rate regime. The results of these tests are described below.

There are unique challenges when using this setup at its highest pressures with a material as soft as rubber. The primary challenge is that the air expelled from the air-gun itself can affect the motion of the specimen, pushing it out of the frame of the camera. Despite this, it is still possible to construct a $y-t$ diagram with the portion that remains in frame. Particle motion can then be traced, and the stretch and velocity histories can be calculated. The rubber specimen is bonded to the slider and the first two lines are marked on the bonded portion of the specimen so that these lines can be used to measure the imposed velocity. There is also some wobbling of the slider just as seen in the polyurea tests described in Section 3.3 which causes some perturbation in the applied velocity. A few successful tests were performed on polyisoprene rubber specimens with an impact speed in the range of 90 m/s to 100 m/s[15]. The $y-t$ diagram is shown in Figure 5.12 demonstrating these phenomena.

The position with respect to time of the midpoint of each line, beginning with the second line, (the last bonded portion of the specimen) is tracked as indicated by the white circles, and stretch and velocity histories are calculated. The time variation of the particle

[15] A video file of this test is included as Supplementary Material in the DVD.

velocity at different material points is shown in Figure 5.13 by the blue lines; the left most line can be taken as the imposed velocity boundary condition. This line indicates that the imposed velocity is not a step change in time, but rather a sharp increase in velocity to about 100 m/s, followed by a decay to about 70 m/s over the next 200 μs. This drop in velocity has two possible sources. First, the rubber specimen provides a resistance that should decelerate the slider. A quick estimate of the force necessary to slow the polycarbonate slider from 100 m/s to 60 m/s in 250 μs suggests that the rubber specimen should support an engineering stress on the order of 1 GPa, which is unrealistic. Second, and the more likely cause of the deceleration, is the wobbling of the slider within the guiding slot shortly after impact causing frictional resistance and the initial sharp decrease in the projectile velocity. After this initial drop the velocity likely remains nearly constant with negligible frictional forces and only minimal resistance provided by the rubber. The corresponding time variation of the stretch at the different material points in the specimen is shown in Figure 5.14. The stretch histories for the first two lines (2.2 and 4.4 mm from the impact point) show a sharp jump to a stretch of 4.5 and then a plateau. However, the stretch histories of the next six lines show a sharp jump and plateau to a smaller stretch, in the range of 3 – 3.5. This behavior suggests that a shock wave may have formed initially but propagated only over a short distance into the specimen before the unloading waves (as indicated by the drop in the velocity of the projectile) propagated faster than the shock and diminished the strain levels so as to dissipate the shock; therefore, we have not been able to obtain propagating tensile shocks in initially unstretched material.

5.3 FINITE VOLUME METHOD FOR AXISYMMETRIC MEMBRANE DEFORMATION

5.3.1 Godunov Method for General Quasilinear Systems of Equation with a Source Term

The primary change that must be incorporated in the FVM from the previous section to adapt it to the solution of axisymmetric deformation of a membrane is the need to take into account the addition of a source term to Eq. (5.11). This modification is wholly contained in the development of the Godunov method. Before we describe this minor adjustment, we review the key findings from solution of the linearized Riemann problem which, will still apply in this case.

Making the assumption of a linear approximation to the actual solution at each time step we can use the result given in Eq. (5.6). Replacing ΔR^{α} with q^{α} to emphasize that we are no longer dealing with the characteristic variable and making note that for the case of the membrane there will be four waves, we can write

$$\mathbf{u}^R - \mathbf{u}^L = \sum_{\alpha=1}^{4} \mathbf{r}^{\alpha} q^{\alpha} \tag{5.30}$$

The continuity relation above allows us to solve for q^{α}. We then have the solution to the local linearized problem.

$$\mathbf{u}\left(\frac{\eta_0}{\xi}\right) = \begin{cases} \mathbf{u}^L = \mathbf{u}^R - \mathbf{r}^1 q^1 - \mathbf{r}^2 q^2 - \mathbf{r}^3 q^3 - \mathbf{r}^4 q^4 & x < -C^3\xi \\ \mathbf{u}^L + \mathbf{r}^3 q^3 = \mathbf{u}^R - \mathbf{r}^1 q^1 - \mathbf{r}^2 q^2 - \mathbf{r}^4 q^4 & -C^3\xi < x < C^1\xi \\ \mathbf{u}^L + \mathbf{r}^1 q^1 + \mathbf{r}^3 q^3 = \mathbf{u}^R - \mathbf{r}^2 q^2 - \mathbf{r}^4 q^4 & -C^1\xi < x < C^2\xi \\ \mathbf{u}^L + \mathbf{r}^1 q^1 + \mathbf{r}^2 q^2 + \mathbf{r}^3 q^3 = \mathbf{u}^R - \mathbf{r}^4 q^4 & -C^2\xi < x < C^4\xi \\ \mathbf{u}^L + \mathbf{r}^1 q^1 + \mathbf{r}^2 q^2 + \mathbf{r}^3 q^3 + \mathbf{r}^4 q^4 = \mathbf{u}^R & x > C^4\xi \end{cases} \tag{5.31}$$

Note, C^3 and C^4 refer to the faster moving axial waves and C^1 and C^2 are the slower kink waves. The above solution procedure allows a jump in $\mathbf{u}$ to be propagated along the characteristics to future time steps. The next question is to determine how the local linearized solution can be applied to spatially varying conditions; this is accomplished by the Godunov method.

As mentioned, we now must incorporate a source term. The governing equation, expressed in vector form was given in Eq. (4.14). We must first discretize the nondimensionalized spatial and temporal domain into finite volume cells. A cell can then be defined by the following two relations.

$$I_i = \left[\eta_{0_{i-\frac{1}{2}}}, \eta_{0_{i+\frac{1}{2}}} \right] \tag{5.32}$$

$$V \equiv I_i \times \left[\xi^n, \xi^{n+1} \right] \tag{5.33}$$

The key idea in this method is to consider the vector $\mathbf{u}$ to be constant in each spatial interval and use the governing Eq. (4.14) integrated or averaged over each cell, first with respect to space and then with respect to time:

$$\frac{d}{d\xi} \int_{\eta_{0_{i-\frac{1}{2}}}}^{\eta_{0_{i+\frac{1}{2}}}} \mathbf{u}(\eta_0, \xi)\, d\eta_0 + \int_{\eta_{0_{i-\frac{1}{2}}}}^{\eta_{0_{i+\frac{1}{2}}}} \mathbf{A}\mathbf{u}_{\eta_0}(\eta_0, \xi)\, d\eta_0 + \int_{\eta_{0_{i+\frac{1}{2}}}}^{\eta_{0_{i+\frac{1}{2}}}} \mathbf{b}(\eta_0, \xi)\, d\eta_0 = 0 \tag{5.34}$$

$$\int_{\eta_{0_{i-\frac{1}{2}}}}^{\eta_{0_{i+\frac{1}{2}}}} \mathbf{u}(\eta_0, \xi^{n+1})\, d\eta_0 - \int_{\eta_{0_{i-\frac{1}{2}}}}^{\eta_{0_{i+\frac{1}{2}}}} \mathbf{u}(\eta_0, \xi^{n})\, d\eta_0 + \int_{\xi^n}^{\xi^{n+1}} \int_{\eta_{0_{i-\frac{1}{2}}}}^{\eta_{0_{i+\frac{1}{2}}}} \mathbf{A}\mathbf{u}_{\eta_0}(\eta_0, \xi)\, d\eta_0 + \int_{\xi^n}^{\xi^{n+1}} \int_{\eta_{0_{i-\frac{1}{2}}}}^{\eta_{0_{i+\frac{1}{2}}}} \mathbf{b}(\eta_0, \xi)\, d\eta_0 = 0 \tag{5.35}$$

Now we approximate the solution by defining cell averages just as described in the previous chapter with the addition of a cell average of the source term which is given below in Eq. (5.36). The remainder of the procedure is the same as described in Sec. 5.2.3 and results in Eq. (5.37). Note that all superscripts referring to the current time step have been suppressed.

$$\mathbf{B}_i = \frac{1}{\Delta\eta_0 \Delta\xi} \int_{\xi^n}^{\xi^{n+1}} \int_{\eta_{0_{i-\frac{1}{2}}}}^{\eta_{0_{i+\frac{1}{2}}}} \mathbf{b}(\eta_0, \xi)\, d\eta_0 \tag{5.36}$$

$$\mathbf{U}_i^{n+1} = \mathbf{U}_i - \frac{\Delta\xi}{\Delta\eta_0} \left[\lambda^1_{i-\frac{1}{2}} \left(\mathbf{r}^1 q^1 \right)_{i-\frac{1}{2}} + \lambda^3_{i-\frac{1}{2}} \left(\mathbf{r}^3 q^3 \right)_{i-\frac{1}{2}} + \lambda^2_{i+\frac{1}{2}} \left(\mathbf{r}^2 q^2 \right)_{i+\frac{1}{2}} + \lambda^4_{i+\frac{1}{2}} \left(\mathbf{r}^4 q^4 \right)_{i+\frac{1}{2}} \right] - \mathbf{B}_i \Delta\xi \tag{5.37}$$

It is worth remembering that as shown, this method is at best first order accurate. Depending on how nonlinear our relations are and if there are shocks, we can expect less accuracy. The presence of the source term and the fact that we deal with four equations instead of just two as in the 1D case suggests that this problem has the potential to be highly nonlinear and therefore obtaining accurate solution could prove challenging.

As before, there are corrections to extend this method to higher order accuracy. In this case there are two additional terms; the first correction term, Eq. (5.38), is similar to that introduced in Section 4.6.3 and the second correction term accounts for inclusion of a source term in the formulation and is defined in Eq. (5.39). The complete form is given in equation Eq. (5.40), where the limiter function has already been included. We have found the monotonized centered function produced problems with numerical instabilities; therefore, the minmod function was used exclusively.

$$\tilde{\mathbf{F}}_{i+\frac{1}{2}} = \frac{1}{2}\sum_{p=1}^{4}\left|\lambda^{p}_{i+\frac{1}{2}}\right|\left(1-\frac{\Delta\tau}{\Delta\eta_0}\left|\lambda^{p}_{i+\frac{1}{2}}\right|\right)\lambda^{p}_{i+\frac{1}{2}}\left(\mathbf{r}^{p}q^{p}\right)_{i+\frac{1}{2}}\phi\left(\theta^{p}_{i+\frac{1}{2}}\right) \tag{5.38}$$

$$\tilde{\mathbf{G}}_{i+\frac{1}{2}} = \frac{1}{2}\sum_{p=1}^{4}\lambda^{p}_{i+\frac{1}{2}}\left(\mathbf{r}^{p}q^{p}\right)_{i+\frac{1}{2}}\phi\left(\theta^{p}_{i+\frac{1}{2}}\right) \tag{5.39}$$

The form of Eq.(5.37) with the correction fluxes included is given below, where $\frac{\partial \mathbf{b}_i}{\partial \mathbf{u}}$ is the Jacobian of $\mathbf{b}$ evaluated at η_{0i}. The other terms are as defined in the previous chapter.

$$\begin{aligned}\mathbf{U}_i^{n+1} = \mathbf{U}_i - \frac{\Delta\xi}{\Delta\eta_0}\left[\lambda^{1}_{i-\frac{1}{2}}\left(\mathbf{r}^{1}q^{1}\right)_{i-\frac{1}{2}} + \lambda^{3}_{i-\frac{1}{2}}\left(\mathbf{r}^{3}q^{3}\right)_{i-\frac{1}{2}} + \lambda^{2}_{i+\frac{1}{2}}\left(\mathbf{r}^{2}q^{2}\right)_{i+\frac{1}{2}} + \lambda^{4}_{i+\frac{1}{2}}\left(\mathbf{r}^{4}q^{4}\right)_{i+\frac{1}{2}}\right] - \ldots \\ \ldots \mathbf{B}_i\Delta\xi - \frac{\Delta\xi}{\Delta\eta_0}\left[\tilde{\mathbf{F}}_{i+\frac{1}{2}} - \tilde{\mathbf{F}}_{i-\frac{1}{2}}\right] + \frac{\Delta\xi^2}{2\Delta\eta_0}\frac{\partial \mathbf{b}_i}{\partial \mathbf{u}}\left[\tilde{\mathbf{G}}_{i+\frac{1}{2}} + \tilde{\mathbf{G}}_{i-\frac{1}{2}}\right]\end{aligned} \tag{5.40}$$

As written, the above procedure cannot find $\mathbf{U}^{n+1}$ at the boundary nodes because information is required from an interface a half node outside of the physical space in either direction. We can eliminate this problem by using the balance law along with the

applied boundary conditions to extend our solution to one ghost nodes at either end η_{00} and η_{0N+1}. These nodes are illustrated in Figure 5.15 for clarity.

The boundaries in all of our membrane simulations will be that of an applied velocity. With nondimensionalized horizontal and vertical components of velocity at the first physical node (η_{01}) known at the current and all future time steps we can use Eqs. (5.41) and (5.42) to solve for u and v at the ghost node η_{00} for the current time step from the third and fourth rows of Eq. (4.14) as shown in Eq. (5.43) . Then using the change in u and v at η_{01} from the previous to current time step we can find x and y at the ghost node η_{00} for the current time step from the first and second rows of (4.14) as shown in (5.44).

$$\frac{\partial x_1}{\partial \xi} = \frac{x_1^{n+1} - x_1^n}{\Delta \xi} \tag{5.41}$$

$$\frac{\partial y_1}{\partial \xi} = \frac{y_1^{n+1} - y_1^n}{\Delta \xi} \tag{5.42}$$

$$\begin{Bmatrix} u_0 \\ v_0 \end{Bmatrix} = \begin{bmatrix} F + \frac{u^2}{\lambda_1} F_1 & \frac{uv}{\lambda_1} F_1 \\ \frac{uv}{\lambda_1} F_1 & F + \frac{v^2}{\lambda_1} F_1 \end{bmatrix}^{-1} \begin{Bmatrix} \left(F + \frac{u^2}{\lambda_1} F_1 \right) u + \left(\frac{uv}{\lambda_1} F_1 \right) v - b_x \Delta \eta_0 - \frac{\partial x_1}{\partial \xi} \Delta \eta_0 \\ \left(\frac{uv}{\lambda_1} F_1 \right) u + \left(F + \frac{v^2}{\lambda_1} F_1 \right) v - b_y \Delta \eta_0 - \frac{\partial y_1}{\partial \xi} \Delta \eta_0 \end{Bmatrix} \tag{5.43}$$

$$\begin{Bmatrix} x_0 \\ y_0 \end{Bmatrix} = \begin{Bmatrix} x_1 - \frac{\Delta \eta_0}{\Delta \xi} \left(u_1^n - u_1^{n-1} \right) \\ y_1 - \frac{\Delta \eta_0}{\Delta \xi} \left(v_1^n - v_1^{n-1} \right) \end{Bmatrix} \tag{5.44}$$

Note that all quantities on the right hand side of Eq.(5.43) are evaluated at η_{01}. A similar procedure can be followed for the other end. With $\mathbf{U}_0$ and $\mathbf{U}_{N+1}$ determined, all physical nodes can be treated as interior nodes and the solution procedure outlined above can be performed at each time step, providing a solution to the problem.

5.3.2 Comparison with Solution by Method of Characteristics

With a solution procedure developed that can handle shocks we now need to compare results between FVM and the MC. The best case with which to compare the results is simulation of the 160 m/s rubber impact when using the Q-LP model. As discussed in Sec. 4.5.1, that model provides a secondary stiffening which should lead to shocks.

The results of the MC and the FVM for this initial boundary value problem are plotted together for comparison. The calculated displacement profiles are essentially identical and are not shown. It is only in the derivative quantities that any notable difference is observed. The comparison of predicted meridional stretch and out of plane velocity profiles are plotted in Figure 5.16 and 5.17 respectively. The MC solutions in each of these figures are the same as those in Fig. 4.22 and 4.26. Looking to the stretch profiles, both solution methods show the development of a sharp change in stretch just behind the kink wave, from ~2.5 to 5. Whether or not this change is sharp enough to be considered a shock is unclear. The difference between the MC and the FVM is in the subtle difference in how the profile of this change evolves as it propagates from left to right. The MC shows a slight spreading whereas the FVM predicts consistent shape. The cost of resolving this shaper transition however is the addition of nonphysical numerical oscillations along the top of the profile. The profile of this change remains essentially constant as the kink wave propagates from left to right. The story is similar when looking at the comparison of the evolution of the velocity profiles. The MC shows a spreading of the sharp change whereas the FVM predicts a sharper transitions but adds nonphysical oscillations. Considering that the predicted displacement profiles are identical and that the jumps in derivative quantities are small there seems to be little reason to pay the significantly higher computational cost of the FVM while the MC provides a nearly

equivalent result without the problem of numerical oscillations. The choice of appropriate method will ultimately depend on what is required from the problem. In the case of this boundary initial value problem, without dramatic shocks, the MC provides satisfactory solution.

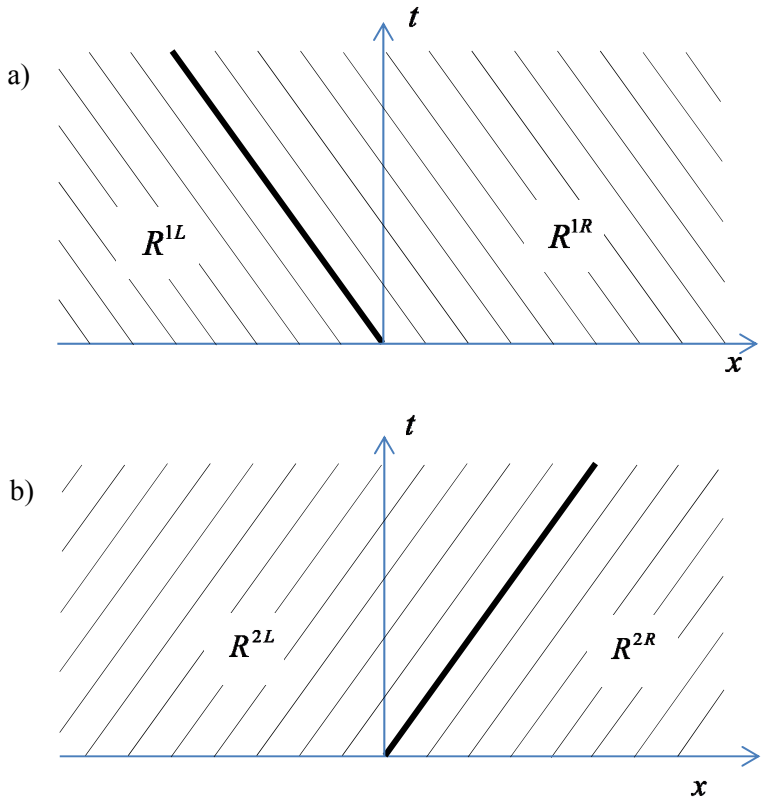

Figure 5.1: Illustrations showing the a) left going and b) right going characteristics. The characteristic over which the jump in the respective characteristic variable occurs is bold

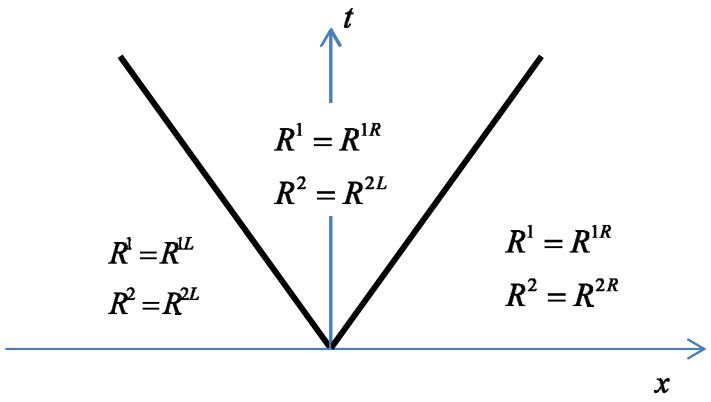

Figure 5.2: Illustration of the solution to the linear Riemann problem. Note the jump in one characteristic variable across each wave

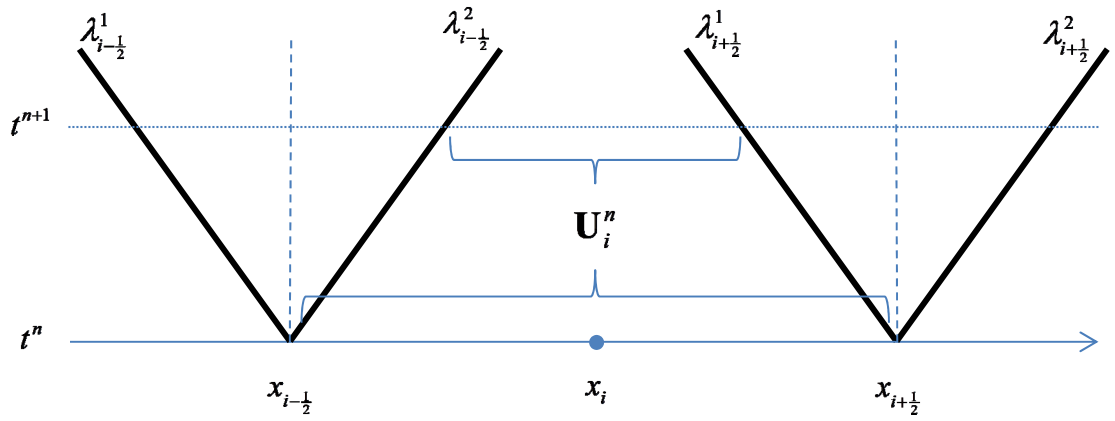

Figure 5.3: Illustration showing the left and right going waves propagating from the interfaces on either side of the cell i. At time t^{n+1} the original state $\mathbf{U}_i^n$ exists in only the central portion of the cell. To the left and right of this central region there is a jump in state across each wave.

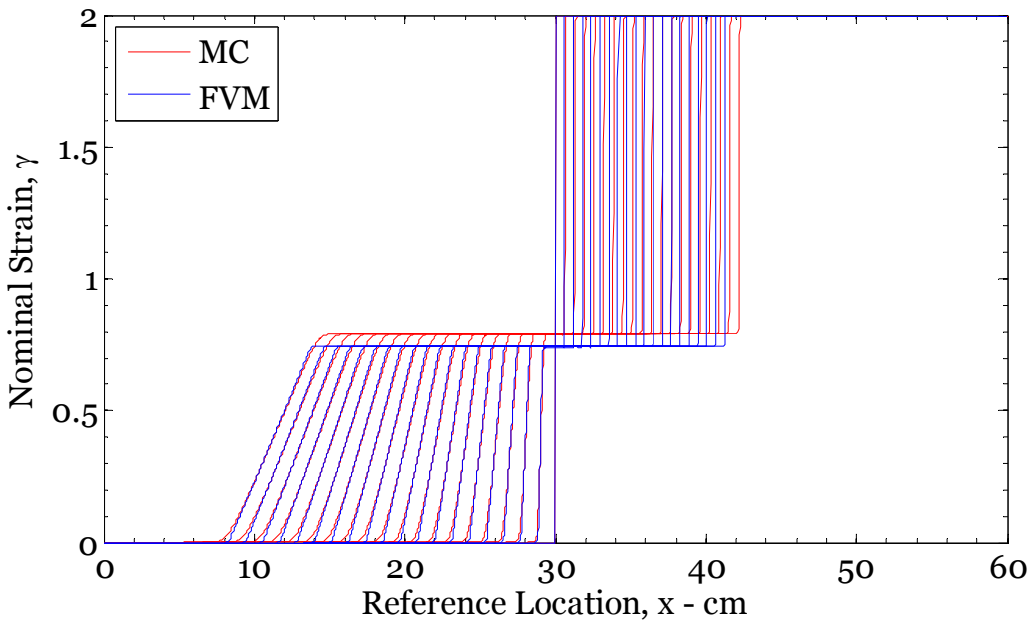

Figure 5.4: Comparison of strain profiles calculated by MC and FV every 300μs

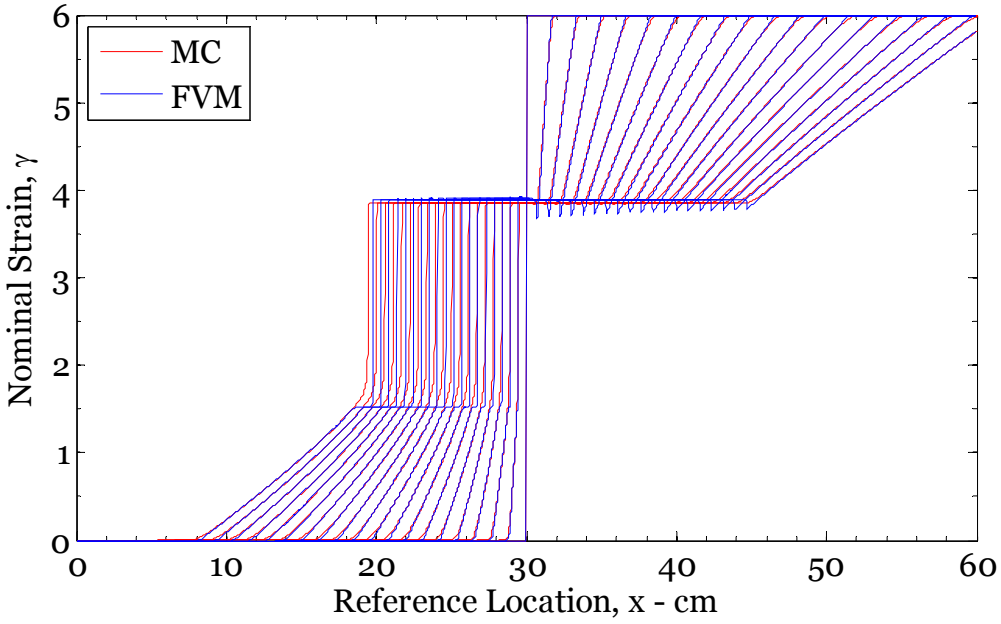

Figure 5.5: Comparison of strain profiles calculated by MC and FV every 300μs

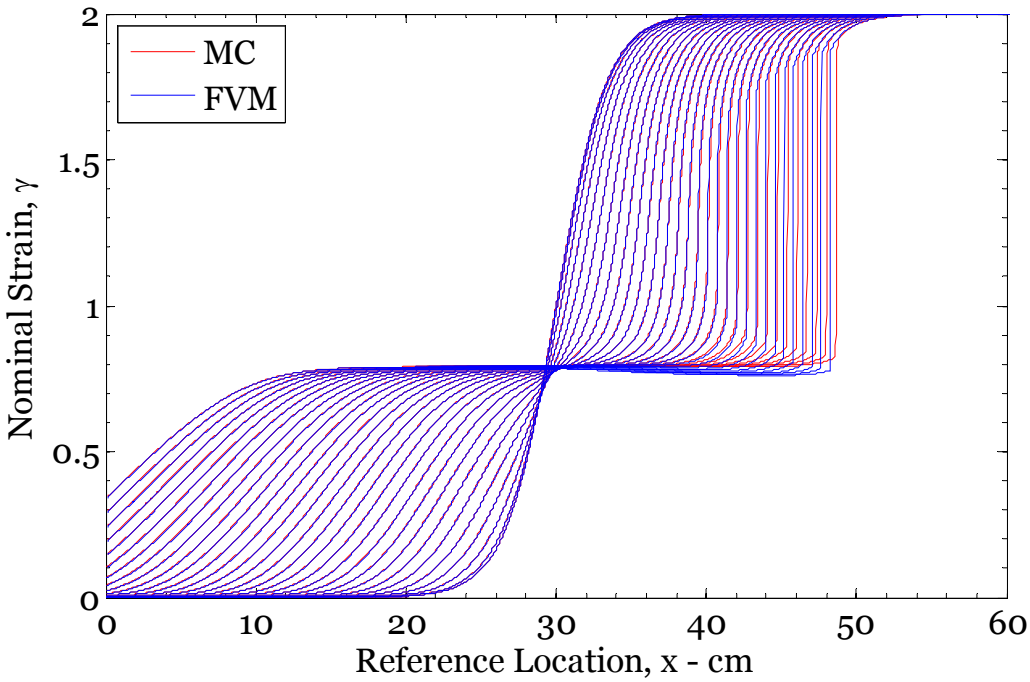

Figure 5.6: Comparison of strain profiles calculated by MC and FVM every 300μs

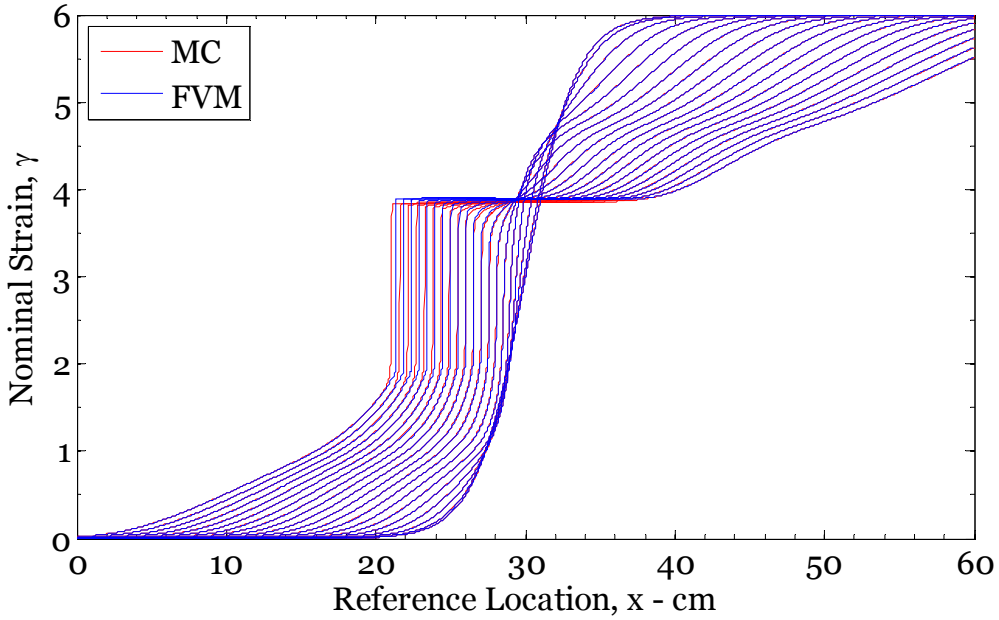

Figure 5.7: Comparison of strain profiles calculated by MC and FVM every 300μs

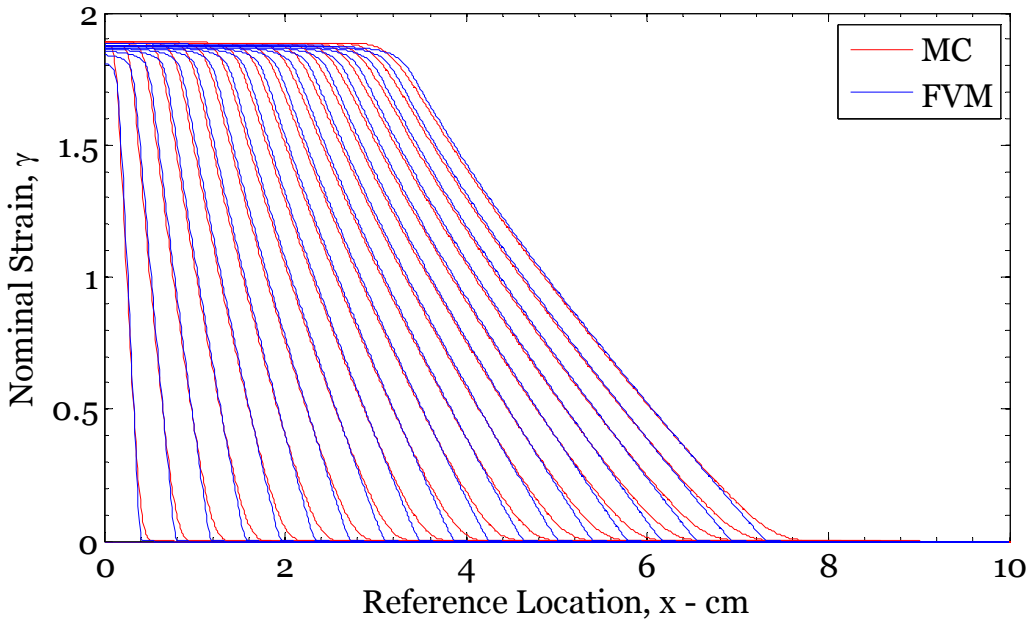

Figure 5.8: Comparison of strain profiles calculated by MC and FVM every 100μs

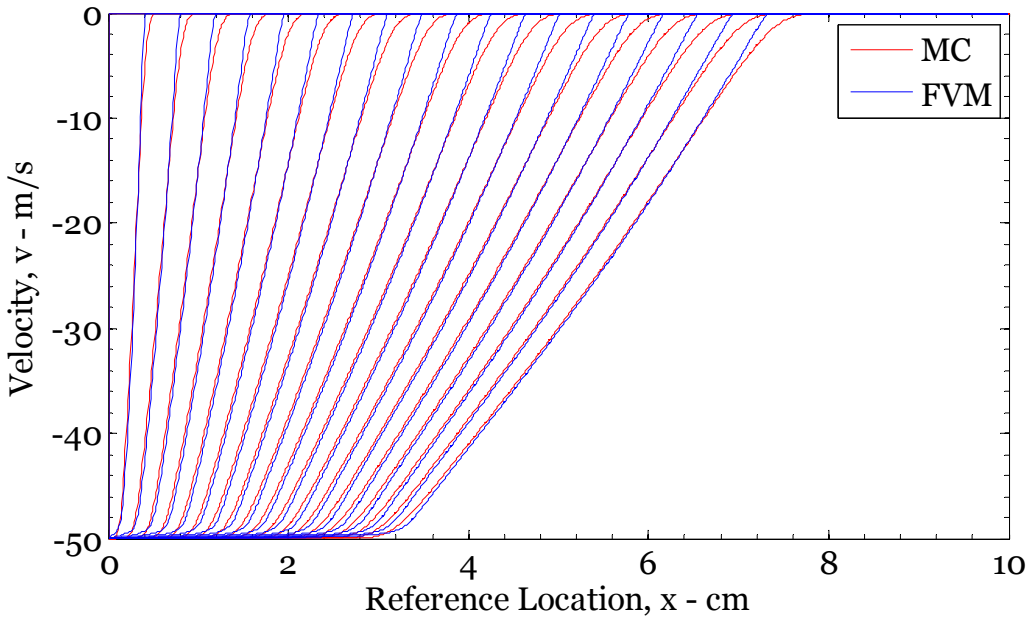

Figure 5.9: Comparison of velocity profiles calculated by MC and FVM every 100μs

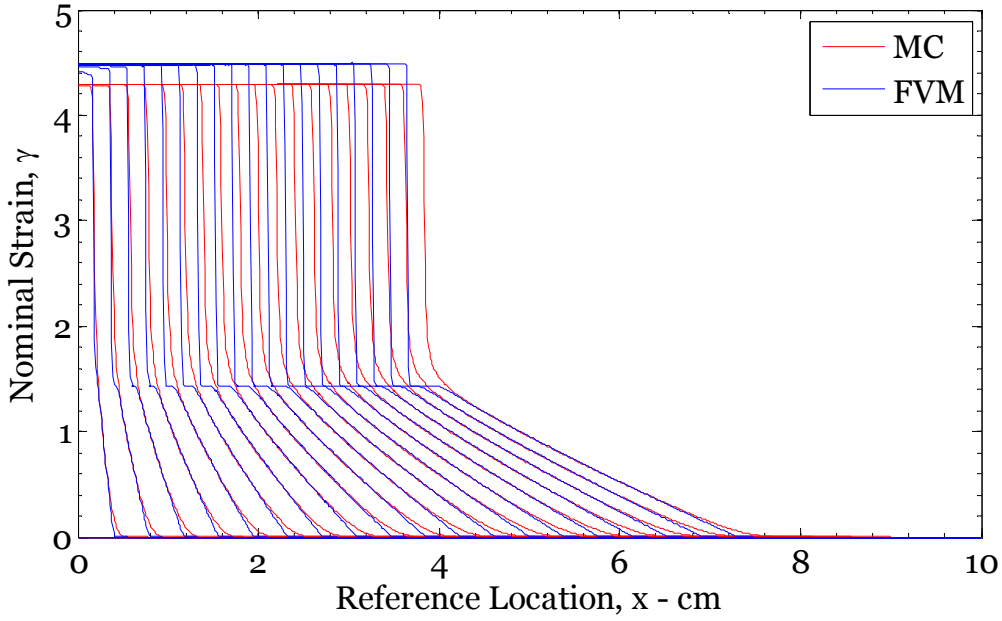

Figure 5.10: Comparison of strain profiles calculated by MC and FVM every 100μs

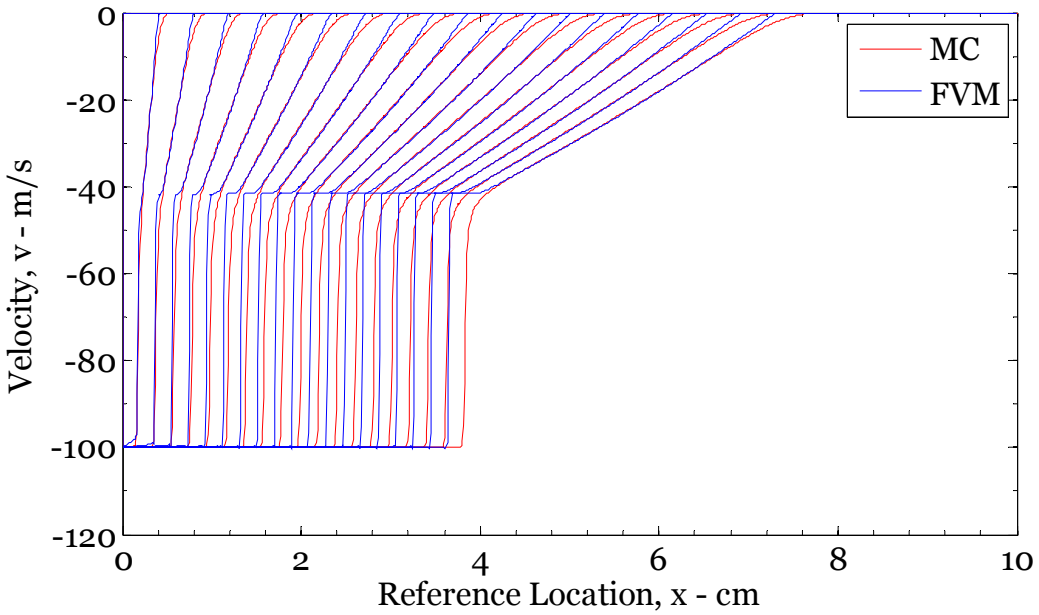

Figure 5.11: Comparison of velocity profiles calculated by MC and FVM every 100μs

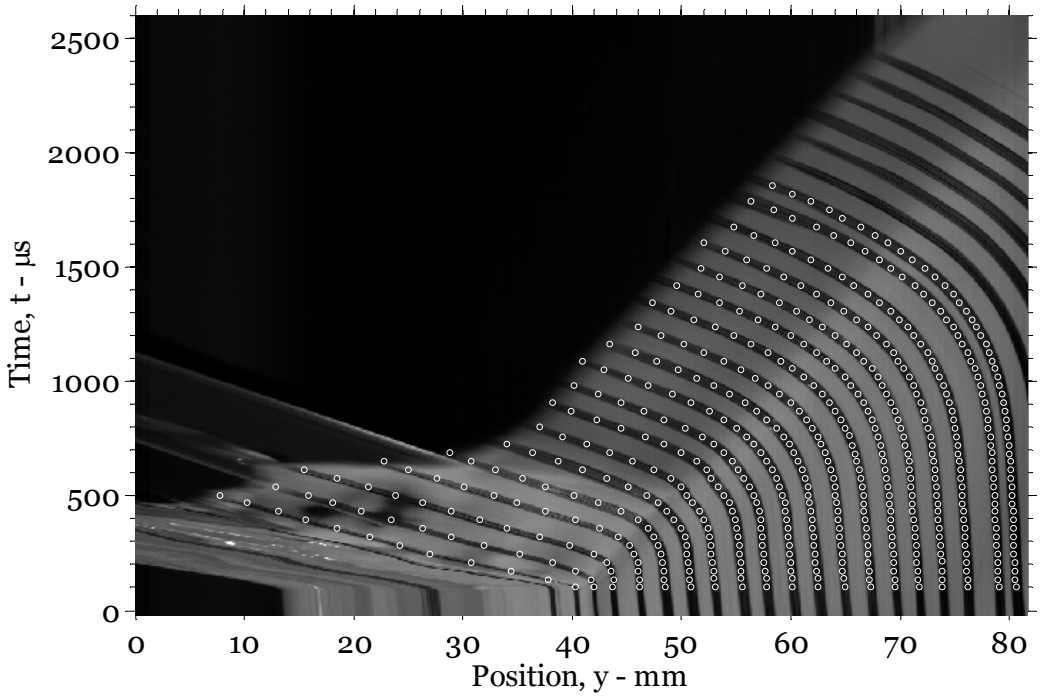

Figure 5.12: Particle trajectory diagram for polyisoprene test in laboratory frame. White circle demark material points used to calculate stretch and velocity profiles.

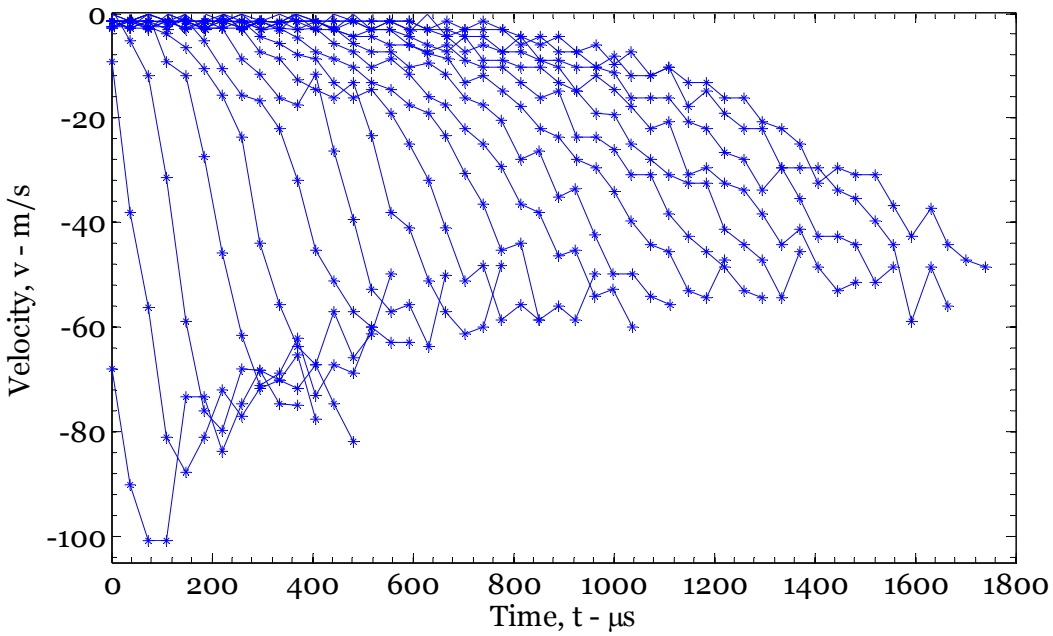

Figure 5.13: Velocity histories at material points spaced 2.2 mm apart

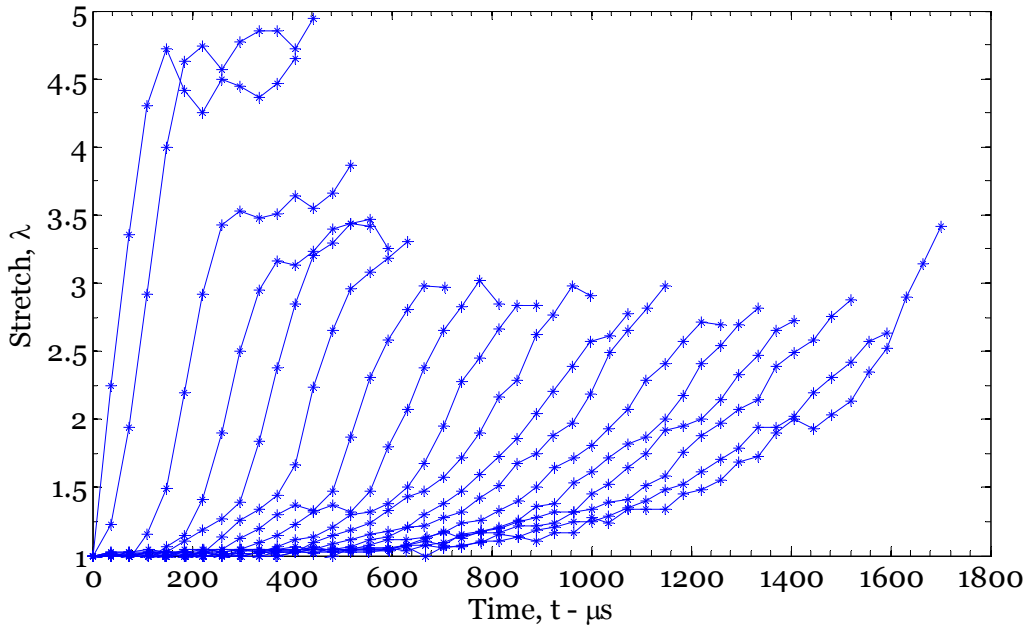

Figure 5.14: Stretch histories for material points spaced 2.2 mm apart.

Figure 5.15: Schematic illustrating the numbering extending the domain to one ghost node along either end of the simulation

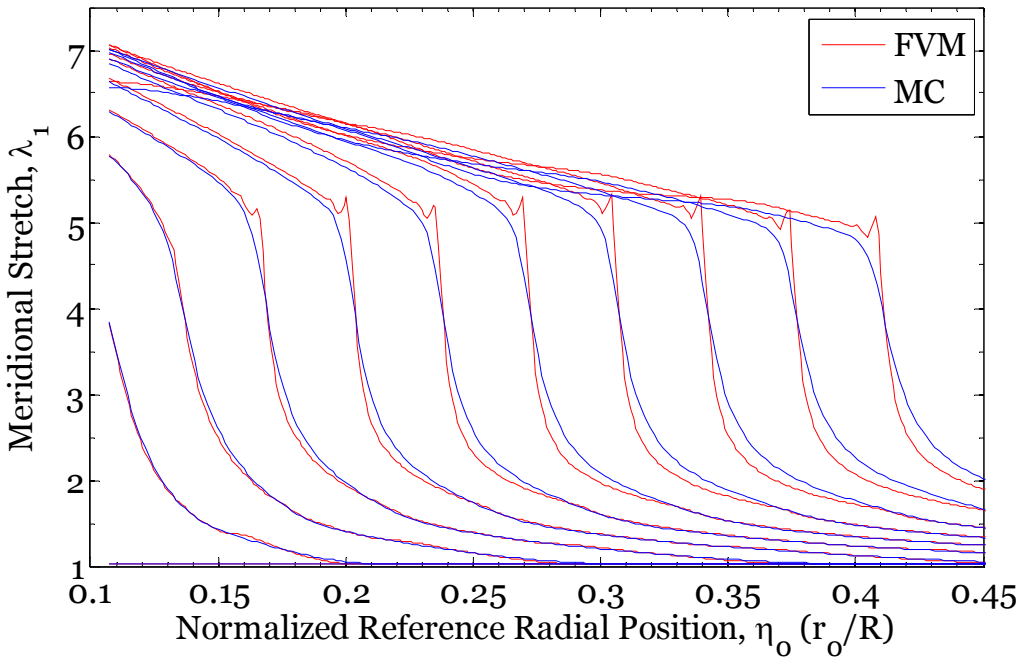

Figure 5.16: Comparison of meridional stretch profiles every 275 μs predicted by the Q-LP model using the MC (blue) and the FVM (red)

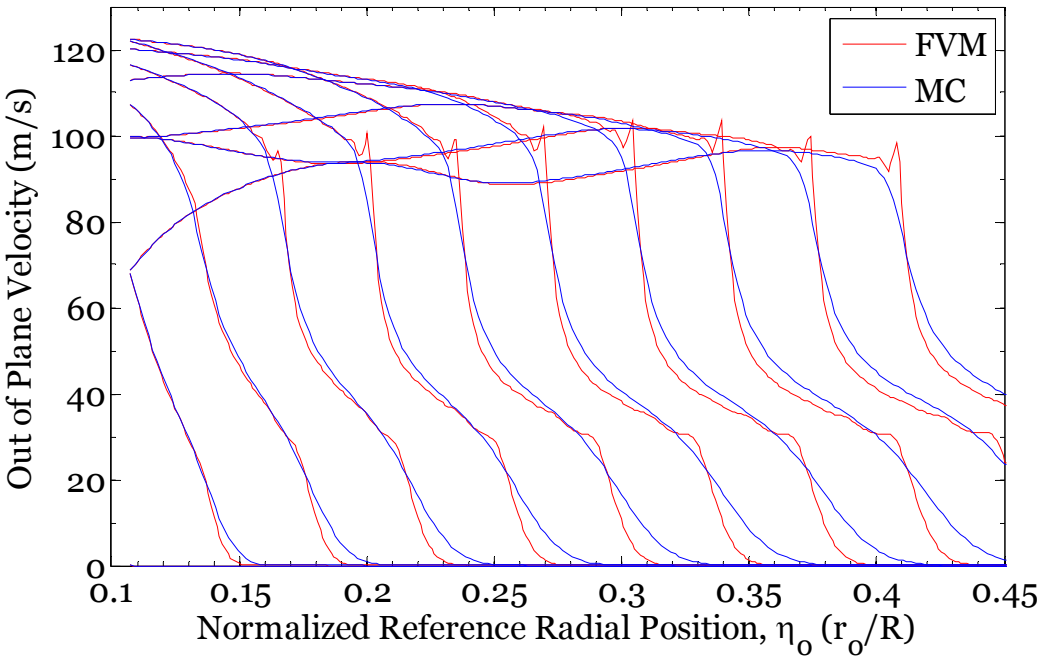

Figure 5.17: Comparison of out of plane velocity profiles every 275 μs predicted by the Q-LP model using the MC (blue) and the FVM (red)

Chapter 6: Conclusions

6.1 SUMMARY

In this report we have explored the various factors which must be considered when attempting to provide a quantitative understanding of the reasons for improved blast resistance of ductile metals coated with an elastomer. This was done through a combination of experimentation and simulation. We now present a summary of the results as well as a discussion of the remaining challenges and avenues by which they may be addressed.

The expanding ring and tube experiments shed light on exactly how the blast resistance of a metal is influenced by the addition of an elastomer coating. Importantly, one thing which is not affected is the localization strain of the metal. The localization strain in the Al-6061O remained essentially unchanged regardless of deformation rate or coating. Instead, the effect of the coatings was to add inertial resistance by adding mass as well as to provide additional load carrying capacity at deformations above which the Al-6061O has localized and can no longer carry load. This realization allowed for the creation of a basic design criterion highlighting the material properties that are truly important to consider when choosing the most effective coating material.

The modeling which produced that design criterion however lacked accurate characterization of the rate dependence of polyurea. The dynamic tension test was introduced as a means to quantify that behavior during high rate uniaxial stretching. By monitoring the nonlinear tensile wave propagation in polyurea specimens with the aid of high speed photography, it was possible to correlate observed particle motion with that predicted by simulations based on nonlinear wave propagation theory. Through these efforts we found the viscoplastic Zhou-Clifton model, with a slight modification, was the most effective choice for capturing the observed motion and hence we were able to

develop a model describing the dynamic tensile response of polyurea in the range of stretch rates between 800-8000 s^{-1}.

In the expanding tube experiments as well as actual blast protection applications however, the stress state in the coating is expected to be more complex than simple uniaxial tension. In an attempt to address this need for a more general model for the constitutive response of polyurea, the membrane test was developed. Similar to its 1D predecessor, the membrane test uses high speed photography to track particle motion which is then correlated with simulation results to determine the appropriate material model through an inverse process; only in this case the stress state is biaxial. The first stage in development of the membrane test pursued the 2D constitutive behavior of polyisoprene, an ostensibly less complex material than polyurea. The response was found to fall somewhere in between the quasi-static behavior and the rate saturated power law response introduced by Niemczura and Ravi-Chandar (2011). Tests were also performed on polyurea membranes but there are challenges, primarily with regard to specimen preparation, that must be addressed before insights can be expected.

Lastly, we introduced a new means by which to simulate the above experiments. Up to this point, the solution procedure was based on the method of characteristics. As discussed, the formation of shocks and their subsequent reflection and interaction poses a risk to the validity of solutions based on this method. A more robust finite volume method was introduced which is better suited to capture shock behavior in both the 1D dynamic tension and 2D dynamic membrane tests. As it turns out, comparison of the two methods demonstrated that for the majority of our experiments, in the absence of shock formation, the difference in results between these two methods was negligible. The highest speed dynamic tension tests on polyisoprene could be the exception but it appears that at these rates there are other complexities in the material response, possibly damage,

that are not captured by the rate independent model we have used up to this stage. Future testing at these highest rates will provide fertile ground for future progress. The inability to form obvious shocks in polyisoprene when the quasistatic response leads us to believe they should form certainly warrants further study. Similarly, the possibility of tensile shock formation in polyisoprene membranes encourages us to continue dynamic membrane testing at higher speeds. Lower speeds are also of interest too. The wrinkling phenomena observed at the kink wave and the idea that there is some threshold impact speed above which wrinkling will not occur has interesting implications and should be examined further. The 1D response of polyurea seems to be quantified well enough so as to provide a reasonable order of magnitude measure necessary for implementation in design criteria; though response at lower rates and higher stretch levels do warrant further study. The question of how this behavior varies with stress state still must also still be addressed. The challenge there is to prepare void free large samples which are thin enough to satisfy the membrane assumptions.

6.2 FUTURE WORK

While the expanding ring/tube experiments provide insight into the reasons a polymer coating can improve the blast performance of a ductile metal, the main focus of this report has been the introduction of methods for quantifying the high rate properties of the individual components of a blast protection system. With the individual behavior of the two constituents adequately captured, the next step is to provide full quantitative characterization of the response of the polymer metal system when subjected to loading scenarios expected during field application. Again, this is to be done through a combination of experimentation and subsequent correlation with simulations. We have

developed an experiment to reproduce such an environment in a laboratory setting by creating an underwater blast load which can be impinged on an uncoated or coated plate. Not only does this setup allow for analysis of stress states similar to those encountered in service, the same facility can be used to probe the dynamic adhesive behavior of the coating, a factor of crucial importance when determining system performance.

When current flows through a wire of some finite resistivity, electrical work is done. That electrical work causes Joule heating, increasing the temperature of the wire. If the heat cannot be dissipated, the temperature of the wire continues to rise. At some temperature the wire will melt, and if heating continues, eventually evaporate. This is exactly what happens in fuses that are designed to protect electrical equipment. If the rate of heating is increased the rate of phase change will increase. A very rapid change in phase results in a rapid expansion of the newly formed gas or in other words an explosion. When performed underwater, this explosion creates a shock wave with amplitudes and durations that are comparable to what is experienced in blast loading of structures.

We built a capacitor bank capable of delivering the energy necessary to produce wire explosion at one end of a water filled cylindrical tank. The blast load is then impinged on a specimen mounted at the other end of the tank. A schematic is shown in Figure 6.1. Real time strain measurements can be recorded on the outward facing surface of the specimen with the use of high speed photography and digital image correlation (DIC). These measurements will allow quantitative examination of the failure of bare metal and polymer coated metal specimens with the aim of examining dynamic strain localization under biaxial loading, ductile crack nucleation and tearing of metals and how these behaviors are affected by the coating.

Before these experiments can be correlated with simulations, the dynamic adhesive behavior of the coating must be quantified. To achieve this we consider the dynamic blister test, a high rate form of the standard quasi-static blister test. The quasi-static blister test provides a method for measuring interface toughness for bonding between a thin film and a stiff substrate. The substrate has a hole in it, allowing for a pressure loading to be applied at the interface. The pressure causes the film to bulge and debond in the shape of a circular blister. If the pressure applied is known, and the deflection of the blister is measured, the energy release rate can then be calculated by comparing the energy necessary to deform the film to that required to create the new free surfaces. The goal in the case of the dynamic blister test is to make a similar measurement during a high rate pressure loading rather than the static loading in the standard test. The high rate loading is created by the underwater wire explosion introduced above but instead of a thin metal sheet, the blast is impinged on a thick steel plate with a 1 in diameter hole in the center over which polymer has been applied. The growth and bulging of the blister is captured by high speed photography and with two cameras, strain measurements can be determined through DIC. If the material properties of the coating are known, correlation of the experimental results with those of the simulation allows us to characterize the rate-sensitivity of the interfacial toughness through an inverse approach by modeling the adhesion as a negative pressure applied over a region of the deforming membrane defined as the cohesive zone. While development work still remains for both of these experiments, preliminary work has already demonstrated the feasibility of the measurement techniques. (Albrecht et al. 2012)

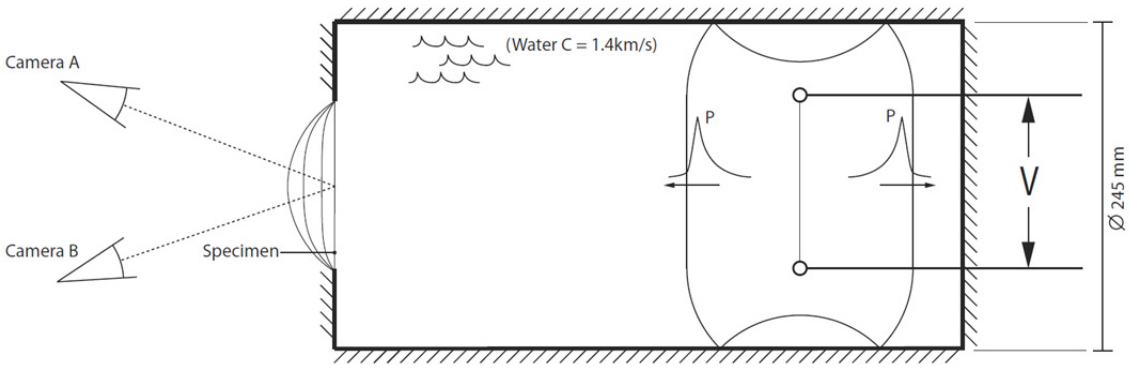

Figure 6.1: Schematic illustration of exploding wire experiment showing location of the exploding wire, the location of the pressure wave after a short time including reflections off the tank side walls, the position of the two cameras, and the general evolution of the shape of the coated/uncoated plate.

Bibliography

Albrecht AB, Liechti KM, Ravi-Chandar K, 2012, Development of a dynamic blast loading facility for characterization of dynamic response of metal-polymer bilayer specimens, Report of the Center for Mechanics of Solids, Structures and Materials.

Amini MR, Isaacs J, and Nemat-Nasser S, 2010, Investigation of Effect of Polyurea on Response of Steel Plates to Impulsive Loads in Direct Pressure-pulse Experiments, Mechanics of Materials, 42.6:628-39.

Amini MR, Simon J, and Nemat-Nasser S, 2010, Numerical Modeling of Effect of Polyurea on Response of Steel Plates to Impulsive Loads in Direct Pressure-pulse Experiments, Mechanics of Materials, 42.6:615-27.

Amirkhizi AV, Isaacs J, McGee J and Nemat-Nasser S, 2006, An experimentally-based viscoelastic constitutive model for polyurea, including pressure and temperature effects, Philosophical Magazine, 86:5847–5866.

Bale D S, LeVeque RJ, Mitran S, and Rossmanith JA, 2003, A Wave Propagation Method for Conservation Laws and Balance Laws with Spatially Varying Flux Functions, SIAM Journal on Scientific Computing, 24.3: 955.

Barsoum RGS, Dudt PJ, 2009, The fascinating behaviors of ordinary materials under dynamic conditions, The AMMTIAC Quarterly, 4:11-14.

Bergstrom JS, 1998, Constitutive Modeling of the Large Strain Time-dependent Behavior of Elastomers, Journal of the Mechanics and Physics of Solids, 46.5 : 931-54.

Bergstrom, JS, and Boyce MC, 2001, Constitutive Modeling of the Time-dependent and Cyclic Loading of Elastomers and Application to Soft Biological Tissues, Mechanics of Materials, 33: 523-30.

Bless S, Chen T, 2010, Impact damage in layered glass, International Journal of Fracture, 162, 151-158.

Chakkarapani V, Ravi-Chandar K, Liechti KM, 2006, Characterization of multiaxial constitutive properties of rubbery elastomers, Journal of Engineering Materials and Technology, Transactions of the ASME, 128:489-494.

Clifton, R. J. 1972, Plastic Waves - Theory and Experiment, Mechanics Today, 1:102-67.

Cristescu, N. 1967, Dynamic Plasticity. Amsterdam: North-Holland Pub.

Farrar CL, 1984, Impact Response of a Circular Membrane Experimental Mechanics, 24.2:144-49.

Grady DE, and Benson D A, 1983, Fragmentation of Metal Rings by Electromagnetic Loading Experimental Mechanics, 23.4:393-400.

Green, AE, and Adkins JE, 1970, Large Elastic Deformations, Oxford: Clarendon.

Haddow JB, Wegner JL, and Jiang L, 1992, The Dynamic Response of a Stretched Circular Hyperelastic Membrane Subjected to Normal Impact Wave Motion, 16:137-50.

Hallquist JO, and Feng WW, 1975, Dynamic Response of Axisymmetric Hyperelastic Membranes Journal of Applied Mechanics, 42.4:890.

Hopkins IL, and Hamming RW, 1957, On Creep and Relaxation Journal of Applied Physics, 28.8:906-09.

Hudson GE, 1951, A Theory of the Dynamic Plastic Deformation of a Thin Diaphragm Journal of Applied Physics, 22.1:1.

Johnson GR and Cook WH, 1985, Fracture characteristics of three metals subject to various strains, strain rates, temperatures and pressures, Engineering Fracture Mechanics, 21, 31-48.

Knowles JK, 2002, Impact-Induced Tensile Waves in a Rubberlike Material SIAM Journal on Applied Mathematics, 62.4 :1153.

Laney CB, 1998, Computational Gasdynamics, Cambridge: Cambridge UP.

LeVeque R, 1997, Wave Propagation Algorithms for Multidimensional Hyperbolic Systems Journal of Computational Physics, 131.2:327-53.

LeVeque RJ, 2002, Finite-volume Methods for Non-linear Elasticity in Heterogeneous Media International Journal for Numerical Methods in Fluids, 40.1-2:93-104.

Lopez-Pamies O, 2010, A New I1I1-based Hyperelastic Model for Rubber Elastic Materials Comptes Rendus Mécanique, 338.1:3-11.

Malvern LE, 1951, Plastic wave propagation in a bar of material exhibiting a strain-rate effect, Quarterly of Applied Mathematics, 8, 405.

Mathews W, 2004, Services test spray-on vehicle armor, Army Times, May 3.

Morales SA, Albrecht AB, Zhang H, Liechti KM, and Ravi-Chandar K, 2011, On the Dynamics of Localization and Fragmentation: V. Response of Polymer Coated Al 6061-O Tubes International Journal of Fracture, 172:161-85.

Mott NF, 1947, Fragmentation of Shell Cases Proceedings of the Royal Society A: Mathematical, Physical and Engineering Sciences, 189.1018:300-08.

Niemczura J and Ravi-Chandar K, 2011, On the response of rubbers at high strain rates: I: Simple waves Journal of the Mechanics and Physics of Solids, 59:423-442.

Ogden RW, 1972, Large Deformation Isotropic Elasticity - On the Correlation of Theory and Experiment for Incompressible Rubberlike Solids Proceedings of the Royal Society A: Mathematical, Physical and Engineering Sciences, 326.1567:565-84.

Patel P, Gilde GA, Dehmer PG, McCauley JW, 2000, Transparent armor. AMPTIAC Newsletter, 4:1-9.

Qiao J, Amirkhizi AV, Schaaf K, Nemat-Nasser S and Wu G, 2011, Dynamic mechanical and ultrasonic properties of polyurea, Mechanics of Materials, 43:598-607.

Roland CM, Twigg JN, Vu Y and Mott PH, 2007, High strain rate mechanical behavior of polyurea, Polymer, 48:574-578.

Schapery RA, 1984, Correspondence Principles and a Generalized J Integral for Large Deformation and Fracture Analysis of Viscoelastic Media International Journal of Fracture, 25.3:195-223.

Shirani A and Liechti KM, 1998, A Calibrated Fracture Process Zone Model for Thin Film Blistering Mechanics of Solids, Structures, and Materials, 93:281-314.

Shockey D, Bergmannshoff D, and Curran DR, 2008, Failure Physics of Glass during Ballistic Penetration, presentation at the 32nd International Conference & Exposition on Advanced Ceramics & Composites, January 27-February 1, Daytona Beach, FL.

Strassburger E, 2009, Ballistic testing of transparent armour ceramics. Journal of the European Ceramic Society, 29, 267-273.

Subhash G, and Ravichandran G, 2000, Split Hopkinson Pressure Bar Testing of Ceramics, ASM Handbook, Mechanical Testing and Evaluation, Volume 8, ASM International, 497- 504.

Tobe T, Kato M, and Obara H, 1978, Energy Consumption at Underwater Exploding-Wire Gap in Electric Discharge Metal Forming Bulletin of JSME, 21.162:1780-786.

Tobe T, Kato M, and Obara H, 1978, Metal Forming by Underwater Wire Explosion: 1st Report, An Analysis of Plastic Deformation of Circular Diaphragms under Impulsive Loading Transactions of the Japan Society of Mechanical Engineers, 44.382:2166-173.

Tobe T, Kato M, and Obara H, 1979, Pressure Pulses Produced by Underwater Wire Explosions in Electric Discharge Metal Forming Bulletin of JSME, 22.166:613-19.

Vermorel R, Vandenberghe N, and Villermaux E, 2009, Impacts on Thin Elastic Sheets, Proceedings of the Royal Society A: Mathematical, Physical and Engineering Sciences 465.2103:823-42.

von Karman T, Duwez P, 1950, The propagation of plastic deformation in solids, Journal of Applied Physics, 21, 987-994.

Whitham, GB, 1974, Linear and Nonlinear Waves. New York: Wiley.

Xue L Mock W Jr, and Belytschko T, 2010, Penetration of DH-36 Steel Plates with and without Polyurea Coating Mechanics of Materials, 42.11:981-1003.

Yang WH and Feng WW, 1970, On Axisymmetrical Deformations of Nonlinear Membranes Journal of Applied Mechanics, 37.4:1002

Yi J, Boyce MC, Lee GF, Balizer E, 2006, Large deformation rate-dependent stress–strain behavior of polyurea and polyurethanes, Polymer, 47:319–329

Youssef G and Gupta V, 2011, Dynamic Response of Polyurea subjected to nanosecond rise-time stress waves, Mechanics of Time Dependent Materials, DOI 10.1007/s11043-011-9164-7.

Zhang H and Ravi-Chandar K, 2007, On the Dynamics of Necking and Fragmentation – I. Real-time and Post-mortem Observations in Al 6061-O International Journal of Fracture, 142.3-4: 183-217.

Zhang H and Ravi-Chandar K, 2008, On the Dynamics of Necking and Fragmentation—II. Effect of Material Properties, Geometrical Constraints and Absolute Size. International Journal of Fracture, 150.1-2:3-36.

Zhang H, Liechti KM, and Ravi-Chandar K, 2009, On the dynamics of necking and fragmentation: III. Effect of cladding with a polymer. International Journal of Fracture, 155, 101-118.

Zhang H and Ravi-Chandar K. 2010, On the Dynamics of Localization and Fragmentation - IV. Expansion of Al 6061-O Tubes International Journal of Fracture, 163 : 41-65

Zhao J, Knauss WG, and Ravichandran G, 2007, Applicability of the time-temperature superposition principle in modeling dynamic response of a polyurea Mechanics of Time-Dependent Materials, 11, 289-308.

Zhou M and Clifton RJ, 1996, Dynamic ductile rupture under conditions of plane strain International Journal of Impact Engineering, 19, 189-206.